Inkjet Printing of Thin Film Transistors

You LI

Supervisors: Prof Christopher Tuck

Prof Richard Hague

Prof Ricky Wildman

Dr Saleh Ehab

Thesis submitted to the University of Nottingham for the degree of Doctor of Philosophy (PhD)

May 2021

Abstract

Currently, the fabrication of functional electronic elements by additive manufacturing (AM) is beneficial due to the minimum structural limitations required for this flexible process. As a result, products can be customised and produced to meet the requirements for specific applications, such as in the medical field and automotive industry. However, thus far, only a few varying electronic devices, such as resistors and capacitors, are manufactured by AM technology due to a limited range of processable materials and the insufficient understanding of the fabrication process. Therefore, to broaden the opportunities of printed electronics in academia and industry, it is imperative to investigate a wider range of useable materials and comprehensively understand the AM process. In this thesis, attention is focused on various aspects involved in the fabrication of thin-film transistors (TFTs) by inkjet printing technology, from ink development to product characterisation, and a comprehensive understanding of this process is provided.

For this research, silver, polyimide, tripropylene glycol diacrylate (TPGDA) and graphene oxide inks are prepared and characterised. In addition, the inter-relation between printing mechanisms, process parameters and sintering approaches of these inks is investigated. Printing performances revealed that stable printing processes are achieved for silver, PI and TPGDA inks; however, printed graphene-oxide flakes are located non-uniformly on the printed specimens due to the Marangoni effect.

Graphene-based TFTs are partially and fully produced by inkjet printing technology. Electrical characterisation results indicate that partially printed

graphene transistors on a silicon wafer exhibit good performance, while fully printed graphene transistors need to be modified due to their output performance. Apart from the investigation on printable inks and transistors, indium selenide (InSe) is examined by the inkjet printing of conductive electrodes on generated InSe flakes to form characterising elements such as Hall bar. The material, which exhibits photosensitive and semiconducting properties during characterisation, is expected to be developed into printable inks for the fabrication of printed semiconductor devices and optoelectronic applications.

Significant achievements of inkjet printing for functional electronic applications are examined. Partially printed graphene TFTs are fabricated by a single process, and UV light is employed for the reduction of graphene oxide in inkjet-printed TFTs for the first time to the best of our knowledge. Meanwhile, InSe is also investigated in this thesis. All these findings provide opportunities for potential printed electronics in the future.

Acknowledgement

The journey of this PhD is tough and challengeable. Without the encouragements and guidance from my family, supervisors, colleagues and friends, this thesis would not have materialized. Therefore, I would like to show my deepest gratitude to people who supported me.

Foremost, I would like to express my greatest appreciation to my family. My father, Shouchun LI and my mother, Daihong XU, give me invaluable support and trust. They make me believe in myself that I am strong enough to overcome all difficulties in my life. Many thanks, and I will never disappoint you. I also say thanks to my wife, Ge ZHAO. Meeting you and marrying you are most worth things in my life. Thanks for your encouragement and understanding in these years. And also thanks for bring my dearest daughter, Willow Xinuo LI, to my life. I will do my best to give you a wonderful life. I love you.

In this PhD, I have found a supervisor, a friend and a guide in my life, Prof Christopher Tuck. Many thanks for your knowledgeable mentoring on my experiments, thesis and also my life. You are the best example for me to learn how to be a kind, aspirant and gentle man. I also want to offer my special thanks to Prof Richard Hague, Prof Ricky Wildman and Dr Saleh Ehab. Thanks for passing me your experiences and suggestions in my PhD, especially when I failed first year review. Your encouragements helped me to build confidence, which is very important at that moment. Many thanks!

I am also deeply grateful to my colleagues who are also my friends, Dr Yinfeng HE, Dr Fan ZHANG, Dr Zuoxin ZHOU, Mr Le MA and Miss Yaan LIU. Thanks for your support and company these years. It is my pleasure to work with you guys. We will be life-time friends in the future.

Contents

List of Figures

List of Tables

Chapter 1. Introduction

1.1 Background

Currently, additive manufacturing (AM), which is also known as 3D printing, is one of the most promising technologies due to its high flexibility and minimum structural limitations (Gebhardt, 2012) (Vaezi, Seitz and Yang, 2013). Depending on different manufacturing mechanisms and material types, AM is classified into seven types: binder jetting, directed energy deposition, material extrusion, material jetting, powder bed fusion, sheet lamination and vat photopolymerization (Gibson, Rosen and Stucker, 2010). Inkjet printing is a typical material jetting technology, which is employed to fabricate products via the layer-by-layer deposition of specific material inks on a target substrate (ASTM International, 2012). Owing to its micron-scale resolution, it can be employed to fabricate micron- and millimetre-sized products in the laboratory and industry, such as printed electronics.

Transistors are one of the most basic semiconductor elements in the field of modern microelectronics. Depending on different structures and working principles, transistors can be mainly categorised into field-effect transistors (FET) and bipolar-junction transistors (BJT). Compared with that of BJT, the structure of FET is more concise and explicit, which is easier to design into a 3D-layered model for inkjet printing. Therefore, FET is expected to be fabricated by inkjet printing technology.

Conductive inks are used to produce FET electrodes. Depending on different solutes, conductive inks are generally classified as nanoparticle inks, organometallic inks and conductive polymer inks (Bidoki *et al.,* 2007). Among

all of the conductive inks, silver nanoparticle inks are attractive due to their high performance stability and conductivity (Kamyshny and Magdassi, 2014) (Rajan *et al.*, 2016). Silver nanoparticle inks are formulated by the dispersion of silver nanoparticles into deionised water or organic solvents such as triethylene glycol monomethyl ether (TGME). Typically, to increase the evaporation speed of solvents and ensure the generation of a conductive film by printed silver nanoparticles, a thermal sintering process is applied after the printing work of silver nanoparticle inks (Jung *et al.*, 2007).

To use polymer inks as dielectric components in FETs, these inks must exhibit excellent dielectric properties and thermal stabilities. Polyimide (PI) and TPGDA are two typical insulation materials that meet these requirements. Typically, PI is prepared by a thermal imidization process from poly(amic acid) (PAA), while TPGDA comprises acrylic monomers (Sroog, 1967) (Frazier, 1995) (Liu, Hsu and Wu, 2003) (Fukukawa and Ueda, 2008) (Zhang *et al.*, 2016) (He *et al.*, 2017). With advantages of a high dielectric performance, cost-effectiveness and durability, PI and TPGDA are interesting not only for 2D but also 3D applications.

Semiconductor materials are also required for fabricating FETs. Currently, silicon is the predominant semiconductor material for conventional transistors due to its cost-effectiveness. However, a novel semiconductor material, namely graphene, is more attractive due to its significantly high electron mobility and remarkable mechanical properties (Geim and Novoselov, 2007) (Mohan *et al.*, 2018). Graphene is mainly synthesised by mechanical exfoliation and the thermal reduction of graphene oxide (GO) (Kuilla *et al.*, 2010) (Yang *et al.*, 2018). However, both approaches exhibit low efficiencies due to the increased

times required (Gao *et al.,* 2009) (Shen and Lua, 2013). Therefore, in the last few years, the variation of the laser-based reduction of GO has been investigated to improve the efficiency of the synthetic process (Gao *et al.,* 2011) *(Smirnov et al.,* 2011).

In recent years, another 2D semiconductor material, indium selenide (InSe), also has attracted attention. Owing to its remarkable electrical and photosensitive properties, InSe is a candidate for not only high-performance transistors but also optoelectronic applications such as photodetectors and optoelectronic transistors (Tamalampudi *et al.,* 2014) (Chen, Biscaras and Shukla, 2015). However, limited studies on the printability of InSe are available, and InSe is not yet fabricated by inkjet printing technology to the best of our knowledge.

In this thesis, the inkjet printing of printed electronics, especially FET, is focused. Meanwhile, owing to the limitations of processing inks available for inkjet printing processes, the ink formulation, printability studies, optimisation of processing parameters and characterisation of silver, PI, TPGDA, graphene and InSe are also examined and reported in this thesis.

1.2 Significance and Novelty of the Research

Since the report of the concept of inkjet printing technology in 1965, it has been developing rapidly in the past 65 years (Sweet, 1965). However, it is still far from being an alternative to conventional manufacturing due to the limited range of usable materials and product types. In this research, materials such as PI, TPGDA and graphene are investigated, and corresponding inks are also developed and characterised. Meanwhile, by printing these developed inks, various functional electronic applications are successfully fabricated, which

would generate further opportunities for the use of inkjet printing technology in the laboratory and industry.

Thus far, FETs are mainly fabricated by conventional manufacturing technologies such as surface mount technology and injection moulding. As a result, the fabrication of customised and flexible transistors is limited and expensive. Inkjet printing technology can be employed to solve these issues. However, this technology is still challenging because different materials are required for the fabrication of transistors due to their complicated structure. Therefore, only partially printed FETs have been reported. In this thesis, investigations on partially printed FETs and fully printed FETs are reported. With a better understanding of fabricating FETs, the production of integrated circuits and other electronic devices by inkjet printing technology can be realised.

As graphene is a novel semiconductor material with promising properties, it is a significant challenge to develop graphene ink that in turn can enable the fabrication of graphene specimens by inkjet printing technology. In this research, graphene-oxide ink is developed and characterised due to the difficulty associated with the dispersion of pure graphene flakes in liquids. Then, the printed GO specimens are reduced to reduced graphene oxide (rGO). Therefore, the successfully formulated inks satisfy the demands of graphene and GO in the inkjet printing process. Ultraviolet (UV) lasers are employed for GO reduction. Compared to the conventional thermal reduction of GO, the treatment time is significantly reduced, with the thesis demonstrating a high-efficiency GO reduction approach. Therefore, based on the investigation of GO inks and the reduction approach, an increased number of graphene/GO-based applications are expected to be realised via the inkjet printing process in the future.

Meanwhile, in this research, InSe is characterised and used for the fabrication of conductive electrodes on target InSe specimens by inkjet printing technology. The importance of this research is categorised into two aspects: First, the application of inkjet printing to fabricate components on target specimens (especially random or tiny-sized specimens) can be promoted in the future for the investigation of materials. Second, based on characterisation results, InSe is a potential semiconductor material for printed electronics, and it is expected to develop into inks for the inkjet printing process.

1.3 Thesis Aims and Objectives

Overall, the aim of this research is to provide a comprehensive understanding of the application of inkjet printing technology to fabricate functional printed electronics, especially transistors. To achieve this aim, the following objectives are listed:

- To design structures for target functional applications and classify compulsory materials.
- To investigate materials and develop corresponding formulations based on the investigation results.
- To produce functional printed electronics by inkjet printing technology and determine the relationship between structure designs, ink performance or printing mechanisms and properties of final products.
- To reveal the reasons for unsatisfactory performance and optimise the properties of the final products based on the reasons.
- To examine other potential materials and printed electronics for the inkjet printing process

1.4 Thesis Outline/Structure

This thesis comprises eight chapters, which provide a comprehensive understanding of all the research work completed in this PhD research. The outline of this thesis is presented as follows (Figure 1.1):

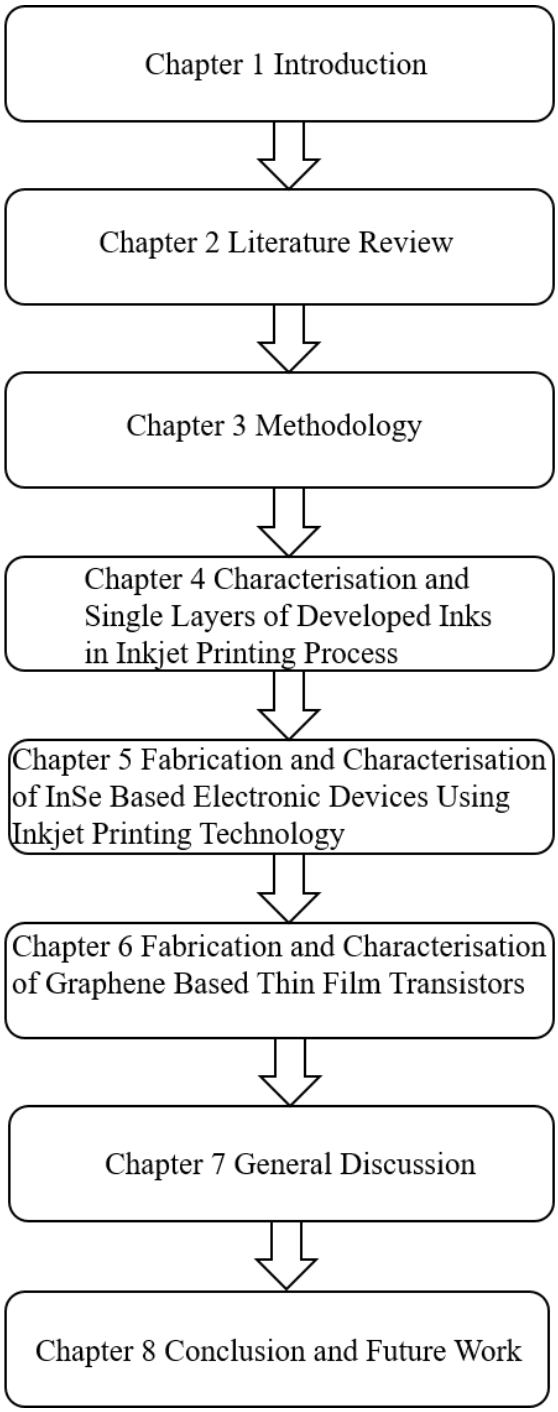

Figure 1.1 Thesis outline.

Chapter 1 provides an overview of this research, including inkjet printing technology, FETs and graphene, followed by its significance and novelty. In addition, the aim and objectives of this PhD research are listed.

Chapter 2 provides a literature review. Chapter 3 starts with the introduction into the development of additive manufacturing (AM) and inkjet printing technology. Next, literature surveys of conductive, insulative and semiconductive inks are presented. As graphene and InSe are two crucial semiconductor materials used in this research, detailed structures, properties and synthetic approaches of the two materials are independently explained after the introduction of semiconductive inks. In the last few sections, the structures and work principles of transistors and other electronic applications are demonstrated because they are aimed to be produced in this research.

Chapter 3 describes all of the materials and methodologies used in this research. The work mechanism of the printer is introduced at the start. Next, the structure design and development work of inks are presented. Finally, characterisation approaches of inks and products are explained.

Chapters 4–6 discuss all of the printing work and characterisation results of the developed inks and fabricated products in this PhD research. Chapter 4 focuses on all of the developed inks. Droplet formations for silver, polyimide, TPGDA and GO inks are examined, and thickness measurement and electrical characterisation are subsequently employed on all of the printed single-layer specimens. Chapter 5 discusses the fabrication and characterisation results for three InSe-based electronic applications, namely a partially printed InSe photodetector, a partially printed InSe Hall bar and a partially printed InSe transistor on a silicon wafer, respectively. As InSe is a photosensitive

semiconductor material, these three printed InSe-based devices are characterised by optical and electrical characterisation methods. Chapter 6 discusses the printing work and characterisation results of the partially printed graphene transistor on a silicon wafer and a fully printed graphene transistor. The measurements are discussed and reasons for these issues are analysed.

Chapter 7 provides a general discussion of this study. The motivation and novelty are introduced at the start of the chapter. After a brief summary of the beneficial outcomes, the contribution of this research to academia and industry is demonstrated.

Chapter 8 provides a full conclusion of this research. All achievements and limitations in this work are highlighted. Furthermore, future work to expand the beneficial outcomes of this study is also discussed.

Chapter 2. Literature Review

2.1 Development of Printed Electronics

Printed electronics can be defined as the fabrication process where printing technologies are utilised to manufacture electronic applications on various substrates (Sílvia *et al*., 2018) (Vimanyu and Patrick, 2020). Albert Hanson was the first to report this concept in 1903 by filing a patent on printed wires and subsequently examining and applying these wires on printed circuit boards (PCBs) (Killeen and Barth, 2003). Compared to traditional electronics fabrication processes (e.g. photolithography), which are subtractive technologies, additive technology is adopted on printed electronics. Therefore, printed electronics are advantageous in terms of fabrication and material efficiency as fewer process steps and less materials are required for the additive technology, as shown in Figure 2.1 (Keskinen, 2012). Currently, although printed electronics are employed in various electronic applications, such as sensors, light-emitting diode (LED) displays and thin-film transistors (TFTs), the process still exhibits tremendous potential for development. According to the latest Electronics Industry Research Reports, the printed electronics market is expected to be worth over $73B by 2027 (Norita *et al*., 2015) (Walker *et al*., 2016) (Wang *et al*., 2016) (Sílvia *et al*., 2018).

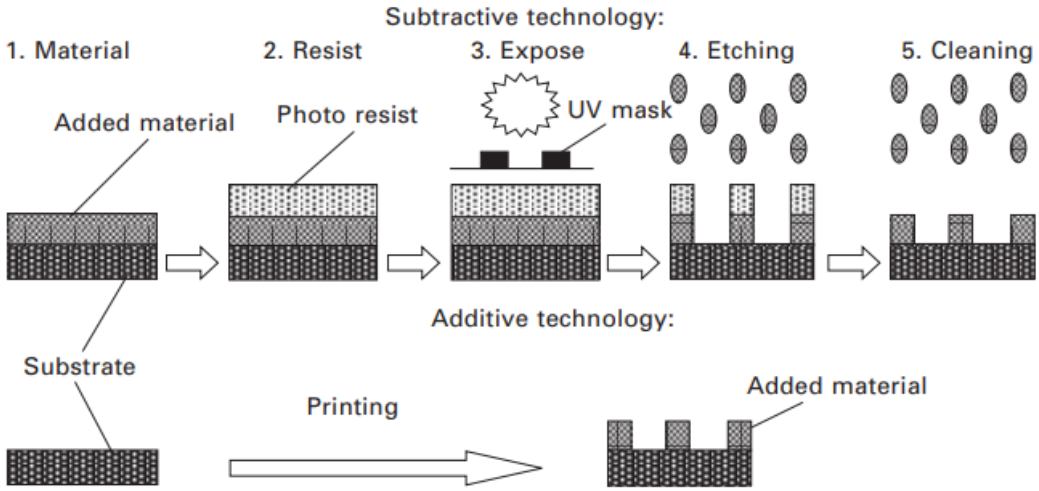

Figure 2.1 Process Steps of Subtractive and Additive Technologies (Keskinen, 2012).

2.2 Printing Technologies

Typically, printed electronics technologies are divided into contact and non-contact techniques depending on whether the substrates are contacted with printing plates (Vimanyu and Patrick, 2020). Several typical contact and non-contact techniques are introduced in the following sections.

2.2.1 Contact Printing Techniques

Screen Printing

Screen printing involves the transfer of a material (i.e. ink) on substrates using a mesh (Dinesh *et al.*, 2020). The mesh is directly contacted with the substrate (Figure 2.2). When the squeegee moves, the ink fills the mesh, and the final image is created (Sílvia *et al*., 2018).

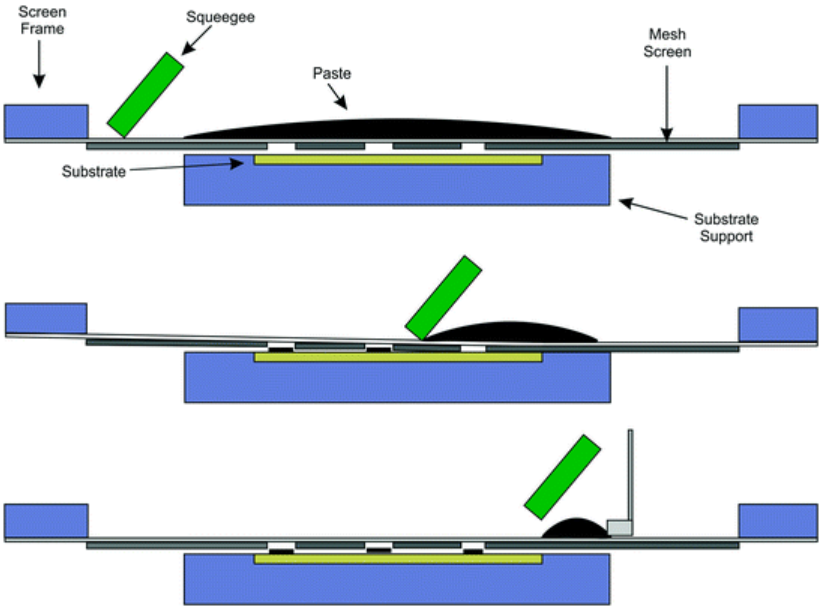

Figure 2. 2 Schematic of the Screen Printing Technology (Christopher et al., 2015).

Currently, screen printing technology is the main printing process due to its high speed and low-cost production (Ochoteco *et al.*, 2010). However, this technology exhibits some limitations and disadvantages. For instance, owing to its resolution ranging from 30 to 100 µm, it is difficult to fabricate high-precision patterns by screen printing technology (Blayo and Pineaux, 2005). Meanwhile, a large amount of materials are wasted due to the continuous process.

Soft Lithography

Soft lithography is classified as a group of printing technologies in which elastomeric materials are used for pattern transfer (Alongkorn and Werayut, 2012). This technology was first introduced in 1989. Since then, it has rapidly developed in the following 30 years (Bain and Whitesides, 1989). Polydimethylsiloxane (PDMS) is the most commonly used elastomeric material in the soft lithography process. PDMS works as a soft stamp and transfers the pattern on a target substrate (Figure 2.3). Patterns of high resolution (ranging

from 30 nm to 100 µm) can be produced by this technique (Qin *et al.*, 2010). However, compared to screen printing, soft lithography is expensive. Meanwhile, this process cannot be employed on non-planar surfaces (Xia and Whitesides, 1998).

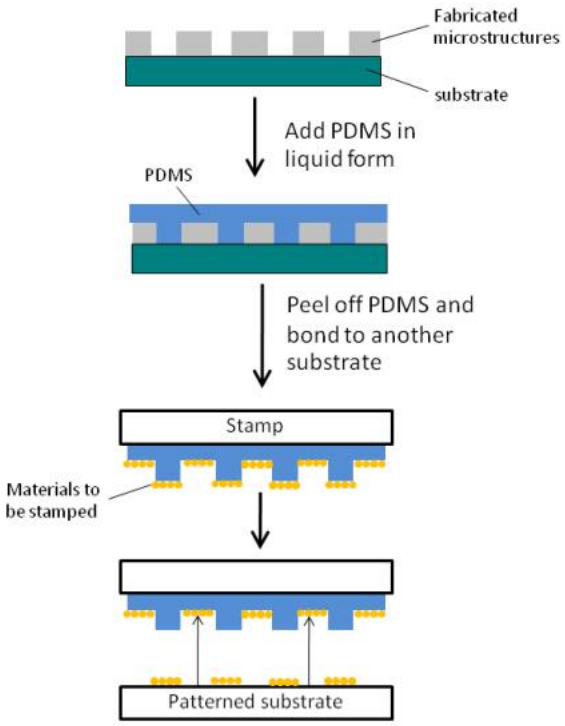

Figure 2. 3 Schematic of Soft Lithography (Alongkorn and Werayut, 2012).

Flexography

Owing to its continuous high-speed fabrication process, flexography has been widely employed as the printing technology in the packaging industry (Rosa, 2015). As shown in Figure 2.4, a ceramic anilox roller is employed in the flexography process to collect the ink from the ink reservoir and then deliver it to the printing plate cylinder for the transformation of a pattern on the target substrates (Blayo and Pineaux, 2005) (Lorenz *et al.*, 2015). Flexography is a simple and rapid process with low maintenance costs. However, the main limitations of this technology include a low resolution, ranging from 30 to 80

µm, and a complicated alignment of multi-layer printed work (Kipphan, 2001) (Sílvia *et al.*, 2018).

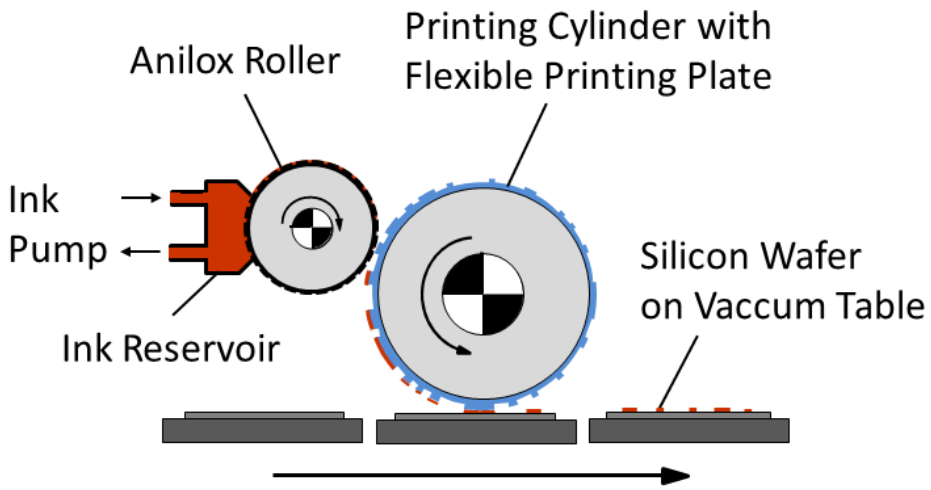

Figure 2.4 Schematic of Flexography (Lorenz et al., 2015).

2.2.2 Non-contact Printing Techniques

Laser Direct Writing

Laser direct writing (LDW) is a direct printing technology, in which patterns are generated without masks or pre-set patterns. As shown in Figure 2.5, lasers are used in the LDW process for the deposition of materials on the donor substrate, and an acceptor substrate is used for the collection of ejected materials (Craig and Alberto, 2007) (Craig *et al.*, 2007). Resolution is the key advantage of LDW: Patterns can be created with dimensions ranging from nanometres to millimetres. Therefore, LDW already has been used for printed electronics such as sensors (Chrisey *et al.*, 2000) (Pique *et al.*, 2003). However, compared to the introduced contact printing techniques, LDW is a high-cost technology due to the expensive equipment (Sílvia *et al.*, 2018).

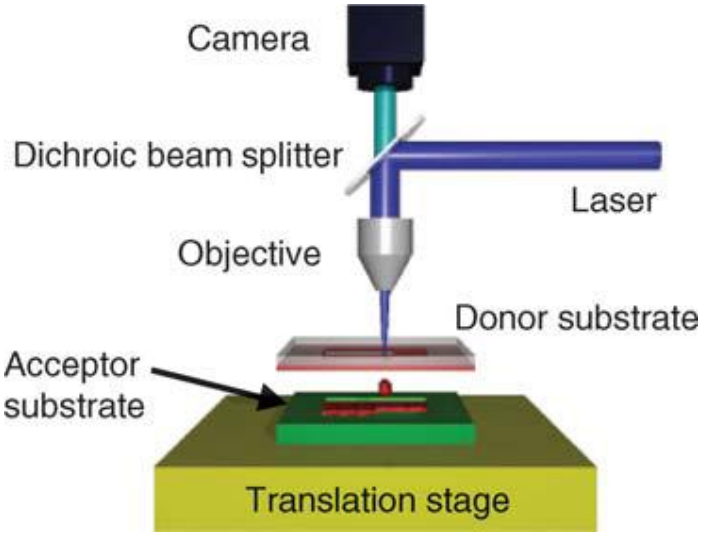

Figure 2.5 Schematic of Laser Direct Writing Technology (Craig et al., 2007).

Inkjet Printing

Inkjet printing, which is classified as material jetting technology, is another non-contact printing technique (Nir *et al.*, 2010). In the inkjet printing process, materials are developed in a liquid form and selectively deposited on the target substrate by a droplet-by-droplet method (Calvert, 2001) (Calvert, Yoshioka and Jabbour, 2004) (Gibson, Rosen and Stucker, 2010) (ASTM International, 2012). Compared to contact printing techniques, inkjet printing technology exhibits the following typical advantages: Non-flat substrates can be applied in the process, and multiple materials can be printed in a single process by simply changing the cartridges (Fuller, Wilhelm and Jacobson, 2002) (Perelaer and Schubert, 2010) (Ando and Baglio, 2011) (Kamyshny, Steinke and Magdassi, 2011). Meanwhile, for polymers that are not processable by lasers, they can be printed by inkjet printing instead of LDW (Sílvia *et al.*, 2018).

In summary, printing technologies are typically categorised into contact and non-contact printing techniques. Most of the contact printing techniques, such as screen printing and flexography, exhibit high efficiency as their processes are

continuous. Currently, contact printing techniques are already applied for printed electronics. For instance, screen printing technology by using flexography also has been employed to fabricate tactile sensors and printed batteries (Ochoteco, 2010) (Adcock and Fenner, 2012).

However, extensive applications of contact printing techniques are limited for several reasons. First, most of the contact printing techniques exhibit low resolution. As mentioned in Section 2.2.1, the resolution range for screen printing is 30–100 μm, while that for flexography is 30–80 μm (Blayo and Pineaux, 2005). Therefore, both techniques are not suitable for the fabrication of nano-scale printed electronics. Second, it is difficult to change the patterns or materials during the contact printing process as the process is continuous. In this case, it is difficult to fabricate printed electronics with complicated structures or multiple materials by contact printing techniques. Finally, as cylinders are made to contact substrates during the printing process, they are easily damaged, leading to high costs.

These issues can be solved by non-contact printing techniques such as LDW and inkjet printing. Compared with that for contact printing techniques, the resolution for non-contact printing techniques is higher (0.7 μm for LDW and 15 μm for inkjet printing technology) (Sílvia *et al*., 2018). Therefore, non-contact printing techniques can be applied for precise printed electronics. Although LDW and inkjet printing technology are advantageous, both these technologies exhibit limitations in terms of materials. For instance, polymers that are not affected by lasers cannot be used in the LDW process, and all materials used in the inkjet printing process need to be developed in the liquid phase (Tiwari, Tiwari and Kim, 2012).

In this PhD research, inkjet printing technology is used for all printing processes. Therefore, in the next sections, details of inkjet printing technology will be introduced.

2.3 Inkjet Printing Technologies

In this section, all details of inkjet printing are summarised. First, the brief development of inkjet printing technology is presented, followed by the two main print-head mechanisms in inkjet printing processes, i.e. continuous and drop-on-demand modes, respectively, along with their advantages and disadvantages. Fluid parameters such as viscosity and surface tension are consequently introduced to explain ink formulation. Finally, jetting parameters are listed to reveal the effect of the jetting performance in the printing process.

2.3.1 Development of Inkjet Printing

Inkjet printing technology involves the generation of material layers by jetting droplets of a specific material ink on the target substrate (ASTM International, 2012). Generally, 2D slice images are printed and then stacked up to form 3D products. This concept was first discussed in the 19th century (Rayleigh, 1878); however, only until 1965, the first continuous inkjet printer was developed by Dr Sweet in Stanford University (Sweet, 1965).

The first commercial 3D inkjet printer was manufactured by Solidscape in 1994, under the name of ModelMaker. As wax converts into printable melts on heating up to 95–115 °C, it is the major jetting material for the printer (Gibson, Rosen and Stucker, 2010). Currently, a number of inkjet printers have been developed and fabricated. Meanwhile, different units are available to add onto the inkjet printers to improve the jetting capacitance and performance. For instance, an

ultraviolet (UV) light source can be installed for the curing of printed polymer inks, providing a wider range of available materials for the inkjet printing process.

2.3.2 Print-head Mechanism

The print head is one of the most crucial components of an inkjet printer because it determines limitations of the printing parameters, such as the maximum printing temperature, in the printing process. Thus far, the working mechanisms of print heads are mainly categorised into two models, i.e. continuous-stream (CS) mode and drop-on-demand (DOD) mode, respectively, which are separately introduced in the next sections (Castrejón-Pita *et al.*, 2013).

Continuous Stream (CS) Mode

Continuous stream (CS) inkjet technology is a conventional printing technique, which is mainly used for marking and coding in industry. First, a steady pressure is applied to the ink reservoir to push a continuous stream of ink out of the nozzles (Figure 2.6). Then, the stream breaks into droplets of ink once it leaves the nozzles, followed by the application of a charging field (Rayleigh, 1878). By modifying the charger of the electrode plate, a variable electrostatic charge is carried by each droplet. Therefore, all of the droplets are steered to the target position by the deflection field—either on the substrate or to the recycle container (Weng *et al.*, 2010).

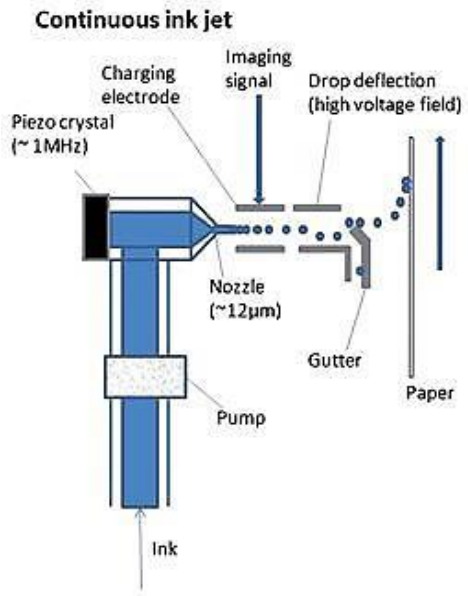

Figure 2.6 Schematic of the continuous-stream mode inkjet print head (Weng et al., 2010).

A high-speed printing process can be achieved due to its high throughput rate of the CS mode. Typically, 64,000 to 165,000 droplets can be ejected per second through the nozzles (De Gans *et al.*, 2004). Because all the nozzles continuously work in the printing process, nozzles are rarely clogged, leading to stable printing. However, printing materials that can be processed by using the CS inkjet system are limited because only a few materials can carry electrostatic charges. Meanwhile, although a recycle container is present within the CS system, a large amount of inks is wasted due to the continuously high volume output. Therefore, the CS model is not widely used in commercial printers.

Drop-on-demand (DOD) Mode

Different from the CS mode, ink droplets are ejected only when required in the drop-on-demand (DOD) mode (Liu and Orme, 2001). Meanwhile, because there is no charging plate, deflection plate or recycle unit in a DOD print head, the structure of a DOD print head is less complex than that of a CS print head.

In the DOD mode, the two individual inkjet printing technologies are further classified as thermal-bubble DOD and piezoelectric DOD. The work principles of thermal-bubble and piezoelectric DOD inkjet printing technologies will be discussed in the following sections.

Thermal-bubble DOD

Mark Naiman was the first to report the thermal-bubble DOD inkjet printing technology in 1965 (Naiman, 1965). Following this report, it was applied widely in the late 20th century due to its simple working mechanism and low fabrication costs. Typically, a heating source is located in the ink chamber of a thermal-bubble DOD device (Figure 2.7). When an imaging signal is applied to the heat source, the ink is heated up to the bubble nucleation temperature, and a bubble is subsequently formed. As the volume of the ink within the ink chamber is reduced due to the expanded bubble, droplets are forced to eject through the nozzles (Cummins and Desmulliez, 2012). After one droplet is ejected, the heating source cools rapidly. Based on the capillary action, the ink chamber is then refilled from the ink channels and ready for the next cycle (Basiricò, 2012). Therefore, the ejection of droplets is controlled by the imaging signal.

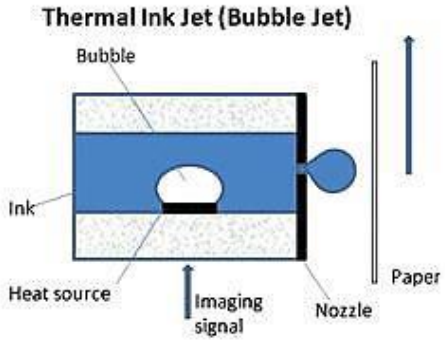

Figure 2.7 Schematic of thermal-bubble DOD print head (Weng et al., 2010).

Although the ejection of droplets in the thermal-bubble DOD printing process can be controlled, some limitations still exist. For instance, a high temperature

of 300°C can be achieved when the heating source is switched on, possible leading to the frequent damage of the nozzles in the thermal-bubble DOD print heads (Gonzalez-Macia *et al.,* 2010). Meanwhile, the high temperature also limits the availability of printable inks: On the one hand, some inks cannot be printed using a thermal-bubble DOD print head due to the rapid evaporation of solvents caused by high temperature. On the other hand, thermal degradation potentially occurs in inks comprising organics or biological materials (Newman, Turner and G. Marrazza, 1992) (Magdassi and Moshe, 2003) (Parashkov *et al.,* 2005). Therefore, the other type of the DOD inkjet printing technology, i.e. piezoelectric DOD, is considered as an alternative approach to the thermal-bubble DOD mode.

Piezoelectric DOD

In comparison to a thermal-bubble DOD system that uses a heat source, mechanical stress is exploited in the piezoelectric DOD system. Thus far, piezoelectric DOD systems are mainly categorised into four types: squeeze mode, bend mode, push mode and shear mode. Although their structures are different, they function by similar principles. As the shear-mode piezoelectric DOD system is used in this PhD research, it is introduced in detail in the following section. Meanwhile, additional information regarding the squeeze mode, the bend mode and push mode can be found in (Stemme, 1972) (Zoltan, 1972) (Kyser and Sears, 1976) (Howkins, 1984).

In 1986, Kenneth Fischbeck and Allen Wright from Xerox Corporation were the first to report about shear-mode piezoelectric DOD print head (Fishbeck and Wright, 1986). Piezoelectric ceramic plates are constructed to connect the ink chambers and nozzles (Figure 2.8). By the application of a signal voltage to the

electrodes, a shear force is generated due to the deformation of the piezo ceramic plate, leading to the ejection of droplets from nozzles. Piezoelectric ceramic plates can revert back to their original position when the voltage signal ends. Then, the ink chamber is refilled by the ink and ready for the next cycle. Currently, shear-mode piezoelectric DOD print heads are commonly used in Xaar and Fujifilm Dimatix printers.

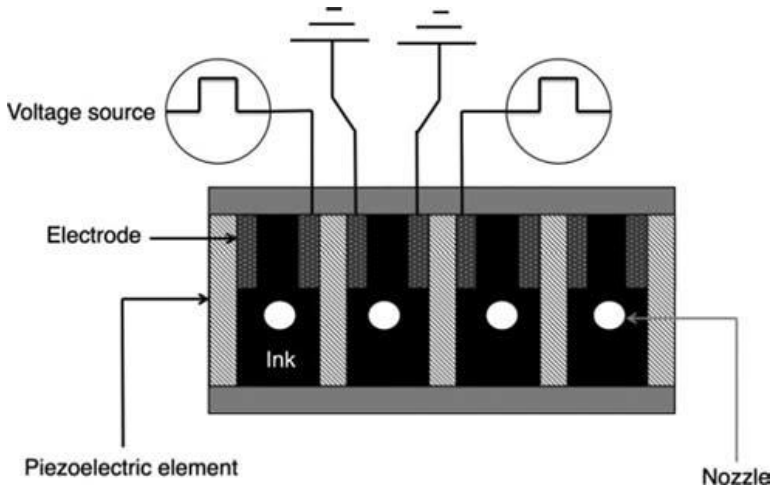

Figure 2.8 Schematic of shear-mode piezoelectric DOD print head (Cummins and Desmulliez, 2012).

Compared to the thermal-bubble DOD mode, the piezoelectric DOD mode is advantageous due to some reasons. First, it is available for a wider range of inks because high temperature is not required in the printing process, which reduces the possibility of thermal degradation. Meanwhile, as heating and cooling steps are absent in the operation cycle, the piezo ceramic plates act more rapidly, leading to a higher-efficiency process. Moreover, complex waveforms can be used in the piezoelectric DOD mode, demonstrating that a more controllable jetting process is available by using piezoelectric DOD mode print heads (Chen and Basaran, 2001). Therefore, piezoelectric DOD mode print heads are used in this PhD research for high-quality controllable printing processes.

2.3.3 Printability Assessment

Once a new ink is developed for the inkjet printing process, fluid properties are always characterised as the first step. Among all fluid properties, viscosity and surface tension are two key factors because they determine the ink printability. In the following sections, details of these two factors and how these factors determine printability will be discussed.

Viscosity

Viscosity is defined as the resistance of a fluid to flow. Based on the relationship between their viscosities and shear rate, fluids are categorised into two groups: When the viscosity of a liquid is independent of the shear rate for a constant temperature, it is classified as Newtonian liquid; otherwise, it is classified as a non-Newtonian liquid (Neil, 1997) (Melissa and William, 2008). In daily life, water is a typical Newtonian fluid, and ketchup is a typical non-Newtonian liquid. In this PhD research, all of the used inks exhibit Newtonian properties.

As mentioned previously, viscosity plays a crucial role in the inkjet printing process. For instance, if the viscosity of an ink is extremely low (<0.002 Pa·s), the ink flows easily from the nozzles without being controlled by input signals. However, if the viscosity of an ink is high (>0.1 Pa·s), it is disadvantageous due to the high energies required to overcome the internal friction (Sílvia *et al.*, 2018). In this case, if the printer applies insufficient energy, droplets are not formed, and the ink cannot be printed.

Viscosities can be modified by adjusting experimental temperatures: By the application of a high temperature, the attractive binding energy between molecules is reduced due to the increased activity of molecules, subsequently leading to a decrease in the viscosity (Vadillo *et al.*, 2010). Therefore, inks with

high viscosities are always printed under thermal treatment in the inkjet printing process to allow for the high viscosities to be within a printable range.

Surface Tension

Surface tension is defined as the tendency of fluid surfaces to form the minimum surface area. It is mainly exploited to determine the energy for creating a new droplet surface (Chan, 1993). When the viscosity of an ink is in printable range, the printability is further determined by surface tension. Owing to the similar backward principle of molecular movement, the surface tension of an ink tends to decrease with the increase in the experimental temperature. Therefore, heating or thermal treatment is a widely used approach for the printability optimisation process of inks as viscosity and surface tension are adjusted.

Printability Index

Besides viscosity and surface tension, ink printability is also affected by other parameters, such as ink density and nozzle diameter. Therefore, to help to indicate the printability of an ink, a printability index (Z number), which is related to Reynolds (Re) number, Weber (We) number and Ohnesorge (Oh) number, is introduced (Ainsley, Reis and Derby, 2002). Their corresponding equations are shown as follows:

$$Re = \frac{v\rho r}{\mu} \tag{1}$$

$$We = \frac{v^2\rho r}{\gamma} \tag{2}$$

$$Oh = \frac{\sqrt{We}}{Re} = \frac{\mu}{\sqrt{\rho r\gamma}} \tag{3}$$

$$Z = \frac{1}{Oh} = \frac{\sqrt{\rho r\gamma}}{\mu} \tag{4}$$

where v is the droplet velocity, ρ is the density of the ink, r is the characteristic length, which is typically the nozzle diameter, μ is the viscosity of the ink and γ is the surface tension of the ink. Generally, when the Z number of an ink lies between 1 and 10, the ink is considered to be printable. When the Z number is extremely high (Oh < 0.1), satellite droplets are formed in the inkjet printing process. However, if the Z number is extremely low (Oh > 1), the stream does not break up into small droplets due to viscous forces (Daly *et al.*, 2015). Figure 2.9 summarises the schematic of the relationship between stable printing and printability factors :

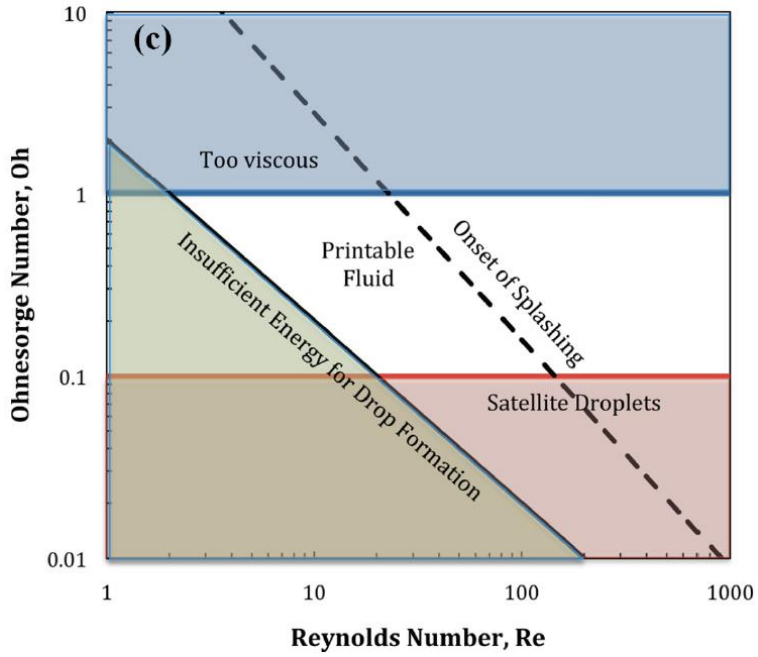

Figure 2.9 Schematic summarising the relationship between stable printing and printability factors (McKinley and Renardy, 2011). Stable printing are affected by both Reynolds number and Ohnesorge number.

The printability index cannot be applied on all inks. It is considered as a guide rather than a law used for the identification of initial materials (Gibson, Rosen and Stucker, 2010). For instance, with a high surface tension of 72.8 mN/m and a low viscosity of 1 mPa·s, water exhibits a printability index of 39.1, which is

considerably greater than the maximum range of the printability index (10). However, water can be inkjet-printed by waveform modification.

2.3.4 Jetting Parameters

Jetting voltage, jetting temperature and jetting waveform are concluded to be the major jetting parameters in the inkjet printing process. These parameters are crucial because the stability of the inkjet printing process is significantly affected by them. In the following parts, details of these factors are introduced separately.

Jetting Voltage

Jetting voltage, which is also called the firing voltage, is typically utilised in the inkjet printing process to control the jetting pressure in the print heads. As mentioned in Section 2.3.2, when the jetting voltage signals are applied on piezoelectric ceramic plates, the drops are ejected due to the deformation of the ink chamber. In the print heads, an increased amount of energy is imparted to generate the droplets by the application of a high jetting voltage. The imparted energy ($E_{imparted}$) is composed of three parts:

$$E_{imparted} = E_{loss} + E_{surface} + E_{kinetic} \quad (5)$$

where E_{loss} is the energy lost (transferred into thermal energy), $E_{surface}$ refers to the energy used to form the new droplet surface and $E_{kinetic}$ is the energy required to eject the droplet. According to equation 5, the imparted energy is affected by the surface tension ($E_{surface}$) and viscosity (E_{loss}) of the ink. Therefore, jetting voltage also is affected by the printability index.

Jetting Temperature

Jetting temperature is another key factor in the inkjet printing process. As explained in Section 2.3.3, viscosity and surface tension are reduced by the

application of a high jetting temperature (Seeton, 2006). Therefore, the printability index is affected by jetting temperature. Moreover, based on Equation 5, by the application of a high jetting temperature, a low imparted energy is required in the inkjet printing process due to the reduced E_{loss} (related to viscosity) and $E_{surface}$ (related to surface tension). Therefore, the jetting voltage is also related to the jetting temperature.

Jetting Waveform

A jetting waveform is typically designed for determining the deformation level of the piezo ceramic plates. Because droplets are ejected by the deformation of the piezoelectric ceramic plates, the frequency and maximum shearing force for droplet ejection can be controlled by modifying the jetting waveform (Gan *et al.*, 2009). Figure 2.10 shows an example of a typical jetting waveform.

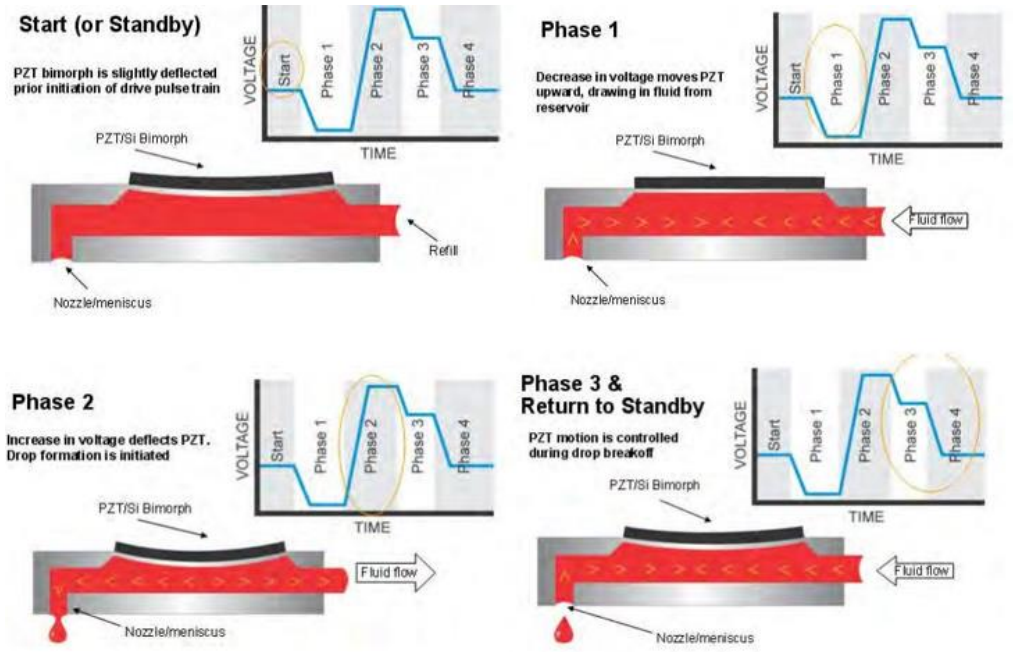

Figure 2.10 Schematic of the work principle of a jetting waveform (FUJIFILM, 2012).

In this schematic, a PTZ (lead zirconate titanate) is used as the piezoelectric ceramic plate. The entire cycle of this jetting waveform is composed of four parts: At the standby position, the PTZ is slightly deformed before the start of the jetting pulse. In phase 1, a low voltage is applied to the PZT, bringing the plate back to the horizontal position. At this stage, the ink chamber exhibits the maximum volume. Subsequently, a rapid increasing voltage is applied in the phase 2. The PZT plate deflects inwardly and renders a large pressure to the ink chamber. The volume of the ink chamber is reduced, and a droplet is ejected through the nozzle. At the final stage, the voltage is decreased again to the original standby level. The ink chamber decompresses, and the cartridge is refilled due to the increase in the chamber volume. Once a cycle is finished, the next cycle repeats when the following voltage signal is delivered.

2.3.5 Droplet Deposition

In the droplet deposition process, the printing performance of printed patterns is determined by two major factors: drop spacing and substrate temperature. These two factors exhibit different effects: the resolution of the printed pattern is mainly decided by the droplet spacing, and the evaporation speed of the remaining solvents in the printed patterns, which is affected by substrate temperature. In this section, both parameters are introduced.

Droplet Spacing

Droplet spacing is defined as the internal distance between the two printed droplets. It is a key factor in the inkjet printing process, which is related to the resolution of a printed pattern (Wilfried Linder, 2016) (Equation 6):

$$Drop\ Spacing[\mu m] = \frac{25400}{Resolution[dpi]} \tag{6}$$

Generally, when a single droplet is printed on the substrate, the droplet size is measured. Then, the suitable droplet spacing is calculated on the basis of the measured results. Generally, a 40% overlap is employed for all of the developed inks in the inkjet printing process to achieve uniform patterns because if the droplet spacing is considerably greater than the diameter of the droplets, the printed droplets are not connected, and gaps are observed in the printed pattern. However, if the drop spacing is extremely small, the printed ink will spread and swell due to the large volume.

Substrate Temperature

Because most inks are based on solvent, substrate temperature, which affects the evaporation speed of the solvents, plays a key role in the inkjet printing process (Kang and Oh, 2016). For instance, if the substrate temperature is low for some inks with a relatively high evaporation temperature, the latest printed ink will merge with the previous landed ink to reduce the surface energy, affording an irregular pattern. However, if the substrate temperature is extremely high, solvents are immediately evaporated when the droplets are still at the nozzle, possibly leading to clogged nozzles (Teichler *et al.,* 2011). Therefore, it is crucial to find and set an optimum substrate temperature in the inkjet printing process to achieve high-quality jetting performance.

2.4 Inks for Inkjet Printing

Functional inks are important in the inkjet printing technology process, especially for printed electronics. Typically, these printable inks are categorised into metallic inks and non-metallic inks (such as graphene inks and polymer inks). However, in this literature review, inks are classified as conductive, insulating and semiconducting groups because they are used for the fabrication

of printed electronics in this PhD research. Therefore, in the following sections, the detailed classification of conductive, insulating and semiconducting inks, as well as several typical inks from each classification, are introduced.

2.4.1 Classification of Conductive Inks

Conductive inks are always used to form conductive tracks for printed electronics. Currently, a large variety of materials have been developed into conductive formulations in the inkjet printing process. Based on different colloidal suspensions, these inks are classified into three groups: nanoparticle inks, organometallic inks and conductive polymer inks (Bidoki *et al.*, 2007). Advantages, disadvantages and typical inks of each group are reviewed.

Nanoparticle Inks

Nanoparticle inks are defined as suspensions of nanoparticles dispersed in water or an organic solvent (Cummins and Desmulliez, 2012). This type of ink is widely used because nanoparticles can be produced in bulk. Metallic nanoparticles, such as silver and gold, are typically selected for nanoparticle inks. Both of these nanoparticles exhibit a relatively low electrical resistivity (silver: 1.59×10^{-8} Ω·m; gold: 2.44×10^{-8} Ω·m) and rarely react with other printed materials (Molesa *et al.*, 2003) (Gans, Duineveld and Schubert, 2004) (Kamyshny, Steinke and Magdassi, 2011) (Li *et al.*, 2012). Therefore, silver and gold inks are commonly used in the inkjet printing process to form conductive channels. However, nanoparticle inks still exhibit some limitations. For instance, nozzles are easily clogged when nanoparticle inks are used because the suspended nanoparticles tend to agglomerate in the ink. To resolve this issue, all nanoparticle sizes are required to be 100 times less than the nozzle diameter to avoid blockage (Cummins and Desmulliez, 2012).

Organometallic Inks

Organometallic ink is another conductive ink used in the inkjet printing process. Different from nanoparticle inks, organometallic inks are solutions instead of nanoparticle suspensions. Therefore, organometallic inks are advantageous because the clogging of nozzles does not occur during the printing process (Tekin *et al.,* 2008). Several materials can be developed as organometallic inks. For instance, in 2006, Smith has reported inks comprising silver organic compounds (Smith *et al.,* 2006). Although the ink can be printed at room temperature, thermal treatment at 150 ℃ is required to reduce the printed silver-containing organometallic pattern to silver tracks. Currently, gold-, copper- and nickel-based organometallic inks are already developed and used. More information can be found in previous studies (Nur *et al.,* 2002) (Rivkin *et al.,* 2002) (Rozenberg *et al.,* 2002) (Dearden *et al.,* 2005).

Conductive Polymer Inks

Conductive polymers are the last type of the predominantly used conductive inks in the inkjet printing process. These polymers are widely used in sensing devices because the electrical properties of conductive polymers are sensitive to environmental factors, including humidity and air (Persaud, 2005) (Weng *et al.,* 2010). Poly(3,4-ethylenedioxythiophene) (PEDOT) is one typically examined conductive polymer due to its high conductivity (400–600 S/cm) and thermal stability (up to 230 ℃) (Chronakis, Grapenson and Jakob, 2006). However, it is still not widely used for practical applications due to insolubility in common solvents (Yin *et al.,* 2010). More information about conductive polymer inks can be found in previous studies (Mortimer, Dyer and Reynolds, 2006) (Ryu *et al.,* 2007) (Gamerith *et al.,* 2007) (Meixner *et al.,* 2008).

2.4.2 Sintering of Conductive Inks

Sintering is typically used in the inkjet printing process, especially for conductive inks. This technique is always applied during or after the printing stage. Sintering exhibits two major functions. On the one hand, it can be employed to improve the electrical and mechanical properties of printed patterns. For instance, nanoparticles are tightly connected to each other due to the sintering stage, leading to a more conductive printed film. On the other hand, a sintering stage is required for the reduction of organometallic inks to form metallic films (Jung *et al.*, 2007). Thermal, electrical, photonic and microwave sintering are the most widely used approaches, which are introduced in the following sections (Cummins and Desmulliez, 2012).

Thermal Sintering

Thermal sintering generally refers to treatment at a high temperature (typically >200 °C) and a long processing time (typically >30 min). It is commonly employed due to its simplicity: The entire substrate is integrated heated in thermal sintering. However, because thermal sintering is not an area-specific treatment, the compatibility of this approach is also limited. For instance, some polymer substrates cannot be heated at a high temperature or for a long sintering time (Kang *et al.*, 2010). The printing performance is also another limitation. As a large volume of the printed ink is rapidly evaporated as a result of thermal treatment, cracks may be formed on the printed specimens (Bordia and Jagota, 1993) (Lee, Oh and Bae, 2010).

Electrical Sintering

Electrical sintering is designated as a resistance heat treatment. Energy is generated by setting a voltage and current on printed conductive tracks (Allen *et*

al., 2008). Compared to thermal sintering, electrical sintering is a high-efficiency approach because it typically takes less than 1 min for the entire sintering process. In addition, it is advantageous because it can be employed on specific areas due to the controllable magnitude and position of the applied voltages (Alastalo *et al.,* 2011). However, as the printed tracks are in contact with the probes of the voltage supplier in electrical sintering, this approach is not compatible for all applications. For instance, in case of using tiny printed specimens, space is not available for the probes, and electrical sintering cannot be applied (Allen *et al.,* 2011).

Photonic Sintering

Photonic sintering refers to treatment using lasers and other light sources. It is mainly used on specific materials that can absorb light to generate energy. In this case, the temperature of the specimens rapidly increases by the application of photonic sintering. (Yun *et al.*, 2008) (Kang *et al.*, 2011) (Rapp *et al.*, 2011). The performance of photonic sintering is affected by several factors, including thermal conductivity of the printed material and substrate, light intensity and light absorption rate of the printed material, etc. Therefore, photonic sintering with different light sources are used for different applications. Based on previous studies, flash lamps are used for large-area sintering, while lasers are ideal for small-area sintering (Chung *et al.*, 2004) (Ko *et al.*, 2007) (H. S. Kim *et al.*, 2009) (Yung *et al.*, 2010). Because the processing time of photonic sintering (typically less than 1 min) is always less than that of thermal sintering, photonic sintering is considered to be an alternative approach to thermal sintering in the inkjet printing process (Cummins and Desmulliez, 2012).

Microwave Sintering

Microwave sintering is a rapid sintering process using a microwave radiation of ~2.54 GHz (Perelaer, De Gans and Schubert, 2006). Because polymers are almost transparent to microwaves, microwave sintering is widely used on printed metallic films on polymer substrates, leading to the maximum absorption of microwaves by the printed metallic films (Perelaer *et al.,* 2012).

In this PhD research, thermal and photonic sintering are used for printed specimens based on properties of the printable materials.

2.4.3 Silver Nanoparticle Ink

Silver, gold and copper are three metals with high conductivities (silver: 6.3×10^7 S/m; gold: 4.1×10^7 S/m; copper: 5.8×10^7 S/m) (Molesa *et al.,* 2003) (Haffarzadeh and Zervos, 2012) (Li *et al.,* 2012). All of these metals can be formulated into conductive nanoparticle inks for the inkjet printing process. Among these three metals, copper is the least expensive, while gold is the most expensive (gold: 1000 dollars/ounce; silver: 20 dollars/ounce; copper: 0.20 dollars/ounce) (Vimanyu and Patrick, 2020). However, copper inks have to be printed under low-oxygen conditions in the inkjet printing process due to the facile formation of copper oxides. Therefore, silver nanoparticle inks are more widely used in printed electronics because silver is more stable (compared to copper) and a cheaper (compared to gold) conductive material (Gans, Duineveld and Schubert, 2004) (Haffarzadeh and Zervos, 2012).

Silver nanoparticles are mainly dispersed in deionised water and/or organic solvents to form silver nanoparticle inks (Iravani *et al.,* 2014) (Zhang *et al.,* 2016). Ethylene glycol and triethylene glycol monomethyl ether are two typically used organic solvents for silver nanoparticle inks because they can be

added into deionised water to prevent the rapid evapouration of silver nanoparticle inks around the nozzles (Balantrapu, McMurran and Goia, 2010). Meanwhile, owing to the high surface tension of deionised water (72 mN/m at room temperature), a surfactant (typically ethanolamine) also may be added to the ink to adjust the overall surface tension of silver nanoparticle inks to meet the printable requirements of printers (Fernandes *et al.,* 2020). Currently, various commercial silver nanoparticle inks have been developed and used in the inkjet printing process with high-quality performance (Magdassi and Moshe, 2003) (Bidoki *et al.,* 2007) (Rajan *et al.,* 2016). In this PhD research, commercial silver nanoparticle ink (Silver Jet Ink, Advanced Nano Products Co., Ltd) is employed for producing conductive tracks.

2.4.4 Development of Insulating Inks

Insulators are crucial components in printed electronics such as capacitors and transistors because they are used to ensure that the separated conductive parts are not connected to each other. Although solid insulators (such as silicon oxide) are typically used in practical electronic applications due to their low costs and high dielectric strength (silicon oxide: 10^7 V/cm), these insulators are not always used in inkjet-printed electronics because they are difficult to develop into ink type (Takano *et al.,* 2010). Therefore, polymers are mainly used in the inkjet printing process as insulating inks (Ginder *et al.,* 1987) (Shin and Kim, 2009) (Caputo *et al.,* 2014).

Poly(4-vinylphenol) (PVP) is one of the most commonly used insulating materials for printed electronics (Lee *et al.,* 2006) (Noh *et al.,* 2006) (Gu and Kane, 2008). Owing to its hydrophilic property, PVP can be easily formulated into insulating inks (Paola and Lolanda, 2020). Therefore, PVP inks are used on

different printed electronics (Fan *et al.*, 2016) (Vimanyu and Patrick, 2020). For instance, in 2002, Klauk et al. have reported spin-coated PVP dielectric layers in thin-film transistors (Klauk *et al.*, 2002). However, printed PVP dielectric films exhibit limitations under ambient conditions due to the remaining hydroxyl groups (attracting water), possibly degrading the insulating performance (Kim, Han and Song, 2008) (Umeda, Kumaki and Tokito, 2008). Therefore, additional insulating materials, such as polyimide (PI), tripropylene glycol diacrylate (TPGDA), polydimethylsiloxane (PDMS) and polyaniline, have attracted attention (Epstein *et al.*, 1987) (Ginder *et al.*, 1987) (Caputo *et al.*, 2014) (Zhang *et al.*, 2016) (He *et al.*, 2017). PI and TPGDA are selected in this PhD research due to their excellent dielectric properties and facile preparation in our laboratory (Centre for Additive Manufacturing).

2.4.5 Polyimide and Tripropylene Glycol Diacrylate

In 1965, DuPont reported the development of polyamides (Sroog, 1967). Polyamides typically refer to a class of ring-chain polymers. Figure 2.11 shows their typical chemical structure (Diaham *et al.*, 2009). As polyimides are durable materials with excellent dielectric properties ($2.2 \times 10^9\ V/cm$) and thermal stability (>500 ℃), they are widely used currently in micro-electro-mechanical systems (MEMS) devices as well as in other microelectronic applications (Frazier, 1995) (Fukukawa and Ueda, 2008) (Arevalo *et al.*, 2015).

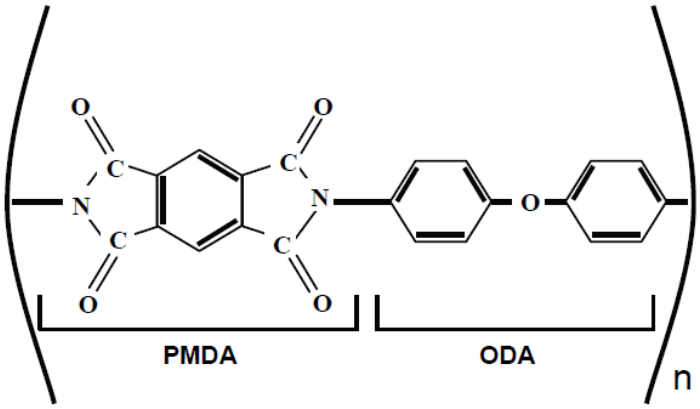

Figure 2.11 Chemical structure of a typical polyimide (Wilson and Atkinson, 2007).

Typically, PI films are prepared by a two-step process: First, PAA precursors are synthesised by blending dianhydride and diamine with N-methylpyrrolidinone (NMP) as the solvent. Next, thermal imidization (150 ℃ to 350 ℃) is conducted to generate PI films via the conversion of PAA, as shown in Figure 2.12 (Inoue, Sasaki and Ogawa, 1996) (Tyan, Liu and Wei 1999) (Fukukawa, Shibasaki and Ueda, 2004) (Zhou *et al.*, 2019). Therefore, PI inks function by a similar mechanism in the inkjet printing process: First, the PAA solution (with NMP) is formulated and jetted on the target substrate, and thermal treatment (temperature of >120 ℃) is subsequently applied on the printed specimens for the conversion of PI from PAA (Liu, Cui and Varahramyan, 2003) (Jensen *et al.*, 2011) (Zhang *et al.*, 2016).

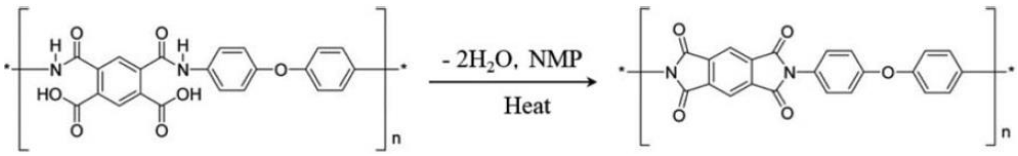

Figure 2.12 Thermal imidization process for the formation of polyimide from PAA (Zhang et al., 2016).

TPGDA is another attractive dielectric material, comprising an acrylic monomer (Figure 2.13). Similar to PI, it is a dielectric material with excellent thermal stability (>145 ℃) (Scherzer and Langguth, 2001). Therefore, it can be used in printed electronics that involve relatively high-temperature fabrication processes (Abbas *et al.*, 2013) (Ding *et al.*, 2013). Unlike PI that utilises thermal treatment, ultraviolet (UV) or electron-beam treatment is typically applied to the TPGDA precursor monomer for the conversion to the cross-linked TPGDA structure (Saleh *et al.*, 2017). Therefore, in the formulation of TPGDA inks for the inkjet printing process, solvents that are not affected by UV or electron beams are selected (He *et al.*, 2017).

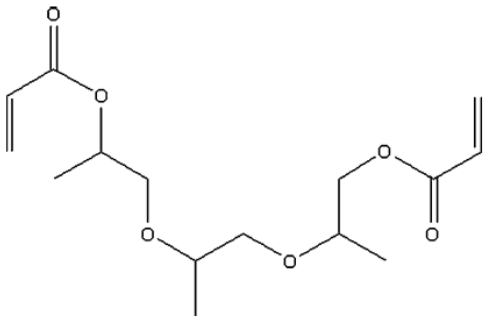

Figure 2.13 Chemical structure of TPGDA (Zhao et al., 2008).

2.4.6 Classification of Semiconducting Inks

Semiconductors are basic components in printed electronics such as an integrated circuit (IC) and transistors. Currently, based on different chemical structures, semiconducting inks are mainly categorised into three types: organic semiconductors, metal-oxide semiconductors and 2D semiconductors (Chung, Cho and Lee, 2019).

Organic Semiconductors

Organic semiconductors comprise a large group of small molecular and polymer semiconductors (Reese *et al.*, 2004) (Reese and Bao, 2007). Because small

molecular- and polymer semiconductors can be developed into low-viscosity inks by formulating organic solvents, they are typically used in the printing process (Briseno *et al.,* 2006) (Mas-Torrent and Rovira, 2008).

6,13-Bis(triisopropylsilylethynyl)pentacene (TIPS-pentacene) is a typical small molecular semiconductor. Figure 2.14 (a) shows the chemical structure *(*Zhu *et al.,* 2018). In the last two decades, it has been one of the most attractive semiconducting materials due to its superior electrical property (mobility > 1 $cm^2V^{-1}s^{-1}$) (Park *et al.,* 2007) (Nicolas *et al.,* 2012). Therefore, TIPS-pentacene already has been reported in several studies (Chung *et al.,* 2011) (Choi *et al.,* 2012) (Choi, Kim and Jang, 2012). Nonetheless, some few optimisation in terms of different aspects of this semiconductor have been reported. For instance, Anthony et al. have reported that the high solubility of TIPS-pentacene in aromatic solvents can be achieved (>100 mg/mL in chloroform) by the substitution of silicon alkynyl at the C6 and C13 positions (Anthony *et al.,* 2001) (Payne *et al.,* 2005). Diao et al. have reported that the electrical property of TIP-pentacene can be further optimised by using a micropillar-patterned printing blade (mobility of up to 11 $cm^2V^{-1}s^{-1}$) (Diao *et al.,* 2013) (Diao *et al.,* 2015). However, most of the currently reported studies focus on contact printing processes (Giri *et al.,* 2011) (Giri *et al.,* 2014). Hence, additional studies on the use of TIP-pentacene in the inkjet printing process are required.

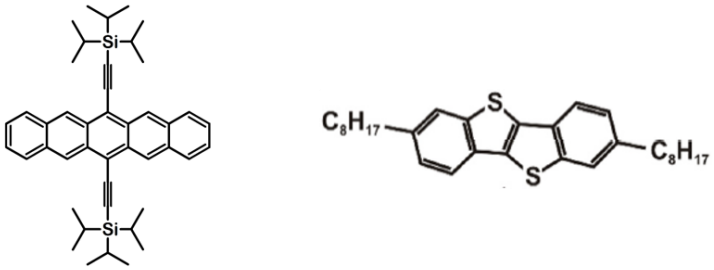

Figure 2.14 structure of small molecular semiconductors (a) TIPS-pentacene (Zhu et al., 2018) (b) C_8-BTBT (Meyers et al., 2017).

2,7-Dioctyl[1]benzothieno[3,2-b][1]benzothiophene (C_8-BTBT) (Figure 2.14 (b)) is a semiconducting material that has been reportedly used in the inkjet printing process (Kumatani *et al.,* 2012). Owing to the high mobility (3 $cm^2V^{-1}s^{-1}$) of this semiconductor and its ability to be printed on different substrates such as poly(methylmethacrylate) (PMMA) and PVP, C_8-BTBT is a semiconductor candidate in printed electronics (Wei *et al.,* 2017). In 2011, the mobility of C_8-BTBT has been reported to be further improved to the maximum value of 31.3 $cm^2V^{-1}s^{-1}$ by the introduction of dual-shot inkjet printing technology (Minemawari *et al.,* 2011). Therefore, C_8-BTBT has currently attracted the attention of a number of researchers, and it has been printed as semiconducting channels in printed transistors (He *et al.,* 2014) (Wu *et al.,* 2016) (He *et al.,* 2017).

Polymer semiconductors are the other group of organic semiconductors. These semiconductors are advantageous in the inkjet printing process as they can be easily developed into printable inks due to their good solubility in organic solvents (Izuhara and Swager, 2009) (Yan *et al.,* 2009) (EK *et al.,* 2015). As a typical polymer semiconductor, regioregular poly(3-hexylthiophene) (RR-P3HT) (Figure 2.15) was first reported by McCullough in 1992, which was used

in solution-processed polymer TFTs since 1998 (McCullough and Lowe, 1992) (Sirringhaus, Tessler and Friend, 1998). Chlorobenzene is the major solvent of currently used RR-P3HT inks. For instance, Speakman *et al.* have formulated an ink by the dissolution of RR-P3HT in chloroform and chlorobenzene, and Baeg et al. have also developed an RR-P3HT ink with anhydrous 1,2,4-trichlorobenzene (Speakman *et al.,* 2001) (Barg *et al.,* 2010). Although varying RR-P3HT inks have been reported currently, one typical disadvantage for these inks is that the printed RR-P3HT specimens exhibit a low mobility (0.1 to 0.4 $cm^2V^{-1}s^{-1}$) compared to the aforementioned small molecular semiconductors (Sirringhaus, Tessler and Friend, 1998) (Kim *et al.,* 2015). Therefore, the optimisation of electrical properties of RR-P3HT inks are required in the future.

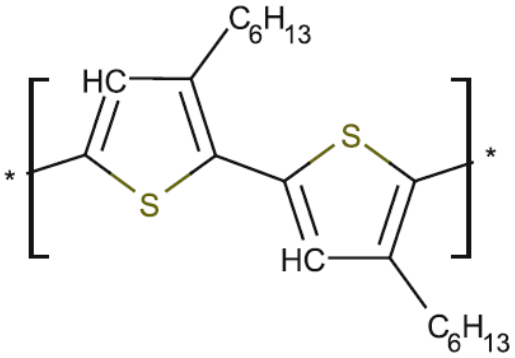

Figure 2.15 Chemical structure of RR-P3HT (Poelking et al., 2014).

Metal-Oxide Semiconductors

In the last decades, metal-oxide materials have been investigated as semiconductors. With a relative high mobility, different metal-oxide materials already have been fabricated in printed electronics (Kim *et al.*, 2014) (Ahn *et al.*, 2015) (Wu *et al.*, 2017). For instance, in 2007, Lee et al. have reported inkjet-printed zinc-indium oxide (ZIO) thin films (Lee *et al.*, 2007). The ZIO ink is prepared by the dissolution of zinc chloride ($ZnCl_2$) and indium chloride ($InCl_3$)

into acetonitrile. Post-annealing treatment was conducted at 600 ℃ for 1 h after the printing work (Han *et al.*, 2009). Based on the electrical characterisation results, the mobility of the printed ZIO thin films is 7.4 $cm^2V^{-1}s^{-1}$.

In 2017, Li has reported a thin-film transistor with another inkjet-printed metal-oxide semiconductor: indium gallium oxide (InGaO) (Li *et al.*, 2017). Indium nitrate $(InNO_3)_3$ and gallium nitrate $(GaNO_3)_3$ are dissolved in 2-methoxyethanol and ethylene glycol to formulate the InGaO ink. Similar to the printing process of ZIO ink, post-annealing treatment (450 ℃) is also required for the printed InGaO film. The mobility of the inkjet-printed InGaO film is 11.7 $cm^2V^{-1}s^{-1}$.

In addition, other metal-oxide semiconductors are widely used in printed electronics such as indium gallium zinc oxide (IGZO) and tin dioxide (SnO_2) (Ellmer, 2001) (Lee *et al.*, 2009) (Hennek *et al.*, 2012) (Avis, Hwang and Jang, 2014) (Jang *et al.*, 2014). However, a high-temperature annealing process (typically greater than 400 ℃) is typically required for metal-oxide semiconductors to completely convert the printed materials (chemical precursors) into metal-oxide semiconducting films (Kim *et al.*, 2014). Therefore, the use of metal-oxide semiconductors is limited in the inkjet printing process because a few substrates (such as rigid silicon) cannot be heated to such a high temperature.

2D semiconductors

2D semiconductors refer to a group of novel semiconductors on the atomic scale (Chung, Cho and Lee, 2019). Among all 2D semiconductors, transition-metal dichalcogenides (TMDCs), including tungsten disulphide (WS_2), tungsten diselenide (WSe_2), molybdenum disulphide (MoS_2) and molybdenum

diselenide ($MoSe_2$), are the main types investigated by researchers (Mark *et al.*, 2010) (Radisavljevic *et al.*, 2011) (Yang *et al.*, 2015) (Desai *et al.*, 2016) (Shin *et al.*, 2018). In 2017, Kelly et al. have reported a MoS_2 ink. MoS_2 flakes are dispersed in an NMP solution and inkjet-printed onto alumina-coated polyethylene terephthalate (PET) substrates. Based on electrical characterisation results, the mobility of printed MoS_2 films ranges from 0.08 to 0.22 $cm^2V^{-1}s^{-1}$ (Kelly *et al.*, 2017). In 2020, another MoS_2 ink is formulated and inkjet-printed by Carey et al. Compared to the MoS_2 ink reported by Kelly et al., this ink is formulated by dispersing few-layer MoS_2 into isopropanol/polyvinylpyrrolidone. The mobility of the printed MoS_2 specimen using Carey's ink is ~0.06 $cm^2V^{-1}s^{-1}$ (Carey *et al.*, 2020). Therefore, compared to polymer and metal-oxide semiconductors, the electrical properties of MoS_2 are not satisfactory and must be modified in the future.

However, some 2D semiconductors still exhibit high mobility. For instance, the electron mobilities of graphene and indium selenide (InSe) are 15000 $cm^2V^{-1}s^{-1}$ and 12700 $cm^2V^{-1}s^{-1}$ (Chen *et al.*, 2008) (Bandurin *et al.*, 2017), respectively. Therefore, these two materials are considered to exhibit immense potential as semiconductors and are investigated in this PhD research. In the following sections, detailed information of both semiconductors is introduced.

2.4.7 Graphene

In this work, graphene was used as the semiconductor; for this reason, it is introduced in detail in this section. The history of graphene is firstly presented to help understanding the discovery of graphene. Next, the structure and properties of graphene, in particular the electrical and mechanical properties, are demonstrated to explain why graphene was employed in this work. A few

synthesis techniques are also discussed in this section. For each technique, the advantages and differences are summarised. In the final part, the preparation and development of graphene inks are introduced. The most important achievements and limitations are also reported.

Brief History of Graphene

The history of graphene spans over more than a century of chemistry research. In 1859, the highly lamellar structure of thermally reduced graphite was discovered by the English chemist Brodie (Brodie, 1859). In 1947, two-dimensional (2D) graphite, which is actually graphene, was firstly reported by the Canadian physicist Wallace (Wallace, 1947). One year later, the first transmission electron microscopy (TEM) images of a few-layer graphite sample were published by Reuss and Vogt (Ashjaran and Oshaghi, 2014). Single-layer graphite was eventually named graphene in 1987 by Mouras (Mouras *et al.*, 1988). Since then, many research efforts have been devoted to monolayer graphene. In 1992, single-layer graphite structures were observed via scanning tunnelling microscopy (STM) (Land *et al.*, 1992). The material was fabricated onto a Pt(111) substrate via hydrocarbon decomposition. In 1997, the thickness of the graphite films was reduced to 30 nm by Ohashi (Ohashi *et al.*, 1997). Tremendous progress in the synthesis of graphene was achieved in 2004. Geim and Novoselov, two researchers from the University of Manchester, reported that a single-atom graphene layer could be extracted from graphite films (Novoselov *et al.*, 2004). A mechanical cleavage technology (repeated peeling), which is also named the scotch tape method, was employed for highly oriented pyrolytic graphite (HOPG) to produce graphene. Due to their pioneering

research on graphene, Geim and Novoselov were awarded the 2010 Noble Prize in Physics (Cooper *et al.*, 2012).

Structure and Properties of Graphene

Basic Structure

Graphene is an atom-scale carbon allotrope that exhibits a 2D structure (Van Noorden, 2006) (Castro Neto *et al.*, 2009). As presented in Figure 2.16, a hexagonal lattice of graphene is generally composed of carbon atoms, and each carbon atom is located at a distance of 1.42 Å from its three neighbours (Meyer, *et al.*, 2007). The σ bonds between the carbon atoms are responsible for the strength and robustness of the structure (Kusmartsev *et al.*, 2014) (Mohan *et al.*, 2018). On the other hand, a π bond was introduced to improve the electrical properties of the material (Choi and Lee, 2011) (Avouris and Dimitrakopoulos, 2012) (Katsnelson, 2012).

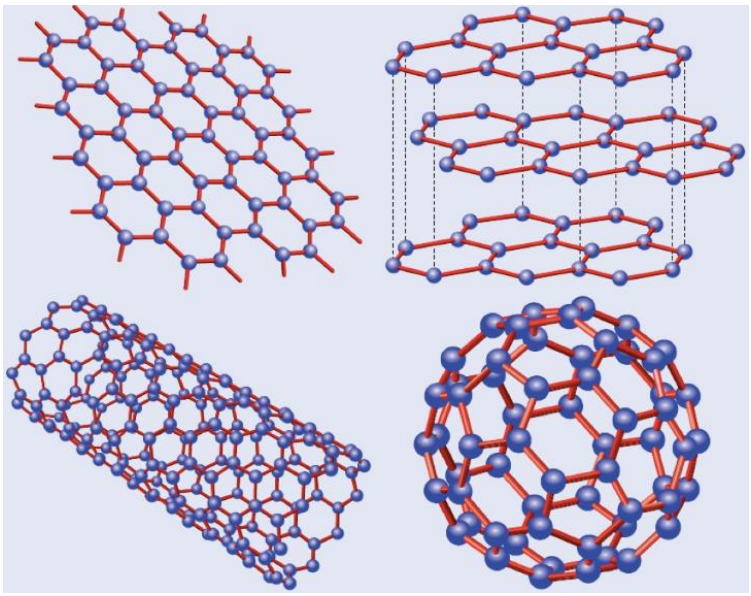

Figure 2.16 Chemical structure of carbon allotropes (top left), graphene (top right), graphite (bottom left), and carbon nanotube fullerene (bottom right) (Castro Neto et al., 2009).

Electrical Properties

Before describing the electrical properties of graphene, the band structure concept is first introduced. Indeed, in solid-state physics, the band structure of a material is one of the most important factors determining the electrical properties of the material (Guo *et al.*, 2011). Two energy bands, namely the valence and conduction bands, are known to determine the electrical conductivity of materials. Generally, the valence band is always completely filled with electrons, while the conduction band is empty. When an electric field is applied, the electrons in the valence band will absorb energy and subsequently jump from the valence band to the conduction band, thus behaving as charge carriers and permitting the material to become conductive. In most materials, an energy gap, known as the bandgap, is present between the valence and conduction bands. The bandgap corresponds to the energy difference between the valence band and the conduction band (i.e., the amount of energy that is required for electrons in the valence band to jump into the conduction band). Therefore, the magnitude of the bandgap is a key factor determining the electrical conductivity of a material.

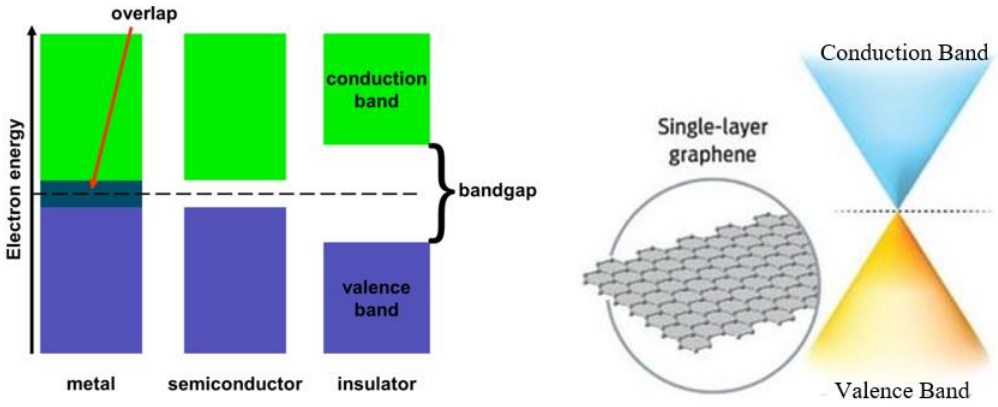

Figure 2.17 Bandgap theory (left) and band structure of single-layer graphene (right) (Savage, 2009).

As seen from Figure 2.17, there is no bandgap for metals (conductors), as the valence and conduction bands are overlapped. Therefore, electrons in the valence band can easily flow to the conduction band to give rise to a current when an electric field is applied. In contrast to metals, a relatively large bandgap exists between the two energy bands for an insulator. Generally, the energy absorbed by the electrons in the valence band of an insulator is insufficient for them to jump to the conduction band. Therefore, only a negligible number of electrons can reach the conduction band of insulators, which means that no current flows in these materials.

Semiconductors are considered to be intermediate between conductors (metals) and insulators. They typically act as insulators under normal conditions, because a small bandgap exists in these materials, preventing electrons in the valence band from jumping easily into the conduction band. However, when a sufficiently high energy is applied, electrons in the valence band can overcome the bandgap and jump into the conduction band, resulting in a current flowing in semiconductors (Compton and Nguyen, 2010).

Graphene is a distinctive semiconductor due to its zero bandgap: the valence band and conduction band meet without any overlap or bandgap (Han *et al.*, 2007) (Lin *et al.*, 2010) (Cooper *et al.*, 2012). Compared with other semiconductors, less energy is required for electrons in graphene to jump from the valence band to the conduction band, leading to a high electron mobility (15000 $cm^2V^{-1}s^{-1}$) (Chen *et al.*, 2008). Therefore, graphene has attracted increasing attention owing to its numerous potential electronic applications (Van Noorden, 2006) (Schwierz, 2010) (Van Noorden, 2011) (Liu and Wicklund, 2014).

Mechanical Properties

Graphene is also a promising candidate for nanoelectromechanical applications owing to its excellent mechanical properties (Mohan *et al.,* 2018). A systematic experimental investigation on the mechanical properties of graphene was firstly reported by Lee *et al.* in 2008 (Lee *et al.,* 2008). Based on experimental results, it was found that graphene samples exhibit a non-linear elastic behaviour and brittle fracture performance. Additionally, two key mechanical factors, namely the yield strength (which refers to the stress at which a non-linear deformation occurs, known as a plastic deformation) and Young's modulus (which determines the stiffness of a material through the relationship between stress and strain), have also been investigated in graphene. With a yield strength of 130 GPa and a Young's modulus of 1 TPa, graphene is the strongest material ever discovered (Lee *et al.,* 2008) (Min and Aluru, 2011) (Ovid'ko and Sheinerman, 2013).

Synthesis Techniques

Graphene is commonly prepared using two different synthesis techniques: top-down and bottom-up methods, which are presented in Figure 2.18. Among all techniques, mechanical exfoliation, reduction of graphene oxide (GO), epitaxial growth, and chemical vapour deposition (CVD) are the four predominantly used synthesis approaches, which have been introduced in details in previous works (Kuilla *et al.,* 2010) (Yang *et al.,* 2018).

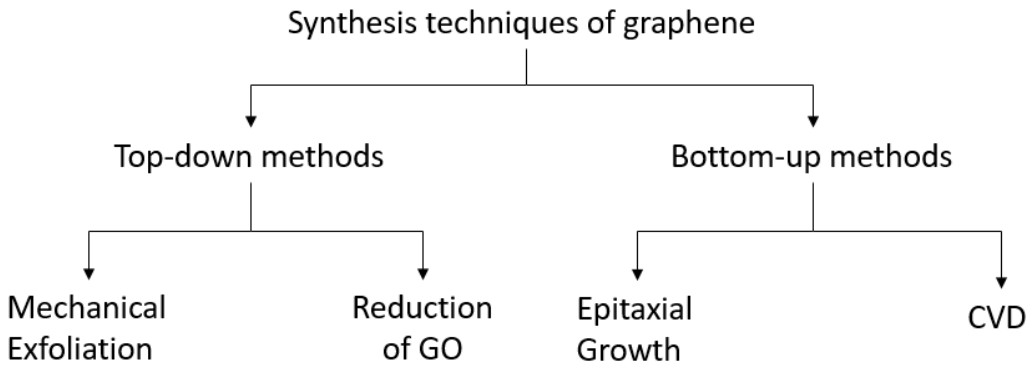

Figure 2.18 Synthesis techniques of graphene.

Mechanical Exfoliation

The mechanical exfoliation technique has been developed by Geim and Novoselov in 2004 (Novoselov *et al.*, 2004). Highly ordered pyrolytic graphite (HOPG) was used as the precursor, and the graphene layers were obtained from the HOPG surface via the repeated peeling process (Figure 2.19) (Yi and Shen, 2015). The advantage of this approach is that high-quality monolayer graphene can be obtained. However, this technique is affected by several limitations. For instance, extremely intensive labour and large amount of time are required for the mechanical exfoliation process. Therefore, this approach cannot be used for large scale production and can only be employed for laboratory research.

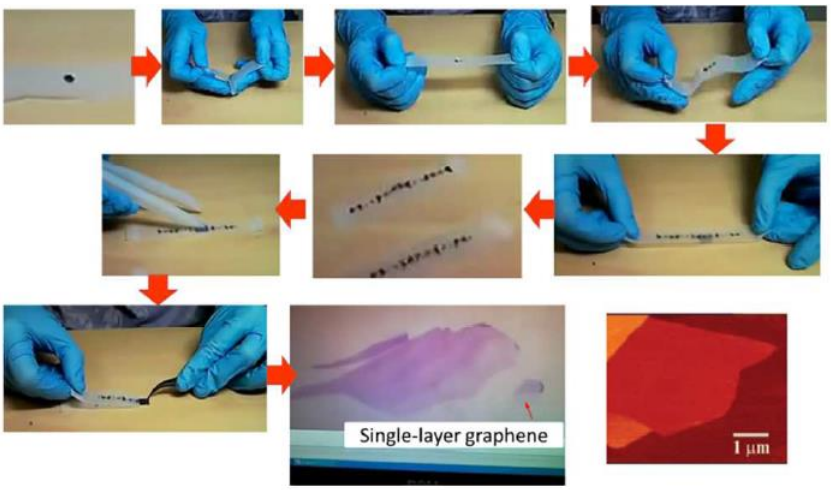

Figure 2.19 Illustration of the mechanical exfoliation process to obtain graphene (Yi and Shen, 2015).

Reduction of GO

GO refers to single-layer graphene with different oxygen-containing functional groups. Graphene can be prepared from GO by removing the oxygen atoms (Figure 2.20) (Schniepp *et al.*, 2006) (Pei *et al.*, 2010) (Park *et al.*, 2011) (Pei and Cheng, 2012) (Balaji *et al.*, 2014). Today, three types of reduction approaches are most commonly used, namely chemical reduction, thermal reduction, and laser reduction (Stankovich *et al.*, 2007) (Marcano *et al.*, 2010) (Zangmeister, 2010).

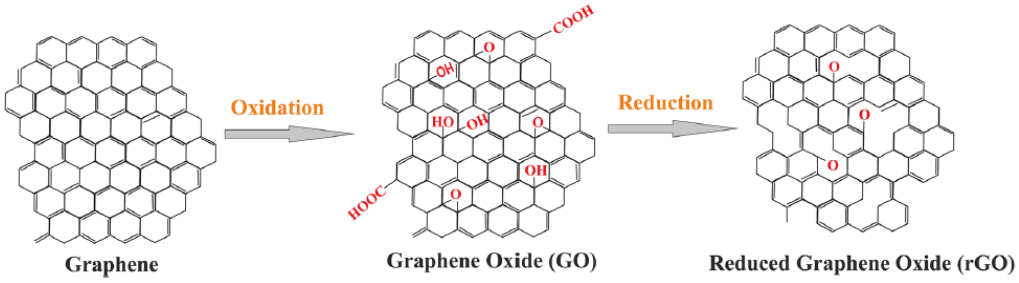

Figure 2.20 Schematic of the oxidation and reduction processes of graphene, GO, and rGO (Priyadarsini et al., 2018).

In chemical reduction process, GO flakes are generally dispersed in deionised water or organic solvents. By adding reductants to the solution, redundant oxygen function groups (such as OH) in GO are removed (Stankovich *et al.,* 2006) (De Silver *et al.,* 2017). Hydrazine is the most widely used reductant in the chemical reduction process of GO (Shen *et al.,* 2009). When hydrazine is added to a GO solution, the GO flakes are reduced to reduced graphene oxide (rGO) flakes when the solution is subjected to a thermal treatment at 100 ℃ for around 24 h (Stankovich *et al.,* 2007). However, hydrazine is a toxic material (Schmidt, 2001). Therefore, alternative sustainable reducing agents are still being investigated (Paredes *et al.,* 2011) (Chua and Pumera, 2013).

Graphene can also be obtained from GO through a high-temperature thermal treatment (around or above 1000 °C) (Gao *et al.,* 2009) (Chen and Yan, 2010). Due to the high temperature, oxygen functional groups are removed through evaporation or burning. This process is highly efficient to prepare rGO powders (McAllister *et al.,* 2007).

Laser-irradiation processes have been used in printed electronics in the last a few years (Ko *et al.,* 2007). These processes are advantageous, as no additional chemical materials are required, and the total reaction time can be significantly reduced from a few hours to several minutes (Kymakis *et al.,* 2014). GO can be reduced to rGO through laser reduction processes (Kim, Parvez and Chhowalla, 2009) (Guan *et al.,* 2016) (Torrisi *et al.,* 2020). GO solutions are more commonly used in this process, as liquid GO absorbs more energy from a laser than powder GO (Wu *et al.,* 2011). Kumar *et al.* reported reduction processes of GO using different light sources (Kumar *et al.,* 2011). They experimentally found that GO is reduced to rGO after a 4-min excimer laser irradiation.

Therefore, using lasers to reduce GO is an effective process, which should be further investigated in the future.

Epitaxial Growth

Large-area graphene can be epitaxially produced via the thermal decomposition of silicon carbide (SiC) (Figure 2.21) (Berger *et al.*, 2006) (Ohta *et al.*, 2006). Upon applying a high-temperature thermal treatment (from 300 °C to 2000 °C), a graphene film is formed on the SiC surface due to the sublimation of silicon from SiC (Yazdi *et al.*, 2016). However, applications of this approach are limited, since the whole process has to be performed using a relatively high temperature and in ultrahigh vacuum (UHV) conditions.

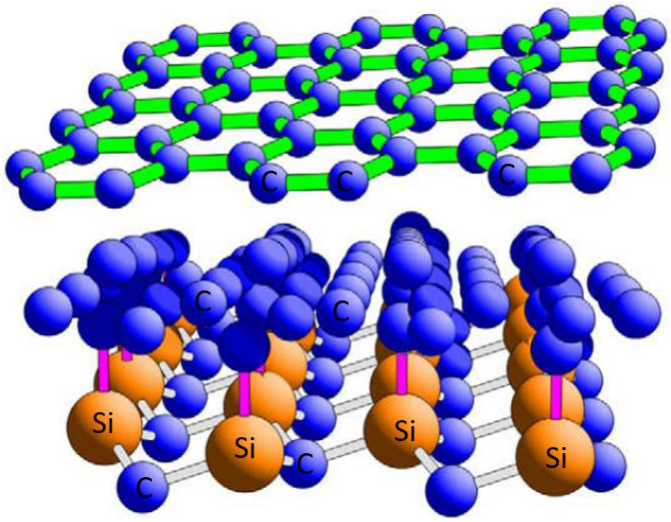

Figure 2.21 Schematic of the epitaxial growth of graphene on a SiC surface (Virojanadara et al., 2010).

Chemical Vapour Deposition (CVD)

CVD is a another synthesis technique to prepare large-scale graphene films (Reina *et al.*, 2009) (Suk *et al.*, 2011) (Chen *et al.*, 2015). The whole process comprises three steps. A catalytic metal, such as nickel, is firstly prepared in an inert gas-protected chamber under a high temperature (900–1000 °C) (Zhang *et*

al., 2012). A hydrocarbon gas is subsequently delivered to the chamber as the precursor. A carbon dissolution process is then applied, and hydrocarbon molecules are dissolved at this stage. In the final step, graphene is segregated via a cool-down treatment (Kim *et al.*, 2009) (Li *et al.*, 2009). Generally, a medium cooling rate (10 °C/s) is used, as carbon atoms diffuse towards a metal body under both a fast (20 °C/s) and slow (0.1 °C/s) cooling rate (Figure 2.22) (Yu *et al.*, 2008). Once the CVD process is completed, the prepared graphene films are generally transferred onto an insulated substrate to be used for microscale electronic applications.

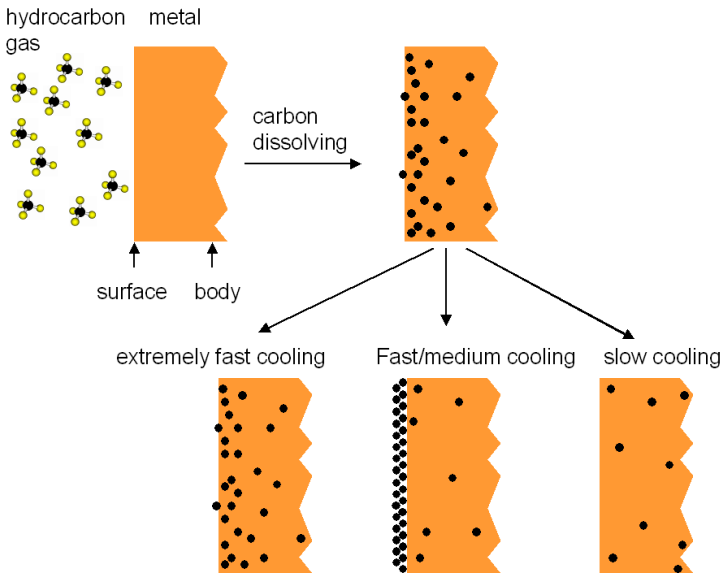

Figure 2.22 Schematic illustration of the CVD process (Yu et al., 2008).

Graphene Ink

To date, liquid phase exfoliation (LPE) has been the most widely used approach to prepare graphene-based inks (Coleman, 2009) (Coleman, 2013) (Tran *et al.*, 2018) (Saidina *et al.*, 2019) (Tran *et al.*, 2019). Graphite is firstly dispersed in organic solvents. With the aid of sonication, graphite is subsequently split into individual platelets, and a few layers of graphene are thus generated. Although

this process is convenient and highly efficient, one typical limitation is that the size of the prepared graphene flakes is not uniform or controllable. Therefore, the inkjet printing process of these prepared graphene inks is affected by an unstable performance due to the clogging caused by large graphene flakes. A common solution to this problem consists of removing the redundant graphene flakes via centrifugation; however, the performance of the prepared graphene solution is significantly affected by the decrease in the concentration of graphene (Antonova, 2016).

A few typical graphene inks have been reported in the last a few years (Li *et al.*, 2013) (Dodoo-Arhin *et al.*, 2016) (Carey *et al.*, 2017) (Karim *et al.*, 2017). For instance, in 2013, a graphene ink prepared with ethanol and ethyl cellulose has been reported by Secor *et al.* (Secor *et al.*, 2013). With a viscosity of 10–12 mPa·s and a surface tension of 33 mN/m, it was possible to inkjet-print this ink using a Fujifilm Dimatix material printer (DMP-2800). In 2016, Majee *et al.* introduced another graphene ink that was dispersed in N-Methyl-2-pyrrolidone (NMP) (Majee *et al.*, 2016). As NMP has a high boiling point (202 °C), the printed samples were subjected to a thermal treatment (350 °C for 150 min) to remove the solvents. A similar graphene/NMP ink was also reported in 2017 by Carey *et al.* (Carey *et al.*, 2017), exhibiting a remarkable mobility (91 $cm^2V^{-1}s^{-1}$).

In recent years, GO has been considered as a precursor in the preparation of graphene inks for the inkjet printing process (He and Derby, 2017) (Li *et al.*, 2017). In contrast with the poor dispersion of graphene in deionised water, GO ink can be easily prepared by dispersing GO flakes/particles in deionised water or other polymer solvents (Huang *et al.*, 2011) (Singh *et al.*, 2011). For instance,

Le *et al.* reported a formulated GO ink in 2011, in which the GO particles were dispersed in deionised water with a concentration of 0.2 wt% (Le *et al.*, 2011). With a measured viscosity of 1.06 mPa·s and a surface tension of 68 mN/m, this prepared ink was successfully inkjet-printed on a titanium foil surface. For all prepared GO inks, graphene films can be obtained through a reduction process at the end of the printing process. However, as mentioned previously, the substrates need to be carefully selected to avoid any damage during the thermal or laser reduction processes.

2.4.8 Indium Selenide (InSe)

InSe is a semiconductor belonging to the III–VI family, as indium (In) is a metal element from group III, while selenium (Se) is from group VI (Feng *et al.*, 2015). Similar to graphene, InSe is a 2D material: bulk InSe is composed of stacked layers of Se–In–In–Se atoms (Figure 2.23) (Lei *et al.*, 2014) (Royo *et al.*, 2014) (Politano *et al.*, 2017) (Segura, 2018).

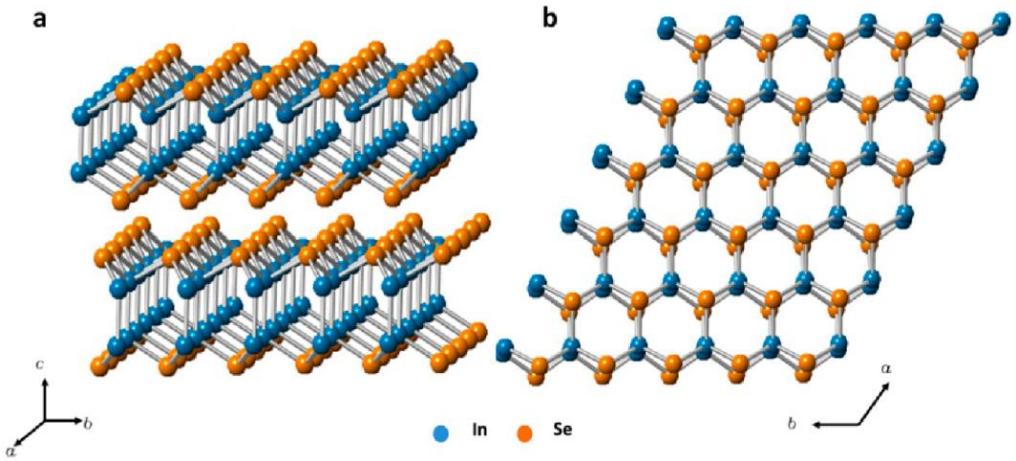

Figure 2.23 Crystal structure of InSe: (a) side view; (b) top view (Lei et al., 2014).

However, while graphene has a zero bandgap, InSe has a narrow bandgap (Damon and Redington, 1954) (Williams *et al.*, 1977) (Gürbulak *et al.*, 2014) (Politano *et al.*, 2017). The quantum confinement effect, which is commonly observed in nanometre-scale materials, occurs in InSe: the bandgap of InSe decreases upon increasing the number of layers (Mudd *et al.*, 2013) (Mudd *et al.*, 2016). It can be seen from Figure 2.24 that the bandgap of a single-layer InSe film is around 1.28 eV.

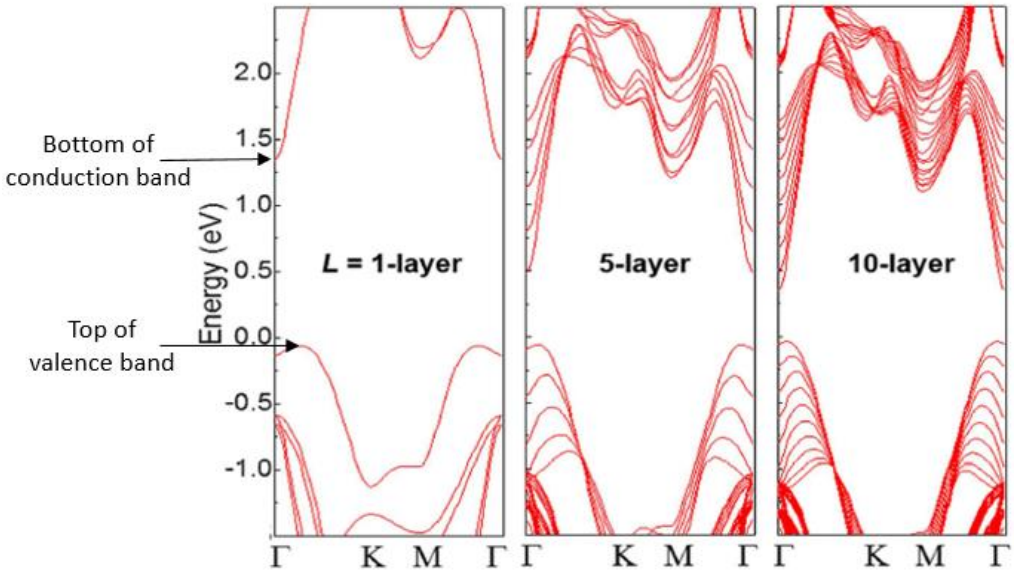

Figure 2.24 Band structure of InSe with different numbers of layers (Mudd et al., 2016).

InSe can be obtained through different approaches, such as the Bridgman–Stockbarger technique (De Blasi *et al.*, 1982) (Chevy, 1984) (Gürbulak *et al.*, 2014), CVD (Park *et al.*, 2003), and vacuum evaporation (El-Sayed, 2003). Among these methods, the Bridgeman–Stockbarger technique is the most widely used one, as it can be employed for large-scale InSe fabrication (Boukhvalov *et al.*, 2017). The major mechanism involved in this method is heating the polycrystalline material to a high temperature (above its melting

point) in vacuum conditions and subsequently cooling down the whole container to form a single crystal (Hoshino *et al.*, 1976) (Imai *et al.*, 1981). The details of the process used to obtain InSe single crystals from an In–Se mixture have been reported by Gürbulak in 2014 (Gürbulak *et al.*, 2014). A mixture of pure In and Se is firstly annealed at a 950 °C in a furnace. Afterwards, a crucible is suspended in the middle of the container, and two areas with different cooling-down rates are formed (Figure 2.25). A solidified ingot is finally generated at a temperature of 250 °C. Similar to the mechanical exfoliation process for graphene, InSe flakes are obtained by repeated peeling from the prepared ingot. Since at present the mechanical exfoliation technique is the only approach employed to cleave InSe flakes from ingots, other techniques, such as LPE, are being investigated as possible alternatives (Tamalampudi *et al.*, 2014) (Boukhvalov *et al.*, 2017).

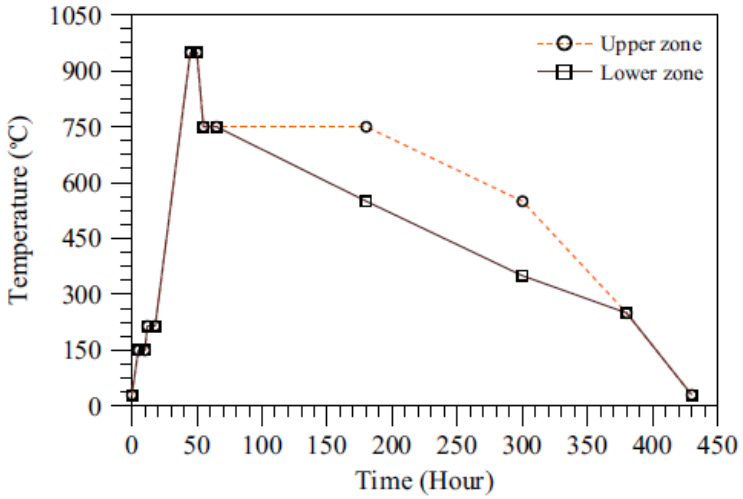

Figure 2.25 Schematic diagram of the growth process of an InSe single crystal using the Bridgman–Stockbarger technique (Gürbulak et al., 2014).

Similar to graphene, InSe is used as the semiconducting channel in transistors (Chen *et al.*, 2015) (Lei *et al.*, 2015) (Sucharitakul *et al.*, 2015) (Politano *et al.*,

2017). As the bandgap of InSe flakes is reduced upon increasing the number of layers, the electron mobility of the fabricated transistor can be controlled by preparing InSe with a specific number of layers. Feng *et al.* reported a multilayer-InSe-based transistor in 2014 (Feng *et al.*, 2014). The InSe film was prepared from an InSe bulk crystal and transferred onto a poly-(methyl methacrylate) (PMMA)/ Al_2O_3 dielectric film (between the two Au/Cr electrodes) (Figure 2.26). In these experiments, a 1055 $cm^2V^{-1}s^{-1}$ mobility was recorded, demonstrating that InSe is an ideal semiconductor for use in high-mobility electronic devices.

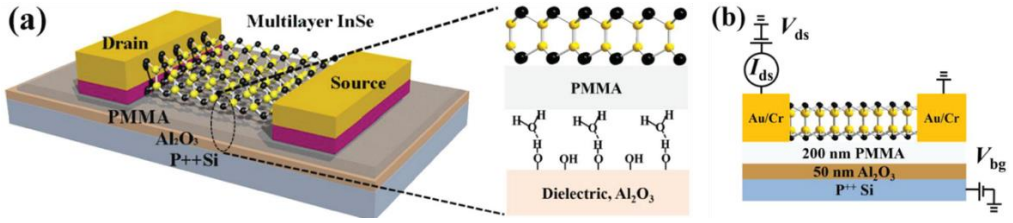

Figure 2.13 Schematic of a multilayer InSe-based transistor: (a) whole structure; (b) cross-sectional view (Feng et al., 2014).

Moreover, since InSe is a photosensitive material (the electrical performance of InSe-based devices is always affected by the intensity of environmental lights), it is also used in optoelectronic devices (Lei *et al.*, 2014) (Mudd *et al.*, 2015) (Huang *et al.*, 2016) (Boukhvalov *et al.*, 2017). For instance, in 2014, an InSe-based transistor was characterised in an ambient environment with a high-density photophase (Figure 2.27(a)) (Tamalampudi *et al.*, 2014). Upon varying the light intensity (180, 39.9, and 12.2 mW cm^{-2} as well as in dark conditions), these characterisation results demonstrated that the channel current increases with increasing the light intensity. Therefore, the performance of InSe-based

transistors can be tuned by adjusting both the input voltage/current and the environmental illumination intensity.

InSe-based devices are also widely used as photodetectors (Chen *et al.*, 2015) (Lei *et al.*, 2015). Tamalampudi et al. reported the preparation of InSe-based photodetectors on polyethylene terephthalate (PET) films (Figure 2.27(b)) (Tamalampudi *et al.*, 2014). It can be seen from Figure 2.27 that the magnitude of the current flowing through the photodetector is affected by varying the illumination intensity.

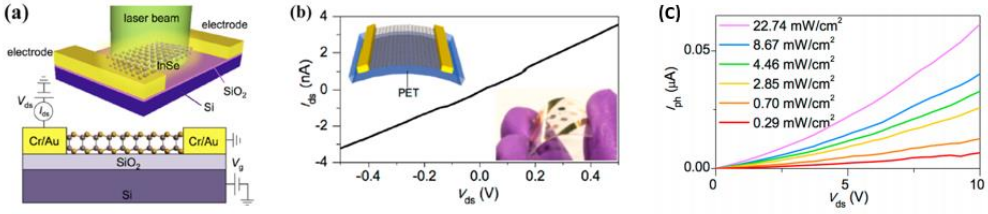

Figure 2.27 Schematic images of InSe-based optoelectronic devices: (a) optoelectronic transistor; (b) photodetector; (c) optoelectronic characterisation results for the photodetector (Tamalampudi et al., 2014).

2.5 Photodetectors, Hall Bars, and Transistors

In this section, photodetectors, Hall bars, and transistors are discussed. In particular, this section focuses on photodetectors and Hall bars to determine the optical and electrical properties of printed semiconducting materials with a transistor, as this is the target electronic application presented in this work. Therefore, in this section, the details about the development, structure, and working principle of these three electronic devices are reported. To understand the structure and working principle of transistors to a deeper level, n-type and p-type semiconductors are also introduced.

2.5.1 Photodetectors

Photodetectors, which are also known as light-dependent resistors (LDRs), are a widely used electronic element to monitor the light intensity (Rammohan and Kumar, 2017). As shown in Figure 2.28, a photodetector is normally composed of a high-resistance photosensitive semiconductor and two conductive electrodes.

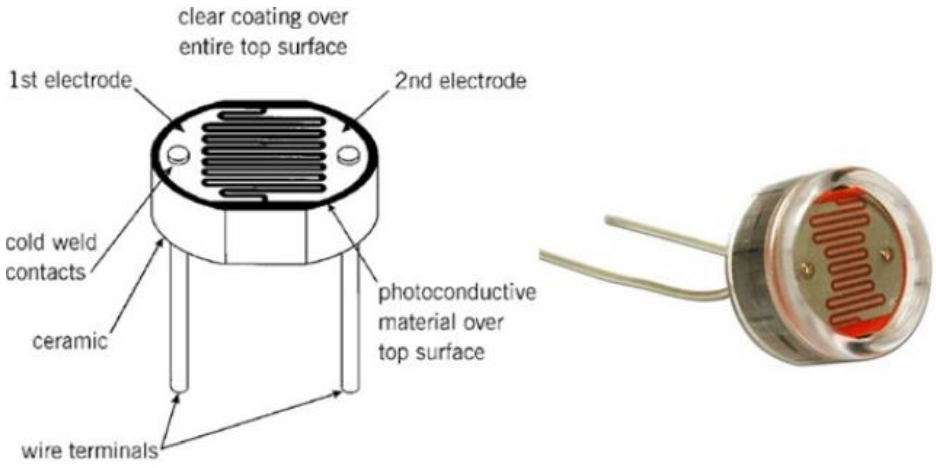

Figure 2.28 Structure of a photodetector (design and photo) (Islam and Saiduzzaman, 2013).

Cadmium sulphide (CdS) is the most commonly used semiconductor in conventional photodetectors owing to its wide resistance range (from less than 100 Ω to more than 10 MΩ). Normally, in a dark environment, CdS exhibits a resistance in the order of a few megaohms, while its resistance decreases rapidly to only a few ohms under strong illumination conditions. Therefore, CdS-based photodetectors are employed in many practical applications, acting as automatic on/off switches. A typical practical application using CdS-based photodetectors is streetlight: lights turn on at night and turn off as ambient light is detected.

Besides streetlights, photodetectors also play an important role in security alarms, camera light meters, etc.

Inkjet-printed photodetectors have been reported in the last few years. Dong et al. introduced a zinc oxide (ZnO)-based photodetector in 2017 (Dong *et al.,* 2017). ZnO nanoparticles were dispersed in ethylene glycol and glycerol mixtures for the formulation of ZnO ink and were printed on a PET substrate. Silver inks were also printed as the conductive electrodes. A responsivity (which refers to the electrical output per optical input) of 0.14 A/W was achieved. Alamri et al. also reported a fully inkjet-printed photodetector with an optimised photoelectric performance (Alamri *et al.,* 2019). A high responsivity of 0.53 A/W was achieved for this graphene/perovskite/graphene photodetector.

2.5.2 Hall Bars

A Hall bar is a pattern geometry that is used for measuring the electrical properties of a specific material, such as the electron mobility and gate dependence (the gate dependence refers to the change of the magnitude of the flowing current through drain and source electrodes when a voltage is applied between them) (Juntunen *et al.,* 2018). A Hall bar device is commonly designed by placing six or eight conductive contacts on the tested samples. Generally, the conductivity of the contacts is always higher than that of the testing materials to minimise the influence of the contact resistance on the measurements (Calabrese *et al.,* 2020).

Kazakova et al. reported a typical six-contact 1–2–2–1 Hall bar geometry, which is presented in Figure 2.29 (Panchal *et al.,* 2012) (Kazakova *et al.,* 2013). This Hall bar was fabricated by spin coating six gold contacts onto graphene samples and was used for the electrical characterisation of the graphene samples. By

measuring different electronic parameters, such as the magnetic field (B), Hall voltage V_H, electronic charge e, graphene sheet resistance R_s, and current I_{bias} through I_{drain} and I_{source}, the mobility of the investigated graphene sample was calculated to be 1673 $cm^2V^{-1}s^{-1}$.

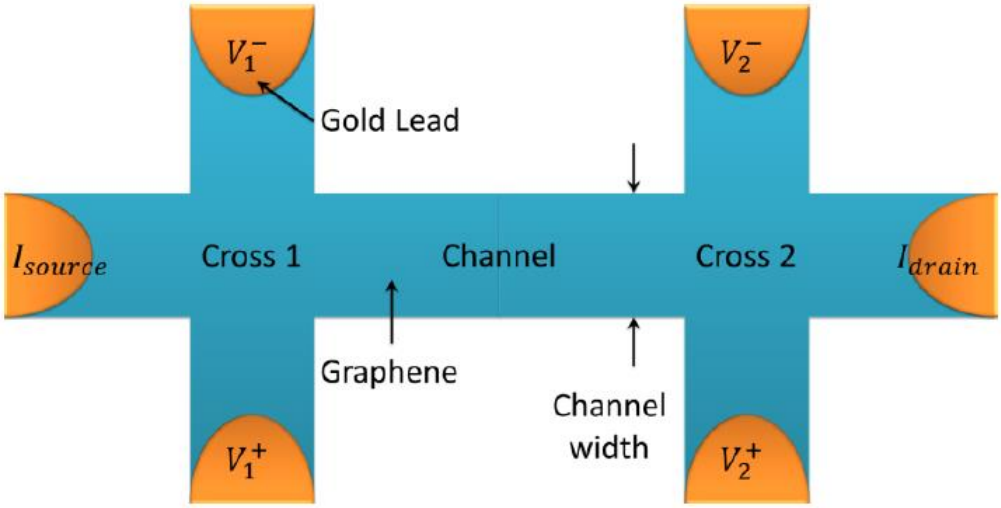

Figure 2.29 Structure of a typical six-contact 1–2–2–1 Hall bar geometry (Kazakova et al., 2013).

2.5.3 Transistors

Transistors are widely used electronic devices that are composed of a conductor, an insulator, and a semiconductor layer. Before introducing transistors, doped semiconductors, which are also known as extrinsic semiconductors, are firstly discussed to help achieving a more comprehensive understanding of transistors. Doped semiconductors are commonly classified into n-type or p-type semiconductors depending on the dopant type. Details of the two types of semiconductors are provided in the following.

Brief Introduction of n-type and p-type Semiconductors

N-type Semiconductors

In n-type semiconductors, a pure semiconductor, such as silicon (Si), is doped with pentavalent impurities. For instance, having five valence electrons, antimony is commonly used as an impurity for n-type semiconductors. When an antimony atom is added to intrinsic silicon, four covalent bonds, involving one electron from the silicon atom and one electron from the antimony atom, are formed between the antimony atom and the four neighbouring silicon atoms to ensure a stable crystal structure. However, one electron remains free, as it is not employed in the covalent bonding, as shown in Figure 2.30.

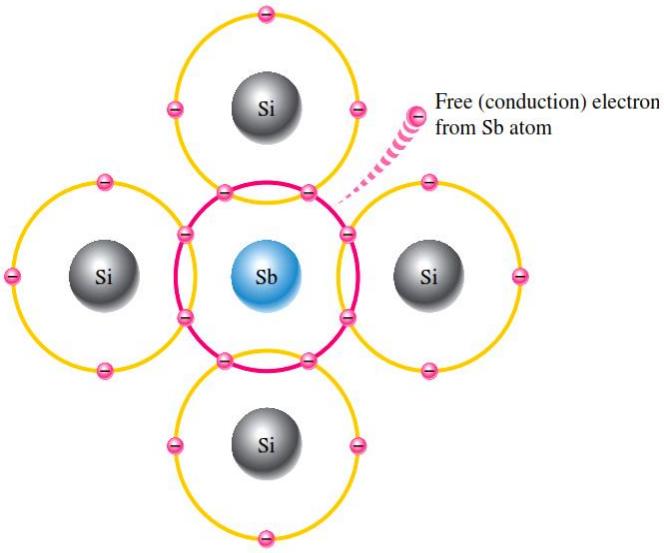

Figure 2.30 Schematic diagram of an n-type silicon semiconductor doped with antimony.

In a doped semiconductor, there is no net electric charge, as the total number of electrons is exactly the same as that of protons. However, the lack of a 'free electron' for each incorporated antimony atom results in an overall positive electric charge with 50 electrons and 51 protons. Therefore, free electrons

become the majority carrier of this doped semiconductor. The term ‘n-type’ refers to the negative charge of these free electrons.

P-type Semiconductors

In p-type semiconductors, a pure semiconductor, such as silicon (Si), is doped with trivalent impurities. For instance, boron is commonly added to silicon as an impurity to form p-type semiconductors because of its three valence electrons. Similar to n-type semiconductors, four covalent bonds are required to generate a stable structure between the boron atom and the four adjacent silicon atoms. However, due to the lack of a valence electron, only three covalent bonds are formed, and a hole is created in the fourth covalent bond, as shown in Figure 2.31. In this case, an electron moves from a nearby atom to fill the hole, and a new hole is subsequently generated in a nearby atom, stripping the adjacent atom of an electron, and so on. Therefore, in these p-doped material, electrons with a negative electric charge move to fill the holes, leaving behind now holes in the process. This situation corresponds to holes with a positive electric charge moving as the majority carrier. The term ‘p-type’ refers to the positive charge of these free holes.

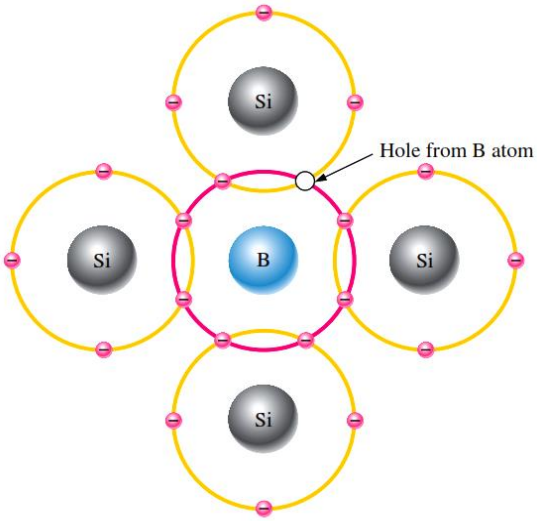

Figure 2.31 Schematic diagram of a p-type silicon semiconductor doped with boron.

Development of Transistors

Research groups started to work on semiconductor devices from the mid-1940s (Ross, 1998) (Riordan *et al.*, 1999). The first transistor was developed in 1947 by Bardeen and Brattain, who were working at the Bell Telephone Laboratories (BTL) (Bardeen and Brattain, 1948). This transistor was fabricated by pressing two separate strips of gold foil on the surface of a germanium crystal leaving a gap of only a few millimetres (Figures 2.32 (a) and (b)). Due to the observed power gain, this electronic device attracted a considerable amount of attention from the research community. Since then, numerous investigations have been conducted on transistors. Further details about the tremendous development of transistors can be found in previous works (Shockley, 1949) (Shockley *et al.*, 1951) (Saby, 1952) (Dacey and Ross, 1955) (Brinkman *et al.*, 1997) (Ross, 1998) (Constable *et al.*, 2004). Today, transistors are one of the crucial functional elements in major electronic devices, reaching a minimum size of a few nanometres (Wulf *et al.*, 2011).

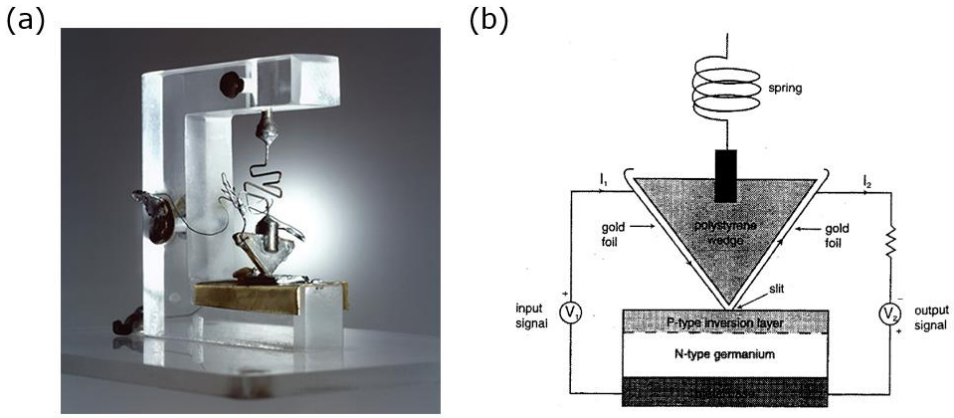

Figure 2.32 The first transistor: (a) physical product; (b) schematic diagram (Riordan, et al., 1999).

Classification of Transistors

Today, transistors are mainly classified into bipolar junction transistors (BJT) and field-effect transistors (FET) depending on their different working mechanisms. BJTs and FETs will be introduced in the following sections. However, FETs will be discussed in more detail, as they were fabricated in this work.

BJTs

BJTs consist of transistors with core pieces of three-division semiconductors (n-p-n or p-n-p). In a BJT, three terminals, which are known as the emitter, base, and collector, are respectively connected to the three divisions of the semiconductor. Generally, in a p-n-p BJT, the n-type semiconductor is connected to the base terminal, and the two p-type semiconductors are connected to the emitter and collector terminals. Conversely, in an n-p-n BJT, the p-type semiconductor is connected to the base terminal, and the two n-type semiconductors are connected to the emitter and collector terminals (Figure 2.33).

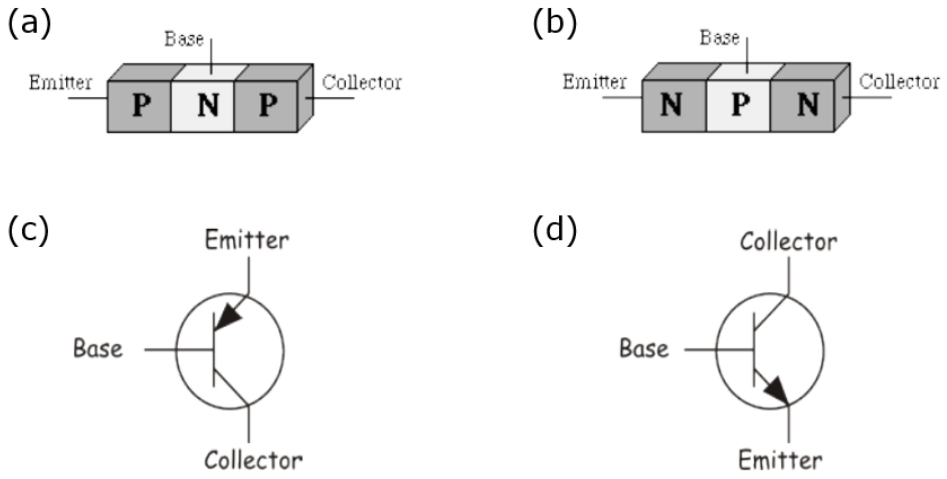

Figure 2.33 Structures and symbols of BJTs: (a) p-n-p BJT (structure); (b) n-p-n BJT (structure); (c) p-n-p BJT (symbol);(d) n-p-n BJT (symbol).

Depending on the external electric field, BJTs can operate in three modes, namely the cut-off, saturation, and active mode. In the cut-off mode, no current flows through the device, while, in the saturation mode, the output current is maximum and is not affected by the input current. BJTs in the active mode are the most attractive, as the input currents can be amplified to relatively high output currents. Further information regarding BJTs is available in a previous work (Kaiser, 2014).

FETs

Another widely used type of transistor is the FET, which can be further classified into junction FET (JFET) and metal–oxide–semiconductor FET (MOSFET). Compared with JFETs, MOSFETs are easier to fabricate and can be operated in both depletion and enhancement modes, while JFETs can only work in the depletion mode. Therefore, MOSFETs are discussed in this work, and more information about JFETs can be found in the literature (Ytterdal *et al.,* 2003) (NXP freescale semiconductor, 2009) (Kaiser, 2014).

As illustrated in Figure 2.34, a FET is composed of five parts, namely the gate terminal, drain terminal, source terminal, insulator (dielectric layer), and semiconductor channel. The gate terminal is separated from the drain terminal, source terminal, and semiconductor channel by the insulator. Therefore, a built-in parallel-plate capacitor is formed between the gate terminal, insulator, and semiconductor channel. When an external voltage is applied to the gate terminal, an electric field is generated through the capacitor, affecting the free electrons/holes in the semiconductor channel. Depending on the type of semiconductor employed (n-type or p-type) and the direction of the generated electric field, FETs are further classified into enhancement-mode FET and depletion-mode FET. Examples of these FETs are provided in the following section.

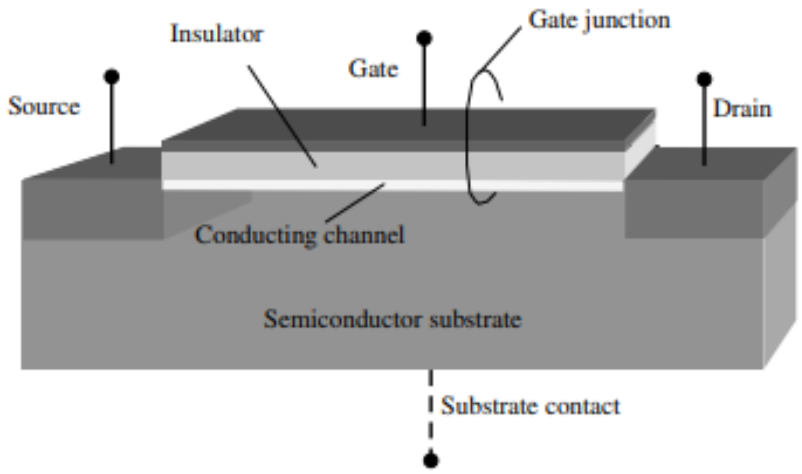

Figure 2.34 Structure of a FET: drain electrode, source electrode, gate electrode, semiconducting channel and insulator.

Figure 2.35 shows an n-channel enhancement-mode FET. The drain and source terminals are separated by a p-type semiconductor in this transistor. Initially, without any external voltage applied to the gate terminal, there is no current flow between the drain and source terminals. However, when a positive external

voltage is applied to the gate terminal, holes and free electrons in the p-type semiconductor are affected by the electric field. The holes are pushed away from the insulator–semiconductor interface, while the free electrons are attracted towards the same interface, giving rise to a negatively charged region between the drain and source terminals. The negative charged region is named an electron inversion layer. When an external voltage is applied to the drain and source terminals, the free electrons flow, and a current flow is established between these two terminals. As the inversion layer can be generated only in the presence of an external voltage, this transistor is named an enhancement-mode FET.

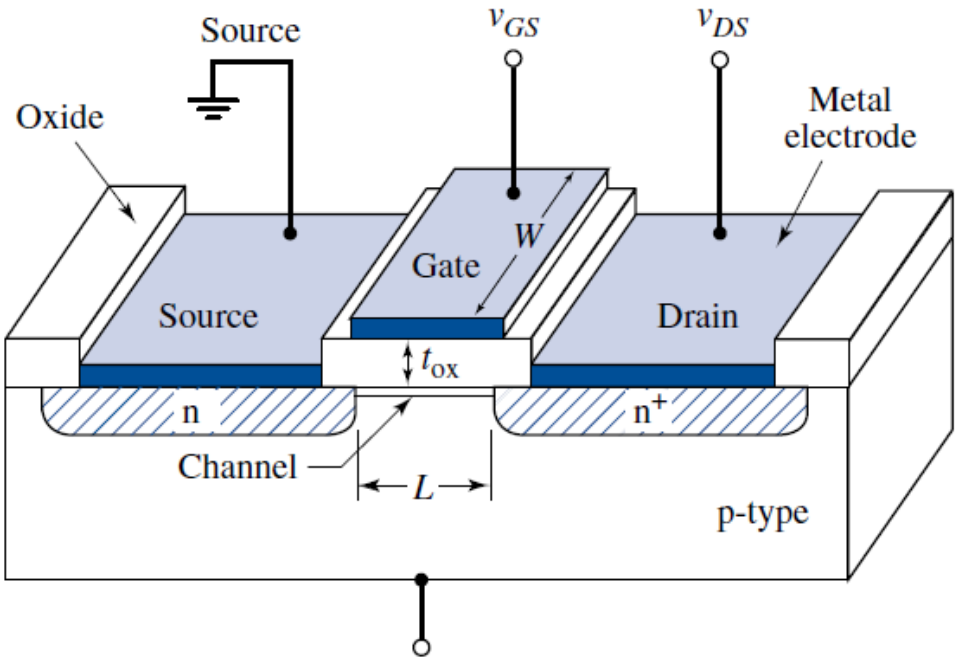

Figure 2.35 Structure of an n-channel enhancement-mode FET.

The n-channel enhancement-mode FET can operate in different modes, depending on the magnitude of the external voltage applied to the gate, drain, and source terminals. Before explaining the working mechanism of each mode, the threshold voltage is first introduced. This voltage is generally indicated as V_{TN} and is defined as the minimum applied gate voltage that is required to

generate the inversion layer. Therefore, when the magnitude of the gate voltage is lower than the threshold voltage (i.e., $v_{GS} < V_{TN}$), no inversion layer is created, demonstrating that the current flowing between the drain and source terminals is zero. When the applied positive gate voltage is larger than the threshold voltage (i.e., $v_{GS} > V_{TN}$), the inversion layer is generated, and the transistor is turned on. Moreover, it can be observed from Figure 2.36 that, when a fixed drain–source voltage (v_{DS}) is applied, a larger gate–source voltage (v_{GS}) leads to a larger drain–source current (i_D).

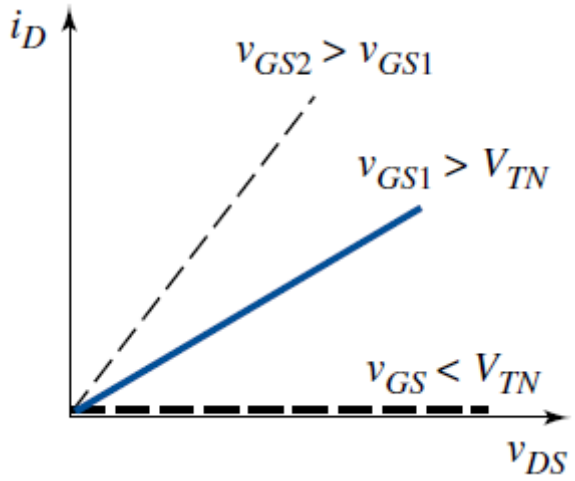

Figure 2.36 Plot of i_D versus v_DS for three different v_GS values (v_GS2 > v_GS1 > V_TN > v_GS).

From Figure 2.36, it can also be observed that, when a fixed positive gate voltage (larger than V_{TN}) is applied, the magnitude of i_D changes linearly with v_{DS}. However, in practical FETs, the electrical performance plot is more complex, as FETs always work in two regions, namely the triode region (non-saturation region) and saturation region.

In the triode region, i_D is linearly proportional to v_{DS} in the initial stage (Figure 2.37(a)). This is because, when an external electric field is firstly generated by

the applied v_{DS}, all free electrons in the electron inversion layer move, and a current flowing through the drain and source terminals is generated. However, since the gate–drain voltage (v_{GD}) is equal to the difference between the gate–source voltage and the drain–source voltage ($v_{GD} = v_{GS} - v_{DS}$), v_{GD} decreases upon increasing v_{DS} (v_{GS} is fixed). The incremental inversion layer density is subsequently decreased at the drain terminal, leading to a decreased slope of the i_D-versus-v_{DS} curve (Figure 2.37(b)).

As v_{DS} increases, it will finally reach a point whereby $v_{GD} = V_{TN}$, which can be expressed as:

$$V_{TN} = v_{GS} - v_{DS}(\text{sat}), \tag{7}$$

or

$$v_{DS}(\text{sat}) = v_{GS} - V_{TN}, \tag{8}$$

where v_{DS} (sat) is the drain–source voltage required to generate the zero inversion layer density at the drain terminal. Therefore, once v_{DS}(sat) is reached, the slope of the i_D-versus-v_{DS} curve decreases to zero, as the inversion layer density does no longer increase (Figure 2.37(c)). i_D becomes finally constant and is not affected by the increase of v_{DS}, demonstrating that a saturation region is reached.

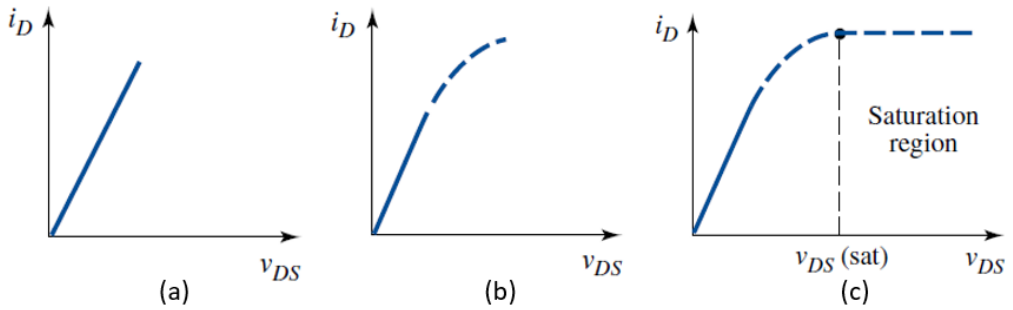

Figure 2.37 Plot of i_D versus v_DS for a fixed v_GS: (a), (b) triode region; (c) saturation region.

The electrical performance of an n-channel enhancement-mode FET is summarised in Figure 2.38. For a specific v_{DS}, a higher v_{GS} results in a larger i_D, which is also described as i_D being amplified by the applied v_{GS}. In addition, for a specific positive v_{GS} ($> V_{TN}$), the triode and saturation regions are observed. If v_{DS} is smaller than v_{DS}(sat), i_D is situated in the triode region; otherwise, i_D is constant and is located in the saturation region.

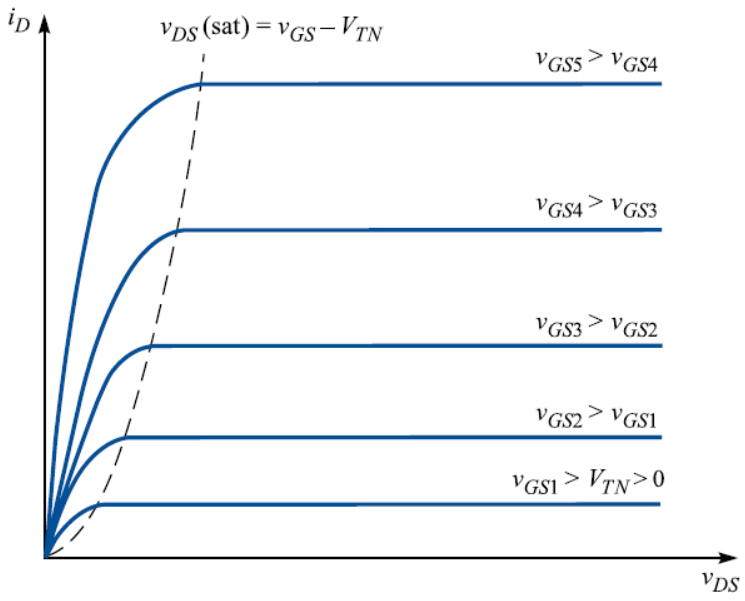

Figure 2.38 Summary of the electrical performance of an n-channel enhancement-mode FET (plot of i_D versus v_DS for varying v_GS).

For a p-channel enhancement-mode FET, the working mechanism is similar. However, as the major conductive carriers in a p-channel enhancement mode FET are holes, a negative gate–source voltage needs to be applied to obtain the maximum effect on the device: holes are attracted by the external electric field generated by the gate–source voltage, and an inversion layer is subsequently created. The threshold voltage is negative. Similarly, the transistor is turned on only when the negative gate–source voltage has a larger magnitude than that of the threshold voltage. Two operation regions are also present in a p-channel enhancement-mode FET, which are separated by the value of v_{DS}(sat).

In addition to the enhancement mode, a FET can also work in the depletion mode. The working mechanism of the depletion-mode FET is here explained. As an example, an n-channel depletion-mode FET is considered.

Different from an enhancement-mode FET, an electron inversion layer initially exists in an n-channel depletion-mode FET even without any external voltage applied to the gate terminal. The pre-existing inversion layer is formed via the introduction of impurities during the fabrication process. Therefore, when an external v_{DS} is applied, a current is observed in this transistor.

v_{GS} is applied to modify the magnitude of i_D in a depletion-mode FET. When the applied gate voltage is positive, the transistor works like an n-channel enhancement-mode FET: more free electrons are attracted towards the inversion layer, leading to a larger i_D. The magnitude of i_D increases with increasing the positive v_{GS} when v_{DS} is fixed, as shown in Figure 2.39.

Conversely, if a negative v_{GS} is applied, the free electrons are pushed away from the inversion layer, leading to a smaller i_D. Moreover, if v_{GS} is equal to the

threshold voltage, all electrons are pushed away from the inversion layer, and no current flows in the device.

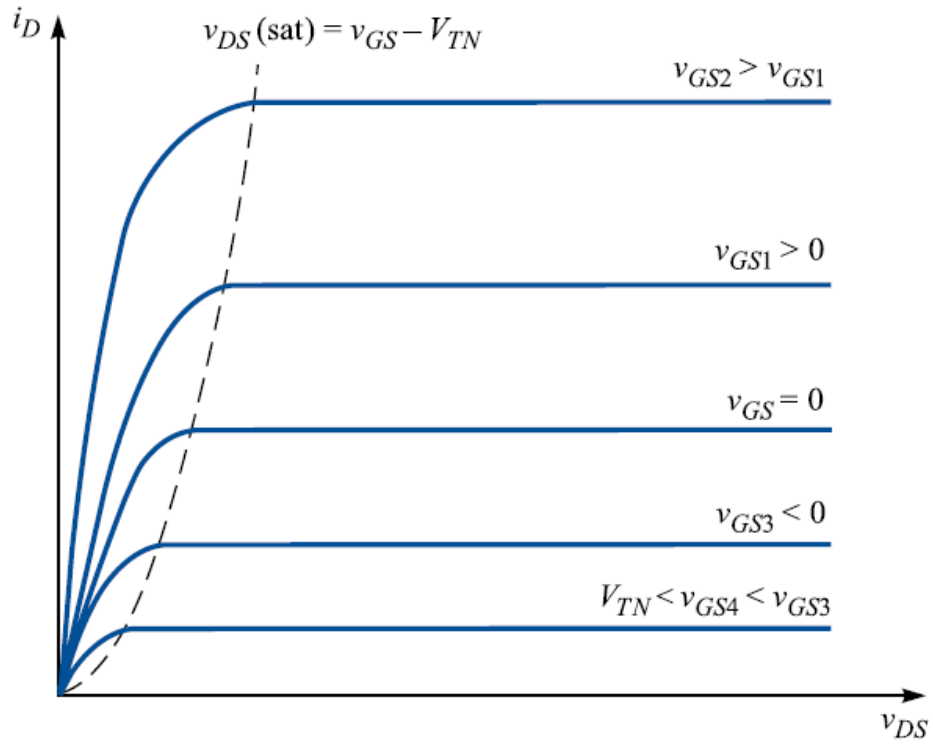

Figure 2.39 Summary of the electrical performance of an n-channel depletion-mode FET (plot of i_D versus v_DS for varying v_GS).

For a p-channel depletion-mode FET, all the directions of the applied external voltage are opposite with respect to those of an n-channel depletion-mode FET. A positive v_{GS} is applied to push the holes away from the inversion layer, while a negative v_{GS} is applied to attract more holes towards the inversion layer. The magnitude of i_D can be controlled by changing the direction and magnitude of v_{GS}. Similarly, there is no current flowing through the device when the applied positive v_{GS} has the same value as the threshold voltage.

2.5.4 Thin-Film Graphene Transistor

Thin-film transistors (TFTs) refer to FETs at the micrometre or nanometre scales. The first group of TFTs were fabricated in 1962 at the RCA Laboratories (Weimer, 1962). Gold electrodes, a cadmium sulphide (CdS) semiconductor layer, and a silicon monoxide insulator layer were prepared on a glass substrate. The structure of these TFTs is presented in Figure 2.40(a).

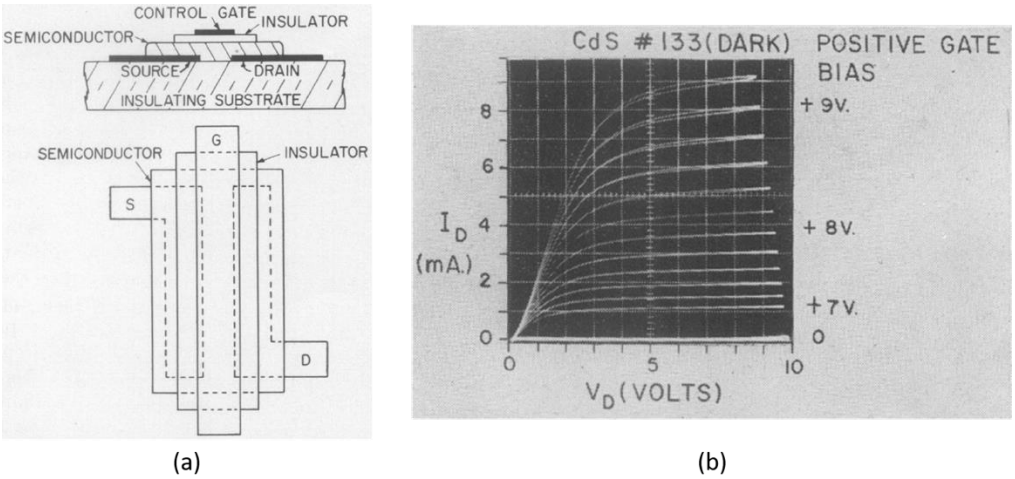

Figure 2.40 The first TFT: (a) structure; (b) electrical performance (Weimer, 1962).

The average thickness of these devices is below 1 μm, and the distance between the drain and source terminals (i.e., the length of the inversion layer) is in the range from 5 to 50 μm. Figure 2.40 (b) shows the typical transistor output performance of one of these TFTs.

Today, TFTs are classified into two groups, depending on the positions of the gate, drain, and source terminals. If the drain/source terminals and gate terminal of the TFT are on the opposite side from the semiconductor channel, the TFT is referred to as a staggered TFT. Otherwise, if all conductive terminals are on the same side as the semiconductor, the TFT is called a coplanar device. Moreover,

as shown in Figure 2.41, both staggered and coplanar TFTs can be further classified into bottom-gate and top-gate TFTs. If the gate is prepared first and placed at the bottom of the TFT, the device is called a bottom-gate TFT; otherwise, if the gate terminal is manufactured as the last layer and laid on the top of the TFT, the device is named a top-gate TFT (Fortunato *et al.*, 2012).

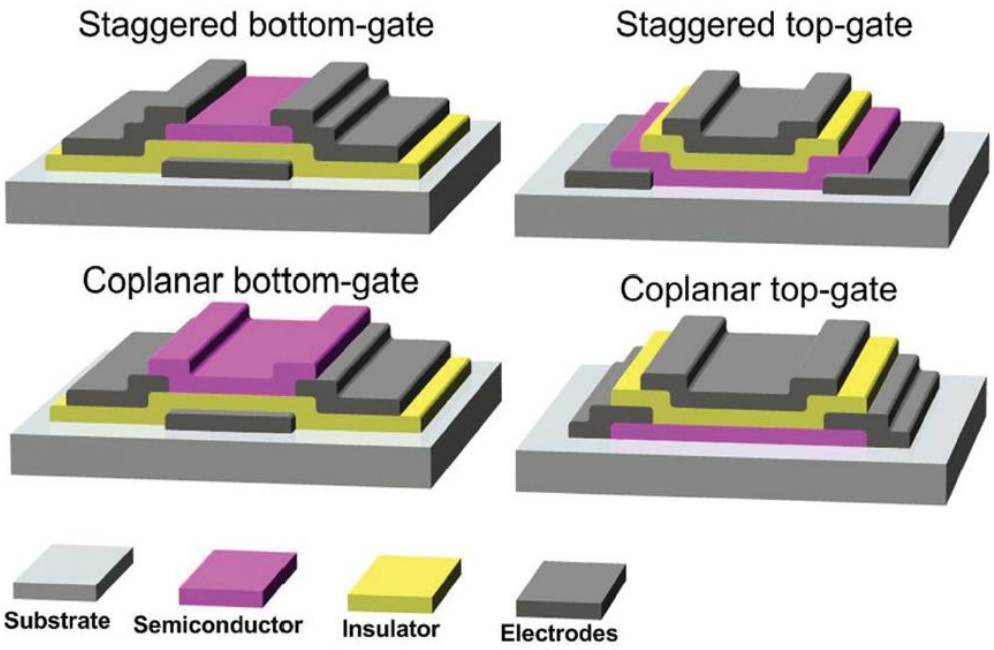

Figure 2.41 Common structures of TFTs: staggered bottom-gate, staggered top-gate, coplanar bottom-gate and coplanar top-gate (Fortunato et al., 2012).

These four TFT structures are used in different situations. For instance, since semiconductors are prepared as the first step in a coplanar top-gate TFT, this structure is suitable for TFTs whose semiconductors require a specific treatment: the semiconductor is treated first without affecting the subsequent preparation of the conductive and insulating materials. In both staggered bottom-gate and coplanar bottom-gate TFTs, the semiconductor layers are prepared as the last step. Therefore, semiconducting materials that require specific treatments (such as high-temperature annealing) are not suitable for use in these two structures.

However, these two structures have several advantageous features. They are commonly utilized as characterisation kits for semiconducting materials, as the prepared semiconductor channels in these structures are exposed to air and easily accessible for testing.

The use of graphene in FETs has been considered since when it was first demonstrated in 2004 (Novoselov *et al.*, 2004). Graphene has been prepared in a few field-effect devices to investigate its gate dependence. For instance, Lemme *et al.* reported a graphene-based field-effect device in 2007 (Lemme *et al.*, 2007). Graphene flakes were prepared through mechanical exfoliation. As presented in Figure 2.42(a), this device was fabricated on a silicon wafer, and gold was used as the material for the conductive electrodes. The drain–source current was measured with and without application of a gate–source voltage. As shown in Figure 2.42(b), it was found that the magnitude of the drain–source current is affected by the presence of the gate–source voltage. Therefore, in this study it was demonstrated that graphene is a gate-dependence material that can be used as the semiconducting channel in FETs.

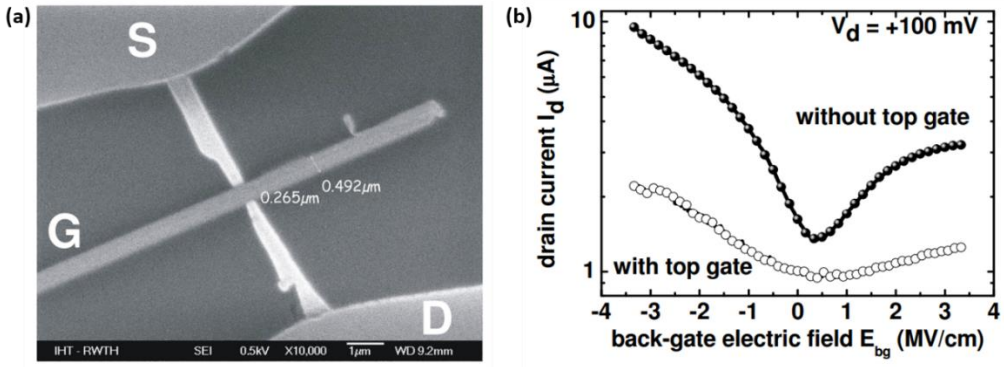

Figure 2.42 (a) SEM image of a graphene-based field-effect device. (b) Electrical characterisation of the drain–source current with and without the application of a gate–source voltage (Lemme et al., 2007).

Since graphene has been proven to be a gate-dependence semiconductor, graphene-based FETs have been extensively investigated, and a few achievements have been reported (Lin *et al.*, 2009). For instance, Moon *et al.* introduced a top-gate graphene FET in 2009 (Moon *et al.*, 2009). In this graphene FET, the drain, source, and gate terminals were made of titanium/platinum/copper layers that were deposited through a lift-off process. Graphene flakes were synthesised on semi-insulating silicon-face 6H-SiC (0001) substrates, and aluminium oxide films were deposited as the dielectric layer. As discussed in Section 2.5.3, it can be observed from Figure 2.43 that this device is a depletion-mode FET, as the drain–source current increases upon application of a positive gate–source voltage and vice versa. However, the variation of the drain–source current is not significant when the gate–source voltage is applied to this FET, and no saturation region is observed in this case. Therefore, a larger drain–source voltage should be applied to this device to analyse the saturation region of the drain–source current, and an optimisation of the materials employed (particularly graphene) or FET structures should be performed to improve the electrical performance of this graphene FET.

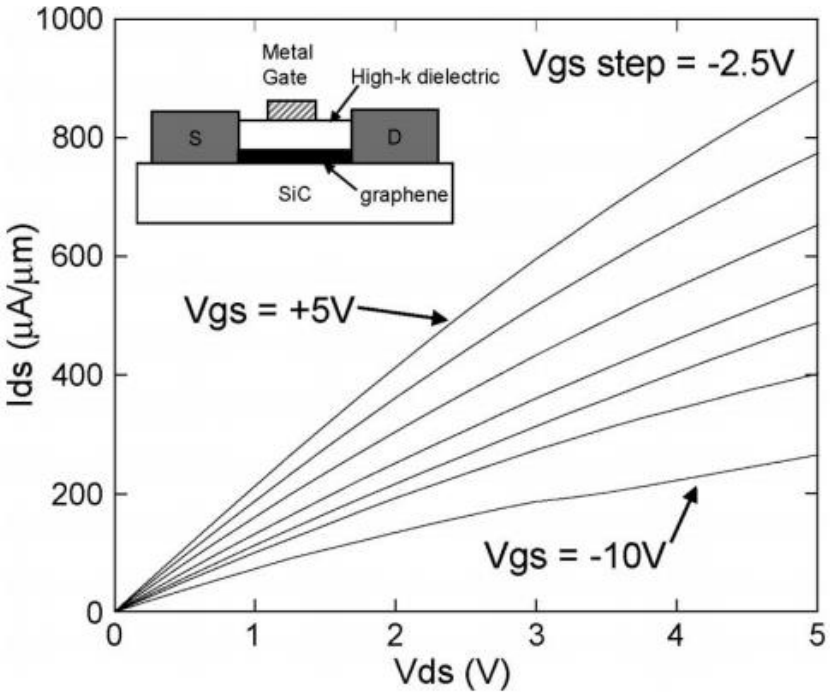

Figure 2.43 Structure and electrical output performance of a graphene FET (plot of i_ds versus v_ds for varying v_gs) (Moon et al., 2009).

In the last decade, several investigations on inkjet printing of graphene TFTs have been conducted. Torrisi *et al.* reported a partially inkjet-printed graphene transistor in 2012 (Torrisi *et al.*, 2012). As illustrated in Figure 2.44, a graphene ink, which was prepared by dispersing graphite flakes in NMP, was printed on a silicon wafer as the semiconducting channel. Two chromium–gold pads were then transferred on top of the semiconducting channel, acting as the drain and source terminals.

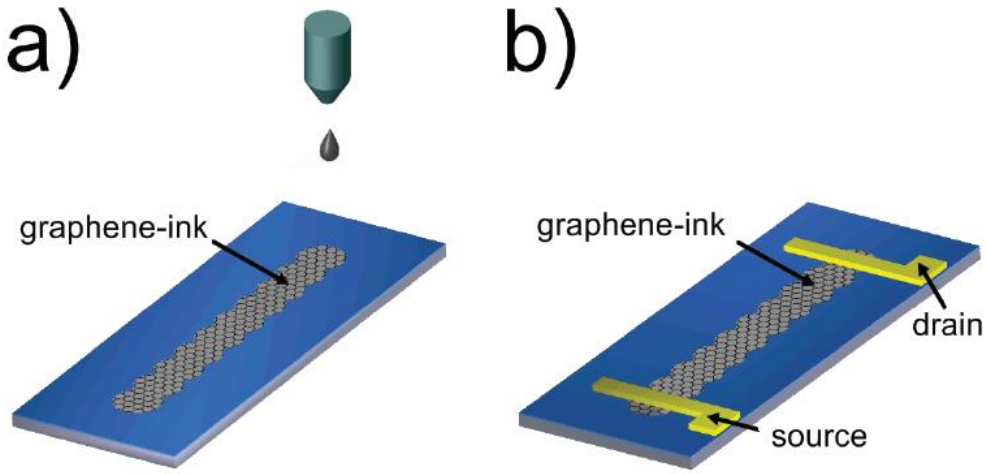

Figure 2.44 Schematic of a partially inkjet-printed graphene transistor: (a) graphene ink on a silicon wafer; (b) chromium–gold pads deposited on top of graphene to act as the drain and source terminals (Torrisi et al., 2012).

Based on the electrical output performance shown in Figure 2.45, this partially printed graphene TFT is a p-type enhancement-mode FET. The magnitude of the drain–source current is amplified when a higher gate–source voltage is applied, and both the linear and saturation region of the drain–source current are observed. However, compared with the electrical performance of the aforementioned graphene FETs, the amplification ratio of this device is low (the drain–source current obtained with a gate–source voltage of −20 V is four times the magnitude of the drain–source current obtained with a gate–source voltage of −2 V).

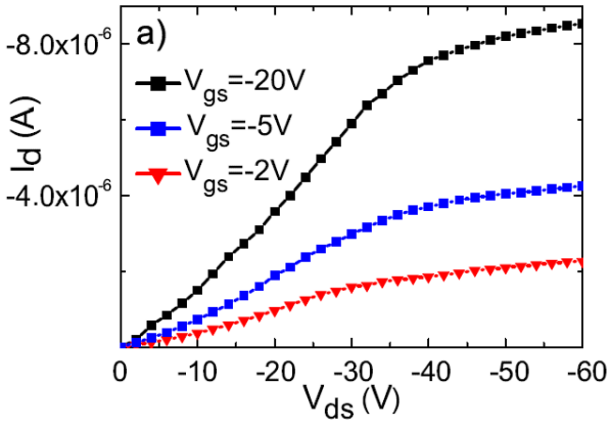

Figure 2.45 Electrical performance of a partially inkjet-printed graphene transistor (plot of i_d versus v_ds for varying v_gs) (Torrisi et al., 2012).

Monne *et al.* reported another partially inkjet-printed graphene-based TFT in 2017 (Monne *et al.*, 2017). Silver nanoparticle inks (Novacentrix) were inkjet-printed for the fabrication of the drain, source, and gate terminals, while the dielectric layer was prepared by spin coating an ethyl acetate solution involving 1-ethyl-3-methylimidazolium bis (trifluoromethanesulfonyl) amide and poly styrene-block-methylmethacrylate-block-styrene. A printable graphene ink was prepared by dispersing the graphene nanoflakes into a mixture of terpineol, cyclohexanone, and ethyl cellulose. However, MoS_2 was introduced into the prepared graphene ink during the inkjet printing process of the TFTs to improve the semiconducting properties of this ink. As shown in Figure 2.46 (a), a staggered top-gate structure was employed for this graphene-based TFT.

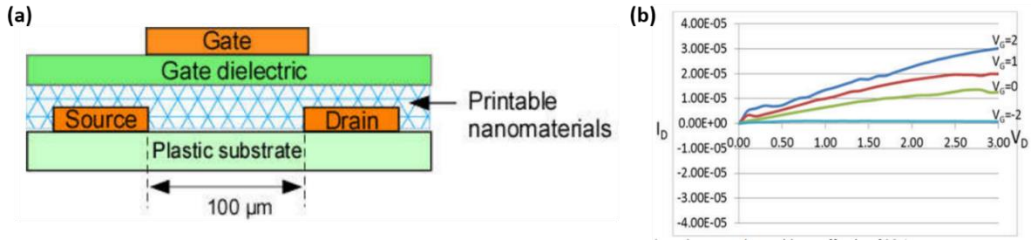

Figure 2.46 (a) Structure of a graphene-based TFT: (b) electrical output performance of the fabricated graphene-based TFT (Monne et al., 2017).

It can be seen from Figure 2.46 (b) that this device is a depletion-mode TFT, and the drain–source current is significantly affected by the application of an external gate–source voltage. For instance, with a fixed drain–source voltage of 3 V, the drain–source current increases from 949 nA to 32.3 µA upon changing the applied gate–source voltage from −2 to 2 V. Therefore, this graphene-based TFT shows a typical transistor performance. However, the graphene ink used in this TFT was doped with MoS_2, and no TFT with a pristine graphene channel has been fabricated or characterised.

The only fully inkjet-printed graphene TFT has been reported by researchers at the Cambridge Graphene Centre (Carey *et al.*, 2017). Silver, graphene, and hexagonal-boron nitride (h-BN) inks were prepared and printed separately on the PET substrate, acting as the conductive electrodes, semiconducting channel, and dielectric layer, respectively. The graphene ink was formulated by dispersing the graphite flakes into NMP. As presented in Figure 2.47, a staggered bottom-gate TFT was fabricated.

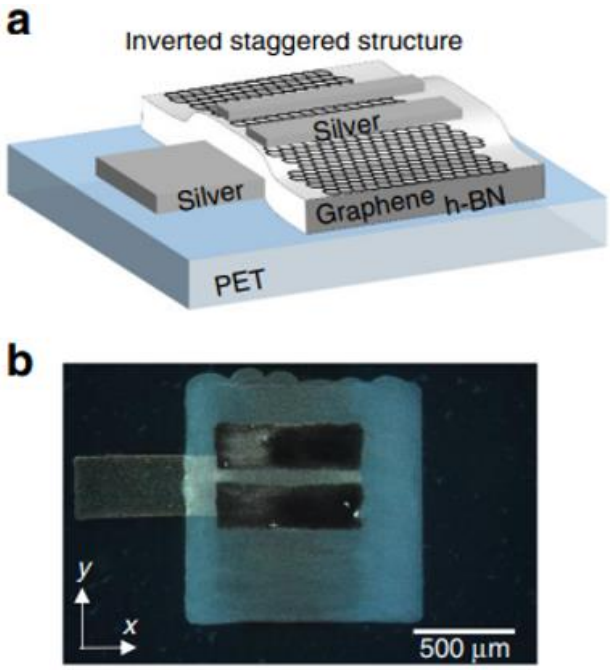

Figure 2.47 Fully-printed graphene transistors: (a) schematic of an inverted-staggered structure FET; (b) optical microscopy image of a practical inverted-staggered structure FET (Carey et al., 2017).

Although the electrical performance of this TFT is unsatisfactory, as only a 1.5-times amplification ratio of the drain–source current was achieved, this work is considered as a milestone in the research of printed electronics, as it provides further opportunities to utilize graphene in complex functional applications.

2.6 Summary

Printed electronics has been employed for different electronic devices in recent years, as fewer process steps and materials are required in this process (Keskinen, 2012) (Norita *et al.,* 2015) (Walker *et al.,* 2016) (Wang *et al.,* 2016) (Sílvia *et al.,* 2018). Contact printing techniques, which are further classified as screen printing, soft lithography, and flexography, are the major printing techniques used for printed electronics owing to their high efficiency output and low operation cost (Xia and Whitesides, 1998) (Ochoteco *et al.,* 2010) (Rosa, 2015).

However, the resolution of these techniques is always low (Kipphan, 2001) (Blayo and Pineaux, 2005). Non-contact printing techniques involving LDW and inkjet printing technology, which have higher resolution, are considered to be a solution to this problem (Chrisey *et al.,* 2000) (Pique *et al.,* 2003). Compared with LDW, the inkjet printing process is simpler and cheaper because no lasers are required. Additionally, the inkjet printing technology is available for polymers which are unresponsive to lasers, thus achieving a larger material selection than that of LDW (Tiwari *et al.,* 2012). Therefore, in-depth investigations on inkjet printing of printed electronics are necessary.

Although a high throughput has been reported using continuous stream mode print heads, drop-on-demand mode print heads are more commonly used in the inkjet printing process, as a more controllable jetting process is possible (Chen and Basaran, 2001) (De Gans *et al.*, 2004). Piezoelectric DOD mode print heads are more advantageous owing to their wider range of available materials and quicker reaction to input signals (Liu and Orme, 2001). Viscosity, surface tension, and printability index are three crucial factors determining which inks are used in piezoelectric DOD mode print heads (Melissa and William, 2008) (Gibson *et al.,* 2010) (Vadillo *et al.,* 2010). Therefore, to ensure that all developed inks used in this work can be inkjet-printed, a printability characterisation is required for these inks.

Different types of conductive inks have been used for printed electronics (Magdassi and Moshe, 2003) (Bidoki *et al.,* 2007) (Rajan *et al.,* 2016). However, silver nanoparticle inks are the most commonly used ones owing to their relatively high conductivity and stable performance (Gans *et al.,* 2004) (Haffarzadeh and Zervos, 2012) (Vimanyu and Patrick, 2020). Since the

development of commercial silver nanoparticle inks is considered to be mature today, a commercially available silver nanoparticle ink (Silver Jet Ink, Advanced Nano Products Co., Ltd) was selected and employed in this work.

Besides conductive inks, insulating inks are crucial in printed electronics to ensure that all conductive/semiconducting components are separated from each other. PVP has been extensively utilized in printed electronics as the insulator layer because it can be conveniently developed into an ink type (Fan *et al.,* 2016) (Vimanyu and Patrick, 2020). However, the insulating performance of printed PVP films is limited in ambient conditions due to the remaining hydroxyl groups (Kim *et al.,* 2008) (Umeda *et al.,* 2008). Therefore, more insulating materials need to be assessed. PI and TPGDA are two insulating material options (Fukukawa and Ueda, 2008) (Arevalo *et al.*, 2015) (He *et al.,* 2017). As both of them exhibit remarkable dielectric properties and thermal stability, a comprehensive investigation of these two materials is worthwhile.

Although organic semiconductors and metal–oxide semiconductors are already used in printed electronics, their poor electrical performance and high annealing temperatures restrict the further development of these semiconductors (Ellmer, 2001) (Lee *et al.,* 2009) (Kim *et al.,* 2014) (Ahn *et al.,* 2015) (Kim *et al.,* 2015) (Wu *et al.*, 2017). In recent years, 2D semiconductors have been investigated by research groups and are considered to be the future of semiconductors owing to their high electron mobility (Chung *et al.,* 2019). Graphene is a typical 2D semiconductor which exhibits a zero bandgap (Han *et al.,* 2007) (Lin *et al.,* 2010) (Cooper *et al.,* 2012). Instead of using pristine graphene, GO is more commonly selected to be developed into an ink type because pristine graphene is difficult to disperse in solvents (He and Derby, 2017) (Li *et al.,* 2017).

Conventionally, a long high-temperature thermal treatment is required to reduce the printed GO specimens to rGO (Gao *et al.,* 2009) (Chen and Yan, 2010). However, it has been recently shown that laser reduction approaches can be used to significantly reduce the treatment time (Kumar *et al.,* 2011) (Wu *et al.,* 2011). Therefore, investigations on GO inks and laser reduction processes are beneficial.

InSe is a 2D material exhibiting both semiconducting and photosensitive properties (Gürbulak *et al.,* 2014) (Politano *et al.,* 2017). Therefore, InSe is a potential semiconductor candidate for both printed electronics and optoelectronic devices (Huang *et al.,* 2016) (Boukhvalov *et al.,* 2017). However, only few InSe-based electronic applications have been proposed until now, and InSe inks have never been reported due to a limited understanding of this material (Feng *et al.,* 2014) (Lei *et al.,* 2014) (Mudd *et al.,* 2015). Therefore, an in-depth study on InSe is necessary. In this work, photodetectors and Hall bars were selected for fabrication to gain a better understanding of InSe.

TFTs are one of the most important components in printed electronics because they are active devices which work as amplifiers (Fortunato *et al.,* 2012). To date, a few partially inkjet-printed graphene TFTs have been reported, but only one fully printed graphene TFT has been fabricated (Lin *et al.,* 2009) (Moon *et al.,* 2009) (Torrisi *et al.,* 2012) (Carey *et al.,* 2017) (Monne *et al.,* 2017). Therefore, more information is required to understand how to successfully fabricate fully printed graphene TFTs. GO inks were employed in this work. As it has been shown that laser treatment can considerably improve the efficiency of the GO reduction process, an ultraviolet (UV) treatment was employed on printed GO specimens in a work by Kumar *et al.* (Kumar *et al.,* 2011).

In conclusion, an in-depth study of fully inkjet-printed graphene TFTs is worthwhile because it provides further opportunities to develop a wider range of printed electronics materials. To achieve a comprehensive understanding of fully inkjet-printed graphene TFTs, investigations on different aspects, such as ink preparation and printing parameters, were carried out in this work.

Chapter 3. Methodology and Experimental Setup

3.1 Research Outline

The overall research on inkjet printing of graphene and InSe based electronic devices is subdivided into 6 stages, including:

1. Product design;
2. Ink preparation;
3. Printability assessment;
4. Droplet deposition optimisation;
5. Characterisation of the printed specimens;
6. Characterisation of the final products.

In the following parts, a brief description of these six stages is presented.

Stage 1: Design of Product Structures

Structures and patterns are designed prior to the fabrication of graphene and InSe based electronic devices, including:

1. A partially-printed InSe photodetector;
2. A partially-printed InSe hall bar;
3. A partially-printed InSe transistor on silicon wafer;
4. A partially-printed graphene transistor on silicon wafer;
5. A fully-printed graphene transistor.

Stage 2: Ink Preparation

It is critical to ensure that all solutes are dispersed uniformly in the solvents to form inks. Otherwise, agglomeration of the 2D solid content could occur in the inks, resulting in unstable droplet formation or nozzle failure (clogging) during

the printing process. To achieve a uniform dispersion, once an ink is developed, it is stirred in the lab for several hours (time depends on the inks). Some post-treatments are applied in this work to help release air bubbles. For instance, TPGDA ink is degassed for 15 minutes and graphene oxide ink is left in the lab overnight (He *et al.*, 2017).

Stage 3: Assessment of Piezoelectric Inkjet Printability

Viscosity and surface tension are two of the most important parameters that determine whether an ink is printable or not. A Dimatix DMP-2800 printer (FUJIFILM, USA) is used in this work, which has specific requirements for viscosity (10 – 12 cP) and surface tension (28 – 33 dynes/cm) of inks processed using this equipment. Therefore, inks are modified to ensure that both viscosities and surface tension fall into the printable range. Addition of diluent or surfactant is commonly used to achieve this purpose.

Stage 4: Droplet Deposition Optimisation

Once an ink is developed with good printability, its droplet formation ability is evaluated. This step focuses on determining whether the prepared ink can form stable droplets without any nozzle failure. A drop view system (based in Dimatix printer) is applied to continuously monitor the droplet states in real time. Droplets are ejected under the control of various parameters, including jetting temperature, voltage and waveform. Based on the printing performance (shown by the drop view system), the printing parameters for each ink are further optimised to ensure a reliable and robust printing process.

Stage 5: Characterisation of the Printed Specimens

Different characterisation methods are applied to printed specimens to obtain a comprehensive understanding of their properties. For instance, electrical characterisation is employed to assess the resistance and dielectric properties of all materials; morphology tests are employed to measure the thickness and roughness of the printed specimens; and optical characterisation is performed to evaluate the photosensitivity of InSe based electronic samples.

Stage 6: Characterisation of the Final Products

In the final stage, the performance of all fabricated products is evaluated. A testing circuit is designed in this research for the electrical characterisation of printed electronics. The effects of structures and printing parameters on the performance of the products are analysed.

A flow chart of the research approach is presented in Figure 3.1:

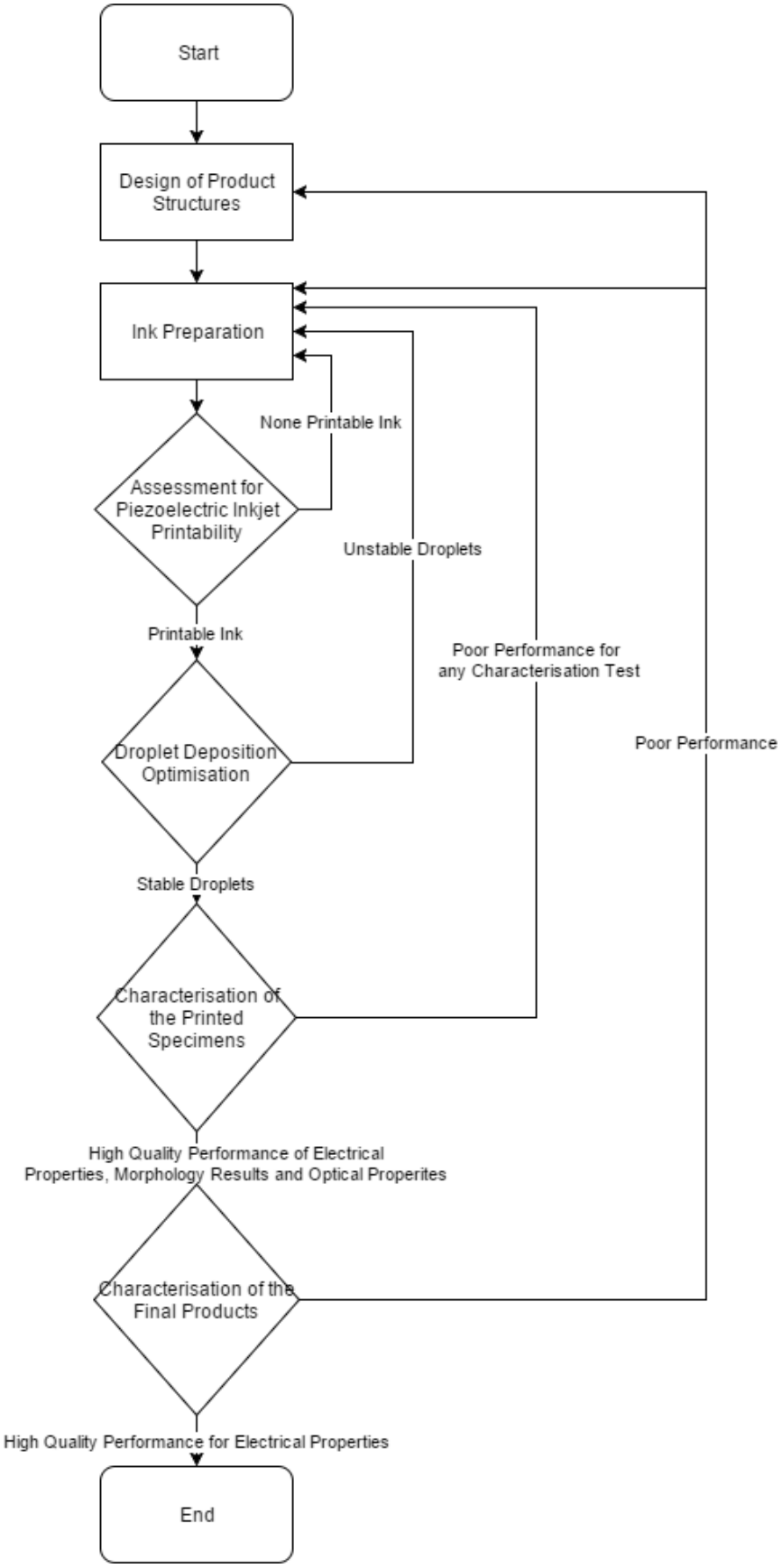

Figure 3.1 Flow chart of research approach.

3.2 Jetting Apparatus

In this work, a Dimatix DMP-2800 printer is used for all inkjet printing. Dimatix DMP-2800 is a piezoelectric drop-on-demand (DOD) research inkjet printer, which is produced by FUJIFILM Dimatix. The printer is operated by a proprietary software: Dimatix Drop Manager. All patterns designed for printing need to be converted to bit-map files so that they can be recognised by the software.

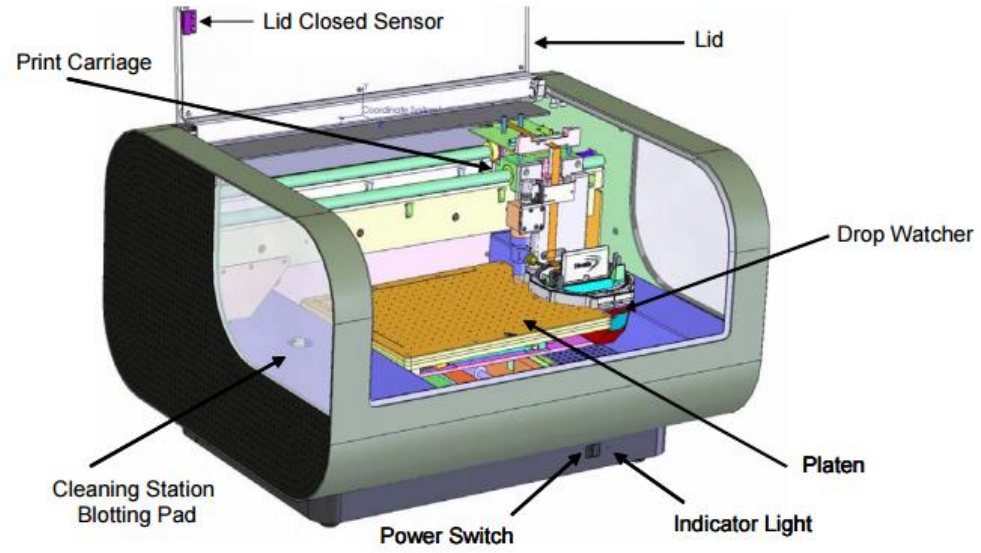

Figure 3.2 Structure of Dimatix DMP-2800 printer (FUJIFILM, 2012).

Regarding the hardware configuration, Dimatix DMP-2800 printer is mainly composed of printing unit, monitoring unit and maintenance station, which are shown in Figure 3.2. In the following sections, the three components are introduced separately and specifically.

3.2.1 Printing Unit

Figure 3.3 presents the whole structure of a Dimatix cartridge. The Dimatix cartridge is composed of two separate parts – a fluid module and a jetting module.

A built-in fluid bag, a fluid case, a fill port and a pressure port are included in the fluid module. The fluid bag is used as an ink reservoir, where the ink is filled into the fluid bag through the fill port. The pressure port is connected to the pressure supply system. The pressure produced by the pressure supply system can be transferred to the fluid module for cartridge cleaning functions (the process will be explained in detail in the maintenance station section).

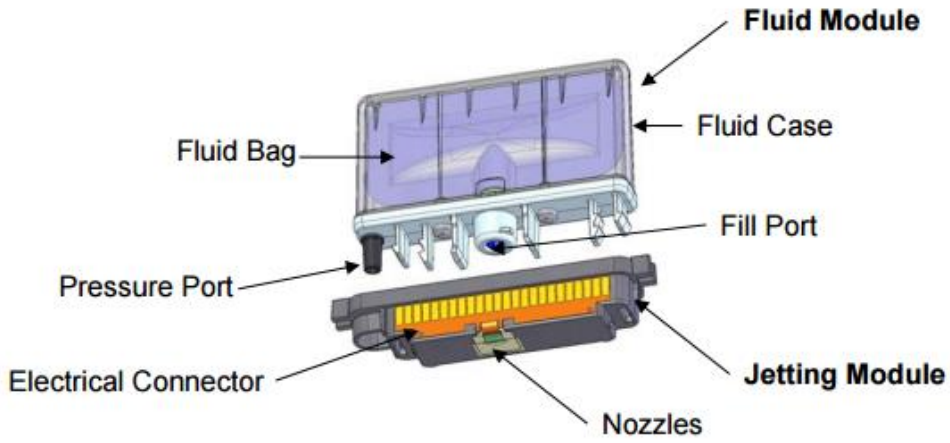

Figure 3.3 Structure of Dimatix cartridge, including fluid module and jetting module (FUJIFILM, 2012).

In each cartridge, the jetting module contains 16 piezoelectric jetting nozzles, which are placed in a row. Each nozzle has its own pumping chamber. The electrical connector in the jetting module receives the voltage waveform signal and transfers the signal to each nozzle. When an input voltage is applied, the pumping chamber is pushed down by the piezo element and a droplet is ejected. In this case, each nozzle can eject ink individually in a DOD regime.

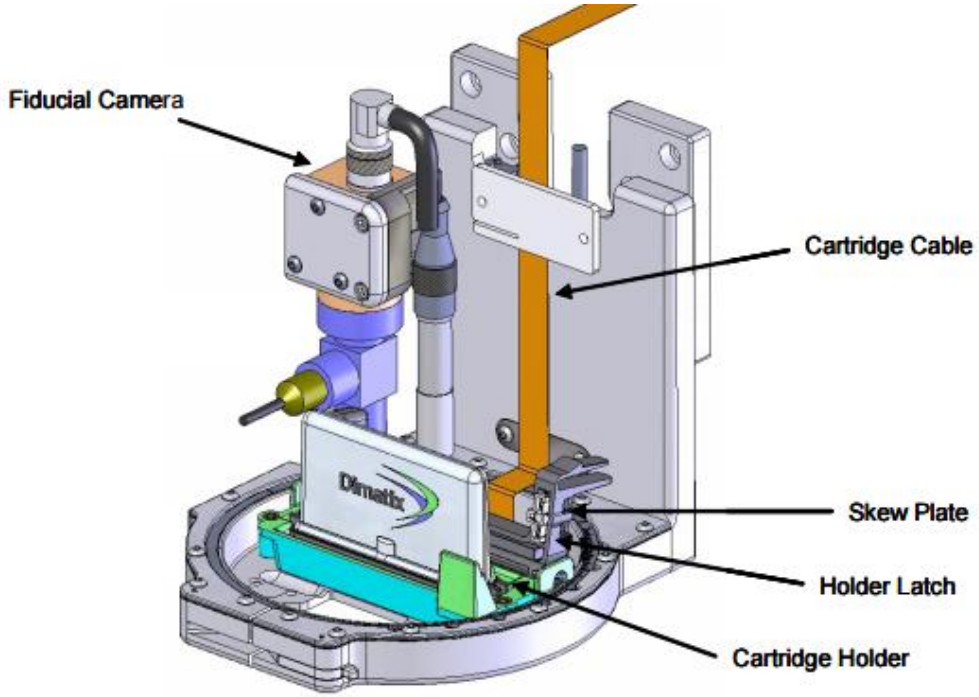

Figure 3.4 Cartridge holder part of Dimatix printer (FUJIFILM, 2012).

The detailed structure of a Dimatix cartridge is shown in Figure 3.4. When a printing job starts, the cartridge moves along the X axis (from left to right). Therefore, the drop spacing in X axis can be adjusted by controlling the moving speed of cartridge synchronised with nozzle jetting frequency. Different from drop spacing in X axis, the drop spacing in Y axis depends on the interval distance between nozzles. This parameter can only be adjusted by changing the mounting angle by rotating the skew plate. For the relationship among resolution, mounting angle and drop spacing, refer to Appendix A.

3.2.2 Droplet Monitoring Unit

The droplet monitoring unit consists of three parts: drop watcher camera, ink collector and light source, as presented in Figure 3.5.

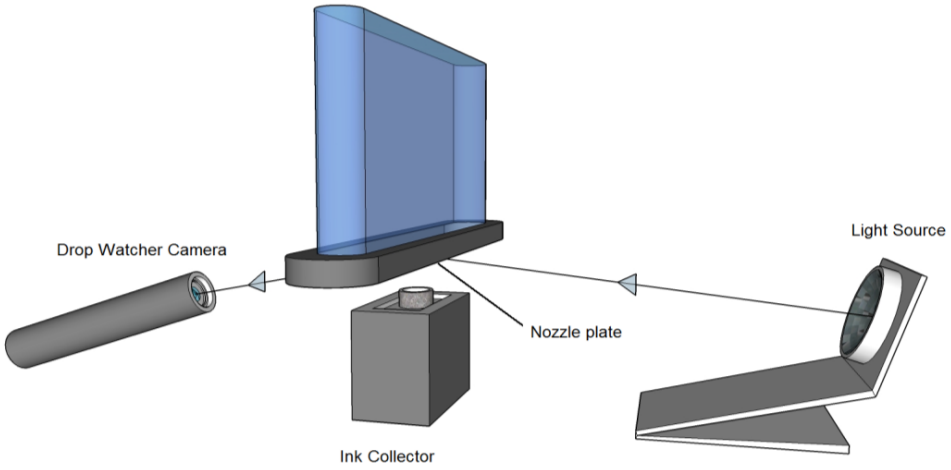

Figure 3.5 The monitoring unit of Dimatix DMP-2800 printer, including drop watcher camera, ink collector and light source.

When the drop watcher function is applied, the cartridge moves to the monitoring unit and stops above the ink collector. Inks are ejected from nozzle plate continuously and disposed by the ink collector. A stroboscopic camera is turned on to observe the jetting performance of the sample ink.

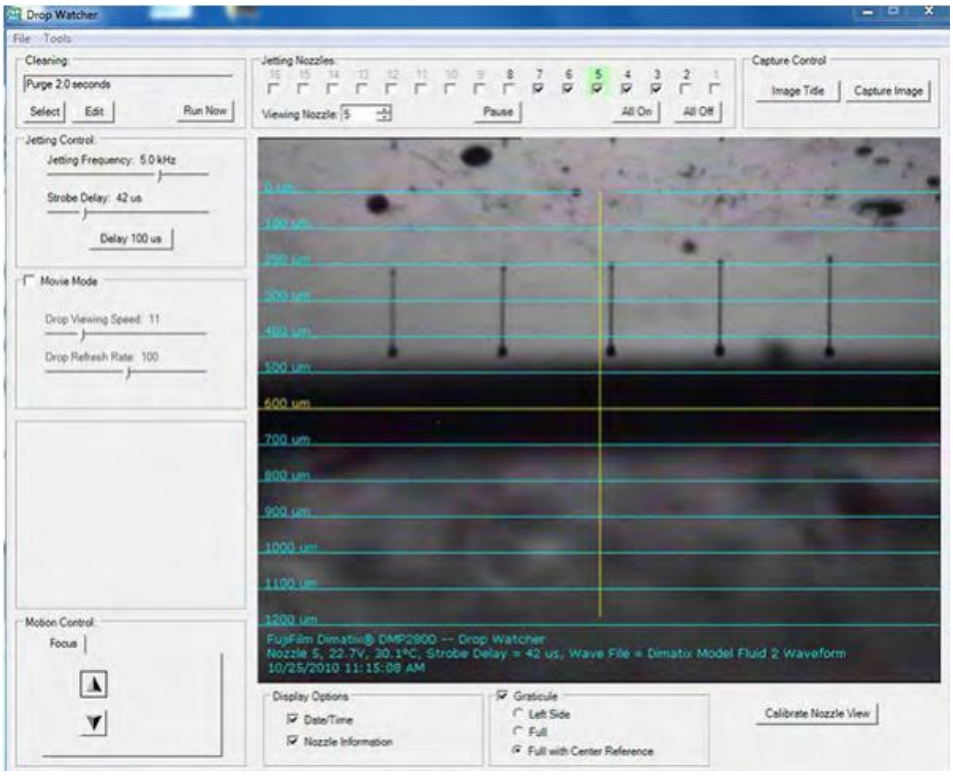

Figure 3.6 Interface of drop watcher function on Dimatix.

Five nozzles (nozzles No. 3 to 7) are observed at the same time in figure 3.6. The observation point can be shifted to view the jetting performance of all 16 nozzles.

3.2.3 Maintenance Station

The maintenance station is designed for the cleaning cycle of the cartridge. When the cleaning function is selected, the printing unit moves to the cleaning pad and goes through a cleaning programme. The cleaning programme consists of three parts – purging, blotting and spitting, which are explained in detail as follows:

Purging:

This procedure is applied to push the ink out of the fluid bag, where the pressure exerted by the pressure supply system is transferred through the pressure port.

This procedure can help to remove the trapped air inside the ink and is generally regarded as the first step of the cleaning cycle.

Blotting:

This procedure focuses on nozzle plate cleaning. During the printing process, clogged nozzles may cause inks to spread everywhere and puddles are easily formed around the nozzles. By lowering the cartridge to the cleaning pad to absorb the excess ink on the nozzle plate, the blotting function can remove the puddles on the nozzle plate to ensure that the nozzle plate is clean.

Spitting:

The spitting function is used to eject droplets with a certain frequency. It is normally arranged as the last cleaning procedure because it can be applied to perform some initial jetting work and help nozzles to be stable.

3.3 Post-processing Unit

In this work, two different post-processing units are used, which are thermal reaction unit and ultra-violet (UV) reaction unit. In the following sections, these two reaction units are introduced respectively.

3.3.1 Thermal reaction unit

Thermal reaction is used for solvent based inks that require solvent evaporation. The substrate heating function provided by the printer's platform can provide heat up to 60℃. Hence, for most inks, the solvents are evaporated at this temperature and the solutes remain to form patterns. However, some inks, such as silver ink, need a higher temperature because their solvents have a higher boiling point (boiling point of TGME is 216 ℃). In such a case, an additional heating device is necessarily employed (Figure 3.7):

Figure 3.7 Thin film heater with a power of 10W.

The thin film heater (KHLV-103/5 Kapton insulated flexible heater, Omega) is made of polyimide and electronic heating wires, with a working power of 10W. This heater is used for the thermal treatment process of high-temperature ink because a temperature as high as 200℃ can be achieved in 40 seconds. The heater is powered by a DC power supply. The relationship between the temperature and supply power is calculated as shown in Figure 3.8. Thus, the temperature of the heater can be controlled by adjusting the input power of the DC power supply.

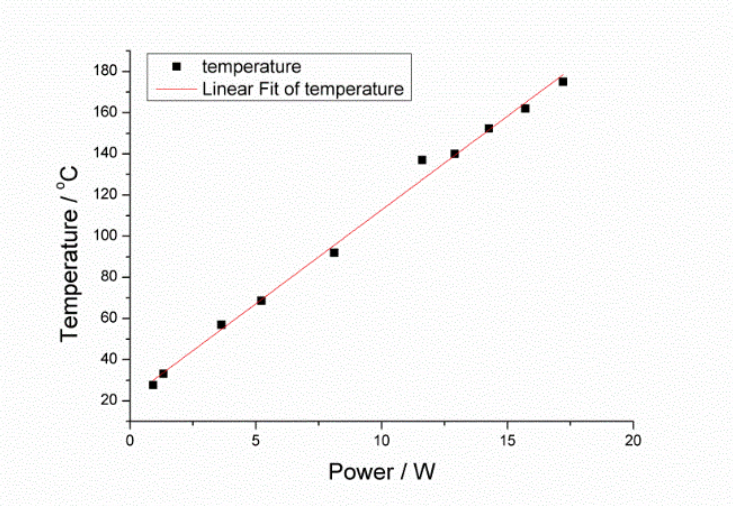

Figure 3.8 Relationship between the temperature and power of DC power supply.

3.3.2 UV Curing Unit

A UV curing unit from Phoseon (FireFly range) is used for UV curable ink. Figure 3.9 presents a photograph of this UV illumination unit:

Figure 3.9 Photo of the UV illumination reaction unit.

With a maximum power of 4 W and a wavelength of 395 nm, the UV irradiation unit is used for the graphene oxide reduction process in this research.

3.4 Design of Product Structure

In this section, designed patterns for indium selenide (*produced by the University of Nottingham's School of Physics and Astronomy) and graphene based electronic products are demonstrated. Photodetector, hall bar and transistors are the three main fabricated products in this work. Based on varying shapes and dimensions of samples, specific customised patterns are designed.*

3.4.1 Partially-printed InSe Photodetector

As mentioned in section 2.5.1, the photodetector is made of a semiconductor with two conductive contacts. In this work, silver ink is inkjet-printed to form conductive electrodes and InSe flakes act as semiconductor.

Figure 3.10 Designed pattern for an InSe based photodetector. Two conductive parts are printed on the sample material.

For each electrode, the pattern is designed as a rectangle due to several reasons. First, as the print head moves from left to right, regular patterns such as square and rectangle, are easier to be fabricated than circle or any other complex patterns. Second, since the probes of testing kits need to be placed on the conductive electrode during the characterisation process, the printed conductive electrodes should be large enough for the probes. As shown in figure 3.10, a rectangular pattern meets this requirement. Therefore, in this work, two rectangular silver electrodes are printed on InSe flakes. However, exfoliated InSe flakes normally have different sizes and shapes. In this work, the dimensions of electrodes and gaps between the designed electrodes are specifically measured and designed based on the measured sizes of InSe flakes. This work highlights the flexibility of inkjet printing technology for fabricating electronic elements compared to conventional masking methods.

3.4.2 Partially-printed InSe Hall Bar

As a photodetector can only be used to check photosensitivity, a hall har is printed to gain a better understanding of the prepared InSe specimens. Similar to the design of partially-printed photodetector, rectangular conductive electrodes are manufactured on semiconductor sample.

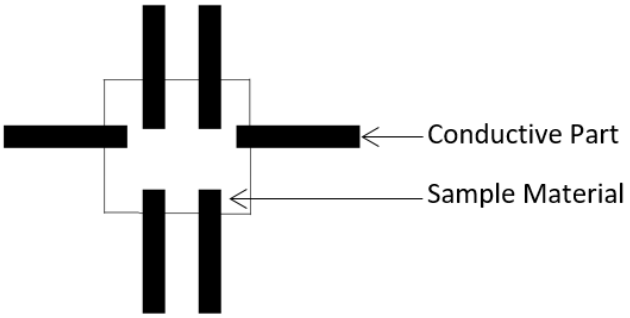

Figure 3.11 Designed pattern for a six-contact 1-2-2-1 hall bar.

As mentioned in section 2.5.2, six electrodes are typically required for a hall bar (Figure 3.11). Therefore, six rectangular silver electrodes are printed on each InSe flake. Due to different sizes of the InSe flakes, dimensions of electrodes and gaps between all electrodes are varied.

3.4.3 Partially-printed InSe transistor on silicon wafer

Once InSe based photodetector and hall bar are successfully fabricated and characterised, InSe transistors are fabricated. However, different from using large InSe flakes (dimensions ranging from 800 μm to 2000 μm) in partially-printed InSe photodetector and partially-printed InSe hall bar, the thickness of the prepared InSe flakes in partially-printed InSe transistors on the silicon wafer is in nano-meter scale (ranging from 30 nm to 50 nm) and the dimensions are in the micro-meter scale (ranging from 20 μm to 50 μm). The reason is as follows: based on the current InSe preparation technology, the thickness of the prepared InSe flake is directly proportional to its dimensions. As the bandgap is tuned by reducing the thickness of InSe flakes, an InSe flake with small thickness is preferred to achieve a high-performance transistor (Mudd *et al.*, 2013).

To form a transistor, silver electrodes (source and drain electrodes) are printed on top of a prepared InSe flake, which is attached on the silicon wafer. The

silicon part of the wafer acts as the gate terminal. A 200 nm thick layer of silicon dioxide (SiO2), which serves as dielectric layer, separates the source/drain terminals from the gate terminal. InSe flake is the semiconductor channel.

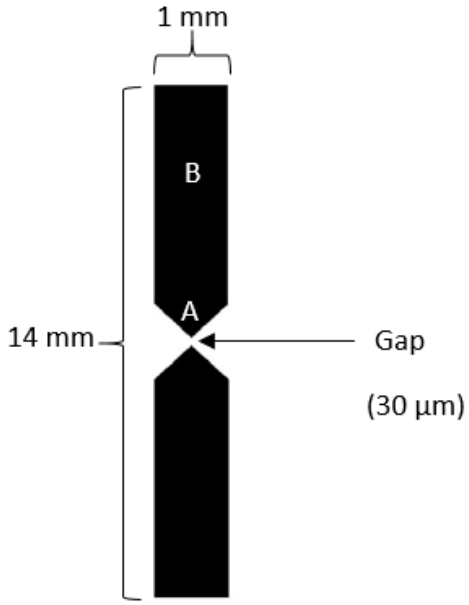

Figure 3.12 Designed pattern for partially-printed InSe transistor on silicon wafer – drain and source electrodes.

The designed pattern for the drain and source electrodes is mirrored with a gap of 30 µm (1 pixel) (Figure 3.12). Each pattern is composed of two parts: (1) part A is used to place test probes; and (2) part B forms the transistor.

3.4.4 Partially-printed Graphene Transistor on Silicon Wafer

A coplanar bottom-gate structure is used for the partially-printed graphene transistor on silicon wafer in this work, because graphene is open to the air and can be easily characterised in this case. A 3D mode is presented in figure 3.13: The gate of the transistor is placed on the bottom and a semiconductor material is placed on top of the whole structure. The bottom of the semiconductor is contacted with both source and drain electrodes (Tseng and Subramanian, 2011).

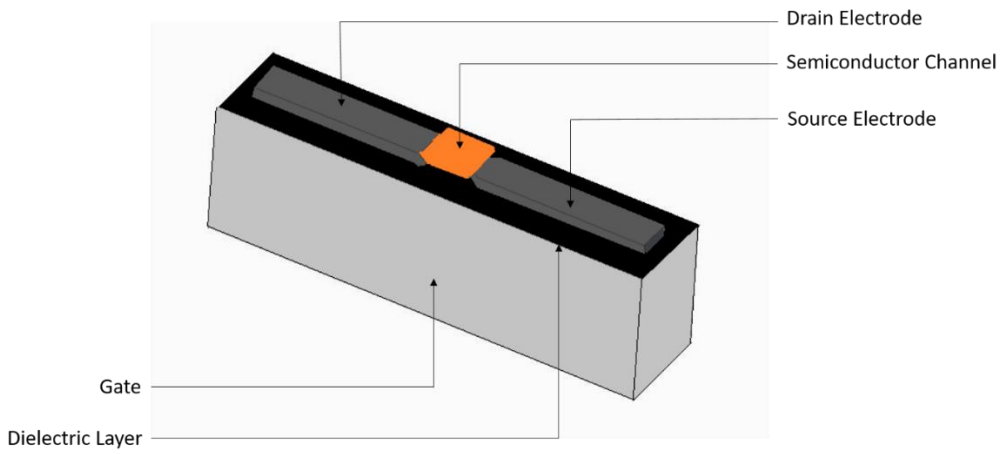

Figure 3.13 3D model of a coplanar bottom-gate transistor. Gate electrode, dielectric layer, drain electrode, source electrode and semiconductor channel are presented from bottom to top.

Similar to partially-printed InSe transistor on silicon wafer, silver electrodes (source and drain electrodes) are printed on top of the silicon wafer first. The graphene oxide ink is printed as the last step to form the semiconductor channel.

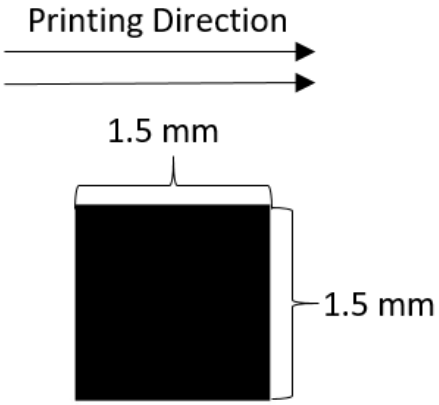

Figure 3.14 Designed pattern for partially-printed graphene transistor on silicon wafer – semiconductor channel.

The designed pattern of drain and source electrodes for partially-printed InSe transistor on silicon wafer is also used for partially-printed graphene transistor on silicon wafer. The semiconductor pattern is designed to be a square, as shown

in figure 3.14. A square pattern is selected due to its simplicity because the only requirement of this pattern is to connect the drain and source electrodes by filling the gap between them.

3.4.5 Fully-printed Graphene Transistor

A staggered top-gate transistor structure is designed for fully-printed graphene transistors in this work, as presented in figure 3.15. In this structure, graphene oxide ink is printed onto a substrate (glass slide) rather than other printed films (such as PI and TPGDA films), reducing the risk of graphene performance being affected by other materials. Drain and source electrodes are printed on the glass slides as the first layer, using the pattern shown in figure 3.12. A square semiconductor channel is subsequently printed to cover the gap between the two electrodes. The dielectric layer is printed as the third layer and a gate electrode is printed on the dielectric layer. The 3D structure of a fully-printed transistor is shown in Figure 3.15.

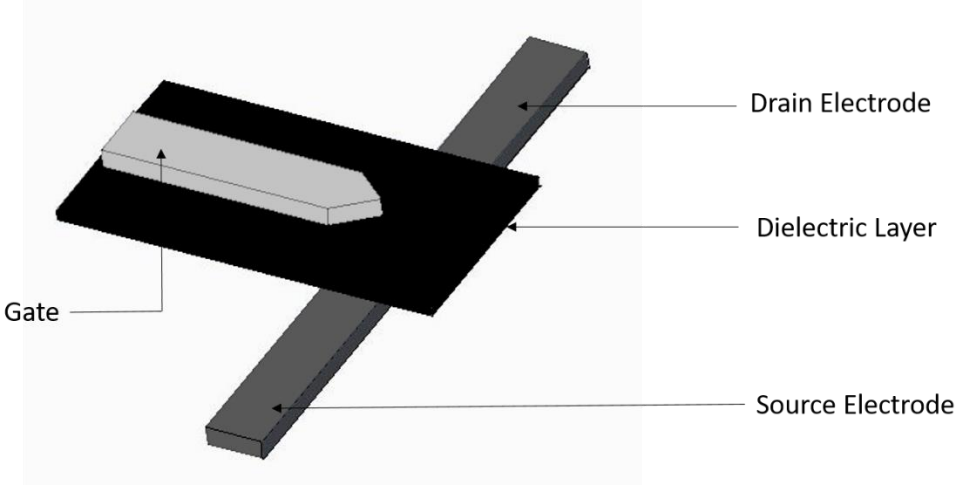

Figure 3.15 3D model of a staggered top-gate transistor. Semiconductor channel, drain electrode, source electrode, dielectric layer and gate electrode are presented from bottom to top.

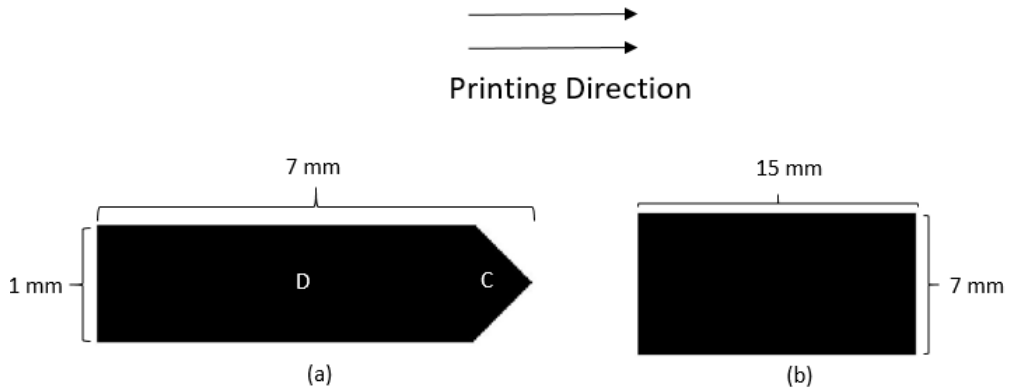

Figure 3.16 Designed pattern for fully-printed graphene transistor (a) gate electrode (b) dielectric layer.

Similar to the pattern of drain and source electrodes, the gate electrode of a fully-printed transistor consists of two parts. As illustrated in figure 3.16 (a), part C is used to form the transistor and part D is used for placing the probes of testing devices. To reduce the capacitance, which affects the electrical performance of the transistor, the needle of the gate should be printed precisely above the gap between drain and source electrodes. There should be a minimum overlap between gate and drain/source electrodes.

A rectangular pattern is used for the dielectric layer in this work, which is shown in figure 3.16 (b). As the only requirement for the dielectric layer is to prevent the drain/source electrodes from touching the gate electrode, the designed dielectric layer should be large enough to cover the drain/source electrodes and a simple rectangular pattern meets this requirement. Therefore, a rectangular pattern with large dimensions (as shown in figure 3.16 (b)) is selected. In this work, gate electrode is printed on the dielectric layer.

3.5 Ink Preparation

In this section, the preparation of conductive ink, insulating ink and semiconductive ink is described. Four types of specific inks are discussed in detail, which are silver ink, polyimide ink, tripropylene glycol diacrylate ink and graphene oxide ink. Since there is a large difference in the printability and properties of developed inks due to addition of varying solvents and treatment under different conditions, all inks are optimised to ensure that they can be printed successfully in the inkjet printing processes.

3.5.1 Conductive Ink

A commercial silver ink (Silver Jet Ink, Advanced Nano Products Co., Ltd) is used as the conductive ink, which is composed of silver nanoparticles (38.853 wt.%) and triethylene glycol monoethyl ether (TGME) (61.147 wt.%). This ink is used to print all conductive electrodes of InSe based and graphene based electronic devices.

3.5.2 Insulating Ink

Both polyimide (PI) and tripropylene glycol diacrylate (TPGDA) inks are used in this research as the insulating ink. These two inks are formulated by researchers from the Centre for Additive Manufacturing (University of Nottingham) (Zhang *et al.*, 2016) (He *et al.*, 2017). In this research, electrical characterisations of these two inks are first performed and the printing characteristics are also optimised. Therefore, a better understanding of PI and TPGDA inks is achieved and a wider range of printed electronics involving insulating components can be fabricated in the near future.

PI Ink

In this work, PI ink is prepared by Fan Zhang from the Centre for Additive Manufacturing. As PI does not dissolve in most conventional solvents, it is printed through a two-step process. First, a commercial poly(pyromellitic dianhydride-co-4,'-oxydianiline) amic acid (PAA) solution (12.8 wt% ± 0.5 wt% PAA in 80% 1-methyl-2-pyrrolidinone (NMP)/20% aromatic hydrocarbon, product number:575771, Sigma-Aldrich) is diluted by NMP (99.5%, product number: 328634, Sigma-Aldrich) to obtain a 1 wt% solution. The diluted solution is then stirred at 800 revolutions per minute (rpm) for 10 minutes at ambient temperature to fully dissolve the PAA. Following that, the solution is subjected to ultrasonication for 30 minutes to remove the bubbles and further disperse the PAA. The resultant PI ink is developed and ready for printing work. A thermal treatment is generally applied to polymerise the PAA for the conversion process of PI (Zhang *et al.*, 2016).

TPGDA Ink

TPGDA ink is prepared by Yinfeng He from the Centre for Additive Manufacturing in this research. Commercial TPGDA (product number: 246832, Sigma-Aldrich) is obtained as a mixture of isomers, which contains technical grade mono methyl ether of hydroquinone (MEHQ) and hydroquinone (HQ) as inhibitors. To the commercial TPGDA, 3 wt% of 2,4-diethylthioxanthone (DETX) (98%, product number: 406368, Sigma-Aldrich) and 3 wt% of ethyl-4-(dimethylamino)benzoate (EDB) (≥99%, product number: E24905, Sigma-Aldrich) are added as the photoinitiator and accelerator, respectively. The mixed solution is then stirred at 800 rpm at room temperature for 30 minutes to improve the dispersion of the initiators, followed by 15 minutes of degassing by bubbling

nitrogen through the ink to minimise the photoinhibition caused by pre-dissolved oxygen (He *et al.,* 2017).

3.5.3 Semiconducting Ink

In this work, graphene oxide inks are used as the semiconducting ink because pristine graphene cannot easily disperse in water or other conventional solvents. Commercial graphene oxide solution (4 mg/mL, product number: 777676, Sigma-Aldrich) is composed of graphene oxide flakes (0.4 wt%) and deionised water (99.6 wt%). Since the surface tension of the deionized water (72 mN/m at 25 °C) is too high for the printing range requirement of the Dimatix printer (28 – 33 mN/m), the solution cannot be used in the experiments directly. Therefore, different solvents with low surface tension are added to the commercial graphene oxide solution to reduce the overall surface tension of the mixture. The characterisation results of the different graphene oxide solutions are listed in Table 3.1 as follows:

Table 3.1 Characterisation results for graphene oxide solution with different solvents (details are explained in section 4.4.5).

Solvent	Percentage (wt%)	Performance	Other Problem
TGME	15/20/25	A stable printing job is applied, but the printed graphene flakes are not connected to each other due to nonuniform dispersion of the mixture.	N/A

Polyethylene Glycol	20	A stable printing job is applied, but the printed graphene flakes are not connected to each other due to nonuniform dispersion of the mixture.	N/A
Tween 20	0.3	A regular sample is fabricated with a stable printing job.	Tween 20 is conductive
Isopropanol	20	A regular sample is fabricated with a stable printing job.	N/A

Based on the characterisation results presented in Table 3.1, commercial graphene oxide solution with 20 wt% isopropanol (22 mN·m at 25 °C) is selected to prepare graphene oxide ink in this work. The mixture of graphene oxide solution and 20 wt% isopropanol is stirred at 800 rpm at room temperature for 1 hour to fully disperse the graphene oxide and left at room temperature overnight to release bubbles. The surface tension of the prepared graphene oxide ink is 34.36 ± 0.78 mN/m.

3.6 Printability Assessment Characterisation

As mentioned in section 2.2.3, viscosity, surface tension and printability index are the three main factors that determine the printability of prepared inks. Therefore, in this section, the characterisation of these three parameters is described.

3.6.1 Viscosity Characterisation

The viscosities of all inks are measured by Malvern Kinexus Pro rheometer (Malvern Instruments Ltd, UK) in this thesis. A cone and plate configuration is used for characterisation process and all measurements are recorded with rSpace for Kinexus Pro 1.3 software. The gap between the cone and plate of sample is 0.15 mm. During the measurement process, a cylindrical cover is placed over the sample inks, creating a closed volume and preventing the evaporation of the inks. Since the viscosity varies with different temperatures and shear rates, inks are mainly measured within the temperature range of 20℃ to 70℃ in this work, which corresponds to the operating temperature range of the Dimatix printer. Moreover, at each shear rate and temperature point, the viscosity is checked at 5 s intervals in a 180 s test period when the machine is in a steady state condition.

3.6.2 Surface Tension Characterisation

The surface tension of the inks is measured by a drop shape analyser DSA100S (KRÜSS GmbH Germany) through the pendant drop method, during which the ink is ejected drop by drop. Once a droplet is in the equilibrium state, the profile is captured and the surface tension is automatically measured by the software. At each temperature point, tens of droplets are measured and recorded in this work to achieve objective results.

3.6.3 Printability Summary

Based on the viscosities and surface tension measurements, the printability index Z is calculated for each ink. As mentioned in section 2.3.3, the ink is typically considered to be printable when Z number of an ink lies between 1 and 10. Therefore, a rough assessment of the printability of each ink can be achieved.

3.7 Printed Sample Characterisation

In this work, varying characterisation approaches are employed on printed samples for different purposes. For instance, all printed specimens are studied with optical microscope (Reichert-Jung MEF3) first to briefly determine the jetting performance. A profilometer (Bruker Contour GT-I) is then employed to measure the thickness and roughness of the printed samples.

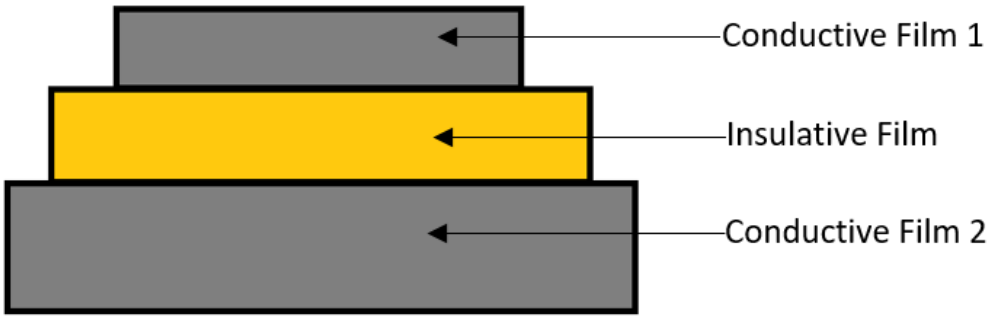

Figure 3.17 Designed sandwich structure for insulating property test. One insulative film is placed between two conductive films.

Basic electrical characterisation is also performed on printed samples: a multi-meter (Fluke 28 II) is used to measure the resistances of the conductive samples and graphene/InSe samples. A sandwich structure, as shown in Figure 3.17, is designed to evaluate the dielectric property of insulating materials. In this sandwich structure, two conductive films are printed with an insulating film between them. By placing two probes of multimeter on the two conductive films, the dielectric properties of the insulating layer can be examined.

3.8 Transistor Test Circuit

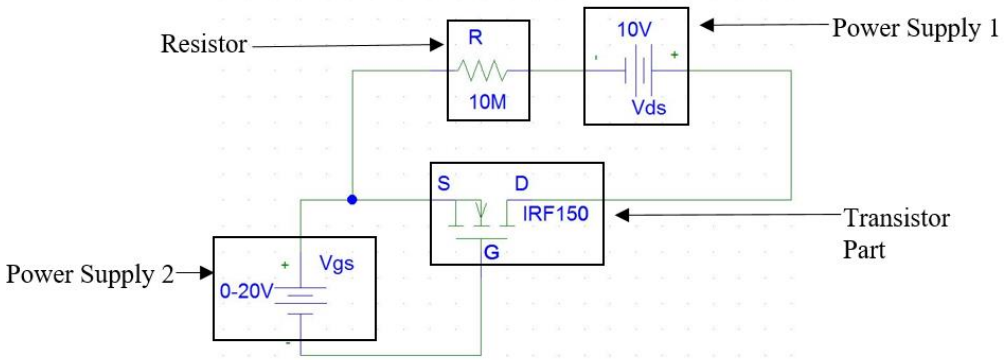

Figure 3.18 Designed testing circuit of printed transistors.

Figure 3.18 shows the designed testing circuit for printed transistors, which is based on the working principle discussed in section 2.5.3. Two DC power supply units are applied in the testing circuit. Power supply 1 provides a fixed voltage (10 V) between drain and source electrodes while power supply 2 applies a variable voltage (0-30 V) between gate and source electrodes. As the current through the channel between drain and source electrodes is generally small ($10^{-9} - 10^{-7} A$) and difficult to be measured with a multimeter, a resistor with a value of 10 MΩ is placed between drain and source electrodes. According to equation (10), the drain-source current can be calculated by measuring the voltage of the resistor.

$$\mathrm{I(current)} = \frac{V(voltage)}{R(resistance)} \qquad (10)$$

Chapter 4 Single Layers of Developed Inks in Inkjet Printing

In this chapter, silver, polyimide, TPGDA, and graphene oxide inks are characterised. Several crucial parameters such as viscosity and surface tension are measured and compared with a printable requirement range of Dimatix printer. For each ink, single layer square specimen was printed because of its simplicity and observed under the optical microscope. The variation parameters led to the different results for the fabricated single layer specimens. Details are explained in sections.

4.1 Silver Ink Characterisation

In this PhD, a commercial silver ink was employed due to the simplicity of its preparation and printing stabilization (Kamyshny, Steinke and Magdassi, 2011) (Balliu et al., 2018) (Xiao et al., 2020). Although a data sheet was provided for this commercial silver ink, a characterisation process was still applied to ensure that the values of all printable parameters matched those in the data sheet. Viscosity and surface tension were measured first to check the printability index of the ink. After the ink was poured into the cartridge, the drop formation of the silver ink was observed through a stroboscopic camera of the Dimatix printer to be sure that the ink was ejected from the nozzles continuously without any clogging occurred. Based on the measured droplet size, a suitable drop spacing was chosen for this ink to make all the printed droplets overlapped. The thermal treatment was applied in the printing process to improve the evaporating efficiency of solvents. Various printing results were observed due to different

thermal treatment strategies. Finally, the electrical properties were analysed for all the printed specimens.

4.1.1 Viscosity Assessment

The viscosity of the silver ink was measured based on the charaqcteristics provided in section 3.6.1 using a Malvern Kinexus Pro rheometer (Malvern Instruments Ltd, UK). Its value was found to be 11.61 ± 0.13 mPa·s. Since the silver ink was ejected at a jetting temperature of 20°C, all measurements were made under the room temperature conditions. Based on the printer guidelines, the viscosity required for the inks used in the Dimatix printer is between 10 and 12 mPa·s at the operating temperature (Dimatix, 2013). Therefore, the viscosity of the silver ink lied in the acceptable range.

4.1.2 Surface Tension Assessment

The surface tension of the silver ink was evaluated using a DSA100S drop shape analyser (KRÜSS GmbH Germany) with respect to a procedure described in section 3.6.2. Its value was found to be 35.91 ± 0.6 mN/m, which is slightly beyond the range suggested by the manufacturer's guidance (28 to 33 mN/m) (Dimatix, 2013). However, since the printability of inks is governed by a combination of viscosity, surface tension, and density, this silver ink may still be used for printing even at a little higher surface tension.

4.1.3 Printability Index of Silver Ink

The printability index is introduced in section 2.2.3 and can be found as follows:

$$Z = \frac{\sqrt{\rho r \gamma}}{\mu}, \tag{4}$$

where Z is the printability index, ρ is the density of the ink, r is the characteristic length which is normally the nozzle diameter, γ is the surface tension of the ink, and μ is the viscosity of the ink.

In this work, the density of the silver ink is 1.45 g/mL and the nozzle diameter is 21 μm. With a viscosity of 11.61 cPs and a surface tension of 35.91 dyne/cm, the printability index is 2.848. As demonstrated in section 2.2.3, an ink is considered to be printable if its printability index is between 1 and 10 (Reis and Derby, 2000). Therefore, the silver ink employed in this research fulfils this condition.

The printability characteristics of this silver ink are summarized in Table 4.1.

Table 1.1 Printability parameters of silver ink.

Ink	Silver
Viscosity (mPa·s)	11.61 ± 0.13
Surface Tension (mN/m)	35.91± 0.6 mN/m
Density (g/mL)	1.45
Printability Index	2.848

4.1.4 Droplet Formation of Silver Ink

A droplet formation of the silver ink was characterised after measuring the viscosity and surface tension. First, the silver ink was poured into cartridges and ejected by the Dimatix printer at room temperature (according to the information appearing in the bottom-left part of Figure 4.1, the jetting temperature was 23.1°C). The stroboscopic camera in the monitoring unit was used to observe the jetting performance.

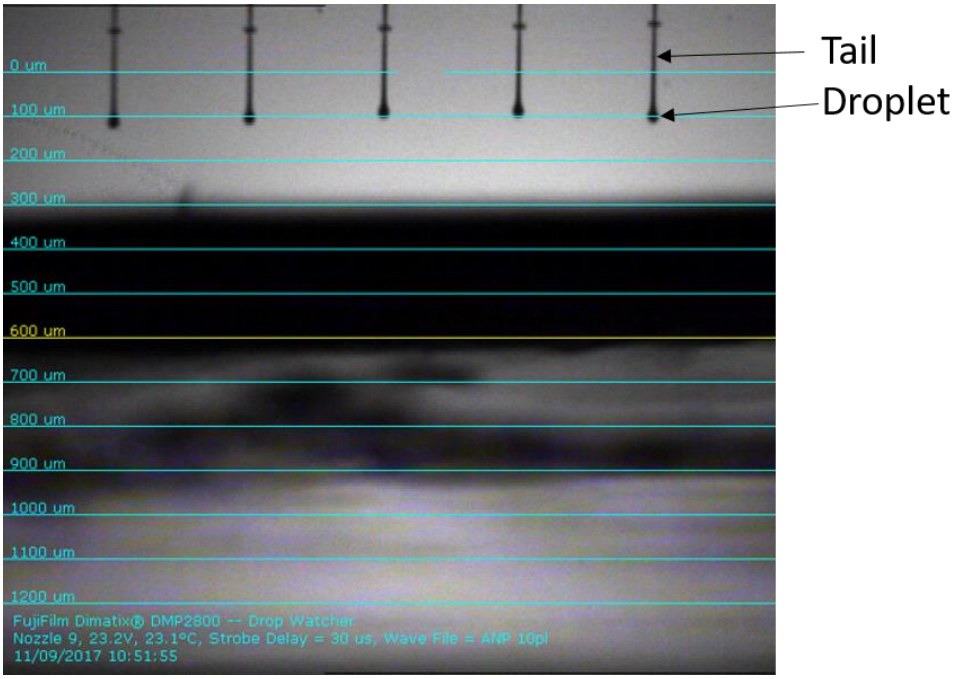

Figure 4.1 Droplet formation of the silver ink. Both silver droplets and tails are observed.

In Figure 4.1, five nozzles emerge simultaneously in this nozzle interface. All nozzles work well without any clogging occurred, demonstrating the silver ink stability during the printing process. However, it also observes the long tails behind the droplets, which are considered as a major disadvantage of the inkjet printing. The problem of tails can be solved, e.g. through their absorption by original droplets under the additional voltage pulse in the jetting waveform (Dong, Carr and Morris, 2006) (see Figure 4.2a). This method is also used in present work, as shown in Figure 4.2b.

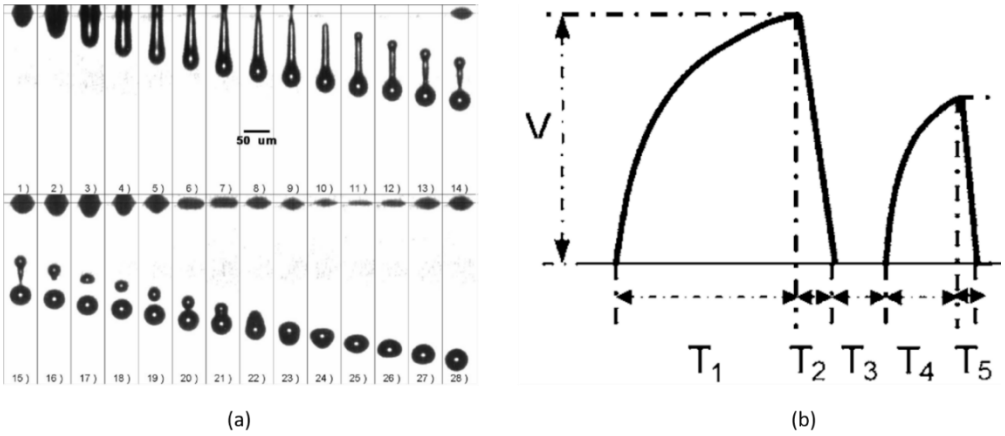

Figure 4.2 (a) Droplet formation of a double voltage waveform. (b) A double voltage waveform (Dong, Carr, and Morris, 2006).

4.1.5 Jetting Performance of Printed Sample

A glass slide was used as the substrate for the printed silver sample because of its relatively uniform surface. A dot square was firstly printed on the glass slide and observed under the optical microscopy to measure the silver droplet size (see Figure 4.3). A drop spacing of 120 µm was selected to avoid the merging of the droplets.

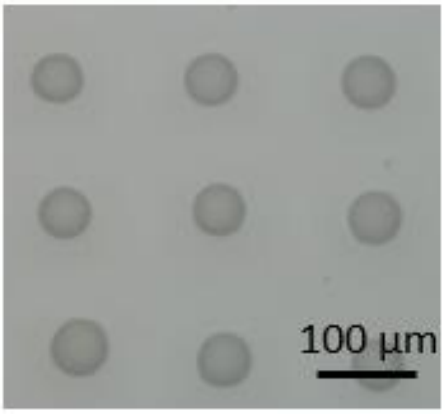

Figure 4.3 Silver ink droplets deposited onto a glass slide via inkjet printing. Drop spacing is 120 µm.

According to the optical image in Figure 4.3, the average droplet size of the silver ink was around 50 μm. In this respect, a 40% ratio of overlap and a drop spacing of 30 μm were further selected in this thesis to ensure that all the silver droplets were overlapped.

To remove TGME solvents from silver nanoparticles, the glass slide during heating was heated to a relatively high temperature (160℃). Two printing mechanisms with a different sequence of thermal treatments were employed on this silver ink, resulting in various printing performances.

In the first, the printing was implemented under continuous exposure of the substrate to a temperature of 160°C. The choice of exactly this temperature of the substrate was due to the following reasons. When it is lower than 160°C, the solvents are not evaporated efficiently when the droplets land on the substrate. In turn, an increase of the temperature above 160°C makes the solvents be evaporated just after or even before the droplets leave the nozzle, which may cause nozzle clogging or even damage.

A single layer specimen with dimensions of 5 mm × 5 mm was printed to determine the jetting performance of this silver ink. Figure 4.4 (a) displays the magnified optical image of the right corner of the printed specimen.

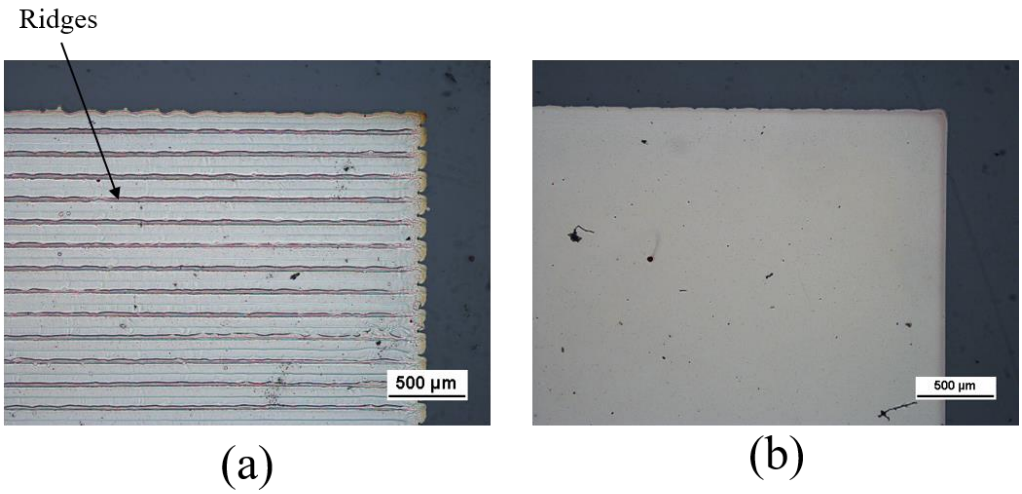

Figure 4.4 The right corner of a square specimen printed from the silver ink using inkjet printing. Here, heating is applied (a) during and (b) after the printing process.

According to Figure 4.4 (a), the solvents of this silver ink were evaporated straightaway when the droplets landed on the substrate. The left-to-right movement of the printer caused the emergence of silver tracks. Furthermore, ridges were observed between the consistent areas due to a 40% ratio of overlap. Although there were some gaps between the tracks at the edge of the specimen, a relative regular pattern was formed. Moreover, no satellite droplets were found outside this printed pattern, which allows one to conclude that the chosen temperature mode provides the silver ink stability during printing.

In the second mechanism, printing was implemented at room temperature, but heating to 160°C was applied after the printing work was finished. This increased the processing time compared to the first printing method. The magnified image of the right corner of the obtained 5 mm × 5 mm pattern is shown in Figure 4.4 (b).

The specimen prepared via the second way evidenced no obvious silver tracks or ridges. This was due to the fact that silver inkjet printing was performed at room temperature and the droplets merged uniformly while landing on the substrate. Applying the post-printing thermal treatment enabled all solvents to be evaporated and silver particles to be uniformly placed. Similarly, no droplets were observed outside the printed specimen and the regular shape of the droplets onto the substrate revealed the printing stability. However, some holes (gaps) arose inside the pattern, which might be caused by impurities on the glass slide substrate or solvent evaporation during heating. To solve this problem, the glass slides were afterwards cleaned with isopropanol to be used for rest experiments. Therefore, both these silver inkjet printing mechanisms can be applied in practice. However, the printed specimens were further characterised via various techniques to determine which printing mechanism was more effective for this study.

4.1.6 Electrical Characterisation and Thickness Measurement of Single Layer Silver Specimen

The resistance of printed silver specimens was evaluated first via a two-probe method using a multi meter (UNI-T UT50B). For this, two probes of the kit on the specimen with a fixed length (1 mm in this work), and the resistivity of the samples was then calculated from the expressions below:

$$R = \rho \times \frac{L}{A}, \tag{11}$$

$$\rho = R \times \frac{A}{L}, \tag{12}$$

where R is the resistance, ρ is the resistivity, and A is the cross-section area of the printed silver specimen and L is the length between the two probes of the kit.

The measurements were made ten times for both printed specimens, and their average resistances are given in Table 4.2.

Table 4.2 Average resistances of silver specimens obtained via various printing mechanisms.

Printing Mechanism	Average Resistance (Ω)
Thermal treatment during printing	1.4 ± 0.2
Thermal treatment after printing	12.6 ± 0.8

According to Table 4.2, there is a significant difference between the average resistances of the silver specimens printed by two different mechanisms. Since printed silver films are used as the conductive components in this work, preference is given to a sample with a low resistance, which was heated while printing.

The resistivity calculation requires the sample thickness measurement. In this respect, a Bruker Contour GT-I profiler was employed to assess the thickness and surface roughness of printed samples. Since the high-speed camera is normally positioned far from the substrate and the glass slide with a printed silver specimen is always thin (around 1 mm), it is difficult to achieve the accurate focusing on the specimen. In this case, a pillar is placed on the substrate and the glass slide is then put on top of the pillar to reduce the distance to the camera and improve the focusing. In present study, the printed silver specimen was exposed to a white light beam, and the corresponding results are shown in Figure 4.5.

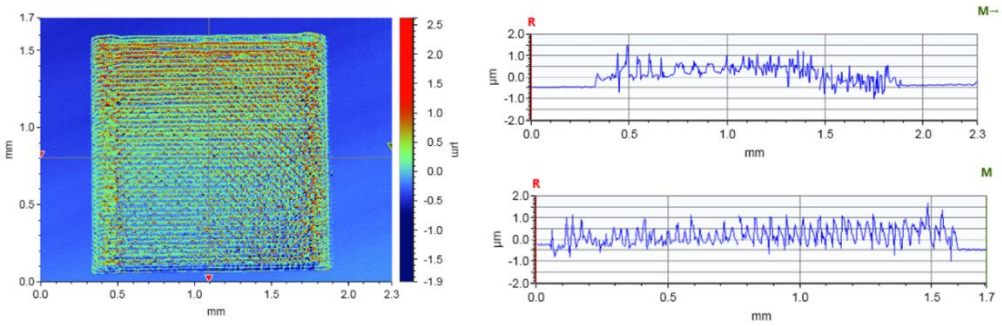

Figure 4.5 Topological scan and thickness profiles of the printed silver specimen.

Based on the experimental data, the thickness of the printed silver specimen was found to be around 0.7 µm. As observed and discussed in section 4.1.5, the roughness fluctuation of the printed silver specimen was due to silver tracks and ridges emerging upon thermal treatment.

Therefore, the thickness of silver specimen is 0.7 µm and the width is around 50 µm, leading to a cross-sectional area of 35 μm^2. The measured average resistance is 1.4 Ω and the fixed length between the two probes is 1 mm. In this case, the resistivity of the printed silver specimen can be calculated using Eq. 12:

$$\rho = R \times \frac{A}{L} = 1.4 \times 35 \div 1000 = 4.9\ \mu\Omega \cdot cm \qquad (12)$$

The resistivity of this printed silver specimen exceeds that of pure silver (1.59 $\mu\Omega \cdot cm$) by 3 times. This means that the printed silver sample is less conductive than pure silver, which can be explained by the following reasons. For instance, the electrical resistivity of silver films is significantly affected by the fabrication methods and nanoscaled structure (Stewart, Kim and Wiley, 2017). Since the printed silver specimen is prepared from silver nanoparticles, whereas pure silver is normally extracted from ores, the resistivity is affected during the fabrication. According to another report (Fernandes *et al.*, 2020), the resistivity

of printed silver specimens is influenced by the temperature employed during the heating, and the higher is the temperature, the lower is the resistivity. Thus, using the higher temperature (e.g. 180℃) is a reliable way to reduce the resistivity of the silver nanoparticle inks to the required level.

4.2 Polyimide Ink Characterisation

Polyimide (PI) and tripropylene glycol diacrylate (TPGDA) are the insulating inks used in this PhD thesis. The polyimide ink was formulated by Dr Fan ZHANG at the Centre for Additive Manufacturing (University of Nottingham). In this section, attention is paid to viscosity and surface tension characterisation as well as the drop formation of polyimide ink. Since polyimide ink spreads over the substrate when printing at room temperature, thermal treatment is applied during the printing process to fix the droplets. Specimens fabricated at different substrate temperatures are observed and analysed, and the results are discussed in the last part of the section.

4.2.1 Viscosity Assessment

The room-temperature viscosity of the polyimide ink was measured using a Malvern Kinexus Pro rheometer (Malvern Instruments Ltd, UK) (Figure 4.7) at a rate of 1000 s-1. Its value was found to be 5.11 ± 0.22 mPa·s, being below the level required for the inks used in the Dimatix printer (10–12 mPa·s). Therefore, polyimide ink is generally considered as unprintable in this kind of printers. However, based on previous experiments taken by Dr Fan ZHANG at the Centre for Additive Manufacturing (University of Nottingham), the polyimide ink is printable in Dimatix printer. In this respect, the polyimide ink is used in present work as the dielectric layer (Zhang *et al.*, 2016).

4.2.2 Surface Tension Assessment

The surface tension of the polyimide ink was assessed using a DSA100S drop shape analyser (KRÜSS GmbH Germany) through a pendant drop method. It was found to be 39.37 ± 0.76 mN/m, which was 19.3% higher than the maximum allowable value for the inks applied in Dimatix printers. However, the previous works revealed the ability to use this type of inks for Dimatix printer.

4.2.3 Printability Index of Polyimide Ink

In the Dimatix printer, a nozzle diameter is 21 µm and the density of polyimide ink is 1.03 g/mL. Since the viscosity of the polyimide ink is 5.11 mPa·s and the surface tension is 39.37 mN/m, the printability index calculated using Eq. 4 from section 2.2.3 is found to be within a printable range (5.71).

The above characteristics of polyimide ink are listed in Table 4.3.

Table 4.3 Printability assessment of polyimide ink.

Ink Property	Average Value
Viscosity (mPa·s)	5.11 ± 0.22
Surface Tension (mN/m)	39.37 ± 0.76
Density (g/mL)	1.03
Printability Index	5.71

4.2.4 Droplet Deposition and Sample Formation

The polyimide ink (PI) droplets were printed on the glass slide with a large drop spacing (60 µm) to allow one to assess their size. As shown in Figure 4.6, the diameter of each droplet was around 50 µm. To ensure that all PI droplets could

be connected to each other, a 40% ratio of overlap was selected to determine the drop spacing in the printing process. According to the results, the drop spacing was 30 µm.

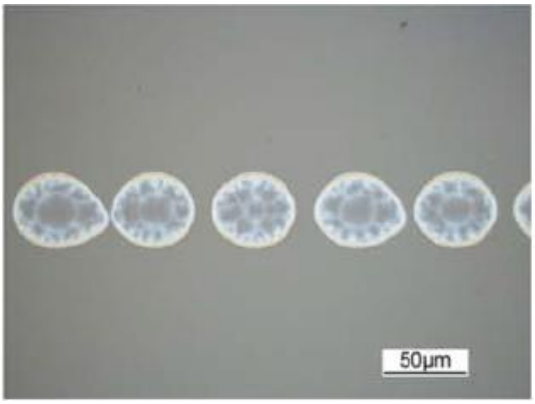

Figure 4.6 Droplet size measurements for polyimide ink. Droplet spacing is 60 µm.

As explained in section 2.4.5, thermal treatment is required for the conversion process of the polyimide ink. Meanwhile, as the PI ink is fluid and spreads over the substrate, while printed at room temperature, heating is employed during the printing process to fix the PI droplets landing on the substrate. At the initial stage, three different substrate temperatures (100°C, 140°C and 160°C) are selected to find out the optimal treatment temperature of the PI ink.

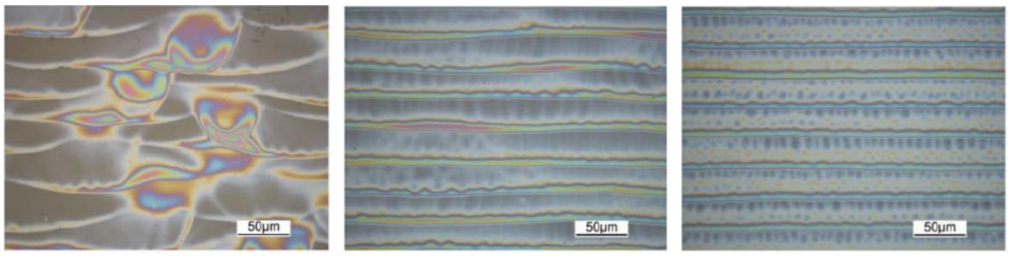

Figure 4.7 Optical images of printed polyimide films with a drop spacing of 30 µm and different substrate temperatures: (a) 100°C; (b) 140°C; (c) 160°C.

As seen in Figure 4.7(a), the heating to 100°C during the printing of the PI ink causes the crater-like formations in the film, which is due to the low evaporation speed of the polyimide ink. In this case, the previously printed droplet remains unsolidified, while the next row of ink is already applied, making the droplets merge and swell. As the result, the surface tension is reduced through the crater-like formations.

According to Figures 4.7(b) and 4.7(c), an increase in the substrate temperature to 140°C and 160 °C during the printing of the PI ink allows one to obtain the specimens with relatively regular structure. This is due to solidification of all the printed PI droplets before coating them with the next row of ink. However, some swelled ink inclusions are still present in the film printed at a substrate temperature of 140°C. Therefore, to achieve a stable polyimide inkjet printing process in this PhD thesis, the polyimide ink was afterwards printed with a drop spacing of 30 µm and a substrate temperature of 160°C. This enabled one to avoid the need for further increase of the substrate temperature to higher values such as 180°C or 200 °C, and, therefore, to reduce the risk of nozzle clogging and damage.

4.2.5 Thickness Measurement of Single Layer Polyimide Specimens

The thickness of single layer polyimide specimens was measured using a Bruker Contour GT-I profiler, as explained in section 4.1.6. Figure 4.8 displays the surface roughness results for two PI samples printed at the substrate temperatures of 100°C and 160°C. As seen in Figure 4.8(a), no ordered PI tracks are observed for the specimen printed at a substrate temperature of 100°C. As explained in section 4.2.4, the irregular PI surface is caused by a low conversion speed of the PI ink. The thickness of this specimen is evaluated to be 3.2 ± 0.70

µm. In turn, the PI film printed at a substrate temperature of 160°C (Figure 4.8(b)) exhibits the ordered PI tracks. However, due to a 40% ratio of overlap of the PI droplets, ridges are also formed between the consistent areas. Their thickness is found to be 2.5± 0.59 µm and the thickness of the consistent areas is 1.9 ± 0.15 µm.

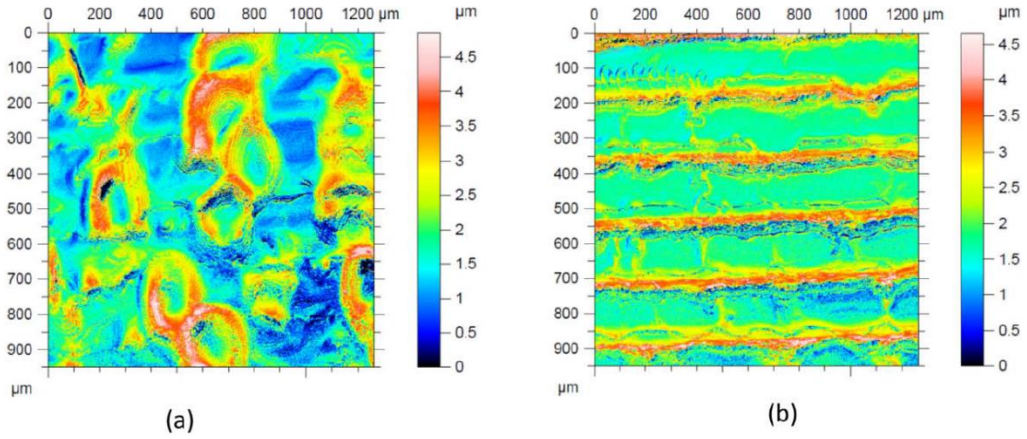

Figure 4.8 Topological scan and thickness evaluation of the polymide specimen printed at a substrate temperature of (a) 100°C and (b) 160°C.

4.2.6 Dielectric Properties of Printed Polyimide Films

Since the polyimide ink is printed with the aim to form the dielectric layer, its dielectric characteristics are determined to ensure that the printed dielectric film is insulating. In this respect, sandwich structures (see a schematic in Figure 4.9(a)) were fabricated on the glass slides, as shown in Figure 4.9(b).

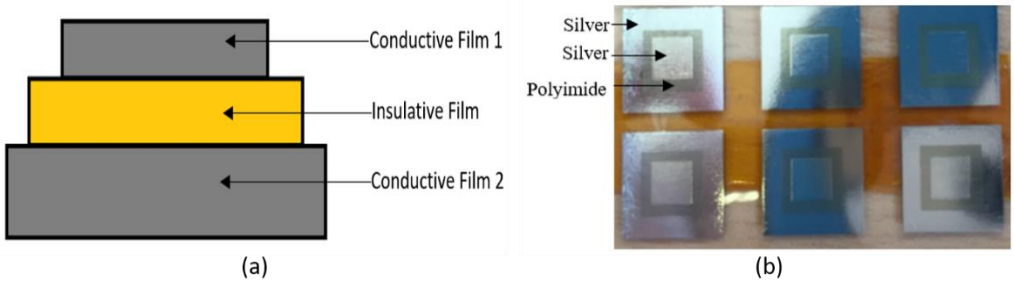

Figure 4.9 Sandwich structures prepared for dielectric testing of polyimide films: (a) schematic illustration;(b) photo.

The dielectric properties of the films were examined by placing the two probes of the multi meter (UNI-T UT50B) on the two printed silver patterns (top and bottom) separately. Three sets, each containing ten samples with one, two or three layers, were tested. Based on the results, the amount of insulating samples among those with one polyimide layer was 80%, whereas that of the films with two and three layers was 100%. In this respect, the two-layer polyimide films with guaranteed insulating properties were afterwards printed.

4.3 TPGDA Ink Characterisation

TPGDA is another insulating ink used in this PhD thesis because of its promising dielectric and thermal stability. It was formulated by Dr Yinfeng HE at the Centre for Additive Manufacturing (University of Nottingham). To ensure that the TPGDA ink possesses stability during printing, its viscosity, surface tension, and droplet size are afterwards evaluated. To improve the polymerisation process of the ink, TPGDA is exposed to UV light irradiation during the printing process instead of heating. The printed specimen is then analysed using the optical microscope and characterised.

4.3.1 Viscosity Assessment

The room-temperature viscosity of the TPGDA ink was measured to be 11.35 ± 0.17 mPa·s at a rate of 1000 s^{-1}, which was within the required range for the inks used in Dimatix printers.

4.3.2 Surface Tension Assessment

The surface tension of the TPGDA ink was 31.46 ± 0.53 mN/m, fulfiling the required range for the inks applied in Dimatix printers. In this respect, both the viscosity and surface tension enabled this type of ink to be considered as printable.

4.3.3 Printability Index of TPGDA Ink

The nozzle diameter is 21 µm and the density of the TPGDA ink is 1.03 g/mL. Thus, based on Eq. 4, the printability index is 2.298 at a viscosity of 11.35 mPa·s and a surface tension of 31.46 mN/m. Therefore, the TPGDA is characterised as printable for the considered type of printers.

The characteristics of the TPGDA ink are summarized in Table 4.4.

Table 4.4 Printability assessment of TPGDA ink.

Ink Property	Average Value
Viscosity (mPa·s)	11.35 ± 0.17
Surface Tension (mN/m)	31.46 ± 0.53
Density (g/mL)	1.03
Printability Index	2.298

4.3.4 Droplet Deposition and Sample Formation

The TPGDA ink was printed on the glass slide with a large drop spacing (120 µm) to measure the droplet size (see Figure 4.10). Based on the optical microscope image, the diameter of each droplet was around 47 µm. Similarly, a 40% ratio of overlap was applied to ensure that all the droplets are connected to each other after landing on the substrate.

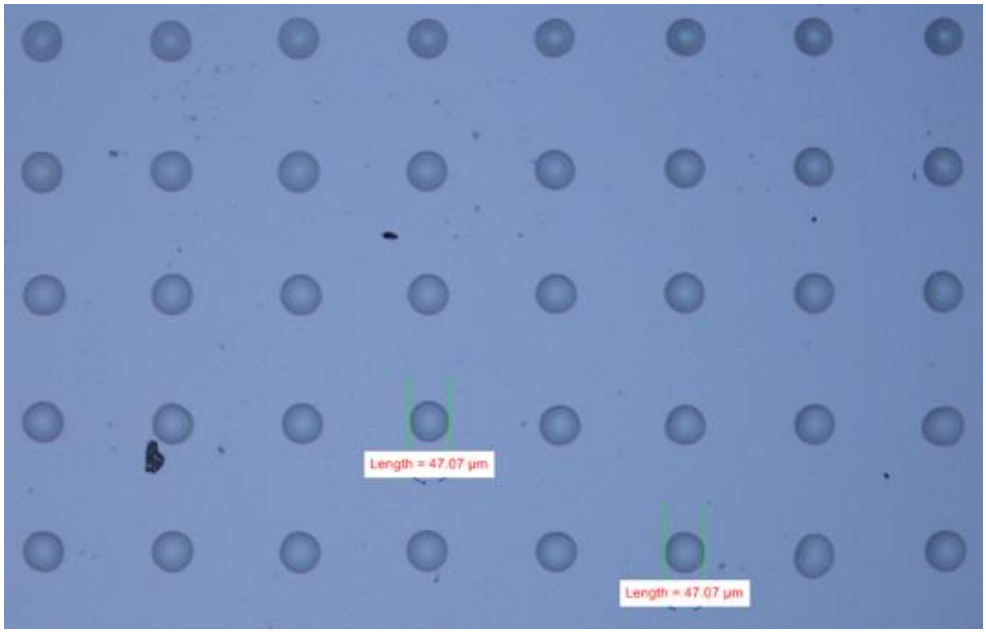

Figure 4.10 Droplet size assessment for TPGDA ink. Drop spacing is 120 µm.

Figure 4.11 displays a printed 1 mm × 1 mm TPGDA square. A 365 nm UV LED unit was employed during the printing process to polymerise the TPGDA ink. No sharp corners were observed on the printed square specimen, meaning that the TPGDA droplets were incompletely solidified when landing on the substrate, and merged together to reduce the surface tension. To solve this problem, the UV radiation power was further increased in the subsequent experiments.

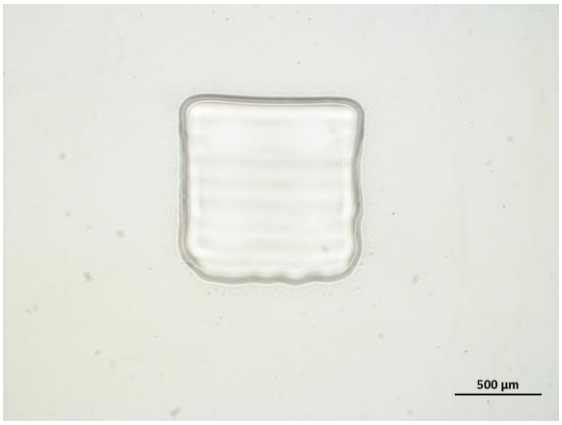

Figure 4.11 1 mm × 1 mm square specimen of TPGDA ink.

4.3.5 Thickness Measurement of Single Layer TPGDA Specimen

Figure 4.12 depicts the thickness measurement results for the printed TPGDA specimen. The thickness of the pattern was found to be around 3.07 µm, being 61.6% larger than that of a single layer polyimide specimen (1.9 µm for the consistent areas). However, unlike the polyimide specimen, the surface of the printed TPGDA specimen was relatively smoother, revealing a small difference (0.2 µm) between the ridges and the consistent areas.

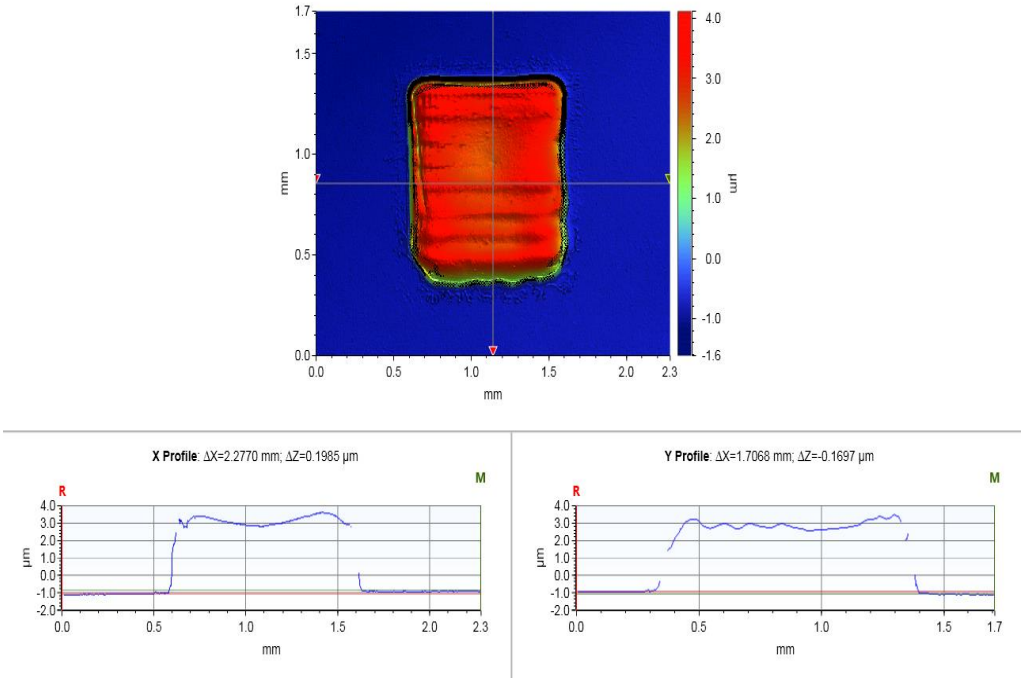

Figure 4.12Topological scan and thickness profiles of the single layer TPGDA specimen.

4.3.6 Dielectric Properties of Printed TPGDA Films

Similar to the sandwich structures produced for evaluating the dielectric properties of printed polyimide films, silver-TPGDA-silver crossings were designed and printed to assess the dielectric characteristics of TPGDA films. For this, a long silver strip was printed on the bottom and a one-layer TPGDA film was printed atop. Subsequently, another short silver strip was fabricated on the top of the TPGDA film and perpendicular to the silver strip on the bottom. Silver pastes were finally deposited on the silver strips to help to place the probes of the multi meter. Twenty silver-TPGDA-silver crossings were printed on the glass slide to achieve the objective results. All printed silver-TPGDA-silver crossings are shown in Figure 4.13.

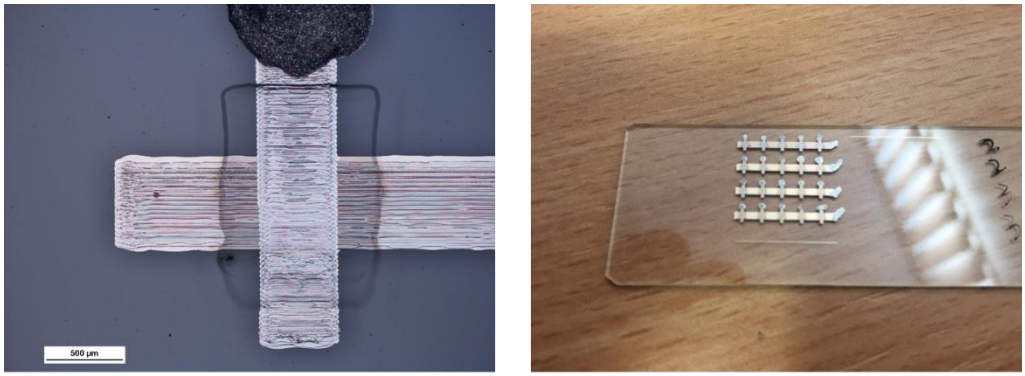

(a) (b)

Figure 4.13 Printed silver-TPGDA-silver crossing for the dielectric property evaluation in the TPGDA film: (a) optical microscope image of one silver-TPGDA-silver crossing; (b) twenty silver-TPGDA-silver crossings on the glass slide.

The dielectric performance of a single layer TPGDA film was checked by placing two multi meter probes on two silver stripes correspondingly. Based on the experimental results, there was no current leakage in the silver-TPGDA-silver crossings, demonstrating that all single layer TPGDA films were insulating. Therefore, a single layer TPGDA film was subsequently used to form the dielectric parts in this work.

4.4 Graphene Oxide Ink Characterisation

A graphene oxide ink is applied in this PhD thesis to form the semiconducting parts. The viscosity and surface tension are first measured to determine the printability index of the graphene oxide ink. Based on the results, a few polymer solutions is added into graphene oxide inks to optimise the jetting performance. However, the printing instability along with other problems are observed on most formulated graphene oxide inks. Isopropanol is finally selected and added

into the graphene oxide ink. A dot square, a single track, and a single layer square specimens are printed and characterised as well.

4.4.1 Viscosity Assessment

The viscosity of the graphene oxide ink was found to be 2.22 ± 0.09 mPa·s, being much lower the required value for the inks used in Dimatix printer (10-12 mPa·s). However, since the printability of inks is determined by the combination of viscosity, surface tension, and density, some inks can still be printed, even though their low viscosity (Zhang *et al.,* 2016). In this ink, deionised water accounts for 79.68 wt % of the solvent and, according to the previous experiments taken in our lab, it could be printed with a Dimatix printer (through the waveform modification). Therefore, this graphene oxide ink is attempted to be printed in the Dimatix printer.

4.4.2 Surface Tension Assessment

The surface tension of the graphene oxide ink was 34.36 ± 0.78 mN/m, exceeding the optimal surface tension range for the inks used in Dimatix printers (28-33 mN/m) by 4%. Since the surface tension of the ink was insignificantly larger than the allowable value, the ink was still attempted to be printed at the beginning. However, in the case of the instable jetting process, surfactant may be added into the ink to reduce the surface tension and improve the printing quality.

4.4.3 Printability Index of Graphene Oxide Ink

In this work, the nozzle diameter of 10 pL Dimatix Materials Cartridge is 21 μm and the density of the graphene oxide ink is calculated to be 0.9548 g/mL. The individual densities of deionised water, isopropanol, and graphene oxide flakes

composing the ink were approximately 0.997, 0.786, and 1g/mL. At the viscosity of 2.22 mPa·s and the surface tension of 34.36 mN/m, the printability index was found to be 11.82 (see Eq. 4). As discussed in section 2.3.3, an ink is considered to be printable when its printability index is between 1 and 10. However, it cannot be spread to all the inks because the printability index is a guide rather than a law (Gibson, Rosen and Stucker, 2010). Some inks with a large printability such as deionised water (39.1) can still be printed through the waveform modification. Therefore, even though the printability index of the graphene oxide ink is out of the optimal range, it is still attempted to assess the jetting performance.

The details about the printability characteristics of the graphene oxide ink are shown in Table 4.5.

Table 4.5 Printability characteristics of graphene oxide ink.

Ink Name	Graphene Oxide Ink
Viscosity (mPa·s)	2.22 ± 0.09
Surface Tension (mN/m)	34.36 ± 0.78
Density (g/mL)	0.9548
Printability Index	11.82

4.4.4 Droplet Formation of Graphene Oxide Ink

According to the discussion in section 3.2.2, the droplet formation of the graphene oxide ink was observed in the monitoring unit of the Dimatix printer at the drop watcher interface using the stroboscopic camera.

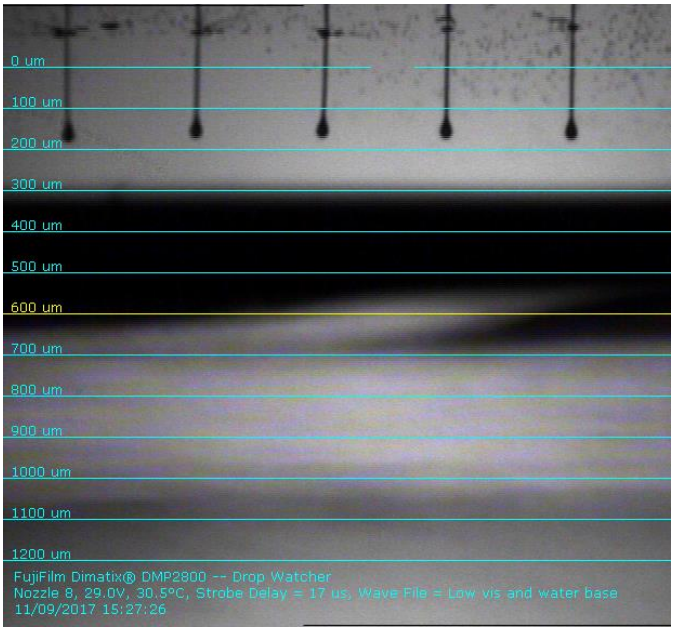

Figure 4.14 Droplet formation of graphene oxide ink. Both graphene oxide droplets and tails are observed.

According to the image in Figure 4.14, the stroboscopic camera captured five nozzles with deposits on the nozzle plate surface. Meanwhile, all nozzles showed the drop ejection without clogging, indicating the stability of the graphene oxide ink and the ability to apply it in semiconducting materials printing. However, the droplet ejection led to the emergence of long tails. As explained in section 4.1.4, a double voltage waveform is expected to be used in the printing work of the graphene oxide ink.

4.4.5 Jetting Performance of Printed Sample

Several solvents with low surface tension were added to the commercial graphene oxide solution to prepare the graphene oxide ink. All these developed graphene oxide inks were afterwards printed using the Dimatix printer. Glass slides were taken as the substrates for all the printed graphene oxide samples

because of their relatively uniform surface. All specimens were scanned via the optical microscopy.

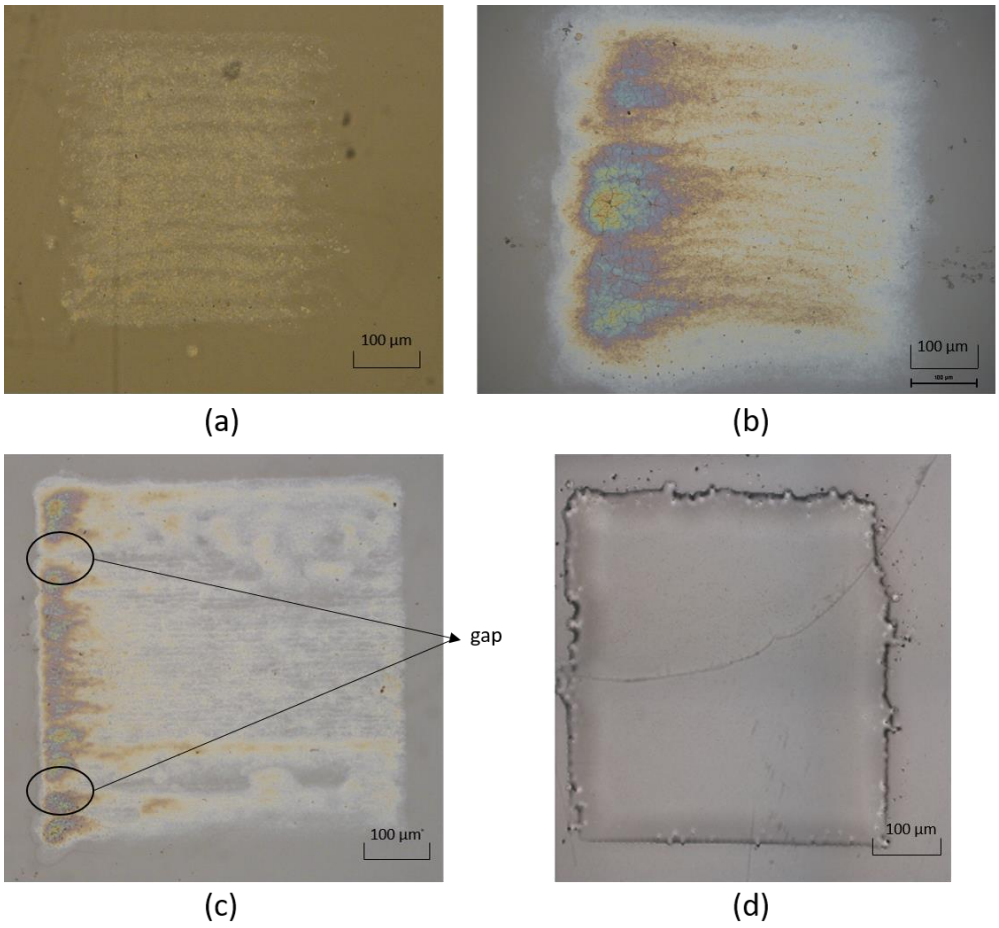

Figure 4.15 Square specimens printed with various graphene oxide solutions using inkjet printing: (a) without additional solvents and (b) with 20 wt % triethylene glycol monoethyl ether (TGME) solvent, (c) 20 wt % polyethylene glycol (PEG) solvent, (d) 0.3 wt % tween 20.

Figure 4.15(a) depicts a printed graphene oxide specimen with a graphene oxide solution only. As seen in the optical image, the printed pattern was irregular in shape and there were some droplets landed outside the square specimen. This indicated the printing instability that, according to the explanation in section 3.5.3, was mainly due to the high surface tension of the graphene oxide solution.

Therefore, to reduce the overall surface tension and optimise the printing performance, additional solvents with lower surface tension were added to the original graphene oxide solution.

TGME is a solvent of the silver ink used in this work. Compared to deionised water, it has a lower surface tension (31.4 mN/m) and can be easily obtained under laboratory conditions. Therefore, it was added to the original graphene oxide solution to formulate a new graphene oxide ink with a reduced surface tension. Figure 4.15(b) displays a regular square specimen printed using this new ink. It can be seen that most graphene oxide flakes are drawn to the left hand side of the printed pattern. This is because the initial droplet is not evaporated completely when the subsequently droplets land on the substrate due to a low evaporation speed of the formulation. Based on the Marangoni effect, a driving force removes the bulk of a material to be merged together, reducing the total surface area due to the fact that the molecules on the surface have more energy than those in the bulk of the material (Hu and Larson, 2006) (Jeong, Kim and Moon, 2008) (Singh *et al.*, 2010). Therefore, all subsequent droplets merge with previously landed droplets by the driving force, decreasing the total surface area. Meanwhile, since the printing direction of the printer is from left to right, all the subsequently deposited droplets are moved from right to left. Therefore, graphene oxide flakes are remained on the left hand side once the solvents are evaporated completely.

PEG is another polymer solution used in this work with a surface tension of 44 mN/m. According to Figure 4.15(c), graphene oxide flakes also remain on the left hand side when a square sample is fabricated using the graphene oxide ink

with PEG. Moreover, gaps are observed on the printed specimen, meaning that the graphene oxide flakes did not dispersed uniformly in the PEG mixture.

Tween 20 is a common surfactant allowing one to reduce the surface tension significantly (Szymczyk, Szaniawska and Taraba, 2018). In this study, 0.3 wt % Tween 20 solvent was added to the original graphene oxide ink and the formulated ink was afterwards printed on the glass slide. As shown in Figure 4.15(d), compared to the printed pattern of the graphene oxide ink with PEG, this specimen has the irregular shape with unsmooth edges. Meanwhile, another major reason for not using Tween 20 is its elevated conductivity. Since the graphene oxide ink is taken to form a semiconducting channel, the highly conductive graphene oxide cannot be employed for this purpose.

Therefore, none of these inks are deemed suitable, leading to a need for searching other solutions.

Isopropanol is a common polymer solution and is easily produced in the laboratory. Furthermore, its advantages such as high evaporation speed at room temperature, low price. and sufficiently low surface tension (23 mN/m), enable it to be added to the graphene oxide solution to reduce the total surface tension and formulate the new ink.

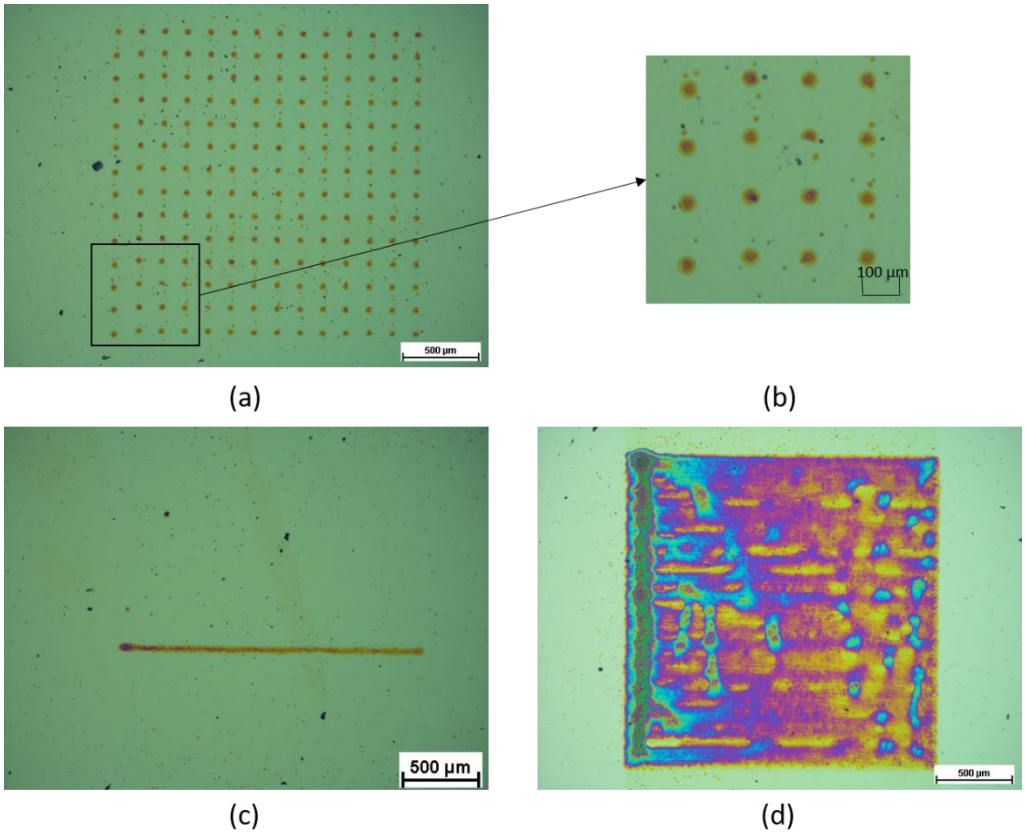

Figure 4.16 Droplets and square specimen of the graphene oxide ink with 20 wt % isopropanol obtained via inkjet printing: (a) dot square; (b) amplified dot square; (c) single track; (d) single layer square pattern.

The dot square was first printed on the substrate once the new ink was prepared. As shown in Figures 4.16(a) and 4.16(b), the graphene oxide ink droplet size with 20 wt % isopropanol was around 50 µm. Due to a 40% ratio of overlap of the droplets, the drop spacing for graphene oxide ink with 20 wt% isopropanol was selected as 30 µm.

Single track and single layer square patterns were inkjet-printed on the glass slides using the formulated graphene oxide ink and characterised using the optical microscope (see Figures 4.16(c) and 4.16(d)). According to the images, most graphene oxide flakes are drawn to the left hand side of the square pattern due to the Marangoni effect. However, in contrast to the graphene oxide inks

with PEG or TGME solvents, a single track without any gaps is observed on the left hand side of the specimen from top left to bottom left. Based on the design patterns in section 3.4.3, drain and source electrodes are mirrored with a gap of 30 µm in the vertical direction and the graphene oxide is printed to cover the gap and connect drain and source electrodes. In this respect, a single track of printed graphene oxide flakes in vertical direction is deemed suitable for further use in present work. Meanwhile, both the single track and single layer square patterns were formed without any spreading, meaning that there was no nozzle clogging and the newly formulated graphene oxide ink remained stable during the printing. Therefore, the graphene oxide ink with 20 wt % isopropanol was employed in this PhD thesis to form semiconducting components.

4.4.6 Thickness Measurement and Electrical Characterisation of Graphene Oxide Specimen

Since single layer graphene oxide specimens were less than 1 µm thin, their thickness was measured on the three layer samples using a Bruker Contour GT-I profiler. Figure 4.17a displays a non-uniform surface where most remained graphene oxide flakes arise on the left-hand side of the specimen, forming a relatively thick area. This phenomenon is caused by the Aufbau principle, which is explained in section 4.4.5. Based on the thickness profiles (Figures 4.17b and 4.17c), the average thickness of this area is around 0.2 µm.

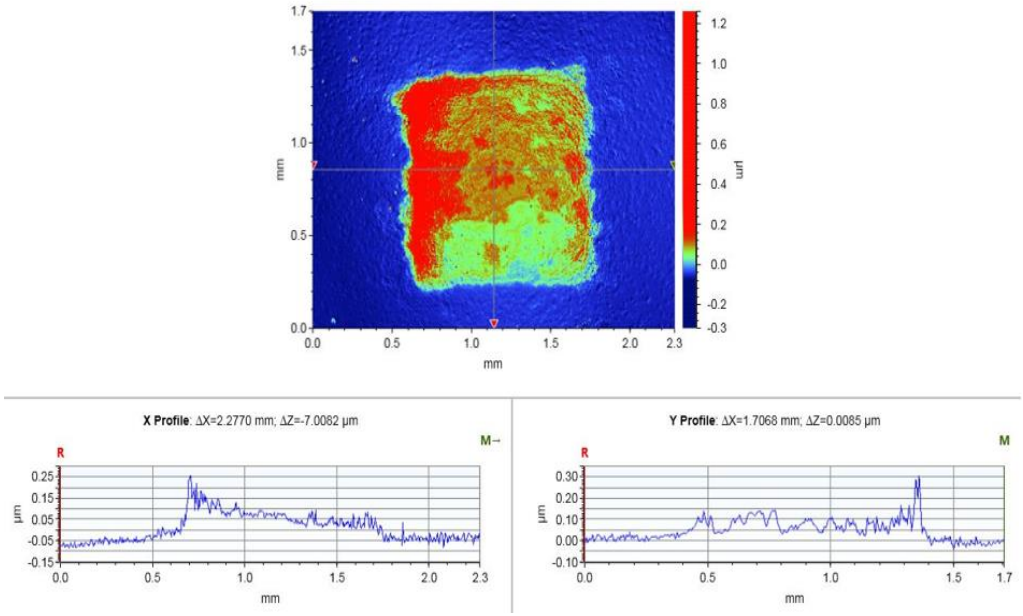

Figure 4.17 (a) Topological scan and (b,c) thickness profiles of the printed graphene oxide specimen.

Similar to the electrical characterisation procedure for a silver specimen, the resistance of the printed graphene oxide specimen was measured by a UNI-T UT50B Modern Digital multi meter in the two-probe contact mode. However, according to the experiment, the resistance of this specimen is significantly high (more than 1000 MΩ), allowing it to be considered as insulating.

As mentioned in section 3.5.3, the printed graphene oxide specimen was reduced to the graphene oxide using UV light radiation (Kim, Parvez and Chhowalla, 2009) (Kumar, Subrahmanyam and Rao, 2011) (Smirnov *et al.*, 2011) (Ji *et al.*, 2013). Since the reduced graphene oxide (rGO) is conductive while the graphene oxide behaves as an insulator, the resistance of the specimen should be decreased significantly once the graphene oxide is converted to the rGO. Therefore, the resistance of the specimen was measured repeatedly after the UV treatment.

The resistance for the UV-treated specimen is assessed to be 1.55 MΩ while the thickness is 0.2 µm and the width is around 50 µm, resulting in a cross-sectional

area of 10 μm^2. A fixed length between the two probes is 1 mm. In this case, the resistivity of the reduced graphene oxide is:

$$\rho = R \times \frac{A}{L} = 1.55 \times 10^6 \times 10 \div 1000 = 1.55 \times 10^4 \mu\Omega \cdot cm \cdots\cdots\cdots\cdots \quad (12)$$

The resistivity of the pure graphene sheets is 1 $\mu\Omega \cdot cm$, which is surprisingly lower than that of silver (1.59 $\mu\Omega \cdot cm$) (Geim and Novoselov, 2007). Compared to the pure graphene sheets, the resistivity of the reduced graphene oxide is found to be 1550 times higher. This is mainly due to the incomplete reduction of the printed graphene oxide, meaning that, unlike pure graphene sheets with a zero bandgap, a small bandgap exists in this reduced graphene oxide. In this respect, the reduced graphene oxide can be regarded as a semiconducting material and is therefore suitable for further analysis.

4.5 Conclusion

- Commercial silver ink is selected to form the conductive components in this work. Even though the ability to choose whether thermal treatment should be performed during or after the printing of the silver ink, the heating at 160℃ upon the printing process is highly desirable due to the possibility to achieve the lower resistivity (4.9 $\mu\Omega \cdot cm$) of the printed film. However, obvious silver tracks are observed on the printed silver specimens.
- Both PI and TPGDA solvents are suitable insulating materials for inkjet-printed electronics but have to be treated in different ways. While the PI needs a thermal treatment at a temperature of 160℃ during the printing to make PAA converted into PI, the TPGDA requires the UV exposure to generate a cross-link structure. Moreover, even though a single layer

PI film (1.9 μm) is thinner than a single layer TPGDA film (3.07 μm), it is only partly insulated, whereas the TPGDA film is a 100% insulator.

- Solvents with low surface tension have to be added to the graphene oxide solution. However, graphene oxide solutions with TGME, PEG or Tween 20 solvents are not able to form high performance graphene oxide specimens. Graphene oxide ink is finally formulated by adding 20 wt % isopropanol to the graphene oxide solution. Graphene oxide specimens are successfully fabricated from graphene oxide flakes that arise on the left-hand side of the pattern during the printing. This phenomenon is due to the Marangoni effect. The UV light is found useful to reduce the printed graphene oxide flakes to the rGO.
- In this work, conductive, insulating, and semiconducting inks are prepared and characterised. The results reveal that these prepared inks are suitable for inkjet-printed electronics applications. Although the specimens are printed on only the glass slides, their behaviour on other types of substrates, e.g. PET, shall be predicted as well. Meanwhile, the complementary analytical techniques such as Raman spectroscopy and XRD are needed for further study of printed graphene oxide flakes and rGO to better understand this UV-induced reduction process.

Chapter 5 Fabrication and Characterisation of InSe Based Electronic Devices Using Inkjet Printing Technology

In this chapter, InSe based electronic devices are introduced. The InSe crystals were grown from $In_{1.03}Se_{0.97}$ *polycrystalline melt on the silicon wafers in accordance with the Bridgman method by Dr Kudrynskyi Zakhar* (*Department of Physics, University of Nottingham*). *A few electronic devices are fabricated based on the prepared InSe flakes and silver electrodes printed using inkjet printing technology. Since InSe is a photosensitive material, its optical characteristics have been first analysed after the printing work of InSe based devices. The specific electrical parameters of InSe were afterwards characterised to determine whether it could be used as the semiconductor in printed transistors. Finally, attention is paid to printed InSe based electronic devices.*

5.1 Partially-printed InSe Photodetector

5.1.1 Printing Work

Photodetector is the first electronic device printed in this work. As explained in section 3.4.1, the prepared InSe specimens have the micrometric size in various dimensions. Since inkjet printing is a reliable technology to manufacture flexible products with a minimum design limitation, it is employed to produce InSe based photodetectors through the fabrication of the conductive electrodes on the specimens. In this respect, the final product is named partially-printed InSe photodetector.

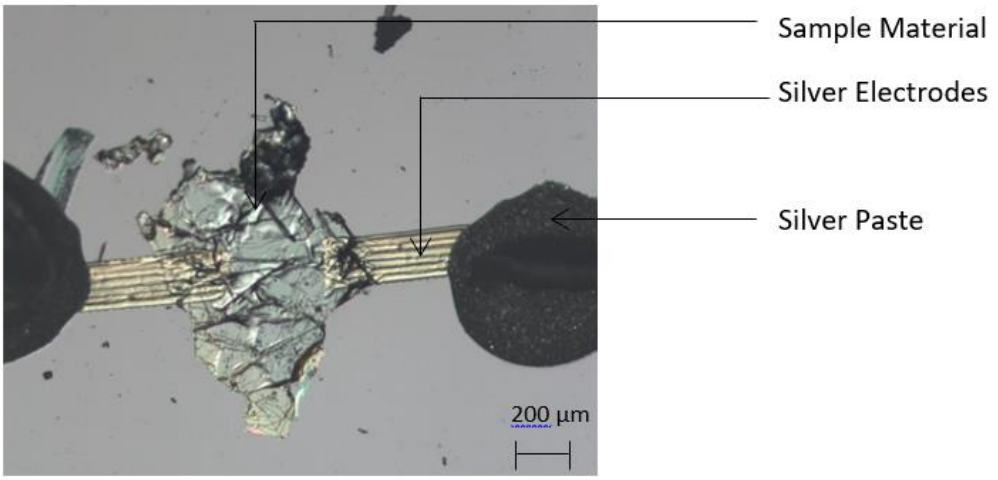

Figure 5.1 Optical microscope image of partially-printed InSe Photodetector. Two silver electrodes are printed on the sample material.

Following the pattern design in section 3.4.1, two rectangle silver electrodes were printed on the prepared InSe flake. Figure 5.1 displays the printing performance of a partially-printed InSe photodetector. Obvious silver tracks observed in the image result from rapid evaporation of the solvent from silver ink droplets while exposed to heating. The fabricated device is mounted on an 8-pin nonmagnetic header using DuPont^{TM} silver paste. In this case, the probes of the testing kit are placed on the silver paste, enabling one to avoid the damage of the printed silver electrodes during the characterisation process.

5.1.2 Optical Characterisation

Partially-printed InSe photodetector was left for drying at room temperature for 24 h in a dry nitrogen atmosphere and then placed into a vacuum cryostat with an optical window to remove any traces of water. The electrical and photoelectrical measurements were afterwards made under high vacuum conditions (≈10-6 mbar) at T = 300 K using Keithley 2400 source meters. The

contact pads were then manually bonded to the header pins using DuPontTM silver paste and silver wire.

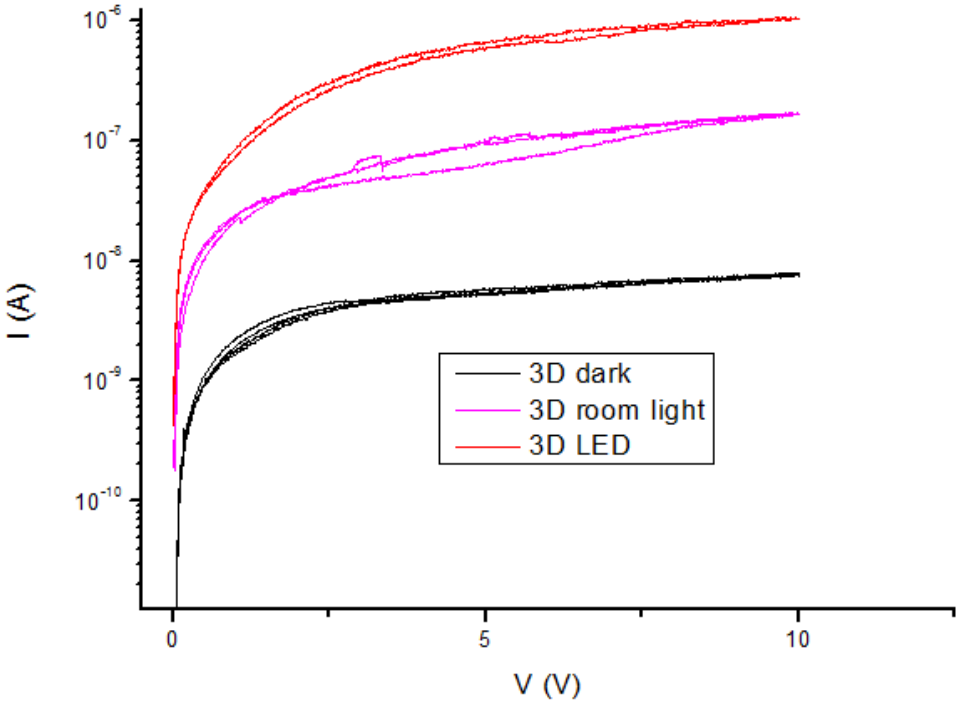

Figure 5.2 Optical characteristics of partially-printed photodetector exposed to various light sources (plot of voltage (V) versus current (I)).

Figure 5.2 displays the current–voltage (I–V) curves of the partially-printed InSe photodetector under different light intensities. According to these curves, the lowest current values ($5 \times 10^{-9}\ A$ at a voltage of 5 V) were obtained in the dark. In turn, the current measured on the specimen while subjected to light radiation noticeably increased to $1 \times 10^{-7}\ A$ in the ambient light environment and $8 \times 10^{-7}\ A$ under the LED lighting conditions. Since the resistance of this partially-printed InSe detector decreased with increasing light intensity, InSe was confirmed to be a promising optical material.

5.2 Partially-printed InSe Hall Bar

5.2.1 Printing Work

A six-contact 1-2-2-1 hall bar geometry is selected to gain a comprehensive understanding of both the optical and electrical properties of InSe. Figure 5.3(a) depicts an InSe sample on the silicon wafer. Similarly, following the pattern design in section 3.4.2, six silver electrodes are expected to be successfully printed on this InSe specimen.

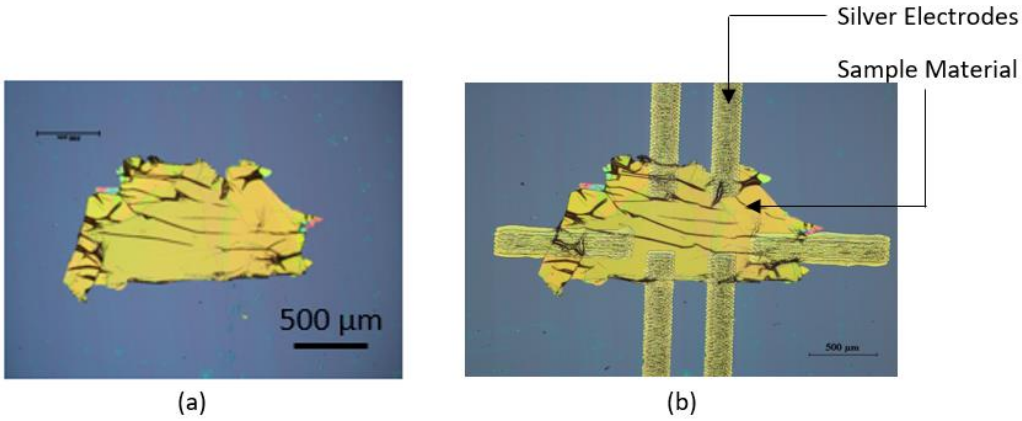

Figure 5.3 (a) Originally prepared InSe flake sample; (b) partially-printed InSe hall bar. Six silver electrodes are printed on the sample material.

Figure 5.3(b) shows the optical images of the partially-printed InSe hall bar. Based on the specific dimensions, the distances between six silver electrodes are calculated to ensure that all silver electrodes are printed on the InSe sample. After the printing work, the printed electrodes were cover with DuPont^{TM} silver paste for further characterisation (not shown in Figure 5.3).

5.2.2 Optical and Electrical Characterisation

Based on the same testing conditions and procedures described in section 5.1.2, both the optical and electrical characteristics are assessed on this partially-

printed InSe hall bar. In this respect, the photosensitive parameters are first investigated, and Figure 5.4 displays the current-voltage curves acquired under different light conditions.

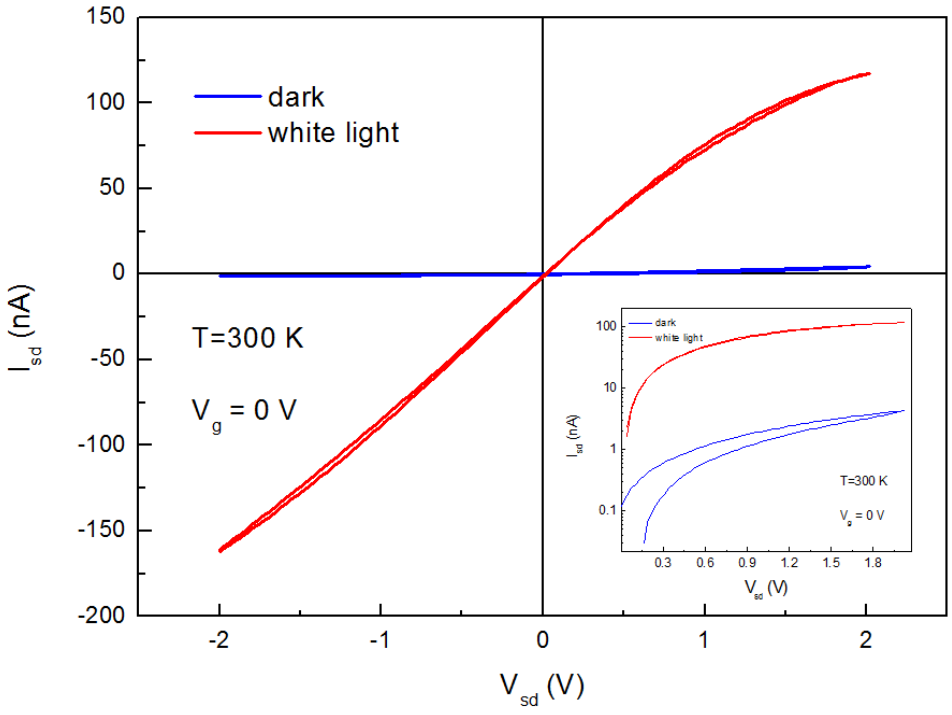

Figure 5.4 Photosensitive determinations results of partially-printed InSe hall bar (plot of V_sd versus I_sd).

Here, the blue curve corresponds to the flowing current measured on the hall bar in the dark. The red curve is the result of the experiment under white light conditions (both with a varied V_{DS} and without V_{GS}). The results demonstrate that applying the same V_{DS} value increases the current flowing through the light-irradiated sample relative to that in the dark. For instance, when V_{DS} is 1.5 V, the flowing current is around 100 nA under the white light condition and not larger than 4 nA in the dark. As the flowing current magnitude is affected by the external light intensity, the partially-printed InSe hall bar is considered to be photosensitive.

The next step is to evaluate the gate leakage of InSe. According to Figure 5.5, applying the gate-to-source voltage (V_{GS}) in a range from -40 to 30 V to the InSe sample results in a tiny amount of gate-to-source current (I_{GS}) (from -0.5 to 0.5 nA only). In the gate leakage testing, the value of I_{GS} above 1 nA indicates the gate leakage, whereas I_{GS} less than 1 nA is regarded as the noise. Therefore, it can be concluded that there is a minimum gate leakage occurring in the partially-printed InSe hall bar.

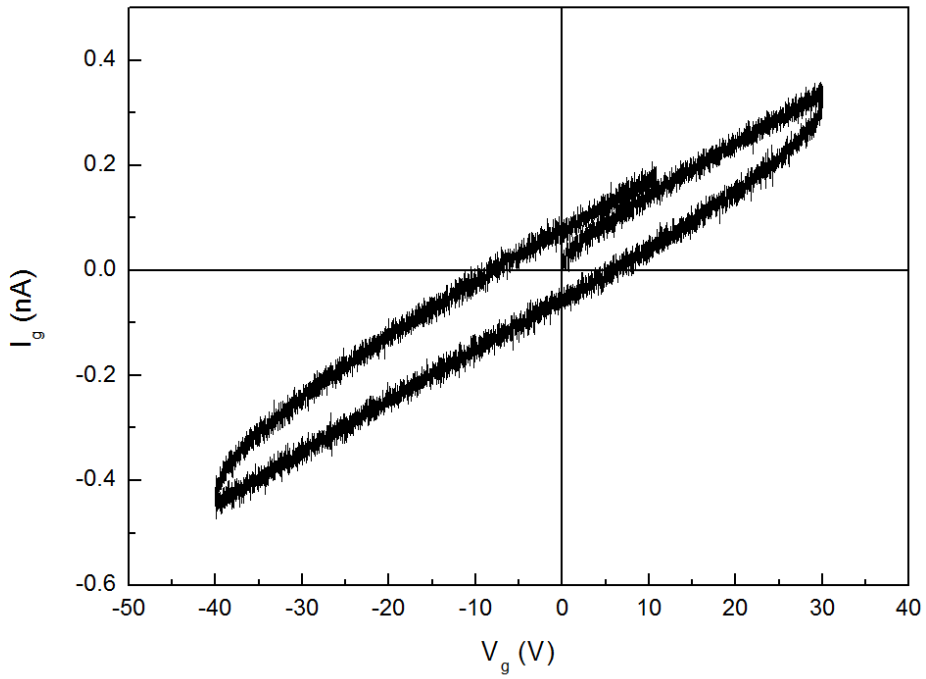

Figure 5.5 Gate leakage testing of partially-printed InSe hall bar (plot of V_g versus I_g).

The last parameter to be evaluated on the partially-printed InSe hall bar is the gate dependence. When the material is gate-dependent, the drain-to-source current I_{DS} flowing through is affected by the external gate-to-source voltage V_{GS}, allowing this material to be used as the semiconductor channel in the transistor. The testing result of this InSe sample is shown in Figure 5.6. It is

obvious that the value of I_{DS} is impacted by the gate-to-source voltage V_{GS}. For instance, when the gate-to-source voltage V_{GS} is reduced from +30 V to -40 V, the drain-to-source current I_{DS} is formed, rising from 0 to 6.5 nA. Although the increment is not significant, the weak gate dependence seems to take place in this InSe sample. Therefore, these InSe flakes are promising as the semiconductor channels for transistors.

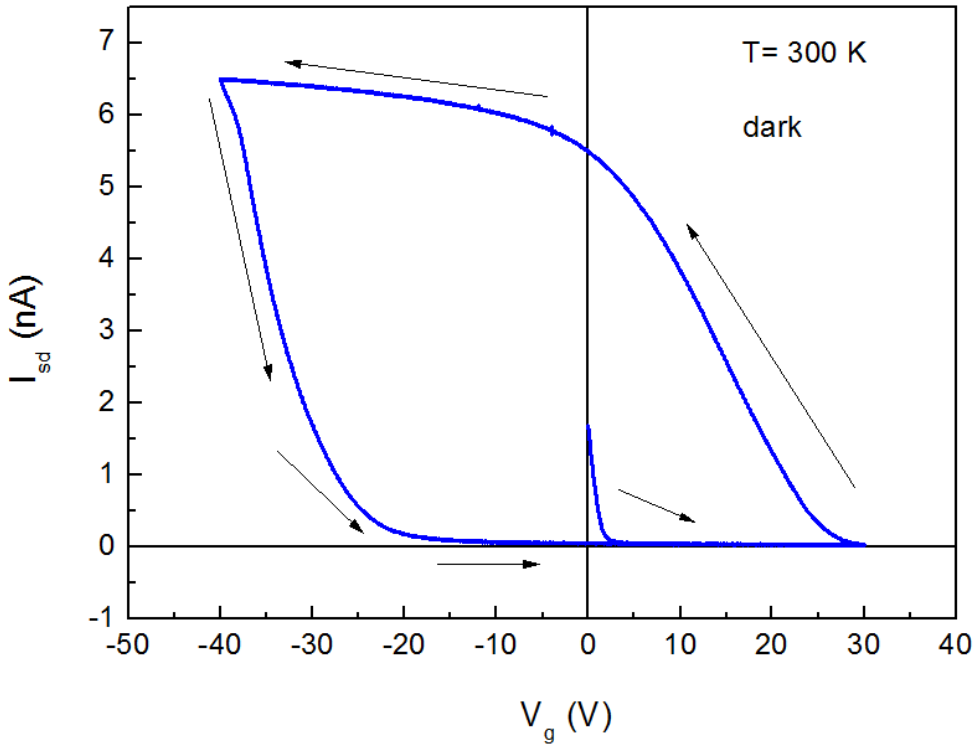

Figure 5.6 Gate dependence results for partially-printed InSe hall bar (plot of V_g versus I_sd).

5.3 Partially-printed InSe Transistors on Silicon Wafers

Based on the characterisation results for InSe in section 5.2.2, partially-printed InSe transistors are subsequently produced on silicon wafers.

As mentioned in section 3.4.3, due to the uncontrolled synthesis technologies, the sizes of InSe flakes used in partially-printed InSe transistors on silicon

wafers are randomly distributed within a nanometer scale (from 12 to 30 nm), whereas their dimensions are at the micrometric level (from 20 to 50 µm). Some of InSe flakes produced in this work are shown in Figure 5.7.

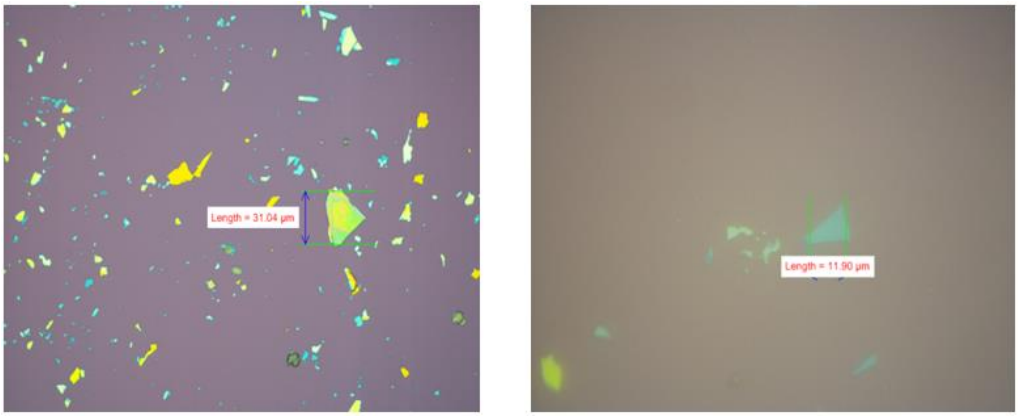

Figure 5.7 InSe flakes for partially-printed InSe transistors on a silicon wafer.

To form the transistors, conductive drain and source electrodes were fabricated on the prepared InSe flakes by silver inkjet printing. To ensure that both electrodes are printed on the InSe flake (see the discussion in section 3.4.3), a one-pixel (30 µm) gap is introduced between the drain and source electrodes due to suitable silver ink droplet size (around 50 µm) and resolution of the printer (847 dpi). The optical image of the partially-printed InSe transistor is shown in Figure 5.8(a) and the magnified image of the formed gap is available in Figure 5.8(b).

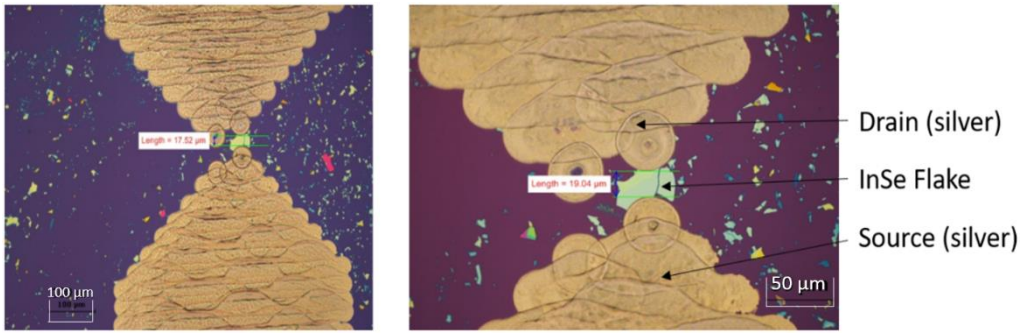

Figure 5.8 (a) Optical image of partially-printed InSe transistor on silicon wafer; (b) magnified image of the gap between the drain and source electrodes.

As shown in Figure 5.8(a), the print head had to be displaced twice because the first attempt to print the drain and source electrodes on the InSe sample failed. Therefore, the position of the print head was optimised using the coordinate axis function in the Dimatix printer. This enabled the electrodes to be accurately printed on the target InSe flake and consider a partially-printed InSe transistor on the silicon wafer as fabricated.

However, the electrical characteristics of this partially-printed InSe transistor are found to be unsatisfactory because the output drain-source current passing through the device is not insufficiently high. This can be owing to the following reasons.

1. Since the InSe flake size is small, being even inferior to the printer resolution, the contact or disconnection between the InSe flake and two printed silver electrodes may be weak. This impedes the successful production of the partially-printed InSe transistor. To avoid it and ensure that the silver electrodes are printed on the InSe flakes, the InSe flakes with larger dimensions shall be employed. However, the output performance will be reduced because the capacitance of the device is increased due to a longer semiconducting channel (Guo and Silva, 2008).

2. The gate dependence of these prepared InSe flakes is weak. Therefore, one possible condition is that the partially-printed InSe transistors are successfully fabricated but the amplification ratio of the output drain-source current is very low due to the weak gate dependence of the semiconductor. Therefore, the InSe flakes with better electrical performance are expected to be prepared and used for further investigations of InSe-based electronic devices.

Due to the limited experiment time, no more partially-printed InSe transistors could be fabricated or characterised. However, based on the optical and electrical characterisation results in this section, it can be concluded that InSe is a potential photosensitive semiconductor for inkjet-printed electronic applications. Therefore, it is worthwhile to produce more partially-printed InSe transistors on silicon wafers and perform their in-depth study.

5.4 Conclusion

- The InSe material obtained in this work is photosensitive. The partially-printed InSe photodetector and partially-printed InSe hall bar are fabricated and characterised to confirm the optical property (photosensitive) of the prepared InSe specimen.
- InSe is shown to be a semiconductor with negligible gate leakage and weak gate dependence. Therefore, even though this InSe specimen is a promising semiconducting material for transistors, the amplification ratio of the output drain-source current of the related InSe-based transistor is still relatively low.

- No partially-printed InSe transistors on the silicon wafers with significant transistor performance could be fabricated in this work because of the insufficient contact between the printed silver electrodes and the InSe specimen. Therefore, optimising the InSe preparation and printing mechanism shall be within the scope of the forthcoming work.
- No InSe inks for inkjet printing could be prepared due to the limited time of experiments. Furthermore, to the best of our knowledge, no InSe inks suitable for inkjet printing have been reported up to date. However, excellent optical and semiconducting characteristics of InSe make it necessary to develop the printable InSe inks. The successfully established large-scale manufacturing of printed electronics including thin film transistors and optoelectronics is possible only if such InSe inks exist.

Chapter 6 Fabrication and Characterisation of Graphene Based Thin Film Transistors

Graphene is the second semiconductor used in this work. As mentioned in chapter 4, graphene oxide ink is prepared and printed graphene oxide specimens are reduced to rGO using UV light. Partially-printed graphene transistor on silicon wafer is first fabricated by printing silver ink (drain and source electrodes) and graphene oxide ink (semiconducting channels). When a significant transistor output performance is observed, two more insulating inks, namely polyimide ink and TPGDA ink, are used for printing to produce fully-printed graphene transistor. All details of the printing process and characterisation results for partially-printed graphene transistor on silicon wafer, fully-printed graphene transistor (using PI) and fully-printed graphene transistor (using TPGDA) are discussed in this section.

6.1 Fabrication and Characterisation of Partially-printed Graphene Transistor on Silicon Wafer

6.1.1 Printing Work

Herein, a commercial silicon wafer is used as the substrate. The silicon part of the wafer works as the gate electrode and the silicon oxide film acts as the dielectric layer. Therefore, only drain electrode, source electrode and a semiconducting channel need to be produced in the inkjet printing process of partially-printed graphene transistor on silicon wafer.

Drain and source electrodes are fabricated according to the pattern design in section 3.4.3. Two stripes are fixed in a vertical direction with a tiny gap (30

μm) between them. The gap is designed for the semiconducting channel. A narrower gap (smaller dimension of semiconducting channel) generally leads to better transistor performance (Nair and Deepa, 2013). Therefore, a minimum gap width of 1 pixel is employed. In this work, based on the droplet size of silver ink (around 50 μm) and resolution of Dimatix printer (847 dpi), 1 pixel equals to 30 μm.

Before using a vertical direction design, drain and source electrodes are designed in the horizontal direction. This is because the printing direction of the Dimatix printer is from left to right (horizontal direction). Consequently, a printing process of drain and source electrodes in the same direction would be highly efficient. Figure 6.1 shows a pair of printed drain and source electrodes in the horizontal direction.

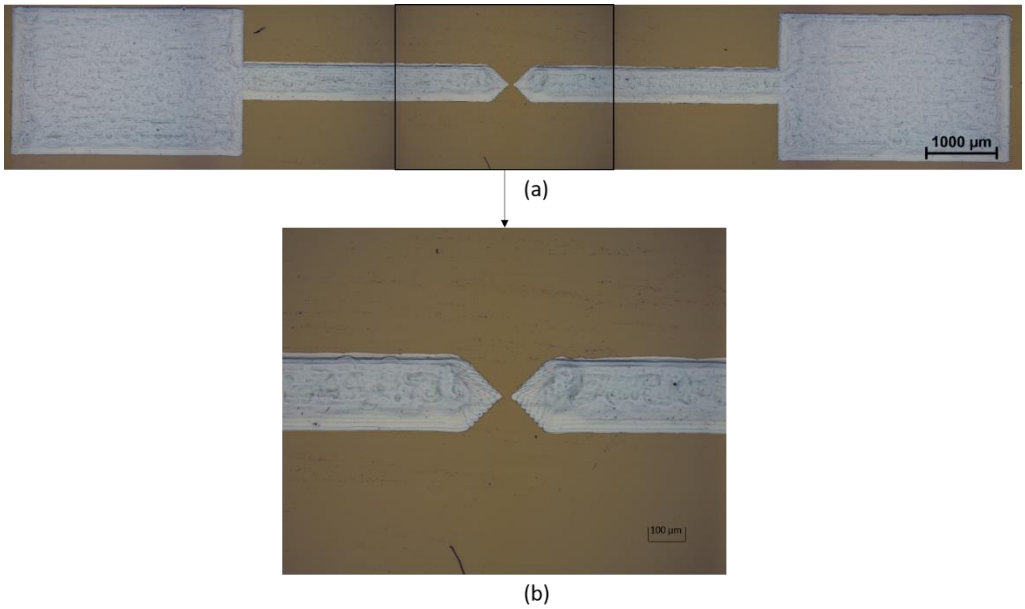

Figure 6.1 Optical microscope image of printed drain and source electrodes on silicon wafer in the horizontal direction (a) whole structure (b) magnified image of the gap between drain and source electrodes.

As shown in figure 6.1 (b), the printed drain and source electrodes are regular and a gap is observed between them. To form a partially-printed graphene transistor on silicon wafer, graphene oxide ink is printed over the gap in the next step. However, one problem is observed as shown schematically in figure 6.2: the drain and source electrodes cannot be connected by the rGO between them. As mentioned in section 4.4.5, graphene oxide flakes are drawn to the left-hand side of the printed pattern due to the Marangoni effect. Thus, a disconnected area on the right-hand side of the pattern is formed. As a result, no current flows through the semiconducting channel and the printed electronic element cannot be used as a transistor.

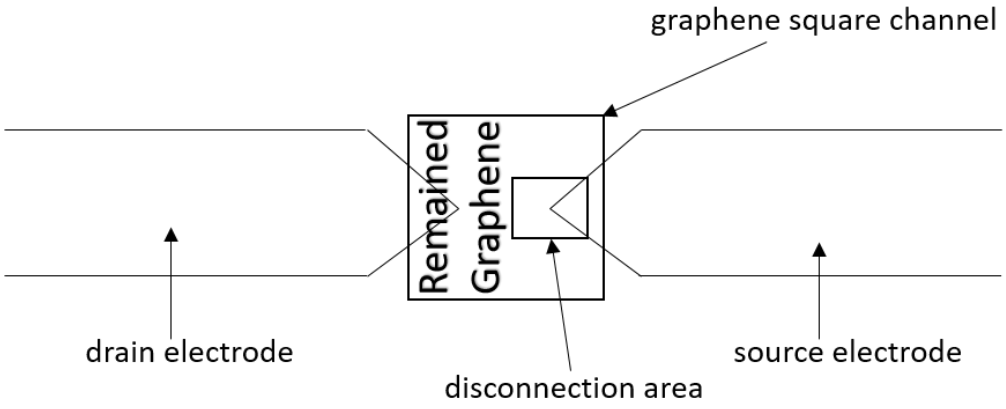

Figure 6.2 Schematic of partially-printed graphene transistor on silicon wafer with drain and source electrodes in the horizontal direction.

The above problem is solved by printing drain and source electrodes in vertical direction. Figure 6.3 (a) presents the optical microscope images of printed drain and source electrodes in the vertical direction, on a silicon wafer. A gap of 26.14 µm between drain and source electrodes is observed in figure 6.3 (b). The width of the gap is less than the designed gap (30 µm) mentioned in section 3.4.3. This is due to the large droplet size (50 µm). In detail, when a silver droplet lands on

the silicon wafer, the area formed by the droplet is larger than a single pixel in the accompanying bitmap design file. Therefore, the gap between the needles of drain and source electrodes is the minimum unit achieved in this work, which would serve as the semiconducting channel area in the TFT.

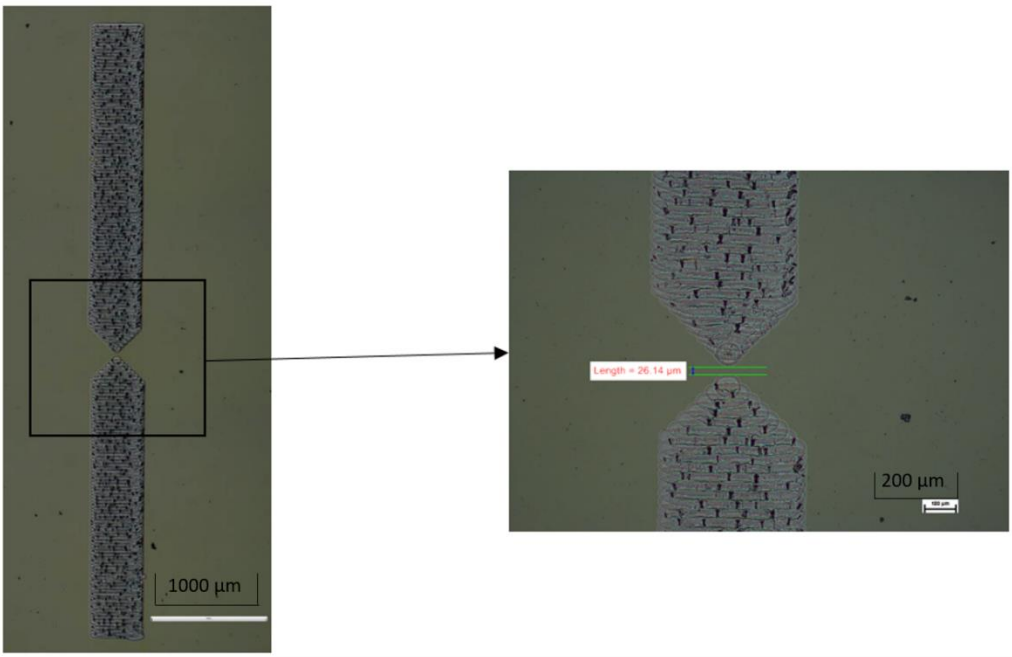

Figure 6.3 Optical microscope images of printed drain and source electrodes on silicon wafer in the vertical direction (a) whole structure (b) magnified image of the gap between drain and source electrodes.

Graphene oxide ink is subsequently printed on the silicon wafer, covering the gap between the needles of drain and source electrodes. The printing performance is presented in figure 6.4 (a) and figure 6.4 (b). It can be seen that a graphene oxide square is successfully printed, which is large enough to cover the gap between the needles of drain and source electrodes. However, splashed droplets are observed outside the printed graphene oxide square. This is caused by a degradation of the prepared graphene oxide ink due to the continuous evaporation of isopropanol in ambient temperature after long-time operation.

Therefore, although this prepared graphene oxide ink can be used to form the printed graphene oxide flakes in the inkjet printing process, it is not stable for long-term use.

Optimisation of this prepared graphene oxide ink is suggested in the future. For instance, more solvents with low surface tension and boiling point (but higher than those of isopropanol and deionised water) can replace isopropanol in the prepared graphene oxide ink. For further fabrication work in this research, freshly prepared graphene oxide ink is preferred.

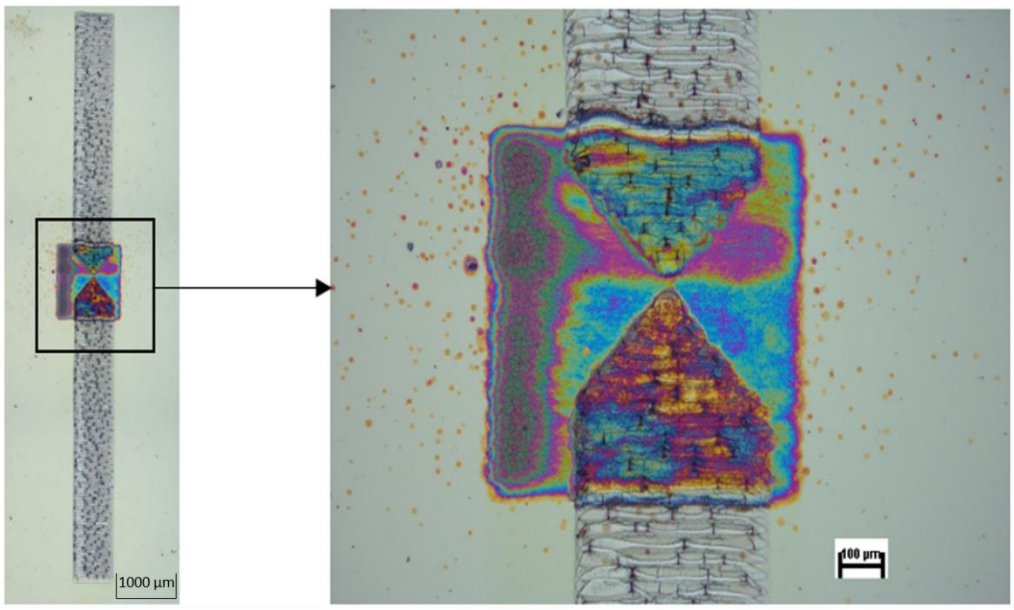

Figure 6.4 Optical microscope images of partially-printed graphene transistor on silicon wafer (a) whole structure (b) magnified image of semiconductor channel.

A UV reduction treatment (30 seconds) is performed on the printed graphene oxide specimens after the printing work. As discussed in section 3.3.2, a UV irradiation unit with a power of 4 W and a wavelength of 395 nm is selected. All

printed graphene oxide specimens are expected to be reduced to rGO after the treatment. Their optical and electrical properties are then determined.

6.1.2 Optical and Electrical Characterisation Results and Discussion

Optical characterisation of the partially-printed graphene transistor on silicon wafer is first conducted. The device is tested both in the dark and under light conditions. This step determines whether the rGO films are photosensitive (i.e., whether resistance is affected by light intensity).

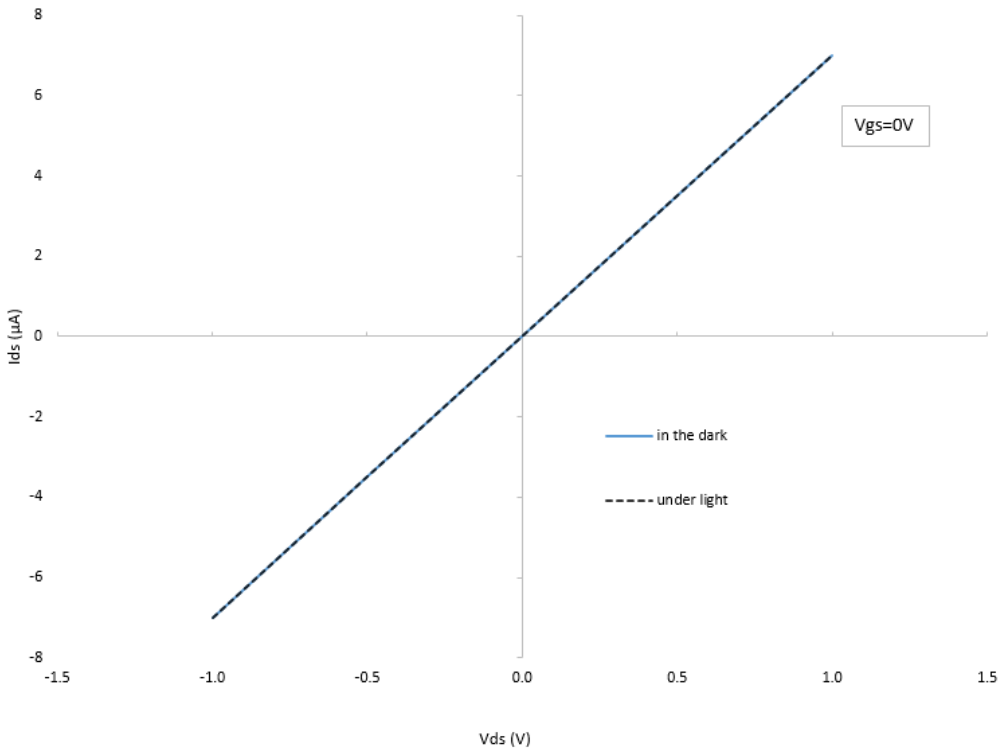

Figure 6.5 Photosensitive measurements of partially-printed graphene transistor on silicon wafer with different light intensities (plot of V_ds versus I_ds).

Figure 6.5 presents the relationship between drain-to-source current (I_{DS}) and drain-to-source voltage (V_{DS}) of the partially-printed graphene transistor on silicon wafer in two situations – in the dark and under light condition (gate-to-

source voltage (V_{GS}) is 0 V). It is observed that the I_{DS} measurements of this electronic device correspond to the same V_{DS} in both situations. For instance, when V_{DS} is 0.5 V, the corresponding I_{DS} is 3 A in both dark condition and light condition. Therefore, this prepared rGO is not photosensitive and the resistance of the semiconducting channel in this partially-printed graphene transistor on silicon wafer is not affected by the light intensity.

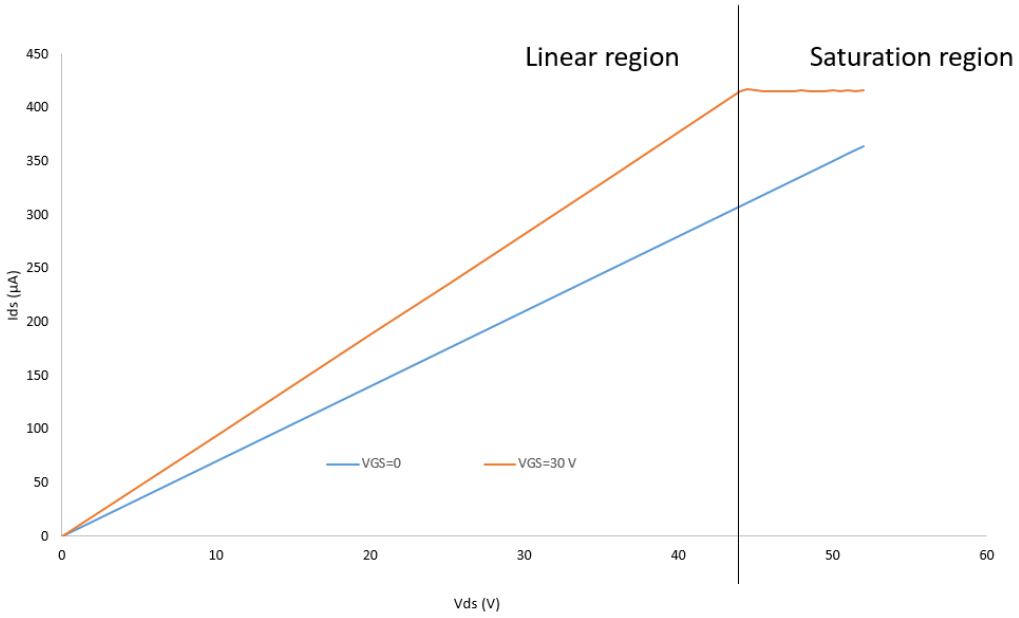

Figure 6.6 Electrical characterisation results for partially-printed graphene transistor on silicon wafer with different applied gate-to-source voltages (plot of V_ds versus I_ds).

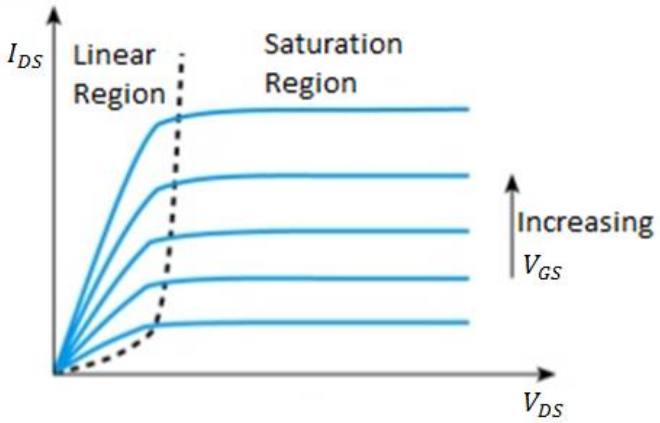

Figure 6.7 Output performance of a typical field effect transistor (plot of V_ds versus I_ds) (Holbrook and Seeley, 2013).

Electrical characterisation of this partially-printed graphene transistor on silicon wafer is performed. Figure 6.6 presents the output performance of the device with and without an external V_{GS}. In this test, the external V_{GS} is fixed as 30 V. The blue line in figure 6.6 represents the I_{DS} measurements without any external V_{GS}. The orange line in figure 6.6 represents the I_{DS} measurements with V_{GS} of 30 V. It can be seen that the magnitude of I_{DS} is amplified when V_{GS} of 30 V is employed. For instance, when V_{DS} is 40 V, I_{DS} is 400 µA when a 30 V V_{GS} is employed but only 275 µA without any applied V_{GS}. Therefore, the drain-to-source current is amplified in this partially-printed graphene transistor on silicon wafer by setting an external gate-to-source voltage.

Moreover, it can be seen in figure 6.6 that a saturation region appears when V_{DS} keeps increasing. Therefore, both linear and saturation regions exist for this partially-printed graphene transistor on silicon wafer. Figure 6.7 presents the typical FET output performance based on the working principles explained in section 2.5.3. It can be seen that the electrical performance of this partially-printed graphene transistor on silicon wafer matches the profile in figure 6.7.

Therefore, it can be concluded that the partially-printed graphene transistor on silicon wafer is successfully fabricated.

6.2 Fabrication and Characterisation of Fully-printed Graphene Transistor

6.2.1 Polyimide Based Fully-printed Graphene Transistor

As two insulating inks (polyimide and TPGDA) are selected in this work, they are printed with silver and graphene oxide inks to form the fully-printed graphene transistors separately. Polyimide ink is first used. A coplanar bottom-gate structure, which is explained in section 2.5.4, is employed for this fully-printed graphene transistor initially because it follows the structure of successfully fabricated partially-printed graphene transistor on silicon wafer.

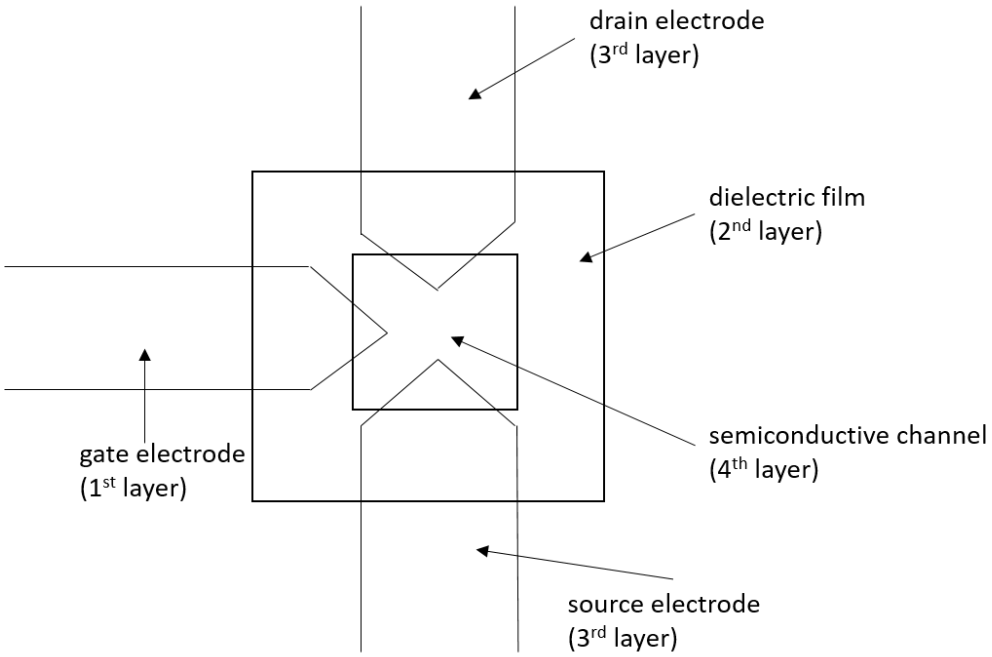

Figure 6.8 Schematic of the structure of polyimide based fully-printed graphene transistor. Gate electrode, dielectric film, drain electrode, source electrode and semiconductive channel are presented from bottom to top.

Figure 6.8 presents the schematic of this coplanar bottom-gate fully-printed graphene transistor. A gate electrode is printed on the bottom and a polyimide film is subsequently printed on the top of the gate electrode. Afterwards, drain and source electrodes are printed as the third layer above the polyimide film with a gap between them. Figure 6.9 (a) and figure 6.9 (b) show a specimen of the coplanar bottom-gate structure without graphene oxide ink printed. Obvious silver tracks are observed because silver ink is evaporated rapidly when silver droplets land on the thermal treated substrate. Regular patterns are formed with both silver and PI inks and no droplets are splashed outside the printed patterns, demonstrating that stable printing processes are achieved for both silver and PI inks.

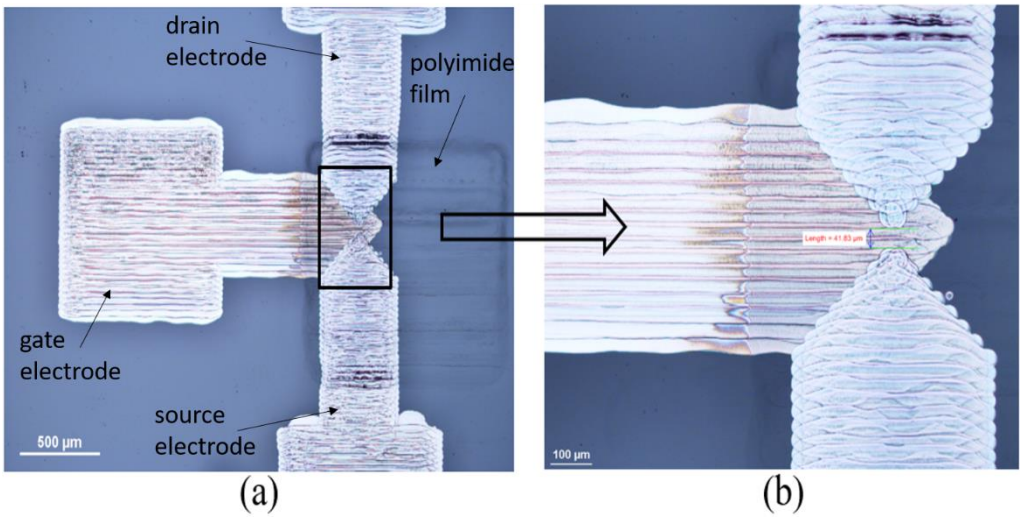

Figure 6.9 Optical microscope images of printed gate electrode, dielectric film, drain and source electrodes on a glass slide (a) whole structure (b) magnified image of 'transistor' area.

Before graphene oxide ink is printed above the gap, electrical characterisation is performed on the current printed structure using a multimeter (UNI-T UT50B). The characterisation process is divided into two steps. First, two probes are

placed on the drain and source electrodes separately to check whether the two electrodes are connected. Since the testing resistance between drain and source electrodes is infinitely high, no conduction channel is formed between drain and source electrodes. Second, one probe of the multi meter is placed on the gate electrode and the other probe is placed on the drain electrode and source electrode successively. The dielectric property of the polyimide layer is measured by this procedure. Based on the measurements, no current leakage is observed between the gate electrode and drain or source electrode, demonstrating that the polyimide film works well as insulator in this case.

However, a current leakage is observed through the polyimide films when the gate-to-source voltage is increased to 5 V. Resistances between gate and source electrodes are measured repeatedly and micro-ohm measurements are achieved. Therefore, the PI film is considered to be at breakdown when a 5 V gate-to-source voltage is applied.

Insufficient conversion of PAA is deemed as the major reason causing the breakdown. In this work, thermal treatment at 160 ℃ is employed for the imidization process of PI from PAA. However, a few researchers report that a higher temperature is required for 100% imidization (Ji *et al.*, 2018). For instance, in the research reported by Kim and Park, the imidization rate of PI is almost 100% at a temperature of 250 ℃, 63% at a temperature of 200 ℃ and only 15% at a temperature of 150 ℃ (Kim and Park, 1997). Li *et al.* also reported that the polymerisation process of PAA is not fully completed until a temperature of 350 ℃ is reached (Li *et al.*, 2014). Therefore, PAA is not fully converted into PI at a temperature of 160 ℃.

When the printed PAA/PI film is first tested by the multi meter, the resistance of this treated film is significantly higher than the low internal voltage (around 0.5 V) of the kit, because PAA is partially converted into PI. Therefore, no flowing current is measured and the treated PAA/PI film is regarded as insulator. However, when a higher voltage (5 V) is applied on this printed structure, the printed PAA/PI cannot hold the voltage due to its impure composition and a current leakage is observed.

This problem can be solved by applying thermal treatment (at about 350 ℃) to ensure that all printed PAA molecules are converted to PI completely. However, it is difficult to achieve the printing process because the nozzle is easily clogged if the substrate temperature is too high (resulting in rapid evaporation of solvents). Therefore, the specimens have to be removed from substrate and treated in a heating equipment such as vacuum oven. The whole fabrication process of fully-printed graphene transistor is complicated and the difficulty of standardized production is increased because more steps are employed in this work.

6.2.2 TPGDA Based Fully-printed Graphene Transistor

TPGDA ink is used as a substitute for PI ink in the printing process of fully-printed graphene transistor because no high-temperature thermal treatment is required for this ink. As discussed in section 2.4.5, TPGDA ink is normally treated using UV light.

As mentioned in section 6.2.1, a coplanar bottom-gate structure is employed for PI based fully-printed graphene transistor. Therefore, graphene oxide ink has to be printed on the surface of both silver (drain and source electrodes) and PI (dielectric film) to cover the gap between drain and source electrodes. Based on

the obvious silver and PI tracks in figure 6.9 (a), one concern becomes apparent: if the graphene oxide ink is printed at room temperature, the droplets landing on the ridges of the tracks will flow due to gravity, which may result in gaps through the printed graphene oxide film. In this case, the drain and source electrodes cannot be connected by the semiconducting channel and TFTs cannot be fabricated.

Although there are a few possible solutions for this problem, such as printing multi-layers of graphene oxide or optimising the printing mechanisms of conductive and insulating inks, most of the solutions complicate the printing process and may result in poorer electrical performance. In this work, a different structure design of staggered top-gate is selected as the suitable solution. As the printing sequence of insulating and semiconducting inks is changed, graphene oxide ink is now printed on the glass slide directly instead of dielectric films. The risk of forming gaps in the printed graphene oxide pattern is reduced.

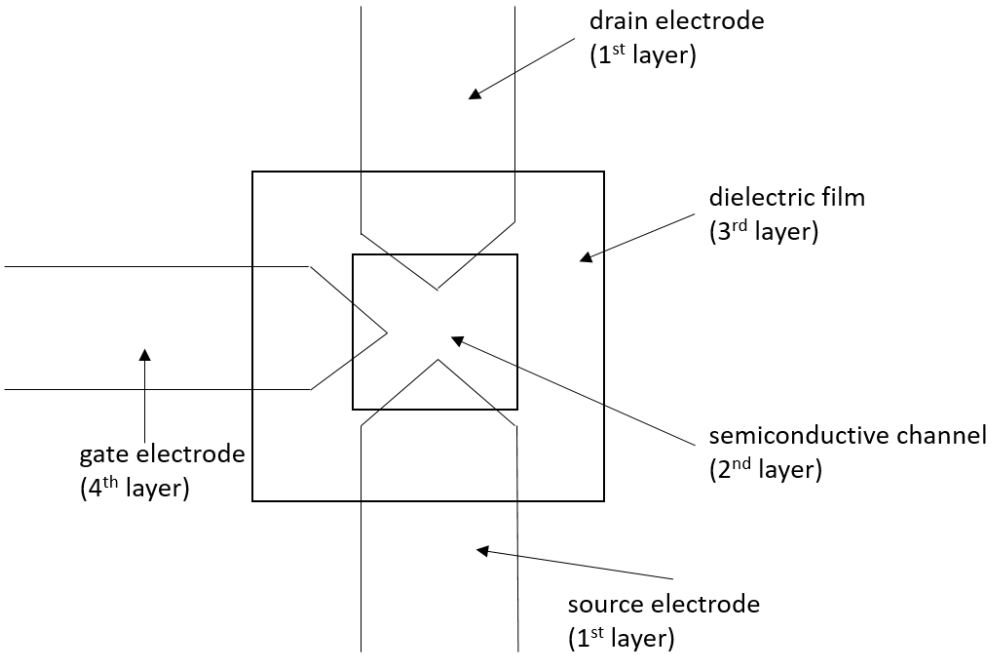

Figure 6.10 Schematic of the structure of TPGDA based fully-printed graphene transistor. Drain electrode, source electrode, semiconductive channel, dielectric film and gate electrode are presented from bottom to top.

Figure 6.10 presents a schematic of a staggered top-gate transistor. As explained in section 2.5.4, drain and source electrodes are first printed on the substrate and a semiconducting channel is fabricated to cover the gap between the two electrodes. Afterwards, dielectric film is printed before the gate electrode to ensure that the gate electrode is separated from drain electrode, source electrode and semiconducting channel.

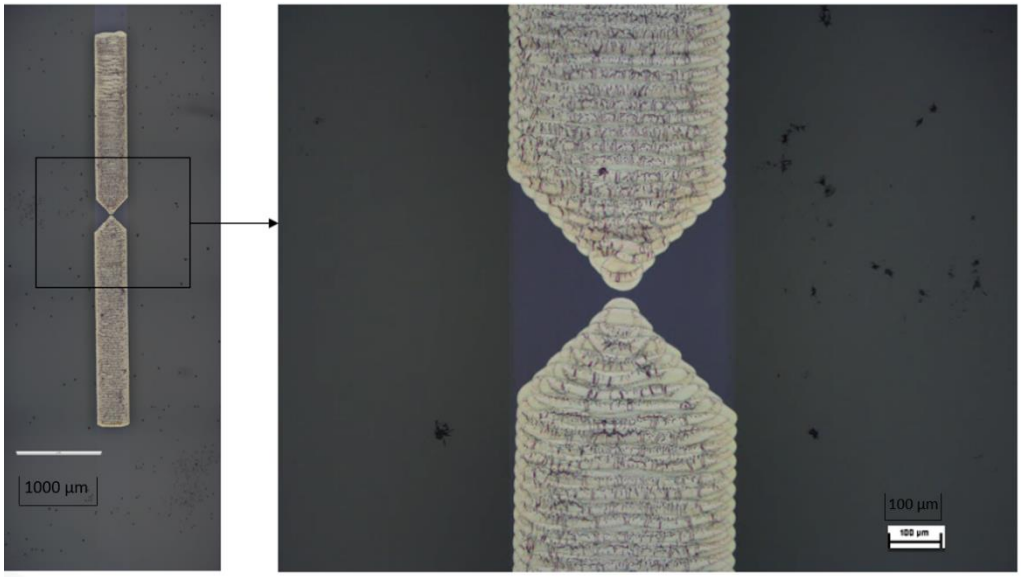

Figure 6.11 Optical microscope images of printed drain and source electrodes on glass slide (a) whole structure (b) magnified image of the gap between drain and source electrodes.

Figure 6.11 (a) presents the images of the printed silver drain and source electrodes on the glass slide and figure 6.11 (b) shows the magnitude of the gap between drain and source electrodes. The width of the gap (distance between drain and source electrodes) is measured as 13.34 µm using the internal measuring function in the optical microscope. The reason for forming a narrower practical gap (compared to pattern design) is explained in section 5.3. Since the printed drain and source electrodes are regular and no droplets are observed outside the two electrodes, the printing process of drain and source electrodes is considered to be stable and successful.

An electrical test is performed on these two electrodes after the printing work to ensure that there is no connection between drain and source electrodes. Two probes of the multi meter are placed on the drain and source electrodes

separately. The measurements demonstrate that the drain and source electrodes are separated completely due to an infinite high resistance.

A graphene oxide square is then printed on top of the drain and source electrodes. As mentioned in section 4.4.4, the graphene oxide ink is printed with a drop spacing of 30 μm at room temperature. Once the printing work is completed, UV treatment is applied on this specimen to reduce the printed graphene oxide to rGO.

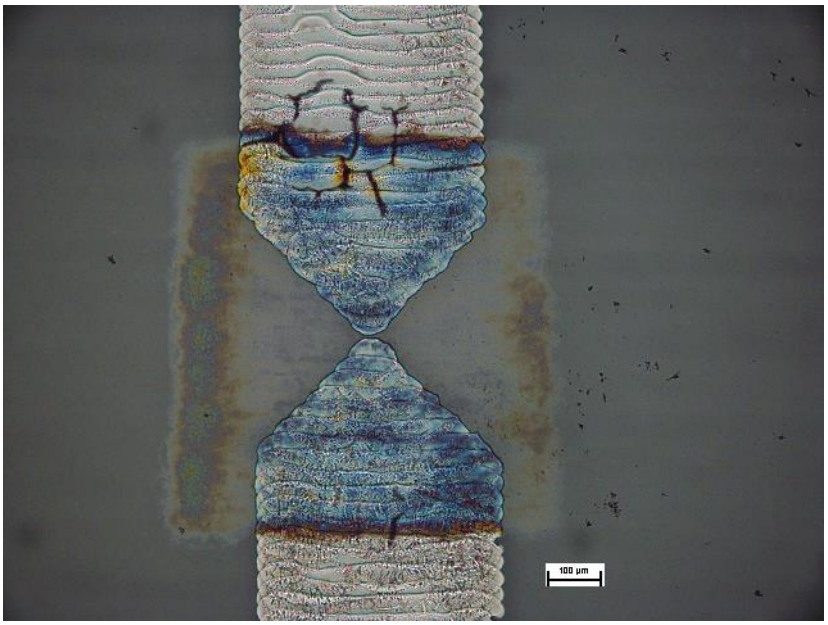

Figure 6.12 Magnified optical microscope image of printed drain electrode, source electrode and semiconductive channel on glass slide.

It can be seen from figure 6.12 that the fabricated rGO square is regular and large enough to cover the gap between drain and source electrodes. However, rGO flakes are mainly drawn to the left-hand side of the pattern due to the Marangoni effect. Therefore, a disconnection between remaining rGO flakes and drain or source electrode may occur.

This problem can be solved by optimising the graphene oxide ink. Adding other solvents with low surface tension is an option. By reducing the total surface

tension of the graphene oxide ink, Marangoni effect is minimised and printed graphene oxide flakes can be placed uniformly instead of drawing to the left-hand side of the pattern. A mild thermal treatment (around 40 – 50 ℃) is also considered in the printing process of graphene oxide ink. The higher substrate temperature helps to increase the evaporation speed of the graphene oxide droplets when they land on the substrate. As a result, the mobility of the graphene oxide droplets is reduced and the printed graphene oxide flakes are more likely to be placed on their landing positions.

Cracks are also observed on the printed silver electrodes after the reduction of printed graphene oxide film. They are formed due to an instantaneous high temperature which is caused by the absorption of a large amount of energy by the graphene oxide film in a relatively short time. By adjusting the UV light intensity, treatment time and distance between the UV light and specimen, this problem is solved.

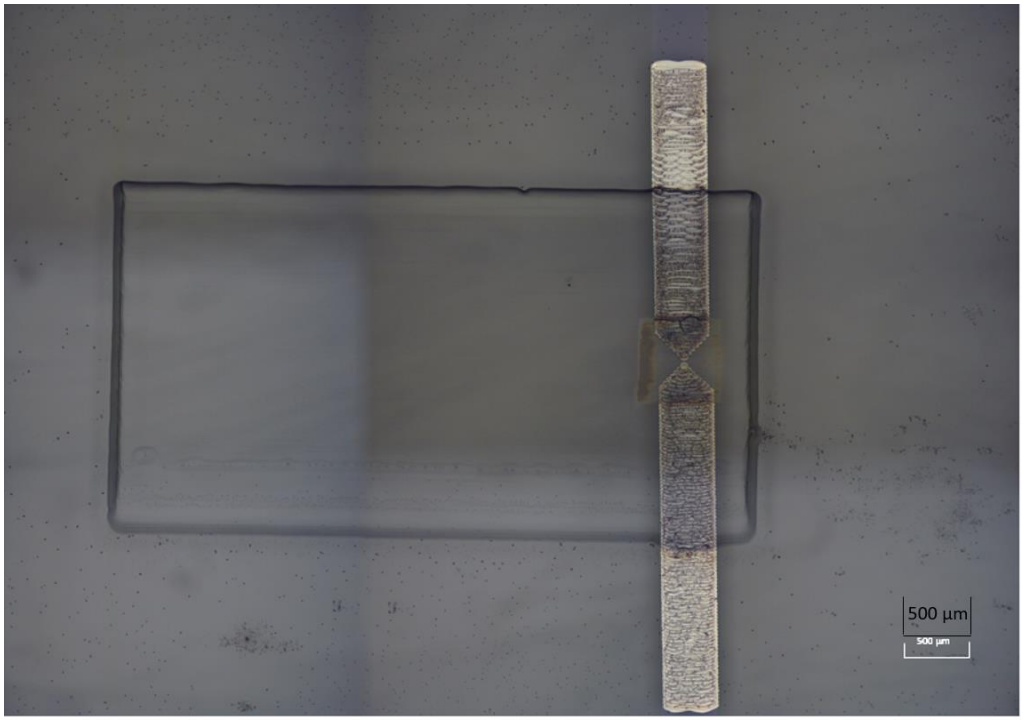

Figure 6.13 Optical microscope image of printed drain electrode, source electrode, semiconductive channel and dielectric film on the glass slide.

Figure 6.13 presents the printing performance of the TPGDA film. The film is large enough to cover all overlapping components including drain electrode, source electrode and semiconducting channel. As discussed in section 2.4.5, UV light is employed in this printing process for the polymerisation of TPGDA film.

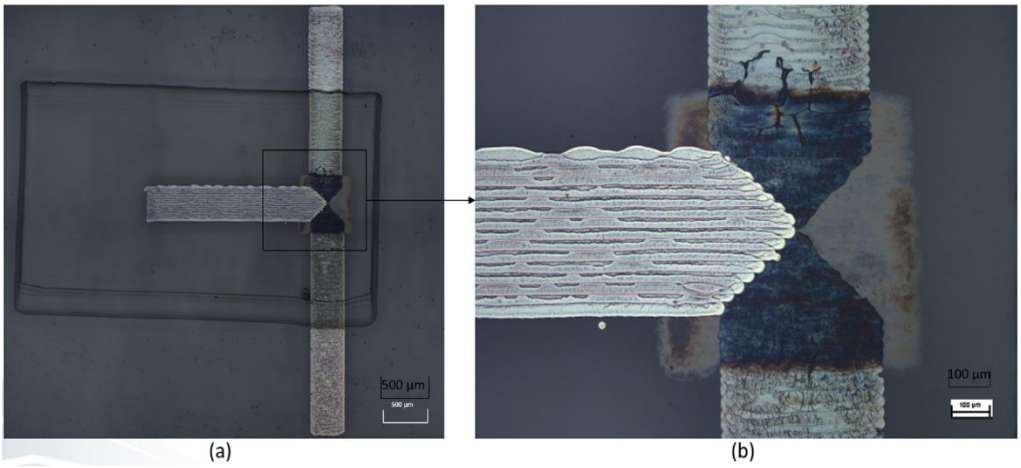

Figure 6.14 Optical microscope images of TPGDA based fully-printed graphene transistor (a) whole structure (b) magnified image of overlapping area.

The gate electrode is printed as the last step in this printing process. Figure 6.14 (a) and figure 6.14 (b) demonstrate that the gate electrode is printed on the TPGDA film and the needle of this printed gate electrode is accurately placed above the gap between the drain and source electrodes. Therefore, a fully-printed graphene transistor is fabricated following the design in figure 6.10.

However, it can also be seen from figure 6.14 (a) that the upper-side edge of the printed gate electrode is not straight, demonstrating that the silver droplets are still slightly flowing after they first land on the TPGDA surface. This phenomenon is caused by insufficient substrate temperature at the beginning of the printing process. To solve this problem, a thermal meter is suggested in the future to ensure that the substrate temperature reaches 160 ℃ before the printing work of silver ink.

A multi meter is used to check the electrical properties of all printed components. Two probes are first placed on the drain and source electrodes separately. The measurements show that the resistance of the printed semiconductor channel is 6.25 MΩ, demonstrating that rGO is reduced from the graphene oxide film. Then,

similar to the testing method of polyimide based fully-printed graphene transistor, one probe of the multi meter is fixed on the gate electrode and the other is placed on the drain electrode and source electrode successively to test the dielectric property of the printed TPGDA film. No current leakage is observed, meaning that this TPGDA film works well as the dielectric layer. As the polyimide film breaks down when a higher voltage is applied on the gate electrode, this TPGDA based device is tested by applying increasing gate-to-source voltage. The testing results show there is no breakdown observed on this TPGDA film when an increasing gate-to-source voltage from 0 to 30 V is applied (0 V – 30 V is the range of the power supply used in the testing circuit in this work). Therefore, all components in this TPGDA based fully-printed graphene transistor work well and the transistor output performance is characterised in the next step.

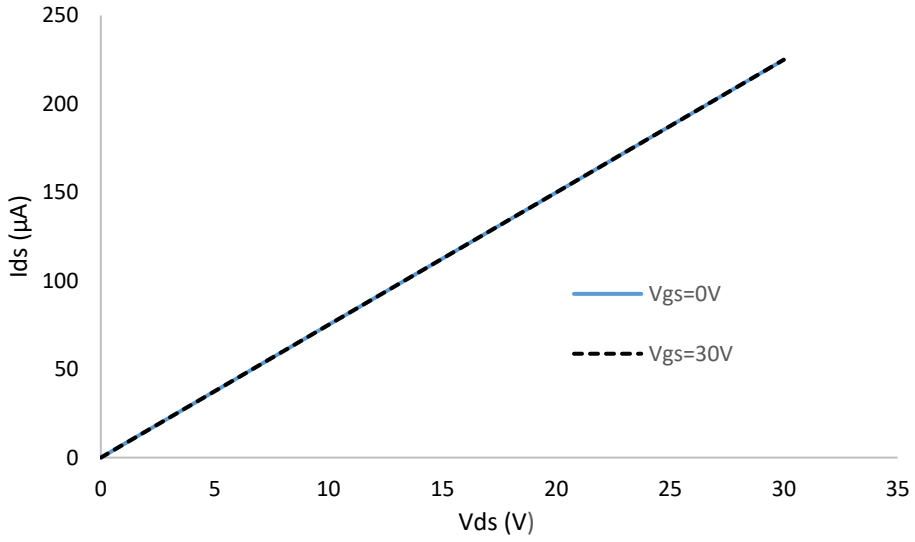

Figure 6.15 Electrical characterisation results for TPGDA based fully-printed transistor (plot of V_ds versus I_ds with different applied V_gs).

Figure 6.15 presents the electrical characterisation results of this fully-printed graphene transistor. Unfortunately, no obvious amplification of drain-to-source current is observed when the applied gate-to-source voltage is increased from 0 V to 30 V. Moreover, no saturation region is present. Therefore, no typical transistor properties are observed for this TPGDA based fully-printed graphene transistor.

There are several reasons affecting the output performance of this fully-printed graphene transistor. First, the dielectric layer is too thick. In the partially-printed graphene transistor on silicon wafer, the silicon dioxide (SiO2) with a thickness of 200 nm is used as the dielectric layer. However, in this TPGDA based fully-printed graphene transistor, the thickness of the dielectric layer is 3.07 μm (measured by Bruker Contour GT-I profiler), which is around 15 times thicker than that of the silicon dioxide layer. Therefore, the free electrons in the semiconductor channel are not significantly affected by the electric field formed between gate electrode and drain/source electrodes. Therefore, the current flowing through the semiconductor channel is not obviously amplified.

There are a few ways to solve this problem. One typical approach is to reduce the droplet size (around 47 μm) of the TPGDA ink, and then to further reduce the thickness of TPGDA film. To achieve this goal, the composition of the TPGDA ink has to be changed or cartridges with smaller nozzles are required.

Printed rGO film in this fully-printed graphene transistor is also a potential factor resulting in the unsatisfactory transistor performance. Based on the optical microscope images in figure 6.12, most rGO flakes remain on the left-hand side of the pattern and only few rGO flakes are located between drain and source electrodes. Therefore, as discussed previously, optimisations such as adjusting

the composition of graphene oxide ink and applying a mild thermal treatment, are required for the printing process of graphene oxide inks.

A higher drain-to-source voltage should be applied to achieve a better understanding of the output performance of this fully-printed graphene transistor. Based on the electrical characterisation results of partially-printed graphene transistor on silicon wafer in section 6.1.2, the saturation region is finally achieved until the drain-to-source voltage reaches 43 V. However, in this characterisation procedure of fully-printed graphene transistor, the maximum employed drain-to-source voltage is only 30 V. Therefore, a higher drain-to-source voltage is suggested in the future.

Although no typical transistor output performance is observed, the printing of fully-printed graphene transistor is still worthwhile because it follows the successful printing of a partially-printed graphene transistor on silicon wafer. Therefore, this printed device is expected to work as a TFT when all discussed optimisations are made in the future (or even with a higher drain-to-source voltage). As reviewed in section 2.5.4, there is only one successfully fabricated fully-printed graphene transistor (staggered bottom-gate structure) reported here whose output performance is still unsatisfactory with only 1.5 times amplification ratio of the drain-to-source current. This device has the possibility to be a fully-printed staggered top-gate graphene TFT for the first time.

6.3 Conclusion

- Partially-printed graphene transistor silicon wafer is successfully fabricated. Silver drain and source electrodes are printed in vertical direction to ensure that the printed graphene oxide pattern, which is affected by Marangoni effect, can fill the gap between drain and source

electrodes. Printed graphene oxide is UV reduced to rGO instead of using traditional high temperature thermal treatment to improve the deoxidization efficiency. In future studies, more characterisations of reduction process of graphene oxide are suggested, such as Raman spectroscopy and XRD, to determine the relationships between processing parameters (such as light intensity, processing time, etc.) and deoxidization ratio.

- Typical transistor output performance is observed for this partially-printed graphene transistor on silicon wafer because both linear region and saturation region are achieved. The output drain-to-source current is amplified by 1.46 times. The amplification ratio is low compared to a few other partially-printed graphene transistor in the literature (amplification ratio of the TFT reported by Moon *et al.* is 3.6 and the TFT reported by Torrisi *et al.* is 3.9) (Moon *et al.*, 2009) (Torrisi *et al.*, 2012).
- Printed PI film in this work cannot be used as the dielectric layer due to insufficient conversion of PAA. PAA is thermal treated at a temperature of 160 ℃ for the conversion process in this research. However, according to literature reports, higher temperatures (from 250 ℃ to 350 ℃) are required to achieve 100% polymerisation of PI (Kim and Park, 1997) (Li *et al.*, 2014) (Ji *et al.*, 2018). Investigations on fully polymerized PI film are worthwhile in the future because the prepared PI ink can be printed stably.
- TPGDA based fully-printed graphene transistor is fabricated without any typical transistor output performance. TPGDA is treated by UV light to

generate a cross-linked structure during the printing process. Possible reasons for the unsatisfactory electrical characterisation results of this TFT are thick dielectric layer, nonuniform distribution of graphene oxide flakes and insufficient applied drain-to-source voltage. More experiments are required to determine the exact reason.

Chapter 7 General Discussion

The aim of this work was to determine the possibility of using inkjet printing technologies to fabricate functional printed electronics. Silver, PI, TPGDA, graphene, and InSe were investigated and fabricated using inkjet printing technology. Photodetectors, Hall bars, and TFTs were fabricated using these materials. The steps undertaken between the printed electronics and inkjet printing process, including the structure design, ink formulation, printing parameter assessment, and characterisation of the final products, were investigated.

7.1 Printable Inks

In this work, an investigation on the printing of a commercial silver ink (Silver Jet Ink, Advanced Nano Products Co., Ltd) was first undertaken. Two printing mechanisms of this silver ink were characterised for the first time, and their influence on the morphology and electrical performance of the printed silver specimens are discussed. Two insulating inks, namely the PI and TPGDA inks, were prepared in the Centre for Additive Manufacturing (the University of Nottingham, UK). Electrical characterisation was conducted on these two inks based on an original 'sandwich' design. An investigation on how the temperature affects the printing performance and morphology of the single-layer PI film was carried out for the first time with the help of Dr. Fan Zhang (Zhang *et al.*, 2016).

GO ink was prepared by dispersing GO flakes in 20 wt% isopropanol. GO flakes dispersed in deionised water, deionised water/ 20 wt% TGME, deionised water/ 20 wt% PEG, and deionised water/ 0.3 wt% Tween 20 could not be used in this

work due to their poor printing performance on glass slides. However, in the work by Le, it was reported that GO inks prepared by dispersing GO particles in deionised water were printable on a titanium foil surface (Le *et al.*, 2011). Therefore, it is suggested that more substrates should be tested for the printing of GO inks in the future. Printed GO specimens were laser-reduced in this work. According to the literature, a significant reduction of the total processing time is achieved by using laser reduction instead of thermal reduction (Gao *et al.*, 2009) (Kymakis *et al.*, 2014) (Guan *et al.*, 2016). In the work by Kumar *et al.*, GO could be reduced to rGO in 4 min using excimer laser radiation (Kumar *et al.*, 2011). Compared with the work by Kumar *et al.*, the processing time was here reduced from 4 to 1.5 min using UV laser radiation. However, Raman spectroscopy and X-ray diffraction (XRD) are required to gain a better understanding (such as for the de-oxidation ratio) of this reduction process.

7.2 InSe-Based Printed Electronics

In this work, the optical properties were determined by fabricating InSe-based photodetectors and Hall bars. According to the results from previous literature, InSe is a photosensitive material (Tamalampudi *et al.*, 2014) (Chen *et al.*, 2015). The gate leakage and gate dependence of InSe were characterised for the first time in this work. A negligible gate leakage and a weak gate dependence were observed. Inkjet-printed InSe-based TFTs did not work successfully in this work, which is possibly caused by the weak gate dependence of InSe films or the insufficient contact area between the conductive electrodes and InSe flakes. More InSe-based TFTs will be fabricated in the future to determine the reasons behind such a failure.

In the work by Feng *et al.*, InSe could be used as the semiconducting channel in TFTs, which were spin-coated (Feng *et al.*, 2014). Therefore, InSe could be used in TFTs, and it is expected to be used in the inkjet printing process. No InSe ink has been reported up to date. Thus, future development and investigations on InSe inks will be beneficial.

7.3 Graphene-Based Printed Electronics

A partially-printed graphene TFT was fabricated in this work by inkjet printing silver (for the drain and source electrodes) and GO inks on a commercial silicon wafer. Compared with the partially inkjet-printed graphene TFTs reported in previous literature, more components were fabricated using the inkjet printing technology in this work (Torrisi *et al.*, 2012) (Monne *et al.*, 2017). In the work by Torrisi *et al.*, graphene TFT was also partially fabricated on a commercial silicon wafer. Graphene ink was inkjet-printed, while the two chromium–gold pads (for the drain and source electrodes) were patterned. The sample had to be removed from the inkjet printer for the lift-off process, resulting in a more complex fabrication process. In the work by Monne *et al.*, silver (for the drain, source, and gate electrodes) and graphene inks were inkjet-printed, while the dielectric layer of the TFT was spin-coated. The fabrication process was also quite complex. Therefore, the single-process fabrication of partially printed graphene transistors achieved in this work is more convenient than the processes reported in previous studies.

The amplified ratios of the output current obtained in the TFTs reported by Torrisi *et al.* (around 4) and Moone *et al.* (around 35) are higher than that of the partially printed graphene TFT (around 1.45) presented in this work. This is probably due to the fact that inks with pure graphene and graphene doped with

MoS_2 were used separately in the TFTs reported by Torrisi *et al.* and Moone *et al.*, while GO ink was used in the partially printed graphene TFT in this work with a post UV reduction process. Using UV lasers to reduce GO to rGO has been reported by a few research groups and has been used in printed TFTs for the first time in this work (Kymakis *et al.*, 2014) (Guan *et al.*, 2016). However, as mentioned previously, further characterisations, such as Raman spectroscopy and XRD, are still required for this reduction process.

PI-based graphene TFTs could not be completely fabricated in this work due to the breakdown of the PI film. The breakdown was probably due to an insufficiently high temperature being employed for the PI polyimidization process. According to the literature, a temperature as high as 350 ℃ was suggested, while a temperature of only 160 ℃ was used in this work (Kim and Park, 1997) (Li *et al.*, 2014) (Ji *et al.*, 2018). A 350 ℃ thermal treatment is recommended for future printed PI specimens.

A TPGDA-based graphene TFT was fully printed using the inkjet printing technology in this work. Unfortunately, no typical transistor performance was observed for this TFT. The reasons behind this result are probably the thick TPGDA film, the non-uniform dispersion of GO flakes, or an insufficient drain–source voltage. The work by Carey *at al.* reported the only successful fully printed graphene TFT fabricated by inkjet printing silver (for the drain, source, and gate electrodes), graphene (semiconducting channel), and h-BN (dielectric film) inks (Carey *et al.*, 2017). According to this previous work, the basic concept (including the structure design and printing mechanism) behind the printing process of the fully printed graphene TFT presented in this work was

proven to be feasible. Therefore, more investigations on fully printed graphene TFTs using the same concept are worthwhile in the future.

In summary, a wide range of printable inks for the inkjet printing process of printed electronics were prepared and characterised in this work. A better understanding of InSe and InSe-based printed electronics was obtained. Graphene-based TFTs could be fabricated in a single process, and further candidates for printed electronics are expected in the future.

Chapter 8 Conclusions and Future Work

8.1 Conclusions

In this study, investigations on printable inks and printed electronics in the inkjet printing process were conducted. Based on both the experimental results and general discussion, the following key findings were obtained:

- A wide range of printable inks were prepared and characterised. The relationship between the printing/electrical performance and printing mechanisms of silver ink was evaluated. The influence of different temperatures on the printing performance of PI was also investigated. It was found that adding polymers with low surface tension into a GO solution (GO flakes dispersed in deionised water) is beneficial to reduce the total surface tension and optimise the printability of the mixture. However, it was not possible to use GO solutions with additional 20 wt% TGME, 20 wt% PEG, and 0.3 wt% Tween 20 in the inkjet printing process due to their poor performance. A GO solution with 20 wt% isopropanol was finally selected as the best option.
- For the first time, the gate leakage and gate dependence of InSe flakes were evaluated. InSe-based photodetectors and Hall bars also demonstrated that InSe is a photosensitive material. A primary study on the fabrication of InSe-based TFT through the inkjet printing technology was constructed. The weak gate dependence of InSe films is a possible reason for the poor output performance of InSe-based TFTs.
- Partially inkjet-printed graphene TFTs were obtained in a single process. In addition, this work reported for the first time the possibility reduce

GO to rGO in inkjet-printed TFTs using UV light. The output drain–source current was amplified from 275 to 400 µm upon applying an external gate–source voltage. Both the linear and saturation regions of this partially printed graphene transistor on a silicon wafer were observed.

- PI-based graphene TFTs could not be fabricated successfully because PI cannot be completely polymerised at a temperature of 160 °C. A TPGDA-based fully printed graphene transistor was manufactured using the inkjet printing technology but failed to work. Optimisation of the ink preparation and testing approaches should be preferred in the future, as the structure design and printing mechanisms were proven to be feasible in the work by Carey *et al*.
- The photodetectors, Hall bars, and TFTs printed using the inkjet printing technology indicate that there is a clear potential for the fabrication of a wider range of printed electronics devices.

8.2 Future Work

Several achievements and findings regarding the formulation of printable inks and the fabrication of printed electronics via the inkjet printing process were presented in this work. However, some investigations could not be performed due to limited experimental time. Therefore, the following suggestions are provided for future work:

- Optimal formulations and printing conditions for all printable inks, particularly for GO ink, are required. The influence of the printing mechanisms on these inks still need to be determined.

- Printed GO films were reduced to rGO using UV lasers. A comprehensive understanding of the deoxidation mechanisms in this process is required. In addition, systematic studies on the influence of the processing parameters and conditions on the resulting rGO would be beneficial.
- InSe ink could not be formulated in this work. However, investigations on how to develop InSe inks are recommended, as they would provide further opportunities to fabricate InSe-based printed electronics.
- Optimisations of the structure designs and printing mechanisms of partially printed graphene transistors on silicon wafer are needed to obtain a higher output performance. Furthermore, the influence of the printing parameters and conditions on the possibility of achieving a controllable and repeatable fabrication process of these electronic devices still needs to be evaluated.
- Further in-depth studies are required to determine the influence of the materials, structures, and printing mechanisms on fully printed graphene transistors. Similarly, controllable and repeatable fabrication processes of fully printed graphene transistors need to be investigated.
- Regarding the long-term impact of this work, it is predicted that practical applications and more complex electronic devices will be fabricated. High throughput and higher resolution fabrication processes are expected to be developed.

Reference

Abbas, G. *et al.* (2013) 'Hysteresis-free vacuum-processed acrylate-pentacene thin-film transistors', *IEEE Electron Device Letters*. IEEE, 34(2), pp. 268–270. doi: 10.1109/LED.2012.2234434.

Ahn, B. Du *et al.* (2015) 'A review on the recent developments of solution processes for oxide thin film transistors', *Semiconductor Science and Technology*, 30(6).

Ainsley, C., Reis, N. and Derby, B. (2002) 'Freeform fabrication by controlled droplet deposition of powder filled melts', *Journal of Materials Science*, 37(15), pp. 3155–3161.

Alastalo, A. T. *et al.* (2011) 'Rapid electrical sintering of nanoparticle structures', *MRS Proceedings*, Volume 1113, pp. 31-44.

Alderman, N. J. (1997) 'Non-Newtonian Fluids: Guide to classification and characteristics', *ESDU 97034*, ESDU International plc, London.

Alongkorn, P. and Werayut, S. (2012) 'Review on Micro- and Nanolithography Techniques and Their Applications', *Engineering Journal*, Volume 16, No. 1.

Ando, B. and Baglio, S. (2011) 'Inkjet-printed sensors: A useful approach for low cost, rapid prototyping', *IEEE Instrumentation & Measurement Magazine*, Volume 14, pp. 36-40. doi: 10.1109/MIM.2011.6041380.

Anthony, J. E. *et al.* (2001) 'Functionalized Pentacene: Improved Electronic Properties from Control of Soled-State Order', *Journal of the American Chemical Society*, Volume 123, Issue 38, pp. 9482-3.

Antonova, I. V. (2016) ‘2D printed technologies with use of Graphene based materials’, *Physics-Uspekhi*, 60(2).

Arevalo, A. *et al.* (2015) ‘A versatile multi-user polyimide surface micromachinning process for MEMS applications’, *2015 IEEE 10th International Conference on Nano/Micro Engineered and Molecular Systems, NEMS 2015*, (July), pp. 561–565. doi: 10.1109/NEMS.2015.7147492.

Arnold, B. C., Serra, P. and Pique, A. (2011) ‘Laser Direct-Write Techniques for Printing of Complex Materials’, *MRS Bulletin*, Volume 32, Issue 1: Laser Direct-Write Processing.

Ashjaran, A. and Oshaghi, H. (2014) ‘Graphene as single layer of carbon atoms: Perusal on structure, properties and applications’, *Research Journal of Pharmaceutical, Biological and Chemical Sciences*, 5(5), pp. 327–335.

ASTM International (2012) ‘ASTM F2792-12a, Standard Terminology for Additive Manufacturing Technologies’. West Conshohocken, PA.

Avis, C., Hwang, H. R. and Jang, J. (2014) ‘Effect of channel layer thickness on the performance of indium-zinc-tin oxide thin film transistors manufactured by inkjet printing’, *ACS Applied Materials and Interfaces*, 6(14), pp. 10941–10945. doi: 10.1021/am501153w.

Avouris, P. and Dimitrakopoulos, C. (2012) ‘Graphene: Synthesis and applications’, *Materials Today*. Elsevier Ltd, 15(3), pp. 86–97. doi: 10.1016/S1369-7021(12)70044-5.

Baeg, K. J. *et al.* (2010) ‘High mobility top-gated poly(3-hexylthiophene) field-effect transistors with high work-function Pt electrodes’, *Thin Solid Films*,

Volume 518, Issue 14, pp. 4024-4029.

Bain, D. C. and Whitesides, M. G. (1989) ‘Modeling organic surfaces with self-assembled monolayers’, *Advanced Materials*, Volume 1, Issue 4, pp. 110-116.

Balaji, M. V., Debes, B. and Krishnan, J. (2014) ‘Characterisation and functional properties of reduced graphene oxide and its nanocomposites’, in *NANOCON 2014 - Conference Proceedings, 6th International Conference*, pp. 31–36.

Balantrapu, K., McMurran, M. and Goia, D. V. (2010) ‘Inkjet printable silver dispersions: Effect of bimodal particle-size distribution on film formation and electrical conductivity’, *Journal of Materials Research*, Volume 35, Issue 5, pp. 821-827.

Balliu, E. *et al.* (2018) ‘Selective laser sintering of inkjet-printed silver nanoparticle inks on paper substrates to achieve highly conductive patterns’, *Scientific Reports*, Volume 8, pp. 10408.

Bandurin, D. A. *et al.* (2017) ‘High electron mobility, quantum Hall effect and anomalous optical response in atomically thin InSe’, *Nature Nanotechnology*, Volume 12, pp. 223-227.

Bardeen, J. and Brattain, W. H. (1948) ‘Transistor, a semiconductor triode’, *Physical Review*, 74(2), p. 230. doi: 10.1109/JPROC.1998.658753.

Basiricò, L. (2012) *Inkjet Printing of Organic Transistor Devices*, *University of Cagliari*.

Berger, C. *et al.* (2006) ‘Electronic confinement and coherence in patterned epitaxial graphene’, *Science*, 312(5777), pp. 1191–1196. doi: 10.1126/science.1125925.

Bidoki, S. M. *et al.* (2007) 'Ink-jet fabrication of electronic components', *Journal of Micromechanics and Microengineering*, 17(5), pp. 967–974. doi: 10.1088/0960-1317/17/5/017.

De Blasi, C. *et al.* (1982) 'Photoconductivity of InSe Single Crystals', *Physica Status Solidi (a)*, 74(1), pp. 291–296. doi: 10.1002/pssa.2210740135.

Blayo, A. and Pineaux, B. (2005) 'Printing processes and their potential for RFID printing', *Proceedings of the 2005 Joint Conference on Smart Objects and Ambient Intelligence: Innovative Context-Aware Services: Usages and Technologies*, pp. 27-30.

Bonea, A. *et al.* (2012) 'Electrical conductivity of inkjet printed silver tracks', *2012 35th International Spring Seminar on Electronics Technology*, Bad Aussee, Austria.

Bordia, R. K. and Jagota, A. (1993) 'Crack growth and damage in constrained sintering films', *Journal of the American Ceramic Society*, Volume 76, pp. 2475-2485.

Boukhvalov, D. W. *et al.* (2017) 'The advent of indium selenide: Synthesis, electronic properties, ambient stability and applications', *Nanomaterials*, 7(11). doi: 10.3390/nano7110372.

Brinkman, W. F., Haggan, D. E. and Troutman, W. W. (1997) 'A history of the invention of the transistor and where it will lead us', *IEEE Journal of Solid-State Circuits*, 32(12), pp. 1858–1864. doi: 10.1109/4.643644.

Briseno, A. L. *et al.* (2006) 'Patterning organic single-crystal transistor arrays', *Nature*, 444(7121), pp. 913–917. doi: 10.1038/nature05427.

Brodie, B. C. (1859) *On the Atomic Weight of Graphite*. London: Proceedings of the Royal Society of London.

Calabrese, G. *et al.* (2020) 'Inkjet-printed graphene Hall mobility measurements and low-frequency noise characterization', *Nanoscale*, Volume 12, Issue 12, pp. 6708-6716.

Calvert, P. (2001) 'Inkjet printing for materials and devices', *Chemistry of Materials*, Volume 13, pp. 3299-3305. doi: 10.1021/cm0101632.

Calvert, P., Yoshioka, Y. and Jabbour, G. (2004) 'Inkjet printing for biomimetic and biomedical materials', *Handbook of Learning from Nature How to Design New Implantable Biomaterials*, pp. 169-180.

Caputo, D. *et al.* (2014) 'Polydimethylsiloxane material as hydrophobic and insulating layer in electrowetting-on-dielectric systems', *Microelectron Journal*, Volume 45, pp. 1684-1690.

Carey, T. *et al.* (2017) 'Fully inkjet-printed two-dimensional material field-effect heterojunctions for wearable and textile electronics', *Nature Communications*. Springer US, 8(1). doi: 10.1038/s41467-017-01210-2.

Castrejón-Pita, J. R. *et al.* (2013) 'Future, opportunities and challenges of inkjet technologies', *Atomization and Sprays*, 23(6), pp. 571–595. doi: 10.1615/AtomizSpr.2013007653.

Castro Neto, A. H. *et al.* (2009) 'The electronic properties of graphene', *Reviews of Modern Physics*, 81(1), pp. 109–162. doi: 10.1103/RevModPhys.81.109.

Chan, C.-M. (1993) *Polymer Surface Modification and Characterization (SPE books)*. Carl Hanser Verlag GmbH & Co.

Chen, A. U. and Basaran, O. A. (2001) ‘A new method for significantly reducing drop radius without reducing nozzle radius in drop-on-demand drop production’, *Physics of Fluids*, 14(1), p. 1063.

Chen, J. H. *et al.* (2008) ‘Intrinsic and extrinsic performance limits of graphene devices on SiO 2’, *Nature Nanotechnology*, 3(4), pp. 206–209. doi: 10.1038/nnano.2008.58.

Chen, W. and Yan, L. (2010) ‘Preparation of graphene by a low-temperature thermal reduction at atmosphere pressure’, *Nanoscale*, 2(4), pp. 559–563.

Chen, X., Zhang, L. and Chen, S. (2015) ‘Large area CVD growth of graphene’, *Synthetic Metals*. Elsevier B.V., 210, pp. 95–108. doi: 10.1016/j.synthmet.2015.07.005.

Chen, Z., Biscaras, J. and Shukla, A. (2015) ‘A high performance graphene/few-layer InSe photo-detector’, *Nanoscale*. Royal Society of Chemistry, 7(14), pp. 5981–5986. doi: 10.1039/c5nr00400d.

Chevy, A. (1984) ‘Improvement of growth parameters for Bridgman-grown InSe crystals’, *Journal of Crystal Growth*, 67(1), pp. 119–124.

Choi, D. *et al.* (2012) ‘High-performance triisopropylsilylethynyl pentacene transistors via spin coating with a crystallization-assisting layer’, *ACS Applied Materials and Interfaces*, 4(1), pp. 117–122. doi: 10.1021/am201074n.

Choi, M. H., Kim, B. S. and Jang, J. (2012) ‘High-performance flexible TFT circuits using TIPS pentacene and polymer blend on plastic’, *IEEE Electron Device Letters*. IEEE, 33(11), pp. 1571–1573. doi: 10.1109/LED.2012.2213294.

Choi, W. and Lee, J. (2011) *Graphene: Synthesis and Applications*. CRC Press.

Chrisey, D. B. *et al.* (2000) ‘New approach to laser direct writing active and passive mesoscopic circuit elements’, *Applied surface science*, Volume 154, pp. 593-600.

Christopher, W. F. *et al.* (2015) ‘Fundamentals of Screen-Printing Electrochemical Architectures’, *Screen-Printing Electrochemical Architectures*, pp. 13-23.

Chronakis, I. S., Grapenson, S. and Jakob, A. (2006) ‘Conductive polypyrrole nanofibers via electrospinning: Electrical and morphological properties’, *Polymer*, Volume 47, Issue 5, pp. 1597-1603.

Chua, C. K. and Pumera, M. (2013) ‘Chemical reduction of graphene oxide: a synthetic chemistry viewpoint’, *Chemical Society Reviews*, 43(1), pp. 291–312.

Chung, J. *et al.* (2004) ‘Conductor microstructures by laser curing of printed gold nanoparticle ink’, *Applied Physics Letters*, 84(5), pp. 801–803. doi: 10.1063/1.1644907.

Chung, S. *et al.* (2011) ‘All-Inkjet-Printed Organic Thin-Film Transistors with Silver Gate, Source/Drain Electrodes’, *Japanese Journal of Applied Physics*, Volume 50, pp. 03CB05.

Coleman, J. N. (2009) ‘Liquid-phase exfoliation of nanotubes and graphene’, *Advanced Functional Materials*, 19(23), pp. 3680–3695. doi: 10.1002/adfm.200901640.

Coleman, J. N. (2013) ‘Liquid exfoliation of defect-free graphene’, *Accounts of Chemical Research*, 46(1), pp. 14–22. doi: 10.1021/ar300009f.

Compton, O. C. and Nguyen, S. T. (2010) ‘Graphene oxide, highly reduced

graphene oxide, and graphene: Versatile building blocks for carbon-based materials', *Small*, 6(6), pp. 711–723. doi: 10.1002/smll.200901934.

Constable, G., Somerville, B. and Lienhard, J. (2004) 'A Century of Innovation: Twenty Engineering Achievements That Transformed Our Lives', *Physics Today*, 57(12), pp. 63–63.

Cooper, D. R. *et al.* (2012) 'Experimental Review of Graphene', *ISRN Condensed Matter Physics*, 2012, pp. 1–56. doi: 10.5402/2012/501686.

Cummins, G. and Desmulliez, M. P. Y. (2012) 'Inkjet printing of conductive materials: A review', *Circuit World*, 38(4), pp. 193–213. doi: 10.1108/03056121211280413.

Dacey, G. C. and Ross, I. M. (1955) 'The Field Effect Transistor', *Bell System Technical Journal*, 34(6), pp. 1149–1189. doi: 10.1002/j.1538-7305.1955.tb03794.x.

Daly, R. *et al.* (2015) 'Inkjet printing for pharmaceutics - A review of research and manufacturing', *International Journal of Pharmaceutics*. Elsevier B.V., 494(2), pp. 554–567. doi: 10.1016/j.ijpharm.2015.03.017.

Damon, R. W. and Redington, R. W. (1954) 'Electrical and Optical Properties of Indium Selenide', *Physical Review*, 96(6), p. 1498.

Dearden, A. L. *et al.* (2005) 'A low curing temperature silver ink for use in ink-jet printing and subsequent production of conductive tracks', *Macromolecular Rapid Communications*, 26(4), pp. 315–318. doi: 10.1002/marc.200400445.

Desai, S. B. *et al.* (2016) 'MoS_2 transistors with 1-nanometer gate lengths', *Science*, Volume 354, Issue 6308, pp. 99-102.

Diaham, S. *et al.* (2009) 'Polyimide passivation effect on high voltage 4H-SiC PiN diode breakdown voltage', *Materials Science Forum*, 615 617(January), pp. 695–698. doi: 10.4028/www.scientific.net/MSF.615-617.695.

Diao, Y. *et al.* (2013) 'Solution coating of large-area organic semiconductor thin films with aligned single-crystalline domains', *Nat Mater*, Volume 12, Issue 7, pp. 665-71.

Diao, Y. *et al.* (2015) 'Flow-enhanced solution printing of all-polymer solar cells', *Nature Communications*, Volume 6, pp. 7955.

Dimatix (2013) *Materials Printer Jettable Fluid Formulation Guidelines*.

Dinesh, M., Binu, B. N. and Massood, A. (2020) 'Recent Progress in Manufacturing Techniques of Printed and Flexible Sensors: A Review', *Biosensors (Basel)*, 10(12): 199. doi: 10.3390/bios10120199.

Ding, Z. *et al.* (2013) 'Improving the performance of organic thin film transistors formed on a vacuum flash-evaporated acrylate insulator', *Applied Physics Letters*, 103(23). doi: 10.1063/1.4839275.

Dodoo-Arhin, D. *et al.* (2016) 'Inkjet-printed graphene electrodes for dye-sensitized solar cells', *Carbon*, 105, pp. 33–41. doi: 10.1016/j.carbon.2016.04.012.

Dong, H., Carr, W. W. and Morris, J. F. (2006) 'An experimental study of drop-on-demand drop formation', *Physics of Fluids*, 18(7). doi: 10.1063/1.2217929.

Dong, Y. *et al.* (2017) 'An all-inkjet-printed flexible UV photodetector', *Nanoscale*, Volume 9, Issue 25, pp. 8580-8585.

EK, P. *et al.* (2015) 'All Ink-Jet Printed P3HT:PCBM Organic Solar Cells on

ITO-Coated Glass Substrate', *Journal of Nanoscience and Nanotechnology*, 15(11), pp. 8790–6.

El-Sayed, S. M. (2003) 'Optical investigations of the indium selenide glasses', *User Modeling and User-Adapted Interaction*, 72(2), pp. 169–175. doi: 10.1016/S0042-207X(03)00139-8.

Ellmer, K. (2001) 'Resistivity of polycrystalline zinc oxide films: current status and physical limit', *Journal of Physics D Applied Physics*, 34(21).

Epstein, A. J. *et al.* (1987) 'Insulator-to-metal transition in polyaniline: Effect of protonation in emeraldine', *Synthetic Metals*, Volume 21, Issues 1-3, pp. 63-70.

Fan, C. L. *et al.* (2016) 'Poly(4-vinylphenol) gate insulator with cross-linking using a rapid low-power microwave induction heating scheme for organic thin-film-transistors', *APL Materials*, Volume 4, Issue 3, pp. 036105.

Feng, W. *et al.* (2014) 'Back Gated Multilayer InSe Transistors with Enhanced Carrier Mobilities via the Suppression of Carrier Scattering from a Dielectric Interface', *Advanced Materials*, 26(38), pp. 6587–6593. doi: 10.1002/adma.201402427.

Feng, W. *et al.* (2015) 'Gate Modulation of Threshold Voltage Instability in Multilayer InSe Field Effect Transistors', *ACS Applied Materials and Interfaces*, 7(48), pp. 26691–26695. doi: 10.1021/acsami.5b08635.

Fernandes, I. J. *et al.* (2020) 'Silver nanoparticle conductive inks: synthesis, characterization, and fabrication of inkjet-printed flexible electrodes', *Scientific Reports*, Volume 10, pp. 8878.

Fishbeck, K. H. and Wright, A. T. (1986) ‘Shear mode transducer for drop-on-demand liquid ejector’. US.

Fortunato, E., Barquinha, P. and Martins, R. (2012) ‘Oxide semiconductor thin-film transistors: A review of recent advances’, *Advanced Materials*, 24(22), pp. 2945–2986. doi: 10.1002/adma.201103228.

Franco, P. and De Marco, I. (2020) ‘The Use of Poly(N-vinyl pyrrolidone) in the Delivery of Drugs: A Review’, *Polymers (Basel)*, Volume 12, Issue 5, pp. 1114.

Frazier, A. B. (1995) ‘Recent Applications of Polyimide to Micromachining Technology’, *IEEE Transactions on Industrial Electronics*, 42(5), pp. 442–448. doi: 10.1109/41.464605.

FUJIFILM (2012) *FUJIFILM Dimatix Materials Printer DMP-2800 Series User MANUAL*. Available at: https://www.manualslib.com/manual/1238531/Dimatix-Dmp-2800-Series.html (Accessed: 30 September 2015).

Fukukawa, K. I., Shibasaki, Y. and Ueda, M. (2004) ‘Efficient Catalyst for Low Temperature Solid-Phase Imidization of Poly(amic acid)’, *Chemistry Letters*, Volume 33, Issue 9, pp. 1156.

Fukukawa, K. I. and Ueda, M. (2008) ‘Recent progress of photosensitive polyimides’, *Polymer Journal*, 40(4), pp. 281–296. doi: 10.1295/polymj.PJ2007178.

Fuller, S. B., Wilhelm, E. J. and Jacobson, J. M. (2002) ‘Ink-jet printed nanoparticle microelectromechanical systems’, *Journal of*

Microelectromechanical Systems, Volume 11, pp. 54-60. doi: 10.1109/84.982863.

Gamerith, S. *et al.* (2007) 'Direct ink-jet printing of Ag-Cu nanoparticle and Ag-precursor based electrodes for OFET applications', *Advanced Functional Materials*, 17(16), pp. 3111–3118. doi: 10.1002/adfm.200600762.

Gan, H. Y. *et al.* (2009) 'Reduction of droplet volume by controlling actuating waveforms in inkjet printing for micro-pattern formation', *Journal of Micromechanics and Microengineering*, 19(5). doi: 10.1088/0960-1317/19/5/055010.

De Gans, B. J., Duineveld, P. C. and Schubert, U. S. (2004) 'Inkjet Printing of polymers: State of the art and future developments', *Advanced Materials*, Volume 16, pp. 203-213. doi: 10.1002/adma.200300385.

De Gans, B. J. *et al.* (2004) 'Ink-jet Printing Polymers and Polymer Libraries Using Micropipettes', *Macromolecular Rapid Communications*, 25(1), pp. 292–296. doi: 10.1002/marc.200300148.

Gao, W. *et al.* (2009) 'New insights into the structure and reduction of graphite oxide', *Nature Chemistry*. Nature Publishing Group, 1(5), pp. 403–408. doi: 10.1038/nchem.281.

Gao, W. *et al.* (2011) 'Direct laser writing of micro-supercapacitors on hydrated graphite oxide films', *Nature Nanotechnology*. Nature Publishing Group, 6(8), pp. 496–500. doi: 10.1038/nnano.2011.110.

Gebhardt, A. (2012) *Understanding Additive Manufacturing*. Hanser Publications.

Geim, A. K. and Novoselov, K. S. (2007) ‘The rise of graphene’, *Nature Materials*, 6, pp. 183–191. doi: 10.1142/9789814287005_0002.

Gibson, I., Rosen, D. W. and Stucker, B. (2010) *Additive Manufacturing Technologies Rapid Prototyping to Direct Digital Manufacturing*. Springer US.

Ginder, J. M. *et al.* (1987) ‘Insulator-to-metal transition in polyaniline’, *Solid State Communications*, Volume 63, Issue 2, pp. 97-101.

Giri, G. *et al.* (2011) ‘Tuning charge transport in solution-sheared organic semiconductors using lattice strain’, *Nature*. Nature Publishing Group, 480(7378), pp. 504–508. doi: 10.1038/nature10683.

Giri, G. *et al.* (2014) ‘High-mobility, aligned crystalline domains of tips-pentacene with metastable polymorphs through lateral confinement of crystal growth’, *Advanced Materials*, 26(3), pp. 487–493. doi: 10.1002/adma.201302439.

Gu, G. and Kane, M. G. (2008) ‘Moisture induced electron traps and hysteresis in pentacene based organic thin-film transistors’, *Applied Physics Letter*, Volume 92, pp. 053305.

Guan, Y. C. *et al.* (2016) ‘Fabrication of Laser-reduced Graphene Oxide in Liquid Nitrogen Environment’, *Scientific Reports*, Volume 6, pp. 28913.

Guo, Q., Bilal, O. R. and Hussein, M. I. (2011) ‘A Fast Method for Electronics Band Structure Calculations’, *ASME 2011 International Mechanical Engineering Congress and Exposition Conference*.

Guo, X. and Silva, S. R. P. (2008) ‘High-Performance Transistors by Design’, *Science*, Volume 320, Issue 5876, pp. 618-619.

Gürbulak, B. *et al.* (2014) 'Structural characterizations and optical properties of InSe and InSe:Ag semiconductors grown by Bridgman/Stockbarger technique', *Physica E: Low-Dimensional Systems and Nanostructures*, 64, pp. 106–111. doi: 10.1016/j.physe.2014.07.002.

Haffarzadeh, K. and Zervos, H. (2012) 'Conductive Ink Markets 2012-2018 Silver & Copper Inks & Pastes and Beyond', *USA: IDTechEX*.

Han, M. Y. *et al.* (2007) 'Energy Band-Gap Engineering of Graphene Nanoribbons', *Physical Review Letters*, 98(20), p. 206805.

Han, S. Y. *et al.* (2009) 'Inkjet-Printed High Mobility Transparent-Oxide Semiconductors', *Journal of Display Technology*, Volume 5, Issue 12, pp. 520.

He, D. *et al.* (2014) 'Two-dimensional quasi-freestanding molecular crystals for high-performance organic field-effect transistors', *Nature Communications*, Volume 5, pp. 5162.

He, D. *et al.* (2017) 'Ultrahigh mobility and efficient charge injection in monolayer organic thin-film transistors on boron nitride', *Science Advances*, Volume 3, pp. 1701186.

He, P. and Derby, B. (2017) 'Inkjet printing ultra-large graphene oxide flakes', *2D Materials*, 4(2).

He, Y. *et al.* (2017) 'A Tripropylene Glycol Diacrylate-based Polymeric Support Ink for Material Jetting', *Additive Manufacturing*. Elsevier B.V., 16, pp. 153–161. doi: 10.1016/j.addma.2017.06.001.

Hennek, J. W. *et al.* (2012) 'Reduced contact resistance in inkjet printed high-performance amorphous indium gallium zinc oxide transistors', *ACS Applied*

Materials and Interfaces, 4(3), pp. 1614–9.

Holbrook, H. D. and Seeley, W. J. (2013) *Basic Electronics*. Pergamon.

Hoshino, H., Schmutzler, R. W. and Hensel, F. (1976) 'High Temperature Vapour Pressure Curve and the Critical Point of Liquid Selenium.', *Berichte der Bunsengesellschaft/Physical Chemistry Chemical Physics*, 80(1), pp. 27–31. doi: 10.1002/bbpc.19760800108.

Huang, L. *et al.* (2011) 'Graphene-based conducting inks for direct inkjet printing of flexible conductive patterns and their applications in electric circuits and chemical sensors', *Nano Research*, 4, pp. 675–684.

Huang, W. *et al.* (2016) '2D layered group IIIA metal chalcogenides: Synthesis, properties and applications in electronics and optoelectronics', *CrystEngComm*. Royal Society of Chemistry, 18(22), pp. 3968–3984. doi: 10.1039/c5ce01986a.

Imai, K. *et al.* (1981) 'Phase diagram of In-Se system and crystal growth of indium monoselenide', *Journal of Crystal Growth*, 54(3), pp. 501–506.

Inoue, H., Sasaki, Y. and Ogawa, T. (1996) 'Comparison of one-pot and two-step polymerization of polyimide from BPDA/ODA', *Journal of Applied Polymer Science*, Volume 60, Issue 1, pp. 123-131.

Iravani, S. *et al.* (2014) 'Synthesis of silver nanoparticles: Chemical, physical and biological methods', *Research in Pharmaceutical Sciences*, 9(6), pp. 385–406.

Islam, S. and Saiduzzaman, M. (2013) 'Design of a Bank Vault Security System with Password, Thermal & Physical Interrupt Alarm', *International Journal of Scientific & Engineering Research*, 4(8), pp. 70–73.

Izuhara, D. and Swager, T. M. (2009) ‘Poly(Pyridinium Phenylene)s: Water-Soluble N-Type Polymers’, *Journal of the American*, 131(49), pp. 17724–17725.

Jang, J. *et al.* (2014) ‘Transparent high-performance thin film transistors from solution-processed SnO2 /ZrO2 gel-like precursors’, *Advanced Materials*, 25(7).

Jang, J. *et al.* (2015) ‘Fully Inkjet-Printed Transparent Oxide Thin Film Transistors Using a Fugitive Wettability Switch’, *Advanced Electronic Materials*, Volume 1, Issue 7, pp. 1500086.

Jensen, G. C. *et al.* (2011) ‘Inkjet-printed gold nanoparticle electrochemical arrays on plastic. Application to immunodetection of a cancer biomarker protein’, *Physical Chemistry Chemical Physics*, 13(11), pp. 4888–4894. doi: 10.1039/c0cp01755h.

Ji, D. *et al.* (2018) ‘Copolymer dielectrics with balanced chain-packing density and surface polarity for high-performance flexible organic electronics’, *Nature Communications*, Volume 9, pp. 2339.

Ji, T. *et al.* (2013) ‘The mechanism of the reaction of graphite oxide to reduced graphene oxide under ultraviolet irradiation’, *Carbon*. Elsevier Ltd, 54, pp. 412–418. doi: 10.1016/j.carbon.2012.11.057.

Jung, H. C. *et al.* (2007) ‘Studies on Inkjet-Printed Conducting Lines for Electronic Devices’, *Journal of Electronic Materials*, 36, pp. 1211–1218.

Juntunen, T. *et al.* (2018) ‘Inkjet Printed Large-Area Flexible Few-Layer Graphene Thermoelectrics’, *Advanced Functional Materials*, Volume 28, Issue 22, pp. 1800480.

Kaiser, C. J. (2014) *The Transistor Handbook*. CJ Publishing.

Kamyshny, A. and Magdassi, S. (2014) ‘Conductive nanomaterials for printed electronics’, *Small*, 10(17), pp. 3515–3535. doi: 10.1002/smll.201303000.

Kamyshny, A., Steinke, J. and Magdassi, S. (2011) ‘Metal-based inkjet inks for printed electronics’, *The Open Applied Physics Journal*, Volume 4, pp. 19-36. doi: 10.2174/1874183501104010019.

Kang, B. J. and Oh, J. H. (2016) ‘Influence of substrate temperature and overlap condition on the evaporation behavior of inkjet-printed semiconductor layers in organic thin film transistors’, *Thin Solid Films*, Volume 598, pp. 219-225.

Kang, J. S. *et al.* (2010) ‘Inkjet printed electronics using copper nanoparticle ink’, *Journal of Materials Science: Materials in Electronics*, 21(11), pp. 1213–1220. doi: 10.1007/s10854-009-0049-3.

Kang, J. S. *et al.* (2011) ‘Sintering of inkjet-printed silver nanoparticles at room temperature using intense pulsed light’, *Journal of Electronic Materials*, 40(11), pp. 2268–77.

Karim, N. *et al.* (2017) ‘All inkjet-printed graphene-based conductive patterns for wearable e-textile applications’, *Journal of Materials Chemistry C*. Royal Society of Chemistry, 5(44), pp. 11640–11648. doi: 10.1039/c7tc03669h.

Katsnelson, M. I. (2012) *Graphene: Carbon in Two Dimensions*. Cambridge University Press.

Kazakova, O., Panchal, V. and Burnett, T. L. (2013) ‘Prevention of graphene restacking for performance boost of supercapacitors-a review’, *Crystals*, 3(1), pp. 191–233. doi: 10.3390/cryst3010191.

Keskinen, M. (2012) ‘End-of-life options for printed electronics’, *Waste*

Electrical and Electronic Equipment (WEEE) Handbook, pp. 352-364.

Killeen, K. and Barth, P. (2003) 'Flexible Circuit', *European Patent EP1304911A1*.

Kim, B. *et al.* (2014) 'High-speed, inkjet-printed carbon nanotube/zinc tin oxide hybrid complementary ring oscillators', *Nano Letters*, 14(6), pp. 3683–3687. doi: 10.1021/nl5016014.

Kim, H. S. *et al.* (2009) 'Intense pulsed light sintering of copper nanoink for printed electronics', *Applied Physics A: Materials Science and Processing*, 97(4), pp. 791–798. doi: 10.1007/s00339-009-5360-6.

Kim, H. T. and Park, J. K. (1997) 'Effect of Imidization Temperature and Spinning Condition on Structure of Polyimide Film Derived from Cyclobutanedianhydride and 2,2-Bis(4-aminophenoxyphenyl)propane', *Polymer Journal*, Volume 29, Issue 12, pp. 1002-1006.

Kim, J. S. *et al.* (2015) 'Tuning Mechanical and Optoelectrical Properties of Poly(3-hexylthiophene) through Systematic Regioregularity Control', *Macromolecules*, Volume 48, Issue 13, pp. 4339-4346.

Kim, K. S. *et al.* (2009) 'Large-scale pattern growth of graphene films for stretchable transparent electrodes', *Nature*. Nature Publishing Group, 457(7230), pp. 706–710. doi: 10.1038/nature07719.

Kim, S. R., Parvez, M. K. and Chhowalla, M. (2009) 'UV-reduction of graphene oxide and its application as an interfacial layer to reduce the back-transport reactions in dye-sensitized solar cells', *Chemical Physics Letters*. Elsevier B.V., 483(1–3), pp. 124–127. doi: 10.1016/j.cplett.2009.10.066.

Kim, T. H., Han, C. G. and Song, C. K. (2008) 'Instability of threshold voltage under constant bias stress in pentacene thin film transistors employing polyvinylphenol gate dielectric', *Thin Solid Films*, Volume 516, pp. 1232.

Kipphan, H. (2001) 'Handbook of Print Media: Technologies and Production Methods', *Springer-Verlag Berlin Heidelberg*. doi: 10.1007/978-3-540-29900-4.

Klauk, H. *et al.* (2002) 'High-mobility polymer gate dielectric pentacene thin film transistors', *Journal of Applied Physics*, Volume 92, Issue 9, pp. 5259-5263.

Ko, S. H. *et al.* (2007) 'All-inkjet-printed flexible electronics fabrication on a polymer substrate by low-temperature high-resolution selective laser sintering of metal nanoparticles', *Nanotechnology*, 18(34). doi: 10.1088/0957-4484/18/34/345202.

Kuilla, T. *et al.* (2010) 'Recent advances in graphene based polymer composites', *Progress in Polymer Science (Oxford)*. Elsevier Ltd, 35(11), pp. 1350–1375. doi: 10.1016/j.progpolymsci.2010.07.005.

Kumar, P., Subrahmanyam, K. S. and Rao, C. N. R. (2011) 'Graphene produced by radiation-induced reduction of graphene oxide', *International Journal of Nanoscience*, 10(4–5), pp. 559–566. doi: 10.1142/S0219581X11008824.

Kumatani, A. *et al.* (2012) 'Solution-processed, Self-organized Organic Single Crystal Arrays with Controlled Crystal Orientation', *Scientific Reports*, Volume 2, pp. 393.

Kusmartsev, F. V. *et al.* (2014) 'Application of Graphene Within Optoelectronic Devices and Transistors', in *Applied Spectroscopy and the Science of*

Nanomaterials. Springer, Singapore, pp. 191–221.

Kymakis, E. *et al.* (2014) 'Laser-Assisted Reduction of Graphene Oxide for Flexible, Large-Area Optoelectronics', *IEEE Journal of Selected Topics in Quantum Electronics*, Volume 20, Issue 1, pp. 6573325.

Land, T. A. *et al.* (1992) 'STM investigation of single layer graphite structures produced on Pt(111) by hydrocarbon decomposition', *Surface Science*, 264(3), pp. 261–270.

Le, L. T. *et al.* (2011) 'Graphene supercapacitor electrodes fabricated by inkjet printing and thermal reduction of graphene oxide', *Electrochemistry Communications*. Elsevier B.V., 13(4), pp. 355–358. doi: 10.1016/j.elecom.2011.01.023.

Lee, C. *et al.* (2008) 'Measurement of the elastic properties and intrinsic strength of monolayer graphene', *Science*, 321(5887), pp. 385–388. doi: 10.1126/science.1157996.

Lee, D. H. *et al.* (2007) 'A General Route to Printable High-Mobility Transparent Amorphous Oxide Semiconductors', *Advanced Materials*, Volume 19, Issue 6, pp. 843-847.

Lee, D. H. *et al.* (2009) 'Inkjet printed high-mobility indium zinc tin oxide thin film transistors', *Journal of Materials Chemistry*, 19(20), pp. 3135–3137. doi: 10.1039/b822893k.

Lee, D. J., Oh, J. H. and Bae, H. S. (2010) 'Crack formation and substrate effects on electrical resistivity of inkjet-printed Ag lines', *Materials Letters*. Elsevier B.V., 64(9), pp. 1069–1072. doi: 10.1016/j.matlet.2010.02.014.

Lee, S. *et al.* (2006) 'Effects of hydroxyl groups in polymeric dielectrics on organic transistor performance', *Applied Physics Letter,* Volume 88, pp. 162109.

Lei, S. *et al.* (2014) 'Evolution of the electronic band structure and efficient photo-detection in atomic layers of InSe', *ACS Nano,* 8(2), pp. 1263–1272. doi: 10.1021/nn405036u.

Lei, S. *et al.* (2015) 'An atomically layered InSe avalanche photodetector', *Nano Letters,* 15(5), pp. 3048–3055. doi: 10.1021/acs.nanolett.5b00016.

Li, J. *et al.* (2013) 'Efficient inkjet printing of graphene', *Advanced Materials,* 25(29), pp. 3985–3992. doi: 10.1002/adma.201300361.

Li, M. *et al.* (2012) 'Recent developments and applications of screen-printed electrodes in enviromental assays-review', *Analytica Chimica Acta*, Volume 734, pp. 31-44.

Li, P. *et al.* (2017) 'Preparation of Graphene Oxide-Based Ink for Inkjet Printing', *Journal of Nanoscience and Nanotechnology*, 18(1), pp. 713–718. doi: 10.1166/jnn.2018.13942.

Li, X. *et al.* (2009) 'Large-area synthesis of high-quality and uniform graphene films on copper foils', *Science,* 324(5932), pp. 1312–1314. doi: 10.1126/science.1171245.

Li, Y. *et al.* (2017) 'All Inkjet-Printed Metal-Oxide Thin-Film Transistor Array with Good Stability and Uniformity Using Surface-Energy Patterns', *ACS Applied Materials & Interfaces,* Volume 9, Issue 9, pp. 8194-8200.

Lin, J. *et al.* (2010) 'Gating of single-layer graphene with single-stranded deoxyribonucleic acids', *Small,* 6(10), pp. 1150–1155. doi:

10.1002/smll.200902379.

Lin, Y. *et al.* (2009) 'Operation of Graphene Transistors at Gigahertz Frequencies', *Nano Letters*, Volume 9, Issue 1, pp. 422-426.

Liu, D. and Wicklund, J. (2014) *Graphene – A Two-Dimensional Dirac Material*. Royal Institute of Technology (KTH).

Liu, Q. and Orme, M. (2001) 'High precision solder droplet printing technology and the state-of-the-art', *Journal of Materials Processing Technology*, 115(3), pp. 271–283. doi: 10.1016/S0924-0136(01)00740-3.

Liu, Y., Cui, T. and Varahramyan, K. (2003) 'All-polymer capacitor fabricated with inkjet printing technique', *Solid-State Electronics*, 47(9), pp. 1543–1548. doi: 10.1016/S0038-1101(03)00082-0.

Liu, Y. L., Hsu, C. Y. and Wu, C. S. (2003) 'Polyimides possessing bulky phosphorus groups: Synthesis and characterization', *Journal of Applied Polymer Science*, 89(3), pp. 791–796. doi: 10.1002/app.12292.

Lorenz, A. *et al.* (2015) 'Comprehensive Comparison of Different Fine Line Printing Technologies Addressing the Seed and Plate Approach with Ni-Cu-Plating', *Proceedings of the 30th EUPVSEC 2015*, pp. 732-736.

Magdassi, S. and Moshe, M. Ben (2003) 'Patterning of organic nanoparticles by ink-jet printing of microemulsions', *Langmuir*, 19(3), pp. 939–942. doi: 10.1021/la026439h.

Majee, S. *et al.* (2016) 'Scalable inkjet printing of shear-exfoliated graphene transparent conductive films', *Carbon*. Elsevier Ltd, 102, pp. 51–57. doi: 10.1016/j.carbon.2016.02.013.

Mak. K. F. *et al.* (2016) 'Atomically Thin MoS_2 : A New Direct-Gap Semiconductor', *Physical Review Letters*, Volume 105, Issue 13, pp. 136805.

Marcano, D. C. *et al.* (2010) 'Improved synthesis of graphene oxide', *ACS Nano*, 4(8), pp. 4806–4814. doi: 10.1021/nn1006368.

Mas-Torrent, M. and Rovira, C. (2008) 'Novel small molecules for organic field-effect transistors: towards processability and high performance', *Chemical Society Reviews*, 37, pp. 827–838.

McAllister, M. J. *et al.* (2007) 'Single sheet functionalized graphene by oxidation and thermal expansion of graphite', *Chemistry of Materials*, 19(18), pp. 4396–4404. doi: 10.1021/cm0630800.

McCullough, R. D. and Lowe, R. D. (1992) 'Enhanced electrical conductivity in regioselectively synthesized poly(3-alkylthiophenes)', *Journal of the Chemical Society Chemical Communications*, 1(1).

McKinley, G. H. and Renardy, M. (2011) 'Wolfgang von Ohnesorge', *Physics of Fluids*, 23(12). doi: 10.1063/1.3663616.

Meixner, R. M. *et al.* (2008) 'Characterization of polymer inks for drop-on-demand printing systems', *Microsystem Technologies*, 14(8), pp. 1137–1142.

Meyers, T. *et al.* (2017) 'Low-voltage C8-BTBT thin-film transistors for flexible electronics', *Materials Today: Proceedings*. Elsevier Ltd, 4, pp. S232–S236. doi: 10.1016/j.matpr.2017.09.192.

Min, K. and Aluru, N. R. (2011) 'Mechanical properties of graphene under shear deformation', *Applied Physics Letters*, 98(1), pp. 1–3. doi: 10.1063/1.3534787.

Minemawari, H. *et al.* (2011) 'Inkjet printing of single-crystal films', *Nature*.

Nature Publishing Group, 475(7356), pp. 364–367. doi: 10.1038/nature10313.

Mo, L. *et al.* (2019) 'Silver Nanoparticles Based Ink with Moderate Sintering in Flexible and Printed Electronics', *International Journal of Molecular Sciences*, Volume 20, Issue 9, pp. 2124.

Mohan, V. B. *et al.* (2018) 'Graphene-based materials and their composites: A review on production, applications and product limitations', *Composites Part B: Engineering*. Elsevier, 142(December 2017), pp. 200–220. doi: 10.1016/j.compositesb.2018.01.013.

Molesa, S. *et al.* (2003) 'High-quality inkjet-printed multilevel interconnects and inductive components on plastic for ultrra-low-cost RFID applications', *Materials Research Society Symposia Proceedings*, Volume 769, pp. 1-6.

Moon, J. S. *et al.* (2009) 'Epitaxial-Graphene RF Field-Effect Transistors on Si-Face 6H-SiC Substrates', *IEEE Electron Device Letters*, Volume 30, Issue 6, pp. 650-652.

Mortimer, R. J., Dyer, A. L. and Reynolds, J. R. (2006) 'Electrochromic organic and polymeric materials for display applications', *Displays*, 27(1), pp. 2–18. doi: 10.1016/j.displa.2005.03.003.

Mouras, S. *et al.* (1988) 'Synthesis of first stage graphite intercalation compounds with fluorides', *Chemlnform*, 19(31), pp. 572–582. Available at: https://www.researchgate.net/profile/Sylvie_Mouras/publication/277997801_Synthesis_of_first_stage_graphite_intercalation_compounds_with_fluorides/links/59dbcc57aca2728e2018301f/Synthesis-of-first-stage-graphite-intercalation-compounds-with-fluorides.pdf%250.

Mudd, G. W. *et al.* (2013) 'Tuning the bandgap of exfoliated InSe nanosheets by quantum confinement', *Advanced Materials*, 25(40), pp. 5714–5718. doi: 10.1002/adma.201302616.

Mudd, G. W. *et al.* (2015) 'High Broad-Band Photoresponsivity of Mechanically Formed InSe-Graphene van der Waals Heterostructures', *Advanced Materials*, 27(25), pp. 3760–3766. doi: 10.1002/adma.201500889.

Mudd, G. W. *et al.* (2016) 'The direct-to-indirect band gap crossover in two-dimensional van der Waals Indium Selenide crystals', *Scientific Reports*. Nature Publishing Group, 6, pp. 1–10. doi: 10.1038/srep39619.

Naiman, M. (1965) 'Sudden Steam Printer'. U.S.

Newman, J. D., Turner, A. P. F. and G. Marrazza (1992) 'Ink-jet printing for the fabrication of amperometric glucose biosensors', *Analytica Chimica Acta*, 262(1), pp. 13–17.

Nicolas, Y. *et al.* (2012) 'TIPS-triphenodioxazine versus TIPS-pentacene: Enhanced electron mobility for n-type organic field-effect transistors', *Organic Electronics*, Volume 13, Issue 8, pp. 1392-1400.

Nir, M. *et al.* (2009) 'Electrically Conductive Inks for Inkjet Printing', *Handbook of Chemistry of Inkjet Inks*, pp. 225-254 doi: 10.1142/9789812818225_0012.

Noh, Y. H. *et al.* (2006) 'Root cause of hysteresis in organic thin film transistor with polymer dielectric', *Organic Electronics*, Volume 7, Issue 5, pp. 271-275.

Van Noorden, R. (2006) 'Moving towards a graphene world', *Nature*, 442(7100), pp. 228–229. doi: 10.1038/442228a.

Van Noorden, R. (2011) ‘Chemistry: The trials of new carbon’, *Nature*, 469(7328), pp. 14–16. doi: 10.1038/469014a.

Novoselov, K. S. *et al.* (2004) ‘Electric Field Effect in Atomically Thin Carbon Films’, *Science*, 5(1), pp. 1–12. doi: 10.1126/science.aab1343.

Norita, S. *et al.* (2015) ‘Inkjet-printed copper electrodes using photonic sintering and their application to organic thin-film transistors’, *Organic Electronics*, volume 25, pp. 131-134.

Nur, H. M. *et al.* (2002) ‘Ink-jet printing of gold conductive tracks’, *Journal of materials Science: Materials in Electronics*, 13(4), pp. 213–219.

NXP freescale semiconductor (2009) ‘Field Effect Transistors in Theory and Practice’, *AN211A Application note*, pp. 1–11.

Ochoteco, E. *et al.* (2010) ‘Tactile sensors based on conductive polymers’, *Microsystems Technology*, Volume 16, pp. 765-776. doi: 10.1117/12.821627.

Ohashi, Y. *et al.* (1997) ‘Size Effect inthe In-plane Electrical Resistivity of Very Thin Graphite Crystals’, *Tanso*, 1997(180), pp. 235–238. doi: 10.7209/tanso.1997.235.

Ohta, T. *et al.* (2006) ‘Controlling the electronic structure of bilayer graphene’, *Science*, 313(5789), pp. 951–954. doi: 10.1126/science.1130681.

Ovid’ko, I. A. and Sheinerman, A. G. (2013) ‘Cracks at disclinated grain boundaries in graphene’, *Journal of Physics D Applied Physics*, 46(34).

Panchal, V. *et al.* (2012) ‘Small epitaxial graphene devices for magnetosensing applications’, *Journal of Applied Physics*, 111(7), pp. 4–6. doi: 10.1063/1.3677769.

Panchal, V. *et al.* (2013) 'Epitaxial graphene sensors for detection of small magnetic moments', *IEEE Transactions on Magnetics*, Volume 49, Issue 1, pp. 97-100.

Parashkov, R. *et al.* (2005) 'Large area electronics using printing methods', *Proceedings of the IEEE*, 93(7), pp. 1321–1329. doi: 10.1109/JPROC.2005.850304.

Parades, J. I. *et al.* (2011) 'Environmentally friendly approches toward the mass production of processable graphene from graphite oxide', *Journal of Materials Chemistry*, Volume 21, pp. 298-306.

Park, J. H. *et al.* (2003) 'Chemical Vapor Deposition of Indium Selenide and Gallium Selenide Thin Films from Mixed Alkyl/Dialkylselenophosphorylamides', *Chemistry of Materials*, 15(22), pp. 4205–4210. doi: 10.1021/cm0310420.

Park, S. *et al.* (2011) 'Hydrazine-reduction of graphite- and graphene oxide', *Carbon*. Elsevier Ltd, 49(9), pp. 3019–3023. doi: 10.1016/j.carbon.2011.02.071.

Park, S. K., Jackson, T. N. and Mourey, D. A. (2007) 'High mobility solution processed 6,13-bis(triisopropyl-silylethynyl) pentacene organic thin film transistors', *Applied Physics Letters*, Volume 91, Issue 6, pp. 063514.

Payne, M. M. *et al.* (2005) 'Organic Field-Effect Transistors from Solution-Depositred Functionalized Acenes with Mobilities as High as 1 $cm^2/V \cdot s$', *Journal of the American Chemical Society*, Volume 127, Issue 14, pp. 4986-4987.

Pei, S. *et al.* (2010) 'Direct reduction of graphene oxide films into highly

conductive and flexible graphene films by hydrohalic acids', *Carbon*. Elsevier Ltd, 48(15), pp. 4466–4474. doi: 10.1016/j.carbon.2010.08.006.

Pei, S. and Cheng, H. M. (2012) 'The reduction of graphene oxide', *Carbon*. Elsevier Ltd, 50(9), pp. 3210–3228. doi: 10.1016/j.carbon.2011.11.010.

Perelaer, J. *et al.* (2012) 'Roll-to-roll compatible sintering of inkjet printed features by photonic and microwave exposure: From non-conductive ink to 40% bulk silver conductivity in less than 15 seconds', *Advanced Materials*, 24(19), pp. 2620–2625. doi: 10.1002/adma.201104417.

Perelaer, J., De Gans, B. J. and Schubert, U. S. (2006) 'Ink-jet printing and microwave sintering of conductive silver tracks', *Advanced Materials*, 18(16), pp. 2101–2104. doi: 10.1002/adma.200502422.

Perelaer, J. and Schubert, U. S. (2010) 'Inkjet printing and alternative sintering of narrow conductive tracks on flexible substrates for plastic electronic applications', *Handbook of Radio Frequency Identification Fundamentals and Applications Design Methods and Solutions*, pp. 265-286. doi: 10.5772/7983.

Persaud, K. C. (2005) 'Polymers for chemical sensing', *Materials Today*, 8(4), pp. 38–44. doi: 10.1016/S1369-7021(05)00793-5.

Pique, A. *et al.* (2003) 'Laser processing of polymer thin films for chemical sensor appliccations', *Surface and Coatings Technology*, pp. 293-299.

Poelking, C. *et al.* (2014) 'Morphology and Charge Transport in P3HT: A Theorist's Perspective', in *P3HT Revisited – From Molecular Scale to Solar Cell Devices*, pp. 139–180.

Politano, A. *et al.* (2017) 'Indium selenide: An insight into electronic band

structure and surface excitations', *Scientific Reports*, 7(1), pp. 1–11. doi: 10.1038/s41598-017-03186-x.

Priyadarsini, S. *et al.* (2018) 'Graphene and graphene oxide as nanomaterials for medicine and biology application', *Journal of Nanostructure in Chemistry*. Springer Berlin Heidelberg, 8(2), pp. 123–137. doi: 10.1007/s40097-018-0265-6.

Qin, D., Xia, Y. and Whitesides, M. G. (2010) 'Soft lithgraphy for micro- and nanoscale patterning', *Nature Protocols*, Volume 5, pp. 491-502. doi: 10.1038/nprot.2009.234.

Radisavljevic, B. *et al.* (2011) 'Single-layer MoS2 transistors', *Nature Nanotechnology*, Volume 6, Issue 3, pp. 147-50.

Rajan, K. *et al.* (2016) 'Silver nanoparticle ink technology: State of the art', *Nanotechnology, Science and Applications*, 9, pp. 1–13. doi: 10.2147/NSA.S68080.

Rammohan, A. and Kumar, C. R. (2017) 'Performance analysis of photoresistor and phototransistor for automotive's halogen and xenon bulbs light output', *IOP Conference Series: Materials Science and Engineering*, 263(6). doi: 10.1088/1757-899X/263/6/062056.

Rapp, L. *et al.* (2011) 'Pulsed-laser printing of silver nanoparticles ink: control of morphological properties', *Optics Express*, 19(22), p. 21563. doi: 10.1364/oe.19.021563.

Rayleigh, Lord (1878) 'On the Instability of Jets', *Proceedings of the London Mathematical Society*, 14(June 1873), pp. 4–13.

Reese, C. *et al.* (2004) 'Organic thin film transistors', *Materials Today*. Elsevier Ltd, 7(9), pp. 20–27. doi: 10.1016/S1369-7021(04)00398-0.

Reese, C. and Bao, Z. (2007) 'Organic single-crystal field-effect transistors', *Materials Today*. Elsevier Ltd, 10(3), pp. 20–27. doi: 10.1016/S1369-7021(07)70016-0.

Reina, A. *et al.* (2009) 'Large area, few-layer graphene films on arbitrary substrates by chemical vapor deposition', *Nano Letters*, 9(1), pp. 30–35. doi: 10.1021/nl801827v.

Reis, N. and Derby, B. (2000) *Ink jet deposition of ceramic suspensions: Modelling and experiments of droplet formation*, *Materials Research Society Symposium - Proceedings*. doi: 10.1557/proc-625-117.

Riordan, M., Hoddeson, L. and Herring, C. (1999) 'The invention of the transistor', *Reviews of Modern Physics*, 71(SUPPL. 2). doi: 10.1103/revmodphys.71.s336.

Rivkin, T. *et al.* (2002) 'Direct write processing for photovoltaic cells', *Conference Record of the IEEE Photovoltaic Specialists Conference*, (May 2014), pp. 1326–1329. doi: 10.1109/pvsc.2002.1190854.

Rosa, P. (2015) 'Minimal Computation Structures for Visual Information Applications based on Printed Electronics', *PhD thesis.*

Ross, I. M. (1998) 'The Invention of the Transistor', *PROCEEDINGS OF THE IEEE*, 86(1).

Royo, J. F. S. *et al.* (2014) 'Electronic structure, optical properties, and lattice dynamics in atomically thin indium selenide flakes', *Nano Research*, 7(10), p.

1556.

Rozenberg, G. G. *et al.* (2002) 'Patterned low temperature copper-rich deposits using inkjet printing', *Applied Physics Letters*, 81(27), pp. 5249–51.

Ryu, K. S. *et al.* (2007) 'Polyaniline doped with dimethyl sulfate as a nucleophilic dopant and its electrochemical properties as an electrode in a lithium secondary battery and a redox supercapacitor', *Journal of Physical Chemistry B*, 111(4), pp. 731–739. doi: 10.1021/jp064243a.

Saby, J. S. (1952) 'Fused Impurity P-N-P Junction Transistors', *Proceedings of the I.R.E.*, 40(11), pp. 1951–1953.

Saidina, D. S. *et al.* (2019) 'Recent Development of Graphene-Based Ink and Other Conductive Material-Based Inks for Flexible Electronics', *Journal of Electronic Materials*, 48(6), pp. 3428–3450. doi: 10.1007/s11664-019-07183-w.

Saleh, E. *et al.* (2017) '3D Inkjet Printing of Electronics Using UV Conversion', *Advanced Materials Technologies*, 2(10), pp. 2–9. doi: 10.1002/admt.201700134.

Savage, N. (2009) 'Graphene makes transistors tunable', *IEEE Spectrum*, 46(9).

Scherzer, T. and Langguth, H. (2001) 'The effect of temperature on the induction period in the photoinitiated polymerization of tripropylene glycol diacrylate', *Nuclear Instruments and Methods in Physics Research Section B: Beam Interactions with Materials and Atoms*, Volume 185, Issues 1-4, pp. 276-282.

Schniepp, H. C. *et al.* (2006) 'Functionalized single graphene sheets derived from splitting graphite oxide', *Journal of Physical Chemistry B*, 110(17), pp. 8535–8539. doi: 10.1021/jp060936f.

Schmidt, E. W. (2001) ‘Hydrazine and Its Derivatives: Preparation, Properties, Applications’, *Wiley-Interscience*, New York, 2011.

Schwierz, F. (2010) ‘Graphene transistors’, *Nature Nanotechnology*. Nature Publishing Group, 5(7), pp. 487–496. doi: 10.1038/nnano.2010.89.

Secor, E. B. *et al.* (2013) ‘Inkjet printing of high conductivity, flexible graphene patterns’, *Journal of Physical Chemistry Letters*, 4(8), pp. 1347–1351. doi: 10.1021/jz400644c.

Seeton, C. J. (2006) ‘Viscosity-Temperature Correlation for Liquids’, *Tribology Letters*, 22, pp. 67–78.

Segura, A. (2018) ‘Layered indium selenide under high pressure: A review’, *Crystals*, 8(5). doi: 10.3390/cryst8050206.

Shen, J. *et al.* (2009) ‘Fast and facile preparation of graphene oxide and reduced graphene oxide nanoplatelets’, *Chemistry of Materials*, 21(15), pp. 3514–3520. doi: 10.1021/cm901247t.

Shen, Y. and Lua, A. C. (2013) ‘A facile method for the large-scale continuous synthesis of graphene sheets using a novel catalyst’, *Scientific Reports*, 3, pp. 1–6. doi: 10.1038/srep03037.

Shin, D. *et al.* (2018) ‘Phonon-driven spin-Floquet magneto-valleytronics in MoS2’, *Nature Communications*, Volume 9, Issue 1, pp. 1-8.

Shin, D. Y. and Kim, I. (2009) ‘Self-patterning of fine metal electrodes by means of the formation of isolated silver nanoclusters embedded in polyaniline’, *Nanotechnology*, Volume 20.

Shockley, W. (1949) ‘The Theory of p-n Junctions in Semiconductors and p-n

Junction Transistors', *Bell System Technical Journal*, 28(3), pp. 435–489.

Shockley, W., Sparks, M. and Teal, G. K. (1951) 'p − n Junction Transistors', *Physical Review*, 83(1).

De Silva, K. K. H. *et al.* (2017) 'Chemical reduction of graphene oxide using green reductants', *Carbon*, Volume 119, pp. 190-199.

Simpson, M. M. and Janna, W. (2008) 'Newtonian and Non-Newtonian Fluids: Velocity Profiles, Viscosity Data, and Laminar Flow Friction Factor Equations for Flow in a Circular Duct', *ASME 2008 International Mechanical Engineering Congress and Exposition Conference*. doi: 10.1115/IMECE2008-67611.

Singh, V. *et al.* (2011) 'Graphene based materials: Past, present and future', *Progress in Materials Science*. Elsevier Ltd, 56(8), pp. 1178–1271. doi: 10.1016/j.pmatsci.2011.03.003.

Sirringhaus, H., Tessler, N. and Friend, R. H. (1998) 'Integrated optoelectronic devices based on conjugated polymers', *Science*, 280(5370), pp. 1741–1744.

Smirnov, V. A. *et al.* (2011) 'Photoreduction of graphite oxide', *High Energy Chemistry*, 45(1), pp. 57–61. doi: 10.1134/S0018143911010176.

Smith, P. J. *et al.* (2006) 'Direct ink-jet printing and low temperature conversion of conductive silver patterns', *Journal of Materials Science*, Volume 41, pp. 4153-4158.

Speakman, S. P. *et al.* (2001) 'High performance organic semiconducting thin films: Ink jet printed polythiophene [rr-P3HT]', *Organic Electronics*, Volume 2, Issue 2, pp. 65-73.

Sroog, C. E. (1967) 'Polyimides', *Journal of polymer science: Part C*, 16, pp.

1191–1209.

Stankovich, S. *et al.* (2006) ‘Stable aqueous dispersions of graphitic nanoplatelets via the reduction of exfoliated graphite oxide in the presence of poly(sodium 4-styrenesulfonate)’, *Journal of Materials Chemistry*, Volume 16, pp. 155-158.

Stankovich, S. *et al.* (2016) ‘Graphene-based composite materials’, *Nature*, Volume 442, pp. 282-6.

Stankovich, S. *et al.* (2007) ‘Synthesis of graphene-based nanosheets via chemical reduction of exfoliated graphite oxide’, *Carbon*, 45(7), pp. 1558–1565. doi: 10.1016/j.carbon.2007.02.034.

Sucharitakul, S. *et al.* (2015) ‘Intrinsic Electron Mobility Exceeding 103 cm2/(V s) in Multilayer InSe FETs’, *Nano Letters*, 15(6), pp. 3815–3819. doi: 10.1021/acs.nanolett.5b00493.

Suk, J. W. *et al.* (2011) ‘Transfer of CVD-grown monolayer graphene onto arbitrary substrates’, *ACS Nano*, 5(9), pp. 6916–6924. doi: 10.1021/nn201207c.

Sweet, R. G. (1965) ‘High-frequency oscillography with electrostatically deflected ink jets’, *Review of Scientific Instruments*, 36, pp. 131–6.

Szymczyk, K., Szaniawska, M. and Taraba, A. (2018) ‘Micellar Parameters of Aqueous Solutions of Tween 20 and 60 at Different Temperatures: Volumetric and Viscometric Study’, *Colloids and Interfaces*, 2(3), p. 34. doi: 10.3390/colloids2030034.

Takano, K. *et al.* (2009) ‘Fabrication of Terahertz Planar Metamaterials Using a Super-Fine Ink-Jet Printer’, *Applied Physics Express*, Volume 3, pp. 016701.

Tamalampudi, S. R. *et al.* (2014) 'High performance and bendable few-layered InSe photodetectors with broad spectral response', *Nano Letters*, 14(5), pp. 2800–2806. doi: 10.1021/nl500817g.

Tekin, E., Smith, P. J. and Schubert, U. S. (2008) 'Inkjet printing as a deposition and patterning tool for polymers and inorganic particles', *Soft Matter*, Volume 4, pp.703-713.

Tiwari, N. J., Tiwari, N. R. and Kim, S. K. (2011) 'Zero-dimensional, one-dimensional, two-dimensional and three-dimensional nanostructured materials for advanced electrochemical energy devices', *Progress in Materials Science*, Volume 57, Issue 4, pp. 724-803.

Teichler, A. *et al.* (2011) 'Film formation properties of inkjet printed poly(phenylene-ethynylene)- poly(phenylene-vinylene)s', *Thin Solid Films*. Elsevier B.V., 519(11), pp. 3695–3702. doi: 10.1016/j.tsf.2011.01.274.

Torrisi, F. *et al.* (2012) 'Inkjet-printed graphene electronics', *ACS Nano*, 6(4), pp. 2992–3006. doi: 10.1021/nn2044609.

Torrisi, L. *et al.* (2016) 'Reduction of graphene oxide foils by IR laser irradiation in air', *Journal of Instrumentation*, Volume 15, pp. C03006.

Tran, T. S., Dutta, N. K. and Choudhury, N. R. (2018) 'Graphene inks for printed flexible electronics: Graphene dispersions, ink formulations, printing techniques and applications', *Advances in Colloid and Interface Science*. Elsevier B.V., 261, pp. 41–61. doi: 10.1016/j.cis.2018.09.003.

Tran, T. S., Dutta, N. K. and Choudhury, N. R. (2019) 'Graphene-based inks for printing of planar micro-supercapacitors: A review', *Materials*, 12(6). doi:

10.3390/ma12060978.

Tseng, H. Y. and Subramanian, V. (2011) ‘All inkjet-printed, fully self-aligned transistors for low-cost circuit applications’, *Organic Electronics*. Elsevier B.V., 12(2), pp. 249–256. doi: 10.1016/j.orgel.2010.11.013.

Tyan, H. L., Liu, Y. C. and Wei, K. H. (1999) ‘Enhancement of imidization of poly(amic acid) through forming poly(amic acid)/organoclay nanocomposites’, *Polymer*, Volume 40, Issue 17, pp. 4877-4886.

Umeda, T., Kumaki, D. and Tokito, S. (2008) ‘High air stability of threshold voltage on gate bias stress in pentacene TFTs with a hydroxyl-free and amorphous fluoropolymer as gate insulators’, *Organic Electronics*, Volume 9, Issue 4, pp. 545-549.

Vadillo, D. C. *et al.* (2010) ‘The rheological characterization of linear viscoelasticity for ink jet fluids using piezo axial vibrator and torsion resonator rheometers’, *Journal of Rheology*, 54(4), pp. 781–795. doi: 10.1122/1.3439696.

Vaezi, M., Seitz, H. and Yang, S. (2013) ‘A review on 3D micro-additive manufacturing technologies’, *International Journal of Advanced Manufacturing Technology*, 67(5–8), pp. 1721–1754. doi: 10.1007/s00170-012-4605-2.

Vimanyu, B. and Patrick, J. S. (2020) ‘Printed Electronics as Prepared by Inkjet Printing’, *Materials (Basel)*, 13(3): 704. doi: 10.3390/ma13030704.

Virojanadara, C. *et al.* (2010) ‘Epitaxial graphene on 6 H -SiC and Li intercalation’, *Physical Review B*, 82(20).

Walk, D. *et al.* (2016) ‘High resolution inkjet printed OLED for display applications’, *In Proceedings of the Printing for Fabrication 2016 (NIP32),*

Volume 2016, pp. 469-471.

Wallace, P. R. (1947) 'The Band Theory of Graphite', *Physical Review*, 71(9), pp. 622–634.

Wang, T. *et al.* (2016) 'Fabrication of glucose biosensors by inkjet printing', *In Proceedings of the Printing for Fabrication 2016 (NIP32)*, 1Volume 28, pp. 83-84.

Wei, W. *et al.* (2017) 'High mobility solution-processed C_8-BTBT organic thin-film transistors via UV-ozone interface modification', *Journal of Materials Chemistry C*, Issue 40.

Weimer, P. K. (1962) 'The TFT A New Thin-Film Transistor', *Proceedings of the IRE*, 50(6), pp. 1462–1469.

Weng, B. *et al.* (2010) 'Printing conducting polymers', *Analyst*, 135, pp. 2779–2789.

Wilfried Linder (2016) *Digital Photogrammetry*. 4th edn. Springer-Verlag Berlin Heidelberg.

Williams, R. H. *et al.* (1977) 'The electronic band structure of indium selenide: Photoemission and theory', *Journal of Physics C: Solid State Physics*, 10(8), pp. 1223–1230. doi: 10.1088/0022-3719/10/8/023.

Wilson, W. C. and Atkinson, G. M. (2007) 'Review of Polyimides Used in the Manufacturing of Micro Systems', *Nasa*, (April), pp. 1–16.

Wu, B. *et al.* (2016) 'Precise, Self-Limited Epitaxy of Ultrathin Organic Semiconductors and Heterojunctions Tailored by van der Waals Interactions', *Nano Letters*, Volume 16, pp. 3754-3759.

Wu, S. *et al.* (2017) 'Inkjet printing of oxide thin film transistor arrays with small spacing with polymer-doped metal nitrate aqueous ink', *Journal of Materials Chemistry C*. Royal Society of Chemistry, 5(30), pp. 7495–7503. doi: 10.1039/c7tc01303e.

Wu, T. *et al.* (2011) 'Production of reduced graphene oxide by UV irradiation', *Journal of Nanoscience and Nanotechnology*, 11(11), pp. 10078–81.

Wulf, U., Krahlisch, M. and Richter, H. (2011) 'Scaling properties of ballistic nano-transistors', *Nanoscale Research Letters*. Springer Open Ltd, 6(1), pp. 1–8. doi: 10.1186/1556-276X-6-365.

Xia, Y. and Whitesides, M. G. (1998) 'Soft Lithography', *Annual Review of Materials Science*, Volume 28, pp. 153-184.

Xiao, P. *et al.* (2020) 'Study of Inkjet-Printed Silver Films Based on Nanoparticles and Metal-Organic Decomposition Inks with Different Curing Methods', *Micromachines (Basel)*, Volume 11, Issue 7, pp. 677.

Yan, H. *et al.* (2009) 'A high-mobility electron-transporting polymer for printed transistors', *Nature*, 457(7230), pp. 679–686. doi: 10.1038/nature07727.

Yang, G. *et al.* (2018) 'Structure of graphene and its disorders: a review', *Science and Technology of Advanced Materials*. Taylor & Francis, 19(1), pp. 613–648. doi: 10.1080/14686996.2018.1494493.

Yang, L. *et al.* (2014) 'Lattice Strain Effects on the optical properties of MoS_2 nanosheets', *Scientific Reports*, Volume 4, pp. 5649.

Yazdi, G. R., Iakimov, T. and Yakimova, R. (2016) 'Epitaxial graphene on SiC: A review of growth and characterization', *Crystals*, 6(5). doi:

10.3390/cryst6050053.

Yi, M. and Shen, Z. (2015) ‘A review on mechanical exfoliation for the scalable production of graphene’, *Journal of Materials Chemistry A*, 3(22), pp. 11700–11715. doi: 10.1039/c5ta00252d.

Yin, Z. *et al.* (2010) ‘Inkjet printing for flexible electronics: Marterials, processes and equipments’, *Chinese Science Bulletin*, Volume 55, pp. 3383-3407.

Ytterdal, T., Cheng, Y. and Fjeldly, T. A. (2003) *Device Modeling for Analog and RF CMOS Circuit Design*. Wiley.

Yu, Q. *et al.* (2008) ‘Graphene segregated on Ni surfaces and transferred to insulators’, *Applied Physics Letters*, 93(11). doi: 10.1063/1.2982585.

Yun, J. H. *et al.* (2008) ‘Fabrication of carbon nanotube sensor device by inkjet printing’, *3rd IEEE International Conference on Nano/Micro Engineered and Molecular Systems, NEMS*, 1, pp. 506–509. doi: 10.1109/NEMS.2008.4484382.

Yung, K. C. *et al.* (2010) ‘Inkjet printing and camera flash sintering of silver tracks on different substrates’, *Journal of Materials Processing Technology*, 210(15), pp. 2268–72.

Zangmeister, C. D. (2010) ‘Preparation and evaluation of graphite oxide reduced at 220 °c’, *Chemistry of Materials*, 22(19), pp. 5625–5629. doi: 10.1021/cm102005m.

Zhang, F. *et al.* (2016) ‘Inkjet printing of polyimide insulators for the 3D printing of dielectric materials for microelectronic applications’, *Journal of Applied Polymer Science*, 133(18), pp. 1–11. doi: 10.1002/app.43361.

Zhang, X. F. *et al.* (2016) 'Silver nanoparticles: Synthesis, characterization, properties, applications, and therapeutic approaches', *International Journal of Molecular Sciences*, 17(9). doi: 10.3390/ijms17091534.

Zhang, Y., Zhang, L. and Zhou, C. (2013) 'Review of Chemical Vapor Deposition of Graphene and Related Applications', *Accounts of Chemical Research*, Volume 46, Issue 10, pp. 2329-2339.

Zhao, X. *et al.* (2008) 'Spray deposition of polymer nanocomposite films for dielectric applications', *Materials Science and Engineering B: Solid-State Materials for Advanced Technology*, 151(2), pp. 140–145. doi: 10.1016/j.mseb.2008.05.024.

Zhou, L. *et al.* (2019) 'Preparation of polyimide films via microwave-assisted thermal imidization', *RSC Advances*, Volume 9, pp. 7314-7320.

Zhu, X. *et al.* (2018) 'Improving the performance of TIPS-pentacene thin film transistors via interface modification', *Chemical research in Chinese Universities*, 34(1), pp. 151–154.

Appendix A

The following table shows the relationship of saber angle, resolution, and drop spacing for the resolutions that the printer is capable of printing.

Table 5 - 1 Resolutions Relationships

Resolution [dpi]	Sabre angle [°]	Drop spacing [µm]		Resolution [dpi]	Sabre angle [°]	Drop spacing [µm]
5080.00	1.1	5		188.15	32.1	135
2540.00	2.3	10		181.43	33.4	140
1693.33	3.4	15		175.17	34.8	145
1270.00	4.5	20		169.33	36.2	150
1016.00	5.6	25		163.87	37.6	155
846.67	6.8	30		158.75	39.0	160
725.71	7.9	35		153.94	40.5	165
635.00	9.1	40		149.41	42.0	170
564.44	10.2	45		145.14	43.5	175
508.00	11.4	50		141.11	45.1	180
461.82	12.5	55		137.30	46.7	185
423.33	13.7	60		133.68	48.4	190
390.77	14.8	65		130.26	50.1	195
362.86	16.0	70		127.00	51.9	200
338.67	17.2	75		123.90	53.8	205
317.50	18.4	80		120.95	55.8	210
298.82	19.6	85		118.14	57.8	215
282.22	20.8	90		115.45	60.0	220
267.37	22.0	95		112.89	62.4	225
254.00	23.2	100		110.43	64.9	230
241.90	24.4	105		108.09	67.7	235
230.91	25.7	110		105.83	70.9	240
220.87	26.9	115		103.67	74.7	245
211.67	28.2	120		101.60	79.8	250
203.20	29.5	125		100.00	90	254
195.38	30.8	130				

Note: You may want to copy the above table and place it next to the DMP for future reference.